

# Earthquake Early Warning for Istanbul using Artificial Neural Networks

---

## Entwicklung eines Erdbeben-Frühwarnsystems für Istanbul unter Verwendung Künstlicher Neuronaler Netze

Zur Erlangung des akademischen Grades eines  
DOKTORS DER NATURWISSENSCHAFTEN  
von der Fakultät für Physik der Universität (TH)

Karlsruhe

genehmigte

DISSERTATION

von

Dipl.-Geophys. Maren Böse

aus Hamburg

Tag der mündlichen Prüfung:

10. Nov. 2006

Referent:

Prof. Dr. Friedemann Wenzel

Korreferent:

Prof. Dr. Mustafa Erdik



Für Anne-Merle C. und Anke B. -  
Danke, daß Ihr mich ein Stück begleitet habt!



# Abstract

Earthquake early warning (EEW) systems utilize the capability of modern real-time systems to process and transmit information faster than seismic waves propagate (3-6 km/s); they provide first information on forthcoming ground shaking prior to the arrival of seismic waves at potential user sites. Possible warning times range up to about 70 s, depending on the distances between seismic source, sensor and user sites. The main effort in the design and implementation of EEW systems in the last few years aims to increase warning times and thus to expand areas that can be effectively warned. This requires new strategies and methods for the rapid characterization of earthquakes: *on-site* warning systems are based on observations at single stations for the quick estimate of source parameters. The *on-site* warning approach is significantly faster than the network based *regional* strategy for early warning even though often at the expense of accuracy.

In this thesis, I have developed a methodology for EEW - called PreSEIS (Pre-SEISmic shaking) - that takes advantage of both, *regional* and *on-site* warning paradigms. PreSEIS integrates all available information from a small network of seismic sensors - similar to the *regional* warning approach. In contrast to *regional* warning, however, PreSEIS does not require that seismic waves have arrived at all sensors before warnings are issued. To confine the space of possible solutions for the position of the earthquake hypocenter, PreSEIS also includes information of non-triggered sensors. First estimates are available only 0.5 s after triggering of the first early warning sensor. PreSEIS is therewith as quick as the *on-site* warning approach that is based on single stations at a concurrent higher stability due to a higher number of involved stations. PreSEIS considers EEW as a problem of time-dependent non-linear inversion for source parameters from the available information at different sensors. With ongoing time more and more stations will be triggered by the propagating seismic waves and longer time series at the single sites will become available. Thus, estimates of source locations and magnitudes (and others) are continuously updated every 0.5 s. PreSEIS is based on *Two-Layer Feed-Forward* Neural Networks, that are used for the mapping of seismic observations onto likely source parameters, including hypocenter locations, earthquake magnitudes, rupture expansions and the Fourier amplitude spectrum of ground motion at a specified user site.

PreSEIS has been developed and tested using the example of the *Istanbul Earthquake Rapid Response and Early Warning System (IERREWS)*. The Turkish mega-city Istanbul is exposed to an extremely high seismic risk due to its closeness to seismic fault segments in the Sea of Marmara and the high concentration of human and industrial settlements in the Marmara region. Alike many other cities and regions in the world that are affected by a high seismic threat, the development and verification of a methodology for early warning for Istanbul is aggravated by the lack of moderate and strong motion records. This thesis demonstrates that synthetic records obtained, e.g., from the *Stochastic Simulation Method for Finite Faults* (Beresnev and Atkinson, 1997), can be used.



# Zusammenfassung

## Kapitel 1: Einleitung

Naturkatastrophen wie Erdbeben, vulkanische Eruptionen, Stürme, Überschwemmungen und Dürren fordern jedes Jahr tausende Menschenleben und verursachen Schäden in Millionenhöhe. Anzahl und Ausmaß von Katastrophen sind in den letzten Jahrzehnten deutlich gestiegen, insbesondere zurückzuführen auf die zunehmende Verletzbarkeit unserer Gesellschaft gegenüber den Naturgewalten. Das verbesserte Verständnis der physikalischen Ursachen von Risiko als Zusammenspiel von Gefährdung und Verletzbarkeit hat in den letzten Jahren zur Entwicklung und Verbesserung geeigneter Werkzeuge zur Vorhersage und Linderung von Desastern geführt. Im Bereich der Geowissenschaften, insbesondere bei den Erdbeben, ist man hierbei mit besonderen Herausforderungen konfrontiert: Erdbebenvorhersage im deterministischen Sinne ist aufgrund der Komplexität des Erdbebenprozesses und der Nichtzugänglichkeit der Verwerfungszonen zu direkten Messungen ein schwerwiegendes und ggf. unüberwindbares Problem. Auf der anderen Seite können Seismologen wie auch Ingenieure bereits heute der Gesellschaft entscheidende Unterstützung im Bereich der seismischen Risikominderung geben. Das Ziel der vorliegenden Dissertation ist die Entwicklung und Erprobung einer Methode zur Erdbeben-Frühwarnung - PreSEIS<sup>1</sup> genannt - die auf Verwendung Künstlicher Neuronaler Netze beruht.

Erdbeben-Frühwarnsysteme (EWS) bezeichnen Systeme, die getriggert durch ein entferntes Erdbeben noch vor Eintreffen seismischer Wellen entsprechende Warnungen an Nutzer geben können. Vorwarnzeiten sind abhängig von den jeweiligen Distanzen zwischen Erdbebenherd, seismischen Sensoren und Empfängern der Warnungen. In der Regel steht ein Zeitfenster von einigen Sekunden bis zu über eine Minute zur Verfügung. Innerhalb dieser Zeit muß das EWS die Gefahr durch das Beben anhand der zur Verfügung stehenden Information an einem oder mehreren Sensoren zuverlässig einschätzen können. Idealerweise werden Erdbebenwarnungen vollautomatisch in Maßnahmen zur Reduktion direkter als auch indirekter Schäden infolge des Erdbebens umgesetzt. So können beispielsweise durch Frühwarnsysteme getriggert Hochgeschwindigkeitszüge im Gefahrenbereich abgebremst, die Gaszufuhr zur Reduktion der Feuergefahr unterbrochen, empfindliche Fertigungsanlagen gesichert und Computerdaten zur Vermeidung von Datenverlusten gespeichert werden. Schließlich können Warnungen auch zur Unterstützung halbaktiver Schwingungstilgungen zur Vermeidung von Gebäudeversagen verwendet oder mittels Sirenen oder Rundfunk direkt an die Öffentlichkeit weitergegeben werden.

Entwickelt und demonstriert wird PreSEIS am Beispiel der Millionenstadt Istanbul in der türkischen Marmara-Region. Verwerfungen in der Marmara-See, die als westliche Fortsetzung der Nordanatolischen Störung interpretiert werden, verlaufen teilweise nur zwischen 15 und 20 km südlich von

---

<sup>1</sup>PreSEIS steht für *Pre-SEISmic shaking*, d.h. vor Einsatz seismischer Untergrundserschütterungen (im Bereich potentieller Empfänger von Warnungen).

Istanbul entfernt. Parsons et al. (2000) schätzen, dass sich in den kommenden 30 Jahren mit einer Wahrscheinlichkeit von über 60% ein starkes Erdbeben in der Marmara-Region ereignen wird, welches 40-50.000 Opfern fordern und Schäden von über USD  $1.1 \cdot 10^{10}$  verursachen werden kann (Erdik et al., 2003a). Alarmiert durch die beiden zerstörerischen Erdbeben von Düzce ( $M_w = 7.2$ ) und Kocaeli ( $M_w = 7.4$ ) im Jahr 1999 hat das *Kandilli Observatorium der Bosphorus Universität* in Istanbul in Zusammenarbeit mit Regierungsorganisationen im Herbst 2002 die Installation von zehn Frühwarnstationen in der Marmara-Region im Rahmen des *IERREWS (Istanbul Earthquake Rapid Response and Early Warning System)* erfolgreich abschließen können. Dieses Akzellerometernetz überträgt in Echtzeit die an den Sensoren gemessene Untergrundsbebewegungen zu zwei Datenzentren in Istanbul, wo die eingehenden Informationen zentral ausgewertet werden. Das momentane System basiert auf einfachen Schwellwerten, bei deren Überschreitung das System (nicht-öffentlichen) Alarm gibt (Erdik et al., 2003b). Mit PreSEIS soll eine alternative und zuverlässigere Methode zur Erdbeben-Frühwarnung entwickelt werden. Diese Dissertation wurde in Kooperation mit Prof. Dr. M. Erdik und seinem Team am Kandilli Observatorium durchgeführt.

Die vorliegende Arbeit gliedert sich grob in zwei Teile: Der erste Teil (Kapitel 2, 3 und 4) gibt nach einer kurzen Einführung in die Erzeugung und Ausbreitung von Erdbeben-Wellen eine Beschreibung der Simulation seismischer Untergrundsbebewegungen, auf deren Basis PreSEIS entwickelt werden wird. Im zweiten Teil der Arbeit (Kapitel 5 und 6) werden bereits existierende Frühwarnsysteme vorgestellt und schließlich die PreSEIS Methode entwickelt und demonstriert. Eine Zusammenfassung der wichtigsten Ergebnisse dieser Dissertation wird in Kapitel 7 gegeben.

### **Kapitel 2: Erdbebenherd, seismische Wellenausbreitung und lokale Standorteffekte**

Die Ausprägung der durch ein Erdbeben angeregten Bodenbewegung hängt von zahlreichen Einflußgrößen und Prozessen in den Bereichen des Erdbebenherdes, der seismischen Wellenausbreitung und des lokalen Untergrundes am Beobachtungsstandort ab. Die entscheidenden Faktoren werden diskutiert und quantifiziert. Dadurch werden die nötigen Grundlagen für das Verständnis der in Kapitel 3 eingeführten Methode zur *Stochastischen Simulation der seismischen Bodenbewegung für ausgedehnte Quellen* (Beresnev and Atkinson, 1997) gelegt.

### **Kapitel 3: Stochastische Simulation der seismischen Bodenbewegung**

Eine besondere Herausforderung bei der Entwicklung einer Methode zur Erdbeben-Frühwarnung für Istanbul stellt die geringe Seismizitätsrate in der Marmara-Region dar. PreSEIS wird aus diesem Grund mit Hilfe synthetischer Zeitreihen der seismischen Bodenbewegung entwickelt. Die stochastische Simulationsmethode, ursprünglich vorgestellt von Boore (1983), kombiniert das geschätzte Fourier Amplitudenspektrum der Untergrundsbebewegung mit einer randomisierten Phase. Dadurch wird eine einfache und geeignete Methode zur Simulation von Beschleunigungszeitreihen von mittelstarken bis starken Erdbeben im Frequenzbereich bis zu 10 Hz und ggf. höher zur Verfügung gestellt. Deterministische Modellierungen der Untergrundsbebewegung - wie z.B. mittels der *Finite Differenzen*-Methode - würden in diesem Frequenzband ein unerreicht hochauflösendes Untergrundsmodell erfordern. Die Besonderheit der stochastischen Simulation liegt gerade darin, dass Details sowohl des Erdbebenherdes als auch der Ausbreitungseffekte seismischer Wellen nicht spezifiziert werden müssen. Die Ausweitung der Punktquellen-Methode auf endliche Brüche nach Beresnev and Atkinson (1997) ist eine wichtige Erweiterung zur Berücksichtigung quellnaher Effekte



wie der Direktivität. Diese Effekte sollten aufgrund der geringen Quell-Empfänger-Distanzen in der Marmara-Region unbedingt berücksichtigt werden. Für die Anwendbarkeit der beschriebenen Simulationsmethode auf das Problem der Erdbeben-Frühwarnung in dieser Arbeit ist zunächst eine Erweiterung des für Scherwellen (S-Wellen) entwickelten Ansatzes auf Kompressionswellen (P-Wellen) erforderlich. P-Wellen sind aufgrund ihrer schnelleren Ausbreitung für die Frühwarnung essentiell: Die in der Regel amplitudenschwachen P-Wellen dienen im EWS oftmals als Informationsträger, die amplitudenstarken S-Wellen (und Oberflächenwellen) dagegen als Energieträger (Kanamori, 2005).

Mit Hilfe der Methode der *Stochastischen Simulation der seismischen Bodenbewegung für ausgedehnte Quellen* (Beresnev and Atkinson, 1997) wird für 280 Erdbebenszenarien ( $4.5 \leq M_w \leq 7.5$ ) an jeder der zehn Frühwarnstationen des *IERREWS* die gemittelte Horizontalkomponente der seismischen Bodenbeschleunigung modelliert. Um einen möglichst realistischen Datensatz zu erhalten, werden die der Literatur entnommenen Durchschnittswerte geophysikalischer Parameter in der Marmara-Region innerhalb physikalisch sinnvoller Grenzen zufällig variiert. Daneben enthält der Datensatz Erdbeben mit unterschiedlichen Versatzverteilungen auf den Bruchflächen, mit sowohl uni- als auch bi-direktionalen Bruchverläufen. Die Beben werden entlang der bekannten Verwerfungen in der Marmara-See in verschiedenen Tiefen simuliert. Weitere Beben werden zufällig in der Marmara-Region verteilt.

Definiert durch das Zeitfenster zwischen Erdbeben-Detektion an dem durch die P-Welle erstgetriggerten Sensor und der Ankunft amplitudenstarker S-Wellen betragen Vorwarnzeiten für Istanbul in der Regel zwischen 8 s und 15 s. Für die Erkennung des Gefahrenpotentials eines Erdbebens stehen somit im Schnitt weniger als 4 s zur Verfügung.

#### **Kapitel 4: Parameter der seismischen Bodenbewegung**

Eine grobe Bewertung der simulierten Zeitreihen erfolgt auf Grundlage von extrahierten Parametern der seismischen Bodenbewegung. So genannte *Abminderungsfunktionen* beschreiben die Abnahme dieser Parameter als Funktion der Entfernung vom Erdbebenherd. Für den stochastisch simulierten Datensatz werden Abminderungsfunktionen für Spitzenamplituden, spektrale Beschleunigungswerte und Intensitätsparameter bestimmt, und sowohl mit Abminderungsfunktionen aus anderen seismisch aktiven Regionen (Sadigh et al., 1997; Boore et al., 1997; Campbell, 1997; Erdik et al., 1985) als auch mit beobachteten Spitzenbeschleunigung von zwei Starkbeben (1999 Düzce, Kocaeli) und einem Schwachbeben (2004 Yalova) in der Westtürkei verglichen. In Distanzen ab 30 km wird bei den simulierten Daten ein stärkerer Abfall der Parameter beobachtet. Man beachte allerdings, dass Abminderungsfunktionen aus anderen Gebieten nur eingeschränkt übertragbar sind. Insbesondere die Verteilung der Versätze auf der Bruchfläche bestimmt entscheidend den Level der beobachteten Untergrundsbewegung.

#### **Kapitel 5: Erdbeben-Frühwarnung**

Erdbeben-Frühwarnsysteme existieren bereits in Japan (Nakamura, 1989; Saita and Nakamura, 2003), Taiwan (Wu and Teng, 2002; Wu and Kanamori, 2005a,b) und Mexiko (Espinosa-Aranda et al., 1995). In anderen Ländern wie Kalifornien (Allen and Kanamori, 2003; Cua, 2004; Kanamori, 2005; Wu et al., 2005), Rumänien (Wenzel et al., 1999, 2001) oder der Türkei (Erdik et al., 2003b) sind in den vergangenen Jahren bemerkenswerte Fortschritte erzielt worden. Neben den technologischen

Grundvoraussetzungen der Daten-Echtzeitverarbeitung und -kommunikation ist die Entwicklung schneller und zuverlässiger Algorithmen zur Einschätzung der von einem Erdbeben ausgehenden Gefahr erforderlich. Kapitel 5 beschreibt die bekanntesten Erdbeben-Frühwarnsysteme auf der Welt und gibt eine kurze Einführung in verwendete Algorithmen.

Grundsätzlich haben sich in den letzten Jahren zwei Haupttypen der Erdbeben-Frühwarnsysteme entwickelt: Die so genannten *regionalen* Frühwarnsysteme sind vergleichbar mit herkömmlichen seismischen Netzwerken mit einer Vielzahl an Sensoren, die über hunderte von Kilometern verteilt installiert sind und seismische Daten in Echtzeit zu einer zentralen Verarbeitungseinheit übermitteln. Solche Systeme sind in der Regel sehr zuverlässig bei der Ortung der Erdbebenquelle und der Bestimmung der Erdbebenmagnitude. Auf der anderen Seite haben regionale Frühwarnsysteme den Nachteil, dass sie relativ langsam sind, da zur Auswertung der seismischen Untergrundsbebung viele Stationen die sich ausbreitenden seismischen Wellen registriert haben müssen. Dadurch geht wertvolle Vorwarnzeit verloren. Auf der anderen Seite wurden in den letzten Jahren, insbesondere in Japan, Taiwan und in Kalifornien, Frühwarnsysteme entwickelt - die sog. *on-site* Systeme -, welche auf Beobachtungen an einzelnen Stationen basieren. Die Schwierigkeit bei dem *on-site*-Verfahren liegt vor allem darin, innerhalb weniger Sekunden die Mehrdeutigkeit zwischen Entfernung und Stärke des Erdbebens mit Hilfe einer einzigen Beschleunigungsaufzeichnung zu lösen. Während bei den regionalen Warnsystemen also die Verarbeitungsgeschwindigkeit den limitierenden Faktor darstellt, ist bei den *on-site* Systemen die Robustheit entscheidend. Bei Anwendungen in Taiwan und Kalifornien hat sich in jüngster Vergangenheit wiederholt gezeigt, dass eine gute Abschätzung der Magnitude letztendlich eine Mittelung über Einzelschätzungen von bis zu acht *on-site* Stationen erfordert (Wu et al., 2005; Wu and Kanamori, 2005b; Lockman and Allen, 2005). Dieses Vorgehen steht jedoch im Widerspruch zu der ursprünglichen Idee der *on-site* Systeme und reduziert wiederum die möglichen Vorwarnzeiten.

Bei der Entwicklung eines EWS können im Idealfall Lokationen von Erdbebenquellen von vornherein mit hoher Wahrscheinlichkeit eingegrenzt werden (*a priori* Information). Dieser Fall ist z.B. in Rumänien gegeben, wo das wichtigste Erdbebengebiet des Landes in den südöstlichen Karpaten - der sog. *Vrancea*-Region - liegt, ca. 130 km von der Hauptstadt Bukarest entfernt. Bei den *Vrancea*-Beben handelt es sich um mitteltiefe Beben, die ein enormes Schadenspotential aufweisen. Bei einem starken Beben der Magnitude  $M_w = 7.4$  im Jahr 1977 kamen über 1.000 Menschen ums Leben. In Zusammenarbeit mit Wissenschaftlern vom *National Institute of Earth Physics (NIEP)* in Bukarest und dem *Sonderforschungsbereich (SFB) 461: 'Starkbeben: Von geowissenschaftlichen Grundlagen zu Ingenieurmaßnahmen'* an der Universität Karlsruhe ist ein Frühwarnsystem für Bukarest entwickelt worden, welches mittels der epizentralen P-Wellenamplituden die parametrisierte Untergrundsbebung in Bukarest abschätzen kann. Am Ende des Kapitels 5 werden solche Skalierungsgesetze formuliert, ihre jeweiligen Unsicherheiten quantifiziert und schließlich mit Hilfe des Erdbebens vom 27. Oktober 2004 ( $M_w = 5.9$ ) verifiziert. An diesem Beben wird auch die grundsätzliche Verknüpfbarkeit von Erdbeben-Frühwarnung mit der *Urbanen Shakemap für Bukarest* (Wirth, 2004; Bartlakowski et al., 2006) demonstriert.

### **Kapitel 6: PreSEIS: Erdbeben-Frühwarnung durch Künstliche Neuronale Netze**

Die in dieser Arbeit entwickelte PreSEIS-Methode versucht unter Ausnutzung bzw. Vermeidung der jeweiligen Vor- und Nachteile *regionale* und *on-site* Systeme miteinander zu kombinieren. PreSEIS invertiert seismische Beobachtungsgrößen an mehreren Sensoren (hier: an den on-line Stationen des *IERREWS*) nach seismischen Herdparametern, wie der Lage des Hypozentrums und

der Momentenmagnitude. Die Methode basiert also wie die regionalen Frühwarnsysteme auf Stationsnetzwerken. Auf der anderen Seite setzt PreSEIS aber nicht voraus, dass die sich ausbreitenden seismischen Wellen bereits alle Stationen des Netzes erreicht haben: Auch eine nicht-getriggerte Station liefert entscheidende Hinweise auf die Lage des Erdbebenherdes, durch welche der Lösungsraum schrittweise mit fortschreitender Zeit eingeschränkt werden kann. Erste Schätzungen liefert PreSEIS bereits 0.5 s nachdem die P-Welle den ersten Sensor im Netzwerk erreicht und getriggert hat. Damit ist die Verarbeitungsgeschwindigkeit von PreSEIS vergleichbar mit der der *on-site* Systeme, ist aber zugleich stabiler, da eine Vielzahl an Sensormessungen in die Inversion eingehen. Mit fortschreitender Zeit werden mehr und mehr Sensoren die P-Wellen registrieren und längere Zeitreihen der Untergrundbewegungen an den verschiedenen Lokationen verfügbar. PreSEIS aktualisiert die prognostizierten Werte in regelmässigen Abständen von einer halben Sekunde.

Der Zusammenhang zwischen gemessener Bodenbewegung an den Sensoren und seismischen Herdparametern wird in PreSEIS über Künstliche Neuronale Netze (KNN) hergestellt. KNN können sowohl lineare als auch komplexe nicht-lineare Systeme und Prozesse modellieren. Sie bestehen aus einer Vielzahl einfacher Verarbeitungseinheiten - *Neuronen* genannt - die durch ein Netz gewichteter Verbindungen miteinander in Kontakt stehen. Die entsprechenden Gewichtungparameter werden iterativ mit Hilfe eines Trainingsdatensatzes mit bekannten Ein- und Ausgabewerten angepasst, indem der Netzwerkfehler schrittweise durch geeignete Algorithmen reduziert wird (z.B. Zell, 1994). Um eine zu starke Anpassung der Neuronalen Netze an die Trainingsdaten auf Kosten ihrer Verallgemeinerungsfähigkeit zu verhindern, wird der Netzwerkfehler parallel zum Trainingsdatensatz an einem unbekanntem Testdatensatz evaluiert: Das Training wird abgebrochen, sobald der Fehler für den zweiten Datensatz steigt (*early stopping rule*). Nach dem Training sind die Neuronalen Netze in der Lage, unbekannte Testdaten, die dem gleichen statistischen Prozess unterliegen, korrekt zu verarbeiten.

In dieser Arbeit werden so genannte *Zweischichtige Vorwärtsgerichtete Netzwerke* verwendet, in denen die Neuronen in einer Eingabe-, einer verborgenen und einer Ausgabeschicht angeordnet sind (z.B. Rojas, 1993). Die Komplexität solcher Netzwerke wird hauptsächlich durch die Anzahl der Neuronen in der verborgenen Schicht gesteuert (z.B. Bishop, 1995). Mit Hilfe eines unabhängigen Validierungsdatensatzes wird die für das hier vorliegende Inversionsproblem optimale Komplexität des Netzes bestimmt. Ein optimales Neuronales Netz wird dabei anhand seines Gesamtfehlers für bekannte Trainings- als auch unbekannte Testdaten bewertet (*accuracy-generalization capability trade-off*). Eine Netzwerkkonfiguration mit sechs verborgenen Neuronen stellt sich für das vorliegende Problem als optimal heraus.

PreSEIS wird auf vier Inversionsprobleme trainiert, zu deren Lösungen jeweils eigene Neuronale Netzwerkarchitekturen entworfen werden: Netzwerk *Hypo* bestimmt die geographischen Koordinaten und die Tiefe des Erdbebenherdes, Netzwerk  $M_w$  bestimmt die Momentenmagnitude, Netzwerk *Rupt* die Lage und Ausdehnung des seismischen Bruches und Netzwerk *Spec* das geglättete Fourier Amplitudenspektrum der Bodenbewegung an einer westlich von Istanbul gelegenen Industrieansiedlung. Die einzelnen Netzwerke sind natürlich nicht unabhängig voneinander, sondern stehen über Netzwerkein- und -ausgaben miteinander in Verbindung. Als parametrisierte Information erhalten die Neuronalen Netze dabei die relativen P-Welleneinsätze und die kumulative absolute Geschwindigkeit der Bodenbewegung an den verschiedenen Sensoren als Eingabe. Diese Parameter werden in regelmäßigen Abständen von 0.5 s aktualisiert und Schätzungen durch die Neuronalen Netze entsprechend neu berechnet. Zur Erhöhung der Stabilität der Inversionen werden in den Trainingsatz neben korrekt auch fehlerhaft gepickte Ereignisse integriert. Damit wird auch eine verbesserte Übertragbarkeit von PreSEIS auf Realdaten erzielt.

In vier Durchläufen mit jeweils unterschiedlicher Startinitialisierung der Netzwerkgewichte zu Beginn der Trainingsphase und zufällig vertauschten Trainings-, Test- und Validierungsdatensätzen (*Bootstrapping*), werden die Neuronale Netze auf die Inversionsaufgaben trainiert und die Modelle anschließend bewertet. Durch die Wiederholungen wird die Stabilität der Inversionsergebnisse sichergestellt. Für die Anpassung der Netzwerkgewichte während der Trainingsphase werden nacheinander drei Optimierungsalgorithmen getestet: (1) *Gradientenabstieg mit Momententerm* (Plaut et al., 1986), (2) *Resilient Propagation (RPROP)* (Riedmiller and Braun, 1993) und (3) *Levenberg-Marquardt* (Levenberg, 1944; Marquardt, 1963). Die Gradienten der Fehlerfunktion werden mit Hilfe des *Backpropagation* Algorithmus (Rumelhart et al., 1986) berechnet. Analysiert wird erstens der gesamte Datensatz mit allen 280 simulierten Erdbebenszenarien und zweitens zwei einzelne Szenarien im Detail.

Für alle drei Algorithmen wird mit fortschreitender Zeit eine deutliche Erhöhung der Genauigkeit bei den prognostizierten Herdparametern erzielt. Das bedeutet, dass zu jedem Zeitpunkt die Unsicherheit der Prognosen quantifizierbar wird. Wann und wie Nutzer auf Frühwarnungen reagieren sollten, hängt insbesondere von den erwarteten Folgekosten eines möglichen Schadenbebens bzw. Fehlalarms ab. Durch die Einbeziehung der Informationen von nicht-getriggerten Sensoren und der *a priori* Information aus dem Trainingsdatensatz, dass Erdbeben in der Regel um Verwerfungssegmente geclustert auftreten, werden in PreSEIS schnelle und gute Schätzungen der Herdparameter erzielt. Die besten Inversions-Modelle werden nach *Levenberg-Marquardt* Optimierung erhalten mit einem mittleren Lokalisierungsfehler von 8.8 km nach 0.5 s nach Triggerung und 5.9 km nach 4.0 s. In dem gleichen Zeitintervall kann der Magnitudenfehler von  $\pm 0.7$  auf  $\pm 0.5$  (Standardabweichung) reduziert werden. Die *Levenberg-Marquardt* Methode hat außerdem den Vorteil, dass sie wesentlich schneller zum Minimum der Fehlerfunktion konvergiert und dadurch deutlich weniger Trainingsiterationen benötigt werden. Während für den Gesamtdatensatz eine zeitliche Verbesserung der Abschätzung der Herdparameter beobachtet wird, kann bei einzelnen Szenarien eine zwischenzeitliche Verschlechterung der Prognosen auftreten. Verantwortlich sind hier die oben beschriebenen fehlerhaft gepickten Daten im Trainingsdatensatz, die die Neuronale Netze zu einer erhöhten Verallgemeinerung zwingen.

Kombiniert mit empirischen Abminderungsfunktionen können die geschätzten Herdlokationen und Magnituden zu punktuellen oder flächenhaften Prognosen der seismischer Bodenbewegung verwendet werden. Flächenhafte Abschätzungen der Bodenbewegung werden auch Alarmkarten (*alert maps*) genannt. Betreiber von Netzwerken wie z.B. für Transport, Elektrizität, Wasserversorgung oder Kommunikation, können Alarmkarten für eine schnelle Entscheidungsunterstützung nutzen, z.B. bei der Frage, welche Netzwerkknoten besonders gefährdet und welche Umkonfiguration der Netze jeweils sinnvoll erscheint, um Ausfallszeiten zu minimieren oder ganz zu vermeiden. Durch die Einbeziehung von Standorteffekten werden Alarmkarten deutlich verbessert. Magnituden- und standortabhängige Verstärkungsfaktoren für verschiedene Bodenklassen nach der NEHRP-Klassifizierung (Building Seismic Safety Council, 1995) werden in Kapitel 4 mit Hilfe der stochastischen Simulationen der Bodenbeschleunigung bestimmt. Eine weitere Verbesserung der Alarmkarten erfolgt durch die Einbeziehung dynamischer Brucheffekte wie der Direktivität. PreSEIS schätzt daher nicht nur die Lage des Hypozentrums, sondern auch die Ausdehnung des entsprechenden Bruches mit Hilfe des Neuronale Netzwerkes *Rupt* ab. In Abhängigkeit von der Bruchlänge und des Azimuts zwischen Bruch und einem gegebenen Ort können dadurch Direktivitätseffekte grob abgeschätzt werden.

Ausschlaggebend bei der Prognose der Untergrundsbebewegung ist in der Regel nicht die Genauigkeit der geschätzten Herdlokation und Magnitude, sondern die Zuverlässigkeit der empirischen Abminderungsfunktionen (Allen, 2005). Bei Realdaten werden insbesondere die lokalen Standorteffekte und ggf. nichtlineare Effekte eine entscheidende Rolle spielen, die in den Abminderungsfunktionen nur gemittelt berücksichtigt werden. Wie in dieser Arbeit anhand der stochastischen Simulationen gezeigt

wird, können Quelleffekte allein bereits eine Unsicherheit im Bereich des Faktors zwei verursachen (Kapitel 4). Aus dieser Problematik der Abminderungsfunktionen heraus, wird in dieser Arbeit ein weiterer Ansatz in PreSEIS verfolgt: die direkte Prognose der Untergrundsbewegung in Form des Fourier Amplitudenspektrums an einem vorgegebenen Ort ohne den Umweg über die empirischen Abminderungsfunktionen zu gehen (Netzwerk *Spec*, s.o.). Das bedeutet, dass in diesem Fall die Neuronale Netze selbst das lokale Dämpfungsverhalten auf die seismischen Wellen erlernen müssen. Anhand von zwei Szenarien wird am Ende von Kapitel 6 dieser viel versprechende Ansatz demonstriert.

## **Kapitel 7: Zusammenfassung und Ausblick**

In dieser Arbeit wird nach einer ausführlichen Einführung in die Erdbeben-Frühwarnung eine Methode (PreSEIS) zur Inversion von seismischen Herdparametern aus zeitabhängigen Beobachtungen an Sensoren innerhalb eines lokalen Netzwerkes entwickelt. PreSEIS verwendet dabei nur die zu dem jeweiligen Zeitpunkt der Inversion zur Verfügung stehenden Informationen an den Sensoren, um Größen wie die Erdbebenmagnitude oder Herdlokation mit Hilfe Künstlicher Neuronaler Netze abzuschätzen. Dabei wird auch die Information nicht-getriggelter Stationen (d.h. Sensoren, an denen noch keine seismischen Wellen angekommen sind) im Netz verwendet, da dadurch der Lösungsraum deutlich eingeschränkt werden kann. Daneben beinhalten die Trainingsdatensätze, mit denen die Neuronale Netze auf das Inversionsproblem trainiert werden, *a priori* Informationen über die Lage der Verwerfungssegmente, an denen Erdbeben geclustert auftreten. PreSEIS ist dadurch in der Lage, sehr schnelle und i.d.R. sehr genaue Abschätzung der Herdparameter zu geben, auf deren Basis Warnungen an potentielle Nutzer innerhalb der gefährdeten Region gegeben werden können. Durch die Vorhersage der wahrscheinlichen Ausdehnung des Bruches können Prognosen der seismischen Untergrundsbewegung, z.B. in Form von Alarmkarten deutlich verbessert werden. PreSEIS wird auf Grundlage von synthetischen Erdbebenaufzeichnungen entwickelt und getestet.

Eine Weiterentwicklung der PreSEIS Methode zur Erdbeben-Frühwarnung ist im Rahmen des *Seismic eArly warning For EuRope (SAFER)* (FP6-2005-Global-4) und des *BMBF/DFG-Sonderprogramm Geotechnologien - Frühwarnsysteme im Erdmanagement* mit der Entwicklung eines Erdbeben-Desaster-Information-Systems für die Marmara Region (*Earthquake Disaster Information System for the Marmara Region, Turkey (EDIM)*) geplant.



# Contents

<b>Abstract</b>	<b>i</b>
<b>Zusammenfassung</b>	<b>iii</b>
<b>1 Introduction</b>	<b>1</b>
1.1 Earthquake Risk Reduction . . . . .	1
1.2 Real-Time Earthquake Information Systems . . . . .	2
1.3 Seismic Hazard in Istanbul and the Marmara Region . . . . .	7
1.4 Outline of this Thesis . . . . .	8
<b>2 Earthquake Source, Path and Site Effects</b>	<b>11</b>
2.1 Earthquake Source Mechanism . . . . .	11
2.2 Path Effects . . . . .	15
2.3 Site Effects . . . . .	17
<b>3 Simulation of Seismic Ground Motion</b>	<b>23</b>
3.1 Common Methods for the Simulation of Seismic Ground Motion . . . . .	23
3.2 Stochastic Simulation of Seismic Ground Motion from Finite Faults . . . . .	24
3.3 Stochastic Simulation of Ground Motion from Finite Faults in the Marmara Region .	32
3.4 Discussions . . . . .	39
<b>4 Seismic Ground Motion Parameters</b>	<b>45</b>
4.1 Parameterization of Seismic Ground Motion . . . . .	45
4.2 Correlating Ground Motion Parameters with Fourier Amplitudes . . . . .	55
4.3 Attenuation Relationships for Seismic Ground Motion Parameters . . . . .	55
4.4 Attenuation Relationships for the Simulated Seismic Ground Motion in the Marmara Region . . . . .	57
4.5 Discussions . . . . .	66

<b>5</b>	<b>Earthquake Early Warning</b>	<b>71</b>
5.1	Design Paradigms for Earthquake Early Warning Systems . . . . .	71
5.2	Earthquake Early Warning Systems in Operation . . . . .	72
5.3	Algorithms for Earthquake Early Warning . . . . .	78
5.4	Discussions . . . . .	86
<b>6</b>	<b>PreSEIS: Earthquake Early Warning through Artificial Neural Networks</b>	<b>91</b>
6.1	Artificial Neural Networks (ANNs) . . . . .	91
6.2	PreSEIS: Estimates of Seismic Parameters Pre-SEISmic Shaking . . . . .	100
6.3	Discussions . . . . .	136
<b>7</b>	<b>Summary and Outlook</b>	<b>139</b>
7.1	Summary . . . . .	139
7.2	Outlook . . . . .	143
<b>A</b>	<b>Response to Earthquake Early Warnings</b>	<b>145</b>
<b>B</b>	<b>Simulated Earthquakes in the Marmara Region</b>	<b>147</b>
<b>C</b>	<b>Coefficients for the Attenuation Laws</b>	<b>155</b>
	<b>List of Figures</b>	<b>159</b>
	<b>References</b>	<b>163</b>
	<b>Used Software</b>	<b>177</b>
	<b>Danksagung / Acknowledgments</b>	<b>179</b>
	<b>Lebenslauf</b>	<b>181</b>



# Chapter 1

## Introduction

Tens of millions people are affected by natural hazards worldwide. Disasters<sup>1</sup> caused by earthquakes, volcanic eruptions, storms, floods and droughts kill thousands of humans and cause economic losses of  $10^9 - 10^{12}$  dollars each year. In 2004, for example, natural disasters claimed more than 180,000 casualties and USD  $1.45 \cdot 10^{11}$  economic losses (Munich Re, 2005); including the victims of the tsunami catastrophe<sup>2</sup> in South Asia on December 26, 2004, the number of deaths amounts to about 300,000.

Over the last decades the number and dimensions of disasters have significantly increased, mainly caused by a heightened vulnerability of society towards hazards. Human vulnerability is a result of complex socio-economic factors such as of population growth and migration, development processes, and interference with natural systems. The better knowledge of physical causes of disasters has in the last few years led to technical developments and enhancements of tools essential for the forecasting and prediction of disasters. In particular, systems for the surveillance of disaster related factors, such as crop status and river levels, as well as modeling techniques for providing possible scenarios have turned out to be useful instruments for risk reduction (EWCII, 2003).

In case of geo-hazards like earthquakes, however, progress is made only slowly. After numerous unsuccessful attempts to predict earthquakes (Wyss, 1997) the possibility of seismic forecasting is today doubted by the majority of experts. Difficulties in earthquake prediction with a reliable specification of time, location, and magnitude of a future earthquake within stated limits (*deterministic prediction*) arise above all from the heterogeneity of the Earth and the inaccessibility of fault zones to direct measurements. The likelihood of the occurrence of a major event depends in a highly non-linear way on fine details of physical parameters within a large volume around the rupture origin; uncertainties about the initial conditions severely limits the predictability of strong earthquakes.

### 1.1 Earthquake Risk Reduction

While most experts are sceptical about the heavy investment in studies of possible earthquake precursors (e.g., Geller et al., 1997), they predominantly agree on the fundamental benefit of earthquake

---

<sup>1</sup>"A disaster is a natural or man-made event that negatively affects life, property, livelihood or industry often resulting in permanent changes to human societies, ecosystems and environment. Disasters manifest as hazards exacerbating vulnerable conditions and exceeding individuals' and communities' means to survive and thrive....", Wikipedia Encyclopedia, 2005

<sup>2</sup>A catastrophe is a "...disaster on a larger scale...", Wikipedia Encyclopedia, 2005

risk<sup>3</sup> reduction from seismology and seismic engineering. Seismic risk reduction has the objectives to (Wieland, 2001):

- protect human lives and to avoid fatalities;
- minimize economic losses;
- maintain vital services;
- minimize operation and production interruptions;
- protect the environment and cultural heritage.

Knowledge and technology for earthquake-proof design are nowadays in many cases available. Poor ethics, low professional standards, as well as little regulation, however, make the enforcement of seismic codes - especially in poor countries - extremely difficult. The main problem pose non-engineered structures. Earthquake risk reduction can be optimized by combing seismic design and other preparative steps with protective measures during or immediately after a large earthquake (Wieland, 2001).

Measures for earthquake risk reduction can be chronologically decomposed in *pre-seismic*, *co-seismic* and *post-seismic* measures, i.e. measures taken several years before, during and immediately after the earthquake, respectively. Fig.1.1 gives an overview of the sequence of possible steps. Pre-seismic measures include seismic hazard assessment and risk evaluation, formulation and enforcement of seismic design codes, enforcement of existing buildings and facilities, elaboration of emergency plans, and informing and education about seismic risk. Recent progress in seismology, instrumentation and communication technologies can be used for the development of rapid and reliable *Real-Time Earthquake Information Systems*<sup>4</sup> (Kanamori et al., 1997). These systems have the purpose to provide rapid notification of earthquake parameters and estimates of ground motion during and immediately after an earthquake catastrophe. These information allow for determining locations where emergency response is needed most as well as for estimating the overall societal impact of the earthquake. Losses of lives and property by earthquake catastrophes can be reduced and recovery times shortened. Real-Time Earthquake Information Systems combine co-seismic measures like earthquake early warning and alert systems with post-seismic measures such as rapid response and aftershock warning systems (see Fig.1.1).

## 1.2 Real-Time Earthquake Information Systems

### 1.2.1 Components of a Real-Time Earthquake Information System

In this section the main components of a Real-Time Earthquake Information System - including earthquake early warning and alert systems as well as rapid response and aftershock warning systems (as shown in Figure 1.1) - are shortly described.

---

<sup>3</sup>"Risk is the potential harm that may arise from some [...] future event [here: earthquake]. [...] Risk combines the probability of a negative event occurring with how harmful that event would be.", Wikipedia Encyclopedia, 2005

<sup>4</sup>Information system means here "... a system that comprises [...] methods organized to collect, process, transmit, and disseminate data that represent [...] information.", Wikipedia Encyclopedia, 2005

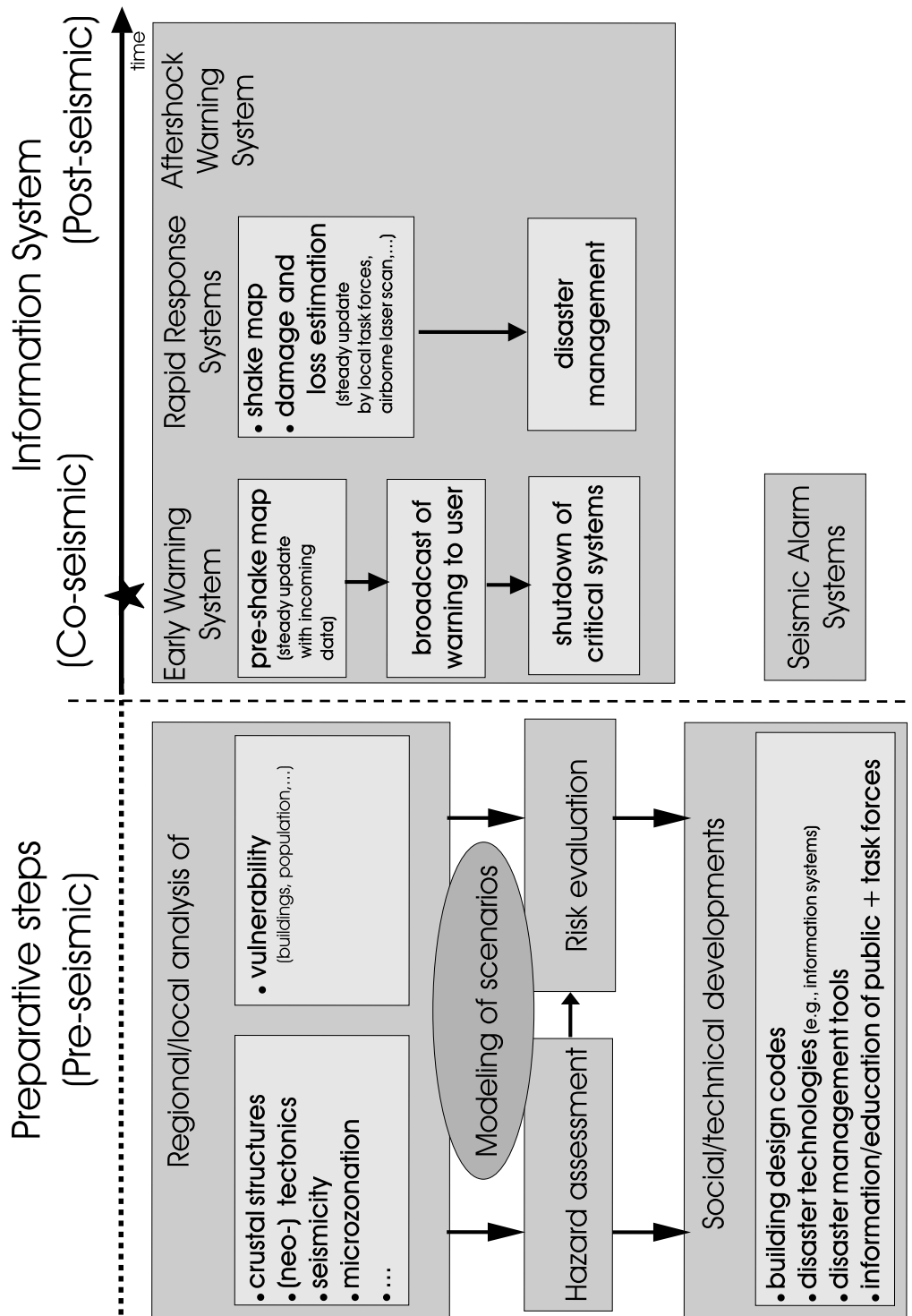


**Figure 1.1:** Preparative steps as well as co- and post-seismic components of a Real-Time Earthquake Information System for seismic risk reduction. The later include early warning, alert, rapid response and aftershock warning systems.

## 1. Earthquake Early Warning Systems

A basic module of Real-Time Earthquake Information Systems is the co-seismic earthquake (or seismic) early warning system. The importance of early warning systems for the mitigation of natural catastrophes such as earthquakes was pointed out by diverse national and international organizations in the last decade, as for example by the *International Strategy for Disaster Reduction (ISDR)*<sup>5</sup> on occasion of the *Second International Conference on Early Warning* in 2003 in Bonn, Germany (EWCII, 2003).

Seismic early warning systems provide warnings of imminent danger that can be either based on simple thresholds or on rapid estimates of the earthquake source parameters; early warning systems utilize the capability of modern real-time systems to process and transmit information faster than seismic waves propagate (3-6 km/s). The possible warning time is usually in the range of up to 70 seconds, depending on the distances between seismic source, seismic sensor and user sites.

The maximum achievable warning time of an earthquake early warning system  $\Delta t_w$  is defined by the time interval between the detection of the faster P-wave by a seismic sensor and the arrival of high-amplitude S-waves at the user site. For epicentral distances  $x_s$  of the sensor and  $x_u$  of the user site, as well as focal depth  $h$ , the warning time  $\Delta t_w$  can be approximated by

$$\Delta t_w \approx \frac{\sqrt{x_u^2 + h^2}}{\beta} - \frac{\sqrt{x_s^2 + h^2}}{\alpha} - \Delta t_p. \quad (1.1)$$

P- and S-waves are assumed to travel with average velocities  $\alpha$  and  $\beta$ , respectively.  $\Delta t_p$  is the time needed for data processing and data transmission which is in the range of a few seconds. For long earthquake ruptures Heaton (1985) proposes to define the warning time as the time interval between P-wave detection and the arrival of direct S-waves from the rupturing fault segment that is closest to the user site (which generally produces the strongest shaking); therewith the theoretical warning time is a few seconds longer than given by (1.1).

From the above descriptions it follows that the seismic stations in an earthquake early warning system - usually equipped with strong motion sensors to avoid saturation - are favorably deployed as close as possible to the seismic source. Early warning systems need a continuous real-time communication link either directly to a user (*on-site* warning system) or to a central processing facility and from there to one or more users (*regional* warning system). Common real-time telemetry systems rely on radio, satellite and telephone links. Modern GSM and UMTS technologies are also applied.

## 2. Seismic Alarm Systems

Seismic alarm (or alert) systems can be considered as the second co-seismic component of Real-Time Earthquake Information Systems. Yet, there are important differences to earthquake early warning systems: the seismic stations of an alarm system - usually also equipped with strong motion sensors - are installed directly in the user's building or premises. Potential users are, e.g., operators of nuclear power plants. Due to very little or non-existing warning times, seismic alarm systems are as a matter of principle unable to quantify the expected level of impending shaking; they simply issue a warning once certain prior defined thresholds of ground motion are exceeded.

---

<sup>5</sup>The ISDR is successor of the *International Decade of Natural Disaster Reduction (IDNDR, 1990-2000)*, proclaimed by the *United Nations General Assembly* in 1989.

### 3. Rapid Response Systems

A few minutes to hours after seismic catastrophes earthquake related information is still crucial and strongly required for the optimized distribution of resources and disaster management in general. Rapid response systems are important post-seismic modules of Real-Time Earthquake Information Systems. They require large numbers of seismic stations that are preferentially distributed uniformly over an urban or regional area. A continuous communication to with a central processing facility is not necessary because the system comes only into action if triggered by a strong earthquake; rapid response systems usually have no monitoring purpose. Stations of a response system can be equipped with mobile phones which send SMS messages with values of parameterized ground motion to the central facility (see Chapter 4). These information are basis for the automatic preparation of shake maps which themselves give essential input to damage and loss estimation tools.

#### Shake Maps

Shake maps show the distribution of ground shaking in terms of ground motion parameters (see Chapter 4); they can cover different scales from urban to regional expansion. The first automatic shake map - called *ShakeMap* - was developed by Wald et al. (1999b) for earthquakes in southern California as part of the TriNet project. Meanwhile, ShakeMaps are routinely also produced in northern California, Seattle and Salt Lake City (Wald et al., 2003). They are made available for public via the World Wide Web within 10 minutes after the occurrence of any significant earthquake in one of the regions. *URL: <http://earthquake.usgs.gov/shakemap/>*

#### Damage and Loss Estimation Tools

Shake maps and databases of geographical information about the disaster area (e.g. on infrastructure, building stocks, distribution of population) combined with technological knowledge and experience gained from previous disasters, are essential inputs to damage and loss estimation tools. These tools enable potential users - for example disaster managers - to gain a quick overview of the situation and to give optimal decision support. Prominent tools are the US-wide applicable *HAZards US (HAZUS)* system, the *Early Post-Earthquake Damage Assessment Tool (EPEDAT)* for southern California (Eguchi et al., 1997), and *EQSIM* for Romania developed at Karlsruhe University (Fiedrich et al., 2004).

### 4. Aftershock Warning Systems

Hours to months after strong earthquakes the likelihood of aftershocks in the disaster area is still very high. Since numerous structures damaged by the mainshock are weakened and thus susceptible to further damage by even small to moderate shaking, there is a need to issue aftershock warnings to rescue and reconstruction crews working close to weakened structures. Aftershock warning systems are aside from rapid response systems important post-seismic modules of Real-Time Earthquake Information Systems. A prototype aftershock warning system was developed by Bakun et al. (1994) after the  $M_w = 7.1$  *Loma Prieta* mainshock in 1989. A statistical time-dependent map of strong shaking probability in California within 24 hours after a mainshock was recently proposed by Gerstenberger et al. (2005); the method combines a time-independent earthquake occurrence model based on fault data with local time-dependent earthquake clustering models.

## 1.2.2 Benefits of Real-Time Earthquake Information Systems

Real-Time Earthquake Information Systems provide rapid disaster related information that is strongly required to reduce losses of lives and property during and shortly after strong ground shaking. Post-seismic rapid response systems are designed to mainly serve large urban or industrial areas, e.g. to coordinate emergency services and to support rescue operations. Earthquake early warning and seismic alarm systems, on the other hand, are most effective if used for triggering and execution of automatisms to prepare vulnerable systems and dangerous processes for the imminent danger. Seismic warnings can, e.g., be used to (Harben, 1991):

- slow down rapid-transit vehicles and high-speed trains to avoid accidents;
- shutdown pipelines and gas lines to minimize fire hazards;
- shutdown manufacturing operations to decrease potential damage to equipment;
- save vital computer information and retract disk heads to inhibit loss of data;
- assist semi-active structural control to prevent building collapse.

In the scope of the *TriNet Project* in California (1997-2001) potential users of earthquake warnings were identified and their specific response potential studied (Goltz, 2002) (see Appendix A of this work). A survey within the project indicated a high interest level of fire and police departments, city and county emergency services agencies, public works departments and schools. Although human reactions are slow compared to automatic systems, audio or visual alarms can clearly save lives if people are properly trained and appropriate response times available. The *TriNet* studies have shown that early warning mostly reduces panic and confusion in the public, while the tolerance level to false alerts is significantly higher than expected. However, at the time being, only Mexico and Japan have experience with public earthquake early warning (e.g., Espinosa-Aranda et al., 1995).

Due to progress in seismic instrumentation and communication technologies during the last decades reliable hardware and data transfer for the implementation of earthquake early warning systems are nowadays available (e.g., Kanamori et al., 1997). Nevertheless, there are still severe problems concerning:

- the discrimination of strong earthquakes and other signals to avoid false alarms;
- the realization of alarm response systems;
- the determination of potential users of warnings<sup>6</sup>;
- the liabilities associated with issued warnings.

Opponents of earthquake early warning systems worry that these systems could divert spending from earthquake preparedness which would be more effective in reducing damage and losses during a catastrophe.<sup>7</sup>

---

<sup>6</sup>This is clearly also an ethic problem since only a limited group of people can be warned and protected (Goltz, 2002).

<sup>7</sup>After Normile (2004) installation costs for earthquake early warning systems in Taiwan amount to USD 930,000, in Mexico (SAS) to USD 1.2 million and Japan (Nowcast) to USD 90 million.

### 1.3 Seismic Hazard in Istanbul and the Marmara Region

With more than 11 million inhabitants in immediate vicinity to one of the largest and most active strike-slip faults in the world, the western continuation of the North Anatolian Fault zone (NAFZ), the Turkish mega-city Istanbul is exposed to an extremely high seismic risk. The NAFZ is the northern boundary zone of the westward moving Anatolian Block that connects the compressional regime in the Caucasus region in the east with the extensional regime in the Aegean in the west (Fig.1.2). Including the entire extension from Eastern Anatolia to the Greek mainland, the total length of the NAFZ is about 1,500 km. In addition to numerous small and moderate earthquakes 9 major events with  $M_w \geq 7.0$  occurred along the NAFZ during the last century. Noticeable is the westward migration of earthquake epicenters along the NAFZ that might indicate possible seismic gaps (e.g., Toksöz et al., 1979; Stein et al., 1997).

A historic earthquake catalogue for the Marmara region over the last 2,000 years, compiled by Ambraseys (2002), reveals that on average at least one medium intensity (VII-VIII) earthquake has hit Istanbul every 50 years; the average return period for high intensity (VIII-IX) events is 300 years (Ambraseys and Finkel, 1991). From the description of earthquakes along the North Anatolian Fault system in the Sea of Marmara combined with the time-dependent effect of stress transfer of the 1999 Kocaeli earthquake ( $M_w = 7.4$ ) Parsons et al. (2000) find a  $62 \pm 15\%$  probability of strong shaking during the next 30 years and  $32 \pm 12\%$  during the next decade. Ignorance of building regulations, specified in the modern Turkish Seismic Code (1998), and a high number of informal settlements increases Istanbul's vulnerability to a possible earthquake catastrophe. Due to the high concentration of industrial facilities in and around Istanbul a large earthquake in the Marmara region might affect a third to a half of the total Turkish industrial activity (Zschau et al., 2003). A detailed study of the possible impact of a major earthquake close to Istanbul is given in the *Earthquake Master Plan for Istanbul* by the Metropolitan Municipality of Istanbul (2003).

Following the devastating  $M_w = 7.4$  Kocaeli and  $M_w = 7.2$  Düzce earthquakes on August 17 and November 12, 1999, major efforts have been undertaken to obtain a better knowledge of the seismic potential of the NAFZ in the Sea of Marmara (Barka, 1999). Since the cruise of French Ifremer R/V Le Suroit in September 2000, first detailed bathymetric and high resolution seismic reflection data aside from previously existing multichannel data (Imren et al., 2001) are available. From these data Le Pichon et al. (2001) conclude the existence of a single, through-going dextral strike-slip fault in the Marmara Sea, the Main Marmara Fault, which connects the Izmit Fault in the east with the Ganos Fault in the west (see Fig.1.3); the Izmit Fault ruptured during the 1999 Kocaeli earthquake, the Ganos Fault during the 1912  $M_w = 7.4$  Sarkoy-Murefte earthquake. The Main Marmara Fault consists of two segments: the 115 km long Western Fault is oriented  $265^\circ$  and is close to pure dextral slip at a rate of 23 mm/yr on its whole length. The shorter Cinarcik Fault parallel to the Prince's Islands has only a length of 36 km and is oriented  $299^\circ$ . Using a simple kinematic model with a rigid Marmara block Le Pichon et al. (2003) postulate for the southern part of the Cinarcik Fault a 8-10 mm/yr extension and a 23 mm/yr of dextral strike slip along the northern part. Yet, the single through-going fault hypothesis is heavily disputed by other authors: Armijo et al. (2002) and Armijo et al. (2005) propose that smaller strike-slip segments and pull-apart basins alternate within the main step-over between the strike-slip Ganos and Izmit faults, combining strike-slip and extension. By modeling of the Coulomb stress Armijo et al. (2005) show a maximum loading with at least 4-5 m of slip deficit for a 70 km long strike-slip segment between the Cinarcik and Central Basins on the western Marmara Fault. If this segment ruptures a large-magnitude earthquake of  $M_w = 7.2$  could be produced. Other segments of the Marmara Fault appear less loaded (Armijo et al., 2005).

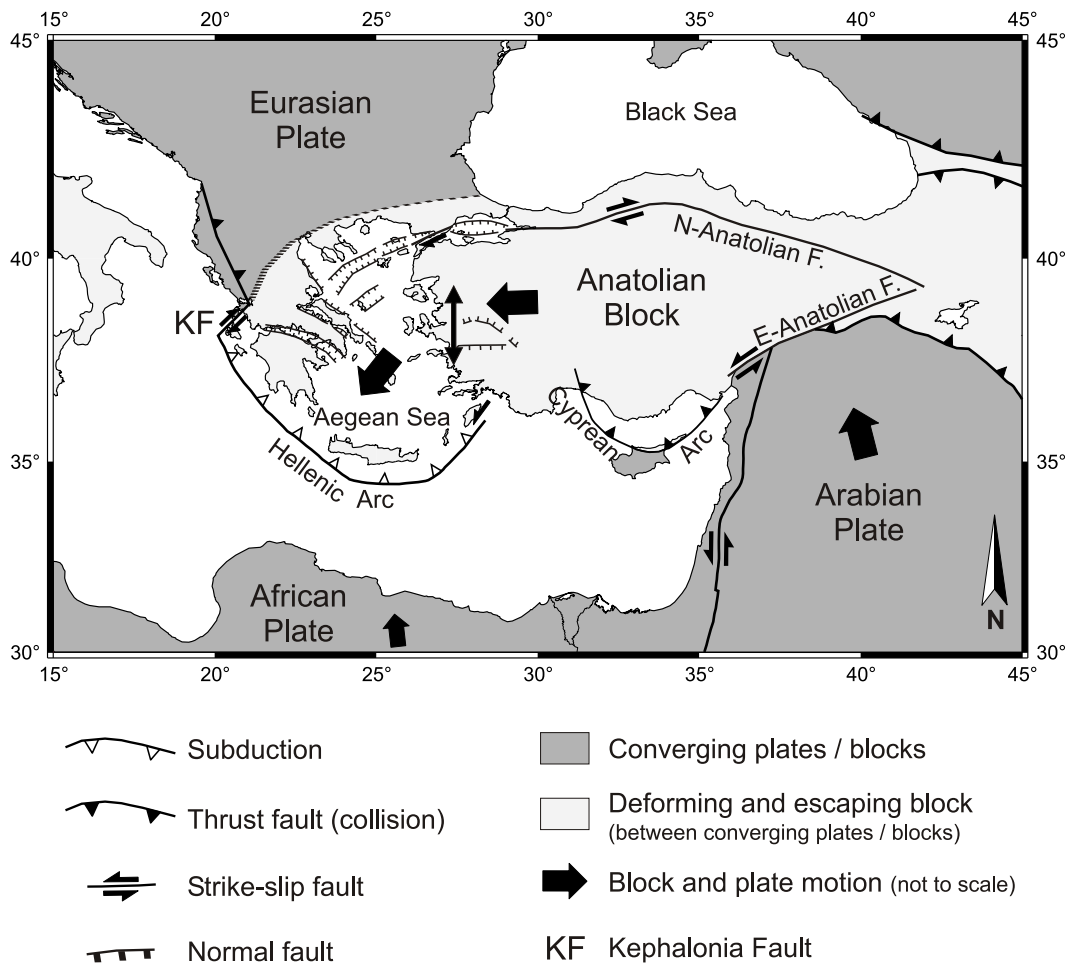


**Figure 1.2:** Schematic sketch of the major tectonics in the eastern Mediterranean after Sperner et al. (2003).

The most credible worst case scenario for Istanbul is after Erdik et al. (2003a) a strike-slip earthquake of  $M_w = 7.5$  associated with the rupture of different fault segments of the Main Marmara Fault with source parameters similar to the 1999 Kocaeli earthquake. Erdik et al. (2003a) estimate that, if this scenario comes true, 35,000 to 40,000 buildings - which is about 5% of the total building stock - will be completely destroyed, about 70,000 buildings will be extensively and about 200,000 moderately damaged. Destructions will amount to about USD  $1.1 \cdot 10^{10}$  losses. The number of deaths is estimated to 40,000 to 50,000, including losses of 1/3 of severely injured people; between 430,000 to 600,000 households will need shelter.

## 1.4 Outline of this Thesis

The devastating Kocaeli and Düzce earthquakes in 1999 have pushed the development and installation of the *Istanbul Earthquake Rapid Response and Early Warning System (IERREWS)* as an important step towards seismic risk reduction in Istanbul and the Marmara region (Erdik et al., 2003b). *IERREWS* comprises two modules of the conceptual Real-Time Earthquake Information System in-



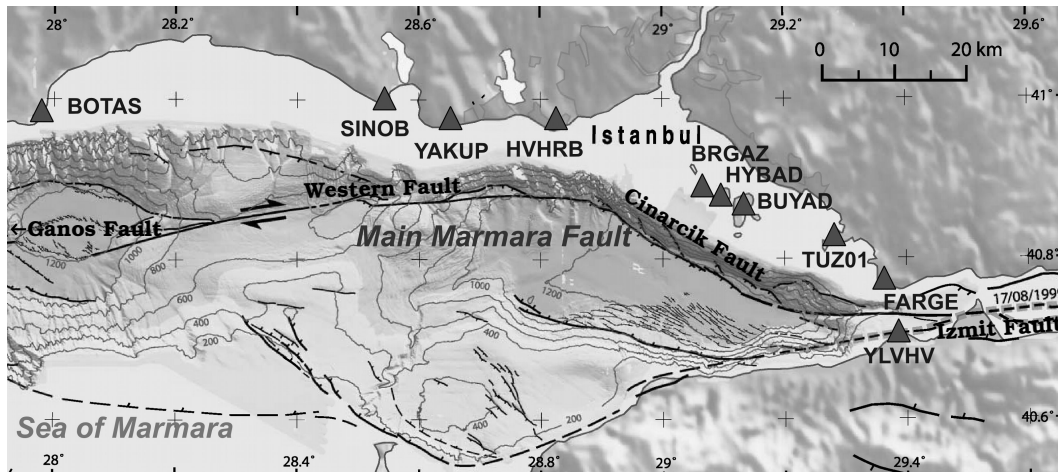


**Figure 1.3:** Fault segments in the *Sea of Marmara* after Armijo et al. (2002) (modified) and distribution of strong motion sensors of the Istanbul earthquake early warning system marked by triangles.

roduced atop: an early warning and a rapid response system. *IERREWS* is operated by the Kandilli Observatory of the Bogazici University in Istanbul. Details on the system will be given in Chapter 5 of this work. This thesis focuses on the earthquake early warning system in *IERREWS*, and is conducted in close cooperation with Prof. Dr. Mustafa Erdik and his team at Kandilli. The Istanbul earthquake early warning system consists of ten strong motion sensors that are deployed along the coast of the Sea of Marmara (Fig. 1.3) and that transmit in real-time ground motion data via a spread spectrum radio modem to two datacenters in Istanbul (Erdik et al., 2003b).

Using the example of Istanbul and *IERREWS* a new methodology for earthquake early warning - called PreSEIS (Pre-SEISmic shaking) - will be developed and tested in this thesis. PreSEIS is based on Artificial Neural Networks (ANNs) and is capable to estimate seismic source parameters within a few seconds after earthquake detection. The tectonic situation in the Marmara region poses a big challenge for the development of an early warning system: short distances between seismic faults and Istanbul metropolitan area reduce possible warning times for strong earthquakes to a few seconds; moreover, strong effects caused by source finiteness of rupturing fault segments - such as rupture directivity - are expected. So far, no algorithm for early warning is capable to take source finiteness into account.

Alike many other cities and regions in the world that are affected by a high seismic threat, the development and verification of a methodology for early warning for Istanbul is aggravated by the lack of moderate and strong motion data (see Figure 1.4). A possible answer to this problem is demonstrated in this thesis by the usage of synthetic records obtained from the *Stochastic Simulation Method for Finite Faults* (Beresnev and Atkinson, 1997). A general description of factors that control seismic ground shaking, including effects of the earthquake source, seismic wave path and local site, is given in Chapter 2. This introduction will support the understanding of the stochastic simulation method presented in Chapter 3. After some modifications of the modelling approach for the additional simulation of compressional (P-) waves, Chapter 3 will describe the simulation of a database of synthetic earthquake records in the Marmara region. This database will establish the basis for PreSEIS.

To simplify time series and Fourier amplitude spectra of earthquake ground shaking, both quantities are frequently reduced to so-called *ground motion parameters* that summarize their main characteris-

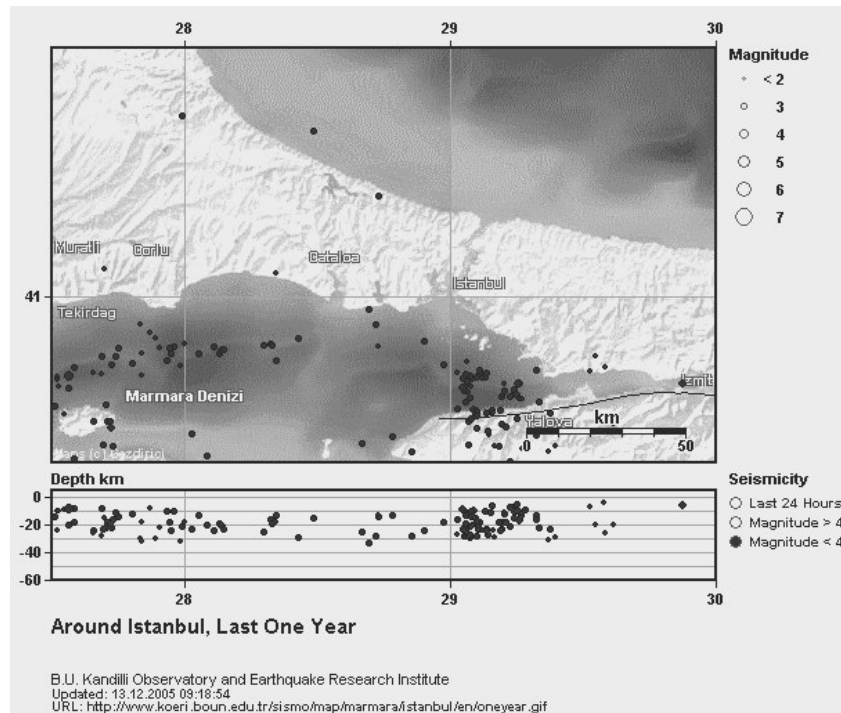


**Figure 1.4:** Seismicity in the Marmara region over the last one year after the B.U. Kandilli Observatory and Earthquake Research Institute.

tics. Chapter 4 will give a short summary of ground motion parameters that are most commonly used in seismic engineering and that are more or less meaningful for the description of potential damage by earthquakes. Based on the stochastically simulated records, attenuation laws will be determined for nine ground motion parameters, among them peak values, spectral values and seismic intensities. For the evaluation of the synthetics the derived attenuation relations will be compared (1) with observational data of earthquakes in northwestern Turkey and (2) with relations determined for other seismic active regions. Alike the magnitude-dependent amplification factors for different soil types determined in Chapter 4, the attenuation laws will play a fundamental role in the calculation of *shake* and *alert maps* in Chapter 6.

General design paradigms for earthquake early warning systems will be discussed in Chapter 5. Earthquake early warning systems generally follow either the *regional* or the *on-site* warning paradigm. The former require dense networks of seismic sensors with real-time communication link to a central processing unit, whereas the latter systems are single station based and therewith much faster at the expense of robustness. The most important early warning systems and algorithms for the fast evaluation of impending ground shaking will be presented in Chapter 5. Special attention will be turned towards the Romanian early warning system. Scaling relations between the maximum P-wave amplitude in the epicentral *Vrancea* region in the SE-Carpathians and ground shaking in Bucharest will be developed to allow for a quick estimate of ground shaking in the Romanian capital before seismic waves arrive. Early warning and rapid response shake maps can be linked to each other as will be demonstrated for the October 27, 2004, *Vrancea* earthquake ( $M_w = 5.9$ ).

Chapter 6 will start with a general introduction to ANNs and will then describe the PreSEIS method developed in this thesis. A summary of this study and an outlook will be given in Chapter 7.

## Chapter 2

# Earthquake Source, Path and Site Effects

Seismic ground motion is controlled by three factors: the earthquake source, seismic wave path and local site effects. Under certain conditions - that will be elaborated within this chapter - it is possible to describe the particle displacement field  $\mathbf{u}(\mathbf{x}, t)$  caused by an earthquake at some point  $\mathbf{x}$  at time  $t$  through a convolution of these effects, or, equivalently, by a multiplication in the frequency domain with

$$U(\mathbf{x}, \omega) = S(\mathbf{x}, \omega) \cdot G(\mathbf{x}) \cdot I(\mathbf{x}, \omega) \cdot H(\mathbf{x}, \omega) \cdot F(\mathbf{x}, \omega) \quad (2.1)$$

$S(\mathbf{x}, \omega)$  accounts for effects of the seismic source,  $G(\mathbf{x})$  and  $I(\mathbf{x}, \omega)$  account for propagation effects describing geometrical spreading and inelastic attenuation. Site effects caused by near-surface deposits and structures close to the point of observation are considered by high-frequency attenuation term  $H(\mathbf{x}, \omega)$  and seismic site response term  $F(\mathbf{x}, \omega)$ .

This chapter will give a description of the different factors in (2.1). The derivations will closely follow Aki and Richards (1980), Udias (1999), Lay and Wallace (1995) and papers cited in the text. I will use common mathematical notations; vectors are denoted by boldface symbols. This introduction to seismic ground shaking will help to better understand the stochastic modeling methodology that will be discussed in Chapter 3. Framed equations will be used in later derivations.

## 2.1 Earthquake Source Mechanism

### 2.1.1 Point Dislocation Source

Earthquakes occur when shear stresses exceed the shear strength on a seismic fault. Starting at the so-called *hypocenter* the earthquake rupture spreads across the fault surface with a speed that is generally less than that of shear waves in the surrounding rock. At each point on the fault the passing rupture front activates a slip of finite duration.

Mathematically described is the earthquake process by a *representation theorem*, such as (Aki and Richards, 1980, (3.2))

$$u_n(\mathbf{x}, t) = \int_{-\infty}^{+\infty} d\tau \iint_{\Sigma} [u_i(\boldsymbol{\xi}, \tau)] c_{ijpq} \nu_j \frac{\partial G_{np}(\mathbf{x}, t - \tau; \boldsymbol{\xi}, 0)}{\partial \xi_q} d\Sigma, \quad (2.2)$$

whereby  $u_n(\mathbf{x}, t)$  is the  $n$ th component of particle displacement at location  $\mathbf{x}$  and time  $t$ . The  $i$ th component of the discontinuity in the slip across the fault is described by  $[u_i(\boldsymbol{\xi}, \tau)] = u_i^+(\boldsymbol{\xi}, \tau) - u_i^-(\boldsymbol{\xi}, \tau)$ , where  $\boldsymbol{\xi}$  is a location on fault surface  $\Sigma$  and  $\tau$  is the time at which the displacement occurs. The  $c_{ijpq}$  are components of a fourth-order tensor that characterizes the elastic constants of the medium; in an isotropic medium it is  $c_{ijpq} = \lambda \delta_{ij} \delta_{kl} + \mu (\delta_{ik} \delta_{jl} + \delta_{il} \delta_{jk})$  with the two Lamé constants  $\lambda$  and  $\mu$ , and Kronecker Delta function  $\delta_{ij}$ , defined by  $\delta_{ij} = 0$  for  $i \neq j$  and  $\delta_{ij} = 1$  for  $i = j$ . Vector  $\nu$  is normal to the fault. The Green's function  $G_{np}(\mathbf{x}, t; \boldsymbol{\xi}, \tau)$  describes the motion in the  $n$  direction at location  $\mathbf{x}$  and time  $t$  caused by a point force acting in the  $p$  direction at location  $\boldsymbol{\xi}$  at time  $\tau$ . Summation is carried out over repeated indices.

Through the integral over space, (2.2) represents ground motions at a given site as a linear combination of the contributions from each point on the fault surface  $\Sigma$ . Through the convolution over time the theorem accounts for the effect of the rupture at each point taking a finite amount of time to reach its final value. The representation theorem has certain limitations (Anderson, 2003): (1) The assumed linear superposition of waves from different parts of the rupturing fault does not apply in case of large wave amplitudes, because the stress-strain relationship then becomes non-linear. (2) If the faulting process affects the propagation of the seismic waves, the assumption that the Green's function is independent of time - which is presumed when writing the time dependence as  $(t - \tau)$  - can break down.

In order to solve (2.2) it is necessary to specify (1) the offset on the fault as a function of location and time, and (2) the Green's function. The first item incorporates earthquake source physics, the second item seismic wave propagation.

In a spherical coordinate system the displacement in the far-field<sup>1</sup> for a double couple in a homogeneous, isotropic, unbounded medium is given by

$$\begin{aligned} \mathbf{u}(\mathbf{x}, t) &= \frac{\mathbf{R}_P^{\theta\phi}}{4\pi\rho\alpha^3 r} \mu A \ddot{\mathbf{u}} \left( t - \frac{r}{\alpha} \right) + \frac{\mathbf{R}_S^{\theta\phi}}{4\pi\rho\beta^3 r} \mu A \ddot{\mathbf{u}} \left( t - \frac{r}{\beta} \right) \\ &= \frac{\mathbf{R}_P^{\theta\phi}}{4\pi\rho\alpha^3 r} \dot{M}_0 \left( t - \frac{r}{\alpha} \right) + \frac{\mathbf{R}_S^{\theta\phi}}{4\pi\rho\beta^3 r} \dot{M}_0 \left( t - \frac{r}{\beta} \right), \end{aligned} \quad (2.3)$$

with  $r = |\mathbf{x}|$ .

$$\boxed{M_0(t) \equiv \mu A \ddot{\mathbf{u}}(t)} \quad (2.4)$$

defines the *seismic moment* of the earthquake source.  $\alpha$  and  $\beta$  are the propagation speed of compressional (P-) and shear (S-) waves described by the Lamé constants  $\lambda$  and  $\mu$  and the density  $\rho$  of the medium:

$$\boxed{\alpha = \sqrt{\frac{\lambda + 2\mu}{\rho}}} \quad (2.5)$$

$$\boxed{\beta = \sqrt{\frac{\mu}{\rho}}} \quad (2.6)$$

<sup>1</sup>The far-field includes positions that are more than a few wavelengths away from the source (Aki and Richards, 1980).

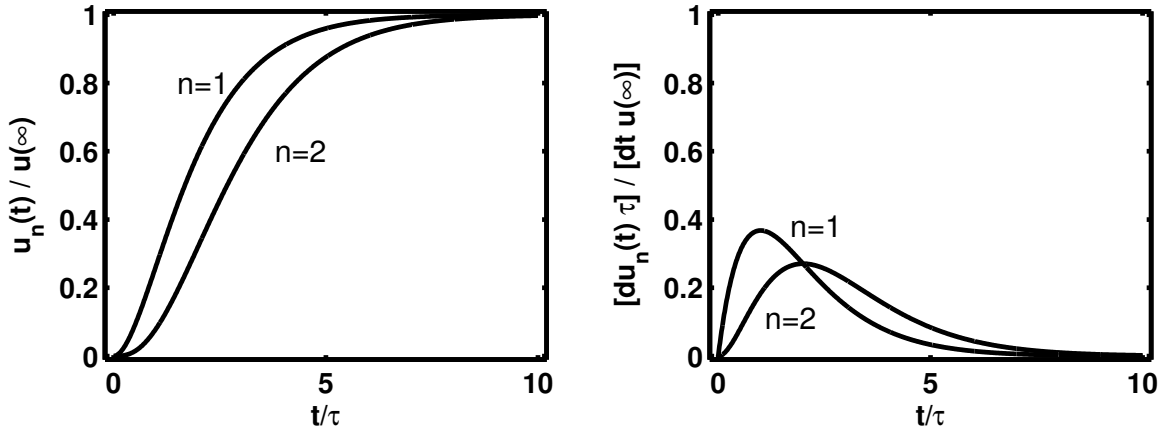


**Figure 2.1:** Source time functions (2.8) and their derivatives (2.9) after Beresnev and Atkinson (1997).

The angular radiation patterns  $\mathbf{R}_P^{\theta\phi}$  and  $\mathbf{R}_S^{\theta\phi}$  are given by

$$\begin{aligned}\mathbf{R}_P^{\theta\phi} &= \sin(2\theta) \cos(\phi) \hat{\mathbf{r}} \\ \mathbf{R}_S^{\theta\phi} &= \cos(2\theta) \cos(\phi) \hat{\boldsymbol{\theta}} - \cos(\theta) \sin(\phi) \hat{\boldsymbol{\phi}},\end{aligned}\quad (2.7)$$

whereby  $\hat{\mathbf{r}}$ ,  $\hat{\boldsymbol{\theta}}$  and  $\hat{\boldsymbol{\phi}}$  are unit vectors pointing into radial and transverse directions, respectively.

Equation (2.3) shows the important result that the displacement in the far-field is proportional to particle velocities at the source  $\dot{\bar{u}}$ , averaged over the fault plane. The source time function  $\bar{u}(t)$  describes the temporal development of slip and is constrained by the fact that the displacement starts from zero and approaches a final amount of slip  $\bar{u}(\infty)$  over the source *rise time*  $\tau_r$ . Beresnev and Atkinson (1997) give some examples of one class of models<sup>2</sup> of time functions which satisfy these conditions:

$$\begin{aligned}\bar{u}_1(t) &= \bar{u}(\infty) \left[ 1 - \left( 1 + \frac{t}{\tau} \right) e^{-t/\tau} \right] \\ \bar{u}_2(t) &= \frac{\bar{u}(\infty)}{2} \left[ 2 - \left[ 1 + \left( 1 + \frac{t}{\tau} \right)^2 \right] e^{-t/\tau} \right],\end{aligned}\quad (2.8)$$

whereby  $\tau$  is a characteristic time parameter that controls the rate of the displacement increase. The derivatives of (2.8) can be written as

$$\dot{\bar{u}}_n(t) = \frac{\bar{u}(\infty)}{n! \tau} \left( \frac{t}{\tau} \right)^n e^{-t/\tau}, \quad n = 1, 2. \quad (2.9)$$

The normalized source time functions (2.8) and their derivatives (2.9) are illustrated in Figure 2.1.

After substituting (2.9) in (2.3) and transforming the result to frequency domain, the modulus of the Fourier transform for compressional waves is

$$|\mathbf{u}_n^P(\mathbf{x}, \omega)| = \frac{\mathbf{R}_P^{\theta\phi} M_0}{4\pi\rho\alpha^3 r} \left[ 1 + \left( \frac{\omega}{\omega_c} \right)^2 \right]^{-(n+1)/2}, \quad (2.10)$$

<sup>2</sup>Another class of models, e.g., are triangular functions for particle velocities.

and for shear waves

$$|\mathbf{u}_n^S(\mathbf{x}, \omega)| = \frac{\mathbf{R}_S^{\theta\phi} M_0}{4\pi\rho\beta^3 r} \left[ 1 + \left( \frac{\omega}{\omega_c} \right)^2 \right]^{-(n+1)/2}, \quad (2.11)$$

where the total released moment is

$$M_0 = \mu A \bar{u}(\infty). \quad (2.12)$$

Parameter  $\omega_c = 1/\tau$  defines the so-called *corner frequency* of the Fourier amplitude spectrum. The corner frequency decreases as magnitude increases. Setting  $n = 1$  in (2.10) and (2.11) gives the well-known *Brune* or  $\omega^2$  source spectrum (Brune, 1970, 1971) which is characterized by an amplitude fall-off proportional to  $\omega^{-2}$  above  $\omega_c$ .

For P-waves it is

$$|S_P^d(\mathbf{x}, \omega)| = \frac{\mathbf{R}_P^{\theta\phi} M_0}{4\pi\rho\alpha^3} \left[ 1 + \left( \frac{\omega}{\omega_c} \right)^2 \right]^{-1}, \quad (2.13)$$

and for S-waves

$$|S_S^d(\mathbf{x}, \omega)| = \frac{\mathbf{R}_S^{\theta\phi} M_0}{4\pi\rho\beta^3} \left[ 1 + \left( \frac{\omega}{\omega_c} \right)^2 \right]^{-1}. \quad (2.14)$$

Index  $d$  stands for *displacement*. The distance  $r$  in the nominator is omitted here and will be separately analyzed in the context of geometrical spreading in Chapter 2.2.1. The  $\omega^2$  source-scaling relation with a constant stress drop (see Chapter 2.1.2) gives a good fit to wave amplitudes and periods for most records of short period instruments of the World Wide Standardized Seismographic Network (Boore, 1986).

Relationships between the Fourier amplitude spectra of displacement  $U$ , velocity  $V$ , and acceleration  $A$  in the frequency domain are given by

$$\begin{aligned} |U(\mathbf{x}, \omega)| & \quad \text{see (2.13) or (2.14)} \\ |V(\mathbf{x}, \omega)| & \approx \omega U(\mathbf{x}, \omega) \\ |A(\mathbf{x}, \omega)| & \approx \omega^2 U(\mathbf{x}, \omega). \end{aligned} \quad (2.15)$$

For the *Brune* source model the  $\omega^2$  decay above the corner frequency  $\omega_c$  in the displacement spectrum is therewith equivalent to a plateau in the acceleration spectrum.

## 2.1.2 Empirical Scaling Relations for Earthquake Sources

The static stress drop  $\Delta\sigma$  of an earthquake defines the change of shear stresses acting on a fault plane *before* and *after* the earthquake rupture. For shear fractures,  $\Delta\sigma$  is proportional to the deformation of the fault, i.e.

$$\Delta\sigma = \frac{C}{L} \mu \bar{u}(\infty), \quad (2.16)$$

whereby  $L$  is a length dimension of the fault and  $C$  is an adimensional factor that depends on the shape of the fracture. Typical stress drop values for intraplate earthquakes are in the order of  $\Delta\sigma \approx 100$  bars (Hanks and McGuire, 1981). Inserting (2.16) into the definition of the seismic moment  $M_0$  (2.4) gives

$$M_0 = L^2 \mu \bar{u} \approx \Delta\sigma L^3 \quad (2.17)$$

i.e. the seismic moment of an earthquake is proportional to the stress drop and the cube of length dimension of the rupturing fault. However, if we follow the relation between corner frequency  $\omega_c$  of the Fourier amplitude spectrum and stress drop given by Brune (1970) and Brune (1971)

$$\omega_c = 2\pi \cdot 4.9 \cdot 10^6 \beta \left( \frac{\Delta\sigma}{M_0} \right)^{1/3}, \quad (2.18)$$

and compare (2.18) with the observed *similarity of earthquake sources* of different magnitudes (Aki, 1967):

$$M_0 \omega_c^3 = \text{const.}, \quad (2.19)$$

it turns out that  $M_0$  is *de facto* independent of  $\Delta\sigma$ . This can be also observed from the scaling relation between  $M_0$  and rupture duration  $\tau_c$ , namely

$$M_0 \sim \tau_c^3, \quad (2.20)$$

whereby it is assumed that the fault width scales approximately as the fault length and therewith  $\tau_c \sim \sqrt{A}$  with rupture area  $A$ .

Hanks and Kanamori (1979) use the seismic moment  $M_0$  (in [Nm]) to define the *moment magnitude*  $M_w$  of an earthquake by

$$M_w = \frac{2}{3} \log(M_0) - 6.03 \quad (2.21)$$

Alike  $M_0$ ,  $M_w$  is in principle independent of the stress drop of the earthquake. An empirical scaling relation between  $M_w$  and rupture dimensions (rupture length  $L$  [km] and rupture width  $W$  [km]) for strike-slip events with  $4.8 \leq M_w \leq 7.9$  is given by Wells and Coppersmith (1994) by

$$M_w = 3.98 (\pm 0.07) + 1.02 (\pm 0.03) \log(LW) \quad \text{with} \quad \begin{cases} L = 10^{-2.57 (\pm 0.12) + 0.62 (\pm 0.02) M_w} \\ W = 10^{-0.76 (\pm 0.12) + 0.27 (\pm 0.02) M_w} \end{cases} \quad (2.22)$$

## 2.2 Path Effects

While propagating through the Earth's crust, seismic waves undergo modifications due to effects of attenuation of seismic wave amplitudes by geometrical spreading and inelastic energy absorption. Reflections and refractions at large-scale heterogeneities, i.e. interfaces of rocks with distinct physical properties, and wave scattering by small-scale heterogeneities in the crust lead to additional modifications of seismic signals.

### 2.2.1 Geometrical Spreading

Geometrical spreading describes the decrease of seismic wave amplitudes due to the increase in area of the wavefront with increasing distance  $r$  from the source. For spherical waves - such as body waves - the amplitude decrease in a homogeneous space can be described by

$$G(\mathbf{x}) = \frac{1}{r(\mathbf{x})} \quad (2.23)$$

### 2.2.2 Inelastic Attenuation

Since the Earth does not behave like a perfect elastic body, propagating seismic waves dissipate energy in form of heat due to internal friction. This inelastic or viscoelastic attenuation leads to a decrease of wave amplitudes with distance and time. The mechanisms of internal friction are complex and depend on different factors, such as on the atomic and molecular structure of crystals in minerals, as well as on the existence of cracks, fractures and inclusions in rocks (Udias, 1999).

The inelastic behavior of a given material is usually described by the quality factor  $Q$  which is reciprocally proportional to the ratio of elastic energy  $\Delta E$  dissipated during one cycle of harmonic motion of frequency  $\omega$  and the maximum or the mean energy  $\bar{E}$  accumulated during the same cycle:

$$\frac{1}{Q} \equiv \frac{1}{2\pi} \frac{\Delta E}{\bar{E}} \quad (2.24)$$

For weak to moderate earthquakes deformation amplitudes of seismic waves are small. In these cases  $Q$  is independent of wave amplitude and attenuation can be expressed by linear laws. However, for strong earthquakes and explosions with large yields the applicability of linear relations fails (Minster et al., 1990).

The amplitude  $A$  of an attenuated, harmonic elastic and plane wave at site  $\mathbf{x}$  and time  $t$  with source-to-site distance  $r(\mathbf{x})$  can be described by

$$A(\mathbf{x}, t) = A_0 \exp [i(\omega t - k r(\mathbf{x}))] \exp [-\alpha(\omega) r(\mathbf{x})], \quad (2.25)$$

whereby  $A_0$  is the amplitude at  $r = 0$ ,  $k$  the wave number and  $\alpha$  the absorption coefficient of the medium. Typical values of  $Q$  for consolidated, compact rocks in the Earth's crust are between 50 to some 1,000 (Sheriff and Geldart, 1995). This means that attenuation is generally small. If  $Q \gg 1$  the relationship between  $\alpha$  and  $Q$  can be approximated by

$$\alpha(\omega) = \frac{\omega}{2 Q(\omega) c(\omega)}, \quad (2.26)$$

where  $c(\omega)$  is the frequency-dependent seismic wave velocity, i.e. for P-waves:  $c = \alpha$  and for S-waves:  $c = \beta$ . Because high frequencies are stronger damped than small frequencies, seismograms recorded at large source-to-site distances contain mostly long period motions. The increase of  $Q$  with increasing frequency  $\omega$  follows a power law with exponent  $\eta$  ( $\eta \geq 1$ ) (e.g., Lay and Wallace, 1995):

$$Q(\omega) = Q_0 \left( \frac{\omega}{2\pi} \right)^\eta \quad (2.27)$$



Note that (2.27) describes a simple parameterization of frequency dependence and is not a physical law. Inserting (2.26) into (2.25) gives

$$A(\mathbf{x}, t) = A_0 \exp [i(\omega t - kr(\mathbf{x}))] I(\mathbf{x}, \omega) \quad (2.28)$$

with

$$I(\mathbf{x}, \omega) = \exp \left[ -\frac{\omega r(\mathbf{x})}{2 Q(\omega) c(\omega)} \right] \quad \text{with} \quad Q(\omega) = Q_0 \left( \frac{\omega}{2\pi} \right)^\eta \quad (2.29)$$

The assumption of  $Q \gg 1$  is only valid for consolidated compact rock. For near-surface unconsolidated material the approximation in (2.26) is not applicable (e.g., Hatherly, 1986); in this case the observed diminution of wave amplitudes is usually treated as local site effect (see Chapter 2.3).

### 2.2.3 Effects on Shaking Duration

Shaking duration is mainly governed by the earthquake *source time function* (see (2.8)) which is determined by *rise time*  $\tau_r$  and *rupture duration*  $\tau_c$ . Rupture duration clearly depends on the dimensions of the rupture, rupture velocity  $v_r$  and the orientation of the observer relative to the fault. Since  $v_r$  is generally smaller than S-wave velocity  $\beta$ , seismic waves stimulated by a close breaking segment of the fault will arrive earlier at a station than waves generated from a segment that ruptures later. The relation of rupture duration  $\tau_c$ , on the one hand, and rupture length  $L$ , rupture velocity  $v_r$  and viewing azimuth  $\Theta$ , on the other hand, is given by

$$\tau_c = \frac{L}{v_r} - \frac{L \cos(\Theta)}{c}, \quad (2.30)$$

where  $c$  is the velocity of seismic waves, e.g.  $c = \alpha$  for P-waves or  $c = \beta$  for S-waves. The area of the source time functions that is proportional to the seismic moment of the earthquake is independent of azimuth; only their duration changes. Therefore we expect a narrow source time function with a high amplitude at stations located along the direction of rupture propagation ( $\Theta = 0^\circ$ ), and a broad source time function with a small amplitude at stations on the opposite side of the rupturing fault ( $\Theta = 180^\circ$ ). The dependence on azimuth due to fault propagation is called *rupture directivity* (e.g., Lay and Wallace, 1995). In dependence on the direction of rupture propagation relative to the site of observation one distinguishes between *forward*, *backward* or *neutral directivity*. Forward and backward directivity are mainly unidirectional while neutral directivity is bidirectional, i.e. the rupture is neither predominately toward nor away from the site of observation.

Shaking duration is also influenced by focusing and scattering processes of seismic waves. Scattering is caused by interactions of the seismic wavefield with small-scale heterogeneities and leads to a partitioning of the high-frequency wavefield into a sequence of arrivals which form the so-called *coda waves* (Sato and Fehler, 1998).

## 2.3 Site Effects

Site effects play a fundamental role in the observed ground shaking. They are independent of traveled distances between earthquake sources and points of observation, and are therefore usually separately

treated from path effects. Site effects are defined as the response of a certain site to incident seismic waves relative to sites that show no response. In principle, each site shows local effects whereby changes are negligible for very hard rock sites, i.e. for sites without sedimentary overburden. Site effects are mainly caused by shallow sediments of a few tens to hundreds of meters thickness, surface topology, and basins (e.g., Field and the SCEC Phase III Working Group, 2000).

Site effects can be assessed on the basis of observational data or by numerical analyses. Observational data comprises weak and strong motion data, as well as records of distant nuclear explosions or ambient noise. Numerical analyses are generally performed for 1D wave propagation through linear and non-linear soil models for one or more directions of shaking by solving equations of motion (e.g., Schnabel et al., 1972). In principle, site effects can be non-linear, i.e. a function of shaking amplitude (e.g., Campbell and Bozorgnia, 2003; Su et al., 1999). Site effects are usually split into two terms: the first term accounts for site amplification of seismic waves close to the point of observation (see Chapter 2.3.1), the second term for high-frequency diminution (see Chapter 2.3.2).

### 2.3.1 Site Amplification

#### Effects of Soft Surface Layers

Amplitude amplification of seismic waves encountering a low-velocity, near-surface sedimentary layer is mainly caused by two physical effects: the amplification of shaking due to the impedance contrast between the two layers as a consequence of energy conservation, and secondly, these amplified waves can be trapped in the top layer. Constructive interference of trapped waves leads to further amplification of amplitudes (e.g., Bard, 1999). As an additional effect of decreased wave velocity in the sediments the wave path is bent to vertical (e.g., Hough, 2004).

Depending on the layer's thickness  $h$  and on the average seismic velocity  $\bar{\beta}$  in the sediments, certain frequencies are preferentially amplified, because the layer will only trap energy of certain wavelengths. Interference of trapped waves lead to resonance patterns. Generally, only layers whose thicknesses are larger than a quarter-wavelength have impact on seismic waves (Kallweit and Wood, 1982; Sheriff and Geldart, 1995). For a 1D structure with one single layer atop of the bedrock layer the resonant frequencies  $f_n$  can be approximated by

$$f_n = (2n + 1) \frac{\bar{\beta}}{4h}, \quad n = 0, 1, 2, 3, \dots, \quad (2.31)$$

whereby  $n = 0$  gives the fundamental frequency  $f_0$ ,  $n = 1$  the first harmonic  $f_1$ ,  $n = 2$  the second harmonic  $f_2$ , and so on (Bard, 1999). The fundamental frequency  $f_0$  is usually in the range of 0.2 to 10.0 Hz (Bard, 1999). Resonance amplitudes are mainly controlled by the impedance contrast  $IC$  between the surface layer and the underlying bedrock, by the material damping in sediments  $\xi_1$ , and by characteristics of the incident seismic waves (Bard, 1999). Peak amplification  $A_0$  at the fundamental frequency for a one-layer 1D structure with vertically impinging plane S-waves is given by

$$A_0 = \frac{1}{IC^{-1} + 0.5\pi \xi_1}, \quad (2.32)$$

where

$$IC = \frac{\rho_2 \beta_2}{\rho_1 \beta_1}, \quad (2.33)$$

$\beta$  is the shear wave velocity and  $\rho$  the density of the medium; index 1 refers to the surface layer, index 2 to the underlying bedrock. Resonance amplitudes are between 3 to 6 higher than those of the impinging seismic waves. Peak values of more than 20 have been observed in Mexico City and San Francisco (Bard, 1999). While the prediction of resonance frequencies gives generally good results, the observed resonance amplitudes are mostly in disagreement with theoretical estimates. One of the problems comes from the simplifying assumption of vertically impinging seismic waves.

### Other Site Effects

Site effects due to surface topology generally manifest in amplification of motion for convex topographic structures, such as on the top of a hill, and in attenuation for concave structures, such as in the valley or base of a hill. Bard (1999) relates these topographic effects to the sensitivity of surface motion to the angle of incidence of seismic waves, to focusing and defocusing effects of seismic waves along the topographic surface, and to the interference of direct and diffracted waves. Topographic effects are mostly frequency-dependent whereby the largest effects are observed for wavelengths comparable to the horizontal dimension of the topographic structure. Spectral amplification due to surface topography can be as much as 10 (Bard, 1999). Further site effects are due to basin-edge-induced waves, subsurface focusing and non-linearities.

### 2.3.2 High-Frequency Diminution

While the theoretical  $\omega^2$ -spectral model of the seismic source predicts a plateau in the Fourier acceleration spectrum for frequencies above the corner frequency  $\omega_c$  (see (2.14)), observational data indicate a rapid fall-off for frequencies higher than 5 to 10 Hz. Hanks (1982) calls this frequency  $f_{max}$  or  $\omega_{max}$  or simply *cut-off frequency*. For the description of high-frequency attenuation Boore (1983) proposes a fourth-order Butterworth filter:

$$H(\mathbf{x}, \omega) = \left[ 1 + \left( \frac{\omega}{\omega_{max}(\mathbf{x})} \right)^8 \right]^{-1/2}. \quad (2.34)$$

Anderson and Hough (1984) suggest to approximate the observed exponential decay by parameter  $\kappa$  [s] with

$$H(\mathbf{x}, \omega) = \exp\left(-\pi\kappa(\mathbf{x})\frac{\omega}{2\pi}\right). \quad (2.35)$$

High-frequency diminution of seismic wave amplitudes is mostly attributed to effects in the near-surface weathered layers. Some authors, however, link the effect to the seismic source (e.g., Hanks, 1982). The quantification of  $f_{max}$  or  $\kappa$ , respectively, is aggravated by trade-offs with other spectral parameters such as with corner frequency  $f_c$ .

### 2.3.3 Site Classification

The integration of site effects is essential in seismic ground motion prediction. While extensive studies of site effects are in most regions in the world not available, the correlation of distinct classes of

NEHRP class	description	$V_{30}$ [m/s]	amplification 0.5 - 1.0 Hz	amplification 2.0 - 6.0 Hz
A	hard rock	> 1,500	< 1.2 (< 0.8)	< 1.2 (< 0.9)
B	firm to hard rock	760-1,500	1.6-1.2 (1.2-0.8)	1.5-1.2 (1.4-0.9)
C	dense soil, soft rock	360-760	2.1-1.6 (1.9-1.2)	1.9-1.5 (2.4-1.4)
D	stiff soil	180-360	2.7-2.1 (2.7-1.9)	2.3-1.9 (3.7-2.4)
E	soft clays	< 180	> 2.7 (> 2.7)	> 2.3 (> 3.7)
F				

**Table 2.1:** Left: soil classification after the *1994 NEHRP building code provisions* (Building Seismic Safety Council, 1995) along with descriptions and specifications of  $V_{30}$ . Right: comparison of amplification factors (for  $\kappa = 0.035$  s) after Boore and Joyner (1997) and Harmsen (1997) (in brackets) for two frequency ranges. There is a good agreement of both results.

site effects to near-surface geology has become a standard procedure in seismic engineering. Such classifications can clearly give only average values of amplification and therefore allow only for a very rough estimation of ground shaking. The actual amplification at a given site during earthquake shaking can be significantly higher (or lower). The most common classification schemes for site amplification are based on surface geology (age, depositional environment, sediment texture), on shear wave velocity  $\beta$ , on geotechnical data (material type, density, stiffness, porosity), or on depth to basement rock, usually defined as  $\beta \approx 2,500$  m/s.

Theoretically, amplification is a function of the impedance contrast between different layers, defined by the product of density  $\rho$  and shear wave velocity  $\beta$ . Since the observed variations in density are generally small, shear wave velocity is assumed to be a suitable proxy for the estimation of amplification. The widely applied *1994 NEHRP<sup>3</sup> building code provisions* (Building Seismic Safety Council, 1995), e.g., classify soil sites according to  $V_{30}$ , which is the shear wave velocity averaged over the uppermost 30 m (Table 2.1).  $V_{30}$  was chosen because most boreholes that are today available are limited to a depth of 30 m, which is the depth that the most commonly available rigs were built to drill during one day. A more sophisticated soil classification scheme is based on the *quarter-wavelength* measure (Wald and Mori, 2000) that allows assigning frequency-dependent amplification functions to different soil sites.

A link between *quarter-wavelength* and  $V_{30}$  has been established by Boore and Joyner (1997): from data of about 210 boreholes the authors have correlated observed amplification values derived from the *quarter-wavelength* method with  $V_{30}$ . The authors have therewith obtained frequency-dependent

<sup>3</sup>National Earthquake Hazard Reduction Program

frequency [Hz]	Node points of amplification for NEHRP classes		
	$V_{30} = 1,070 \text{ m/s}$ (NEHRP class B)	$V_{30} = 520 \text{ m/s}$ (NEHRP class C)	$V_{30} = 255 \text{ m/s}$ (NEHRP class D)
0.01	1.00	1.00	1.00
0.09	1.03	1.21	1.43
0.16	1.06	1.32	1.71
0.51	1.21	1.59	2.51
0.84	1.34	1.77	2.92
1.25	1.49	1.96	3.10
2.26	1.80	2.25	3.23
3.17	2.01	2.42	3.18
6.05	2.39	2.70	3.18
16.60	2.93	3.25	3.18
61.20	3.75	4.15	3.18

**Table 2.2:** Node points of amplification for NEHRP classes B, C and D after Boore and Joyner (1997). Values below 0.5 Hz and above 10.0 Hz are based on subjective judgment and are not constrained by data. Node points for NEHRP class B are determined from non-linear interpolation in this work.

amplification functions for sites with  $V_{30} = 520, 310,$  and  $255 \text{ m/s}$  corresponding to soil sites of NEHRP class C, average soil, and NEHRP class D. By non-linear interpolation I have determined the missing factors for NEHRP class B in this work. These data are essential for the simulations of ground shaking in Chapter 3. Node points of amplification functions are compiled in Table 2.2 and visualized in Figure 2.2 assuming a diminution with  $\kappa = 0.035 \text{ s}$ . The frequency-dependent amplification factors are in good agreement with amplification values found by Harmsen (1997) (see Table 2.1, right). Note that the amplification functions by Boore and Joyner (1997) are for the most part empirically derived from borehole data in Western U.S.; the applicability to any other region in the world is not proven.

Figure 2.3 shows a soil map for the Marmara region following the NEHRP classification scheme (Erdik et al., 2003a): stiff and soft soils dominate in the European part, while the Asian part is mostly covered by firm to hard rock. Exceptions are constituted among others by river basins covered by soft sediments, and the area in eastern Marmara, close to the Izmit Bay. These areas are prone to ground motion amplification. The impact of site effects on the observed damage pattern during strong earthquakes was demonstrated during the August 17, 1999  $M_w = 7.4$  Kocaeli earthquake: almost 1,000 people lost their lives in the collapse of buildings in the Istanbul suburb Avcilar, around 110 km from the epicenter. The Avcilar area is covered by poorly lithified Quaternary Pliocene and Miocene sands and gravel, marls, and limestones to a depth of 200 m (Brinkman, 1976), capable to amplify ground motion by a factor between 5 and 10 for frequencies from 0.5 to about 4.0 Hz (Özel et al., 2002; Ergin et al., 2004). The example of Avcilar demonstrates that the usage of mean amplification spectra assigned to different soil classes as done in this work can clearly underestimate ground motions.

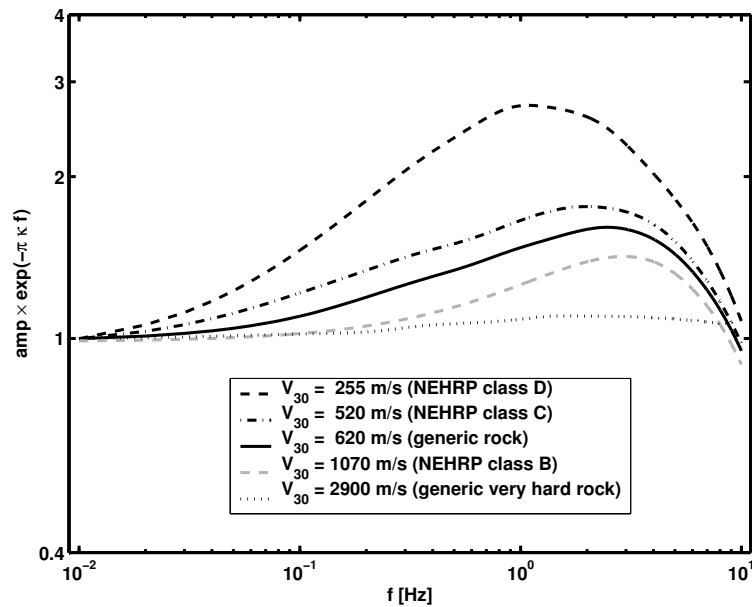


**Figure 2.2:** Combined effect of site amplification and high-frequency diminution after Boore and Joyner (1997) with  $\kappa = 0.035s$ . For generic rock peak amplification of 1.6 occurs at 2.5 Hz, for soft rock (NEHRP class C) sites of 1.8 at 2.0 Hz, and for stiff soil (NEHRP class D) sites of 2.7 at 1.0 Hz. The gray line represents the amplification function for NEHRP class B obtained from non-linear interpolation within this work.

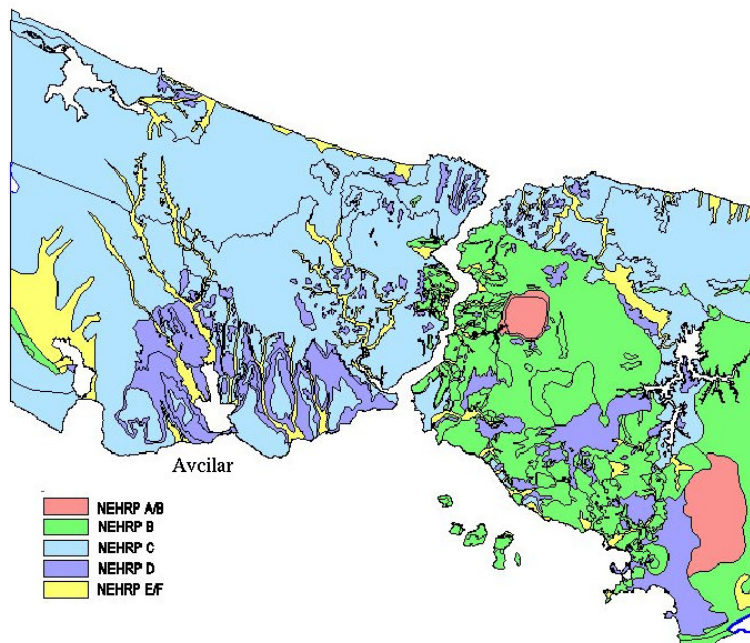


**Figure 2.3:** NEHRP soil classification map for the Marmara region close to Istanbul (Erdik et al., 2003a). Explanations are given in Table 2.1.

## Chapter 3

# Simulation of Seismic Ground Motion

It frequently happens that seismic ground motion records are not available to assess a given seismological or earthquake engineering problem. Typical examples are structural response analyses or the development of regional attenuation relationships, e.g., for seismic hazard assessment. In this study earthquake records are required for the conceptual design and optimization of the PreSEIS methodology for earthquake early warning. The lack of data can be either due to insufficient seismic instrumentation in a particular geographical region or due to missing magnitude and distance ranges which are of interest to assess the given task. Even though the North Anatolian Fault shows a high seismic activity, most of the earthquakes that have occurred during the last decades in northern Turkey were concentrated in the middle and eastern part of the 1,500 km long fault. Seismicity in the Marmara region, on the other hand, is relatively low (see Figure 1.4) - a circumstance that significantly aggravates the design and verification of a seismic early warning system for the region. Simulated time histories of seismic ground shaking help to overcome the lack of appropriate data.

This chapter will give a short overview of different techniques for the simulation of seismic ground motion and will present a detailed review on the *Stochastic Simulation Method of Seismic Ground Motion from Finite Faults* as proposed by Beresnev and Atkinson (1997). After some modifications of the stochastic method a database of synthetic earthquakes for the Marmara region will be generated. This database will establish the basis for subsequent studies of PreSEIS in Chapter 6.2.

### 3.1 Common Methods for the Simulation of Seismic Ground Motion

To produce realistic time series of earthquake shaking, modeling procedures should be capable to account for the three main issues affecting seismic ground motion discussed in Chapter 2: the earthquake source, seismic wave path and local site effects. Amplitudes and time histories of long-period motions are in principle predictable, while short-period motions are hardly forecastable because of the increasing incoherence of seismic source radiation and wave propagation at high frequencies caused by small-scale heterogeneities in the source process and crustal properties. Due to the lack of detailed subsurface models short-period motions are frequently treated as stochastic phenomena (e.g., Boore, 1983).

For the modeling of wave propagation through complex 2D or 3D subsurface models, including for example sedimentary basins, *Finite Difference (FD)* or *Finite Element Methods (FEM)* are usually

applied (e.g., Olsen, 1994; Olsen and Archuleta, 1996). Because these methods are computationally intensive and subsurface models are generally not sufficiently resolved, finite differences and finite element methods, however, are mostly limited to the calculation of long-period ground motions. The two most commonly used procedures for the simulation of seismic ground motion covering the range of frequencies that are relevant for most earthquake engineering problems ( $\sim$  up to 10 Hz) are the method of *Empirical Green's Functions* and *Stochastic Modeling* approaches. *Hybrid Methods* combine different procedures in the short- and long-period range (e.g., Pulido et al., 2004).

The *Empirical Green's Function* (EGF) approach (Hartzell, 1978; Hutchings and Wu, 1990) utilizes records of small earthquakes with presumed impulse-like source time functions and certain seismic moments as approximations of the Earth's Green's functions, including attenuation, propagation and radiation pattern effects. The application of the EGF method requires a sufficient number of small earthquake records for a given region to cover the whole fault surface as well as a certain number of recording stations.

High-frequency ground motions observed at large source-to-site distances can be well described as band-limited Gaussian noise of finite duration with a characteristic  $\omega^2$  Fourier amplitude spectrum (see Chapter 2.1; e.g., Boore, 1983, and references given therein). This observation paves the path for the *Stochastic Point Source Method* as proposed by Hanks and McGuire (1981) and Boore (1983). Since (semi-) empirical and theoretical approaches, such as *EGF* or *FD*, are based on observational data or theoretical considerations, respectively, the pure stochastic simulations are more straightforward and are not limited by the availability of suitable data. By the specification of parameters that describe the shape of the Fourier amplitude source spectrum (e.g., by the seismic moment, the stress drop, or the rupture velocity) and modifications due to propagation and site effects at the point of observation, the stochastic method provides a simple and effective tool for the simulation of ground motion time series at arbitrary sites with the desired spectral features and random phase. A review on the stochastic simulation method for point sources is given by Boore (2003). At smaller source-to-site distances source finiteness has to be taken into account. The following section will give an introduction to the *Stochastic Simulation Method of Seismic Ground Motion from Finite Faults* and implementation in the Fortran program *FINSIM* by Beresnev and Atkinson (1997). A modified version of *FINSIM* will be applied for ground motion simulations in this thesis.

## 3.2 Stochastic Simulation of Seismic Ground Motion from Finite Faults

For the consideration of source dimensions the method of *Stochastic Simulation of Seismic Ground Motion from Finite Faults* treats the rupturing fault as a system composed of a certain number of point sources: each of the  $n$  subfault elements of size  $\Delta l$  is assigned an  $\omega^2$  Fourier amplitude spectrum  $|S_{sf,s}^a(\mathbf{x}, \omega)|$  with seismic moment  $m_0$ . Index *sf* stands here for *subfault*, *s* for *shear wave*, and *a* for *acceleration*.

The following enumeration summarizes the main steps in the *FINSIM* code (Beresnev and Atkinson, 1997) for the stochastic simulation of ground motion time series from finite faults. I will make use of common mathematical notations for continuous signals. The single steps are illustrated in Figure 3.1.

1. For each subfault:
  - Calculation of a *skeleton function* of the desired Fourier amplitude spectrum  $|A_{sf,s}^{desired}(\mathbf{x}, \omega)|$  based on specified input parameters (e.g., seismic moment, stress drop, rupture velocity,



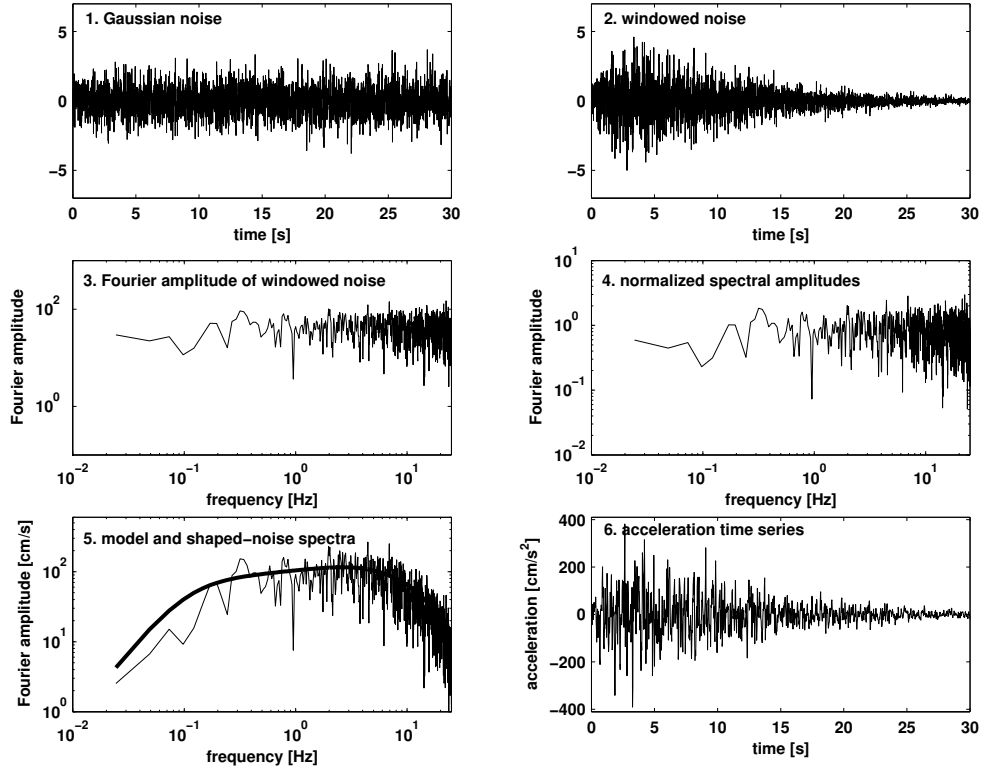


**Figure 3.1:** Main processing steps in the stochastic simulation method as explained in the text.

or distance from the source; see (2.1)):

$$|A_{sf,s}^{desired}(\mathbf{x}, \omega)| = |S_{sf,s}^a(\mathbf{x}, \omega)| \cdot G(\mathbf{x}) \cdot I(\mathbf{x}, \omega) \cdot H(\mathbf{x}, \omega) \cdot F(\mathbf{x}, \omega) \quad (3.1)$$

with Fourier source spectrum  $|S_{sf,s}^a(\mathbf{x}, \omega)|$ , geometrical spreading  $G(\mathbf{x})$ , inelastic attenuation  $I(\mathbf{x}, \omega)$ , high-frequency diminution  $H(\mathbf{x}, \omega)$ , and site amplification  $F(\mathbf{x}, \omega)$ . Relationships between target and subfault spectra have to be considered; they will be discussed aside from the skeleton function in Chapter 3.2.1.

- Generation of a time series of Gaussian white noise  $a_{sf,s}^{noise}(\mathbf{x}, t)$  of length  $T_d$  with zero mean and unit variance (see Figure 3.1, 1.).  $T_d$  depends on the rise time of the source  $\tau_r$  and on an additional distance-dependent term that allows for the consideration of multipathing and scattering effects (see Chapter 2.2.3).

$$T_d = \begin{cases} \tau_r + durmin & , r \leq rmin \\ \tau_r + durmin + b1 (r - rmin) & , rmin < r \leq rd1 \\ \tau_r + durmin + b1 (rd1 - rmin) + b2 (r - rd1) & , rd1 < r \leq rd2 \\ \tau_r + durmin + b1 (rd1 - rmin) + b2 (rd2 - rd1) + b3 (r - rd2), & r > rd2 \end{cases} \quad (3.2)$$

The trilinear duration model can be empirically calibrated from small earthquakes (Atkinson and Boore, 1995).

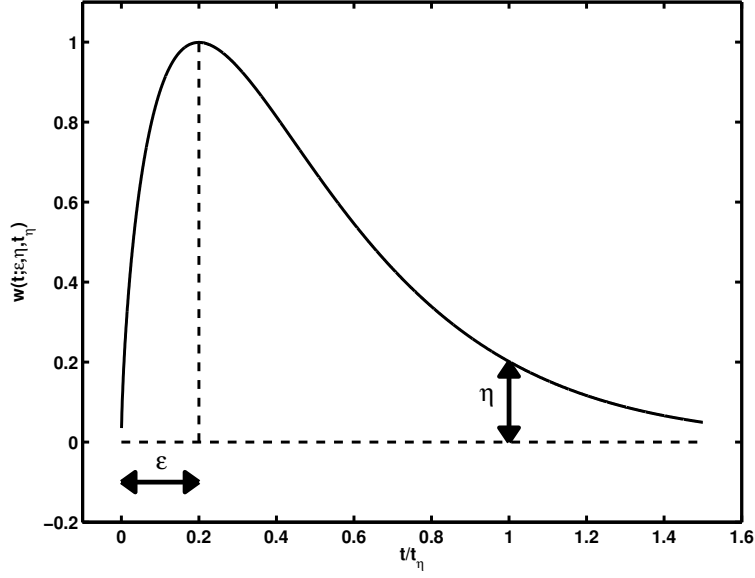


**Figure 3.2:** Shaping window after Saragoni and Hart (1974) to give the time series an earthquake-like shape.

- Application of a *shaping window* to the noise in order to obtain an earthquake-like shape for the acceleration time series (see Figure 3.1, 2.). In this work, I will make use of a so-called *Saragoni Hart window* that has been empirically derived by Saragoni and Hart (1974) from a large set of recorded ground motions during earthquakes. It describes an envelope function given by

$$w(t; \varepsilon, \eta, t_\eta) = a (t/t_\eta)^b \exp(-c (t/t_\eta)) \quad (3.3)$$

with

$$\begin{aligned} a &= (\exp(1)/\varepsilon)^b, \\ b &= -(\varepsilon \ln \eta) / [1 + \varepsilon (\ln \varepsilon - 1)], \\ c &= b/\varepsilon, \end{aligned} \quad (3.4)$$

and  $w(t; \varepsilon, \eta, t_\eta) = \eta$  for  $t = t_\eta = T_d$ . Default values in *FINSIM* are  $\varepsilon = 0.2$  and  $\eta = 0.2$ , i.e.  $a = 5.74$ ,  $b = 0.67$  and  $c = 3.35$  (see Figure 3.2). We obtain

$$a_{sf,s}^{shaped}(\mathbf{x}, t) = a_{sf,s}^{noise}(\mathbf{x}, t) \cdot w(t; \varepsilon, \eta, t_\eta). \quad (3.5)$$

- Transformation of  $a_{sf,s}^{shaped}(\mathbf{x}, t)$  to frequency domain via Fourier transformation (see Figure 3.1, 3.)

$$A_{sf,s}^{shaped}(\mathbf{x}, \omega) = \frac{1}{2\pi} \int_0^{T_D} a_{sf,s}^{shaped}(\mathbf{x}, t) \exp^{-i\omega t} dt. \quad (3.6)$$

- Multiplication of  $A_{sf,s}^{shaped}(\mathbf{x}, \omega)$  with the skeleton function (3.1) after normalization to the

square of unit spectral amplitude (see Figure 3.1, 4. and 5.)

$$A_{sf,s}^{output}(\mathbf{x}, \omega) = \frac{A_{sf,s}^{shaped}(\mathbf{x}, \omega)}{\sqrt{|A_{sf,s}^{shaped}(\mathbf{x}, \omega)|^2}} \cdot |A_{sf,s}^{desired}(\mathbf{x}, \omega)|. \quad (3.7)$$

- Transformation of  $A_{sf,s}^{output}(\mathbf{x}, \omega)$  back to time domain via inverse Fourier transformation. The real part of the complex output ( $\mathcal{R}[\cdot]$ ) gives a time series for each subfault with the desired spectral characteristics (see Figure 3.1, 6.):

$$a_{sf,s}^{output}(\mathbf{x}, t) = \mathcal{R} \left[ \frac{1}{2\pi} \int_0^{T_D} A_{sf,s}^{output}(\mathbf{x}, \omega) \exp i\omega t d\omega \right]. \quad (3.8)$$

2. The summation of contributions of all subfault elements considering time delays between their triggering due to rupture propagation gives the desired acceleration time series  $a_s^{output}(\mathbf{x}, t)$  for shear waves. In order to allow for heterogeneities in the rupture process a small random number is added to the time intervals between the triggering of different subfaults.

### 3.2.1 Description of the Skeleton Function $|A_{sf,s}^{desired}(\mathbf{x}, \omega)|$

This subsection will discuss the different terms of the *skeleton function*  $|A_{sf,s}^{desired}(\mathbf{x}, \omega)|$  given by (3.1). A compilation of free parameters that have to be specified by the *FINSIM* user is given in Table 3.1, second column from left.<sup>1</sup>

#### A. Simulation of the Seismic Source $|S_{sf,s}^a(\mathbf{x}, \omega)|$

*FINSIM* simulates the mean horizontal component of S-wave acceleration (Beresnev and Atkinson, 1998). The Fourier acceleration spectrum  $|S_{sf,s}^a(\mathbf{x}, \omega)|$  is related to the displacement spectrum  $|S_{sf,s}^d(\mathbf{x}, \omega)|$  in (2.14) by a factor  $\omega^2$  (see (2.15)):

$$\begin{aligned} |S_{sf,s}^a(\mathbf{x}, \omega)| &= \omega^2 |S_{sf,s}^d(\mathbf{x}, \omega)| \\ &= \omega^2 \frac{f_s}{\sqrt{2}} \frac{\mathbf{R}_s^{\theta\phi} m_0}{4\pi\rho\beta^3} \left[ 1 + \left( \frac{\omega}{\omega_c} \right)^2 \right]^{-1} \\ &= \omega^2 C_s m_0 \left[ 1 + \left( \frac{\omega}{\omega_c} \right)^2 \right]^{-1}, \end{aligned} \quad (3.9)$$

whereby  $\omega$  indicates the circular frequency and  $\omega_c$  the corner frequency of the spectrum. Index  $d$  stands for *displacement*,  $a$  for *acceleration*,  $sf$  for *subfault*, and  $s$  for *shear wave*. The spectral constant  $C_s$  depends on the radiation pattern  $\mathbf{R}_s^{\theta\phi}$ , the density  $\rho$  and the cube of seismic velocity  $\beta$  of the medium through which the seismic waves propagate, as well as on the free surface amplification<sup>2</sup>  $f_s = 2$ , i.e.

$$C_s = \frac{f_s}{\sqrt{2}} \frac{\mathbf{R}_s^{\theta\phi}}{4\pi\rho\beta^3}. \quad (3.10)$$

<sup>1</sup>In practice, *FINSIM* requires the specification of the number of subfaults  $n$ , rather than of subfault dimension  $\Delta l$ .

<sup>2</sup>Strictly speaking this is only true for horizontally polarized shear waves (SH-waves).

The factor  $1/\sqrt{2}$  comes from an arbitrary distribution of the SH component - for which the theory holds - on instrumental components. The radiation pattern is quasi ignored by assuming that  $\mathbf{R}_s^{\theta\phi} = 0.55$  which is the spatial average for S-waves (Boore and Boatwright, 1984).

### Relationships between target and subsurface spectra

The relationships between the target spectrum of the finite fault  $|S_s^a(\mathbf{x}, \omega)|$  and the subsurface spectra  $|S_{s,f,s}^a(\mathbf{x}, \omega)|$  will be discussed in the following paragraphs. I assume a  $\omega^2$  source model.

- **Link between corner frequency  $\omega_c$  of the target spectrum and subsurface dimension  $\Delta l$ :**

Since the slip duration in the exponential source time functions in (2.8) is formally unlimited, the *rise time*  $\tau_r$  is usually defined as the period of time necessary for the average slip  $\bar{u}$  to reach a certain fraction  $m$  of the total slip  $\bar{u}(\infty)$  (Beresnev, 2001)

$$m \equiv \frac{\bar{u}(\tau_r)}{\bar{u}(\infty)} = \left[ 1 - \left( 1 + \frac{\tau_r}{\tau} \right) e^{-\tau_r/\tau} \right]. \quad (3.11)$$

It is generally assumed that during the (subsurface) rise time  $\tau_r$  the average rupture propagates the half or full length of fault segment  $\Delta l$ :

$$\tau_r = \frac{\Delta l}{v_r} = \frac{\Delta l}{y\beta}. \quad (3.12)$$

The rupture velocity  $v_r$  is here presumed to be a constant fraction  $y$  of the shear wave velocity  $\beta$ ; generally it is  $y \approx 0.8$ . Defining

$$z \equiv \frac{\tau_r}{\tau} = \tau_r \omega_c, \quad (3.13)$$

the corner frequency  $\omega_c$  can be related to source dimension  $\Delta l$  by

$$\boxed{\omega_c = \frac{z}{\tau_r} = K \frac{\beta}{\Delta l} \quad \text{with } K = y z} \quad (3.14)$$

Parameter  $z$  is linked to the maximum slip velocity  $v_{max}$  on the fault (Beresnev, 2001) given by

$$v_{max} = \frac{\bar{u}(\infty)}{\exp(1) \tau} = \frac{y z}{\exp(1)} \frac{\beta}{\mu} \Delta\sigma, \quad (3.15)$$

whereby  $v_{max}$  is obtained by taking the time derivative of (2.8) with  $t = \tau$ . The (static) stress drop  $\Delta\sigma$  is defined by (2.16). Setting in (3.11), e.g.,  $m = 0.5$  gives  $z = 1.68$ . In order to allow  $z$  values distinct from  $z = 1.68$ , *FINSIM* enables the user to specify parameter *sfact* defined by

$$sfact \equiv \frac{z}{1.68}. \quad (3.16)$$

Parameter *sfact* controls the level of high-frequency radiation (Beresnev and Atkinson, 1998). Note the similarity between (3.15) resolved for  $\Delta\sigma$  and the definition of the *dynamic stress drop*  $\Delta\sigma_d$  by Brune (1970) and Kanamori (1994),

$$\Delta\sigma_d \equiv \frac{C_d}{2} \frac{\bar{u}(\infty)}{\tau_r} \frac{\mu}{\beta} \quad (3.17)$$

with  $C_d \approx 2$ . Dynamic stress drops therewith can be controlled in *FINSIM* by parameter *sfact* (3.16), and therewith can be distinguished from static stress drops, unlike in the stochastic simulation code for point sources developed by Boore (1996) (SMSIM).

- **Link between seismic moment  $M_0$  of the target spectrum and subsurface dimension  $\Delta l$ :**

The relation between subfault size  $\Delta l$ , stress parameter  $\Delta\sigma$  and subfault seismic moment  $m_0$  is according to (2.17) given by

$$m_0 \approx \Delta\sigma \Delta l^3. \quad (3.18)$$

The sum of moments  $m_0$  of all  $N$  subsources -  $N$  is not necessarily equal to the number of subfaults  $n$  as will be shown later - has to result in the specified target moment  $M_0$ , i.e.

$$N \equiv \frac{M_0}{m_0}. \quad (3.19)$$

Inserting (3.18) into (3.19) gives the desired relation between seismic moment  $M_0$  of the target earthquake and subfault dimension  $\Delta l$ :

$$M_0 = N \Delta\sigma \Delta l^3. \quad (3.20)$$

In order to consider inhomogeneous slip distributions, *FINSIM* allows for the specification of a weight matrix  $W$  with elements  $w_{ij}$  to vary the subfault moments. The number of triggerings  $n_{s_{ij}}$  of subfault ( $ij$ ) -  $i$  is the subfault number along strike and  $j$  along dip on the fault plane - is given by

$$n_{s_{ij}} = w_{ij} \frac{M_0}{m_0}, \quad \sum_{i,j} w_{ij} = 1, \quad (3.21)$$

whereby  $W$  is normalized to unity in order to conserve the target moment  $M_0$ . The total number of subsources  $N$  is given by the sum of triggerings  $n_{s_{ij}}$  of all  $n$  subfaults, i.e.

$$N = \sum_{i,j} n_{s_{ij}}. \quad (3.22)$$

The displacement  $u$  on subfault ( $ij$ ) is

$$u_{ij} = \frac{n_{s_{ij}} m_0}{\mu \Delta l^2} = \frac{n_{s_{ij}} m_0}{\rho \beta^2 \Delta l^2}. \quad (3.23)$$

- **Link between target spectrum  $|S_s^a(\mathbf{x}, \omega)|$  and the sum of subsurface spectra  $\sum |S_{sf,s}^a(\mathbf{x}, \omega)|$ :**

As the subfault spectra add incoherently, the target amplitude increases only with  $\sqrt{N}$  instead of  $N$  (Joyner and Boore, 1986). Using (3.14) and (3.19) gives

$$\begin{aligned} |S_s^a(\mathbf{x}, \omega)| &= \sum |S_{sf,s}^a(\mathbf{x}, \omega)| \\ &\approx \sqrt{N} |S_{sf,s}^a(\mathbf{x}, \omega)| \\ &\approx C_s \sqrt{M_0 \Delta\sigma \Delta l^3} \omega^2 \left[ 1 + \left( \frac{\omega \Delta l}{K\beta} \right)^2 \right]^{-1}, \end{aligned} \quad (3.24)$$

which can be approximated by

$$|S_s^a(\mathbf{x}, \omega)| \approx C_s \sqrt{\frac{M_0 \Delta\sigma}{\Delta l}} K^2 \beta^2. \quad (3.25)$$

Equation (3.25) indicates that the Fourier amplitude spectrum is in particular sensitive to parameter  $K$  - which itself is related to parameters  $z$  and  $s_{fact}$  via (3.14) and (3.16) - and to the subfault size  $\Delta l$ . Beresnev and Atkinson (1998) point out that  $\Delta l$  is theoretically limited by the following constraints: the lower boundary on  $\Delta l$  is determined by the requirement that the corner frequency lies below the frequency band of interest. The upper boundary on  $\Delta l$  can be attributed to the opportunity of a reasonable number of subsources in order to obtain a realistic shape for the accelerogram. Beresnev and Atkinson (2002) give the following empirical rule for the relationship between subfault size  $\Delta l$  - that can be understood as characteristic size of asperities on the rupturing fault - and moment magnitude  $M_w$  of the target earthquake<sup>3</sup>, valid for  $4 \leq M_w \leq 8$  ( $\Delta l$  in [km])

$$\log \Delta l = -2 + 0.4 M_w \quad (3.26)$$

$M_w$  is related to  $M_0$  via (2.21). A similar relationship between earthquake magnitude and typical asperity size has been found by Somerville et al. (1999):  $\log \Delta l = -2 + 0.5 M_w$ .

## B. Simulation of Path Effects

### Geometrical Spreading $G(\mathbf{x})$

*FINSIM* enables the user to specify a trilinear model to describe geometrical spreading with two distance parameters  $rg1$  and  $rg2$ , and three parameters  $pow1$ ,  $pow2$  and  $pow3$  characterizing the amplitude decay:

$$G(\mathbf{x}) = \begin{cases} r^{pow1} & \text{for } r \leq rg1 \\ rg1^{pow1} (r/rg1)^{pow2} & \text{for } rg1 < r \leq rg2 \\ rg1^{pow1} (rg2/rg1)^{pow2} (r/rg2)^{pow3} & \text{for } r > rg2 \end{cases} \quad (3.27)$$

The idea behind this trilinear model comes from the observation that amplitude decay is distinct from the theoretical value  $r^{-1}$  which has been derived for the elastic space in Chapter 2 (2.23). Layering in the crust causes direct-wave amplitudes to decay more steeply than  $r^{-1}$  (Burger et al., 1987). In the distance range of joint arrivals of direct waves and postcritical reflections off the Moho and intracrustal discontinuities (approximately between 50 to 200 km), amplitudes may increase with distance. At larger distances geometrical attenuation may be significantly greater than  $r^{-0.5}$  - which is the theoretical value for surface waves in a half-space (Hasegawa, 1985) - depending on the nature of the crust-mantle transition: a sharp velocity contrast traps energy within the crustal waveguide, while a velocity gradient allows leakage into the mantle, increasing the apparent geometric attenuation. Further amplitude variations are caused by crustal heterogeneities (Ojo and Mereu, 1986).

### Inelastic Attenuation $I(\mathbf{x}, \omega)$

Inelastic attenuation is implemented in *FINSIM* by specification of parameters  $Q_0$  and  $\eta$ . The

---

<sup>3</sup>In practice, *FINSIM* requires specifications of  $M_w$ , the length  $L$  and width  $W$  of the rupture, and the number of subfaults  $n$ .

inelastic term was derived in Chapter 2 (2.29) with

$$I_s(\mathbf{x}, \omega) = \exp\left(-\frac{\omega r(\mathbf{x})}{2 Q \beta}\right) \quad \text{with} \quad Q = Q_0 \left(\frac{\omega}{2\pi}\right)^\eta \quad (3.28)$$

### C. Simulation of Site Effects

#### Frequency-dependent Amplification $F(\mathbf{x}, \omega)$

Frequency-dependent amplification can be considered in *FINSIM* by the specification of frequency values and respective amplification factors:

$$F(\mathbf{x}, \omega) = \{[\omega_1, \text{amp}_1(\mathbf{x})], \dots, [\omega_m, \text{amp}_m(\mathbf{x})]\} \quad (3.29)$$

The program interpolates automatically between the given values; for frequencies to the left and right of the lowest and highest specified values, *FINSIM* assumes constant amplification.

#### High-Frequency Diminution $H(\mathbf{x}, \omega)$

High-frequency diminution by near-surface deposits and the crustal velocity gradient (see (2.35)) is realized by the specification of (site-dependent)  $\kappa$  values:

$$H(\mathbf{x}, \omega) = \exp\left(-\pi\kappa(\mathbf{x})\frac{\omega}{2\pi}\right) \quad (3.30)$$

Alternatively, *FINSIM* allows for the specification of parameter  $f_{max}$  (see (2.34)).

### 3.2.2 Modifications of the *FINSIM* Code

For the purpose of earthquake early warning the *FINSIM* code by Beresnev and Atkinson (1997) has to be modified in two aspects: first, a correct time axis is required because we are interested in time differences between wave onsets at different seismic stations. Second, the stimulation and propagation of compressional waves have to be considered; compressional waves are less destructive than shear and surface waves but spread with higher velocities and are therewith the firstly recorded seismic waves at the sensor sites. As P-waves have basically similar spectral features like S-waves (Boore, 1986) only some simple modifications of the stochastic method are required that are shortly explained in the following.

- **Velocity  $\alpha$**

Definitions of P- and S-wave velocities as a function of elastic moduli and density have been given by (2.5) and (2.6). Assuming a Poisson's ratio  $\sigma$  of 0.25, which is a typical value for the Earth's crust, it is  $\mu \approx \lambda$  and therewith

$$\alpha \approx \sqrt{\frac{3\mu}{\rho}} \approx \sqrt{3} \beta \quad (3.31)$$

- **Source term**  $|S_{sf,p}^a(\mathbf{x}, \omega)|$

The spectral constant  $C_s$  for S-waves has been defined by (3.10). Analog a spectral constant for P-waves  $C_p$  is defined by

$$C_p = \frac{f_s}{\sqrt{2}} \frac{\mathbf{R}_p^{\theta\phi}}{4\pi\rho\alpha^3} \quad (3.32)$$

The average spatial radiation of P-waves is  $\mathbf{R}_p^{\theta\phi} = 0.33$  (Boore and Boatwright, 1984). Averaged over different angles of incidence the free surface horizontal vector amplification coefficient is  $f_s \approx 2.0$  for a plane P-wave (Jiang et al., 1998). A further term accounts for the angle of incidence  $\varepsilon$  of seismic P-waves. Thus in the case of compressional waves (3.9) is modified

$$|S_{sf,p}^a(\mathbf{x}, \omega)| = \omega^2 C_p \sin(\varepsilon) m_0 \left[ 1 + \left( \frac{\omega}{\omega_c} \right)^2 \right]^{-1} \quad (3.33)$$

- **Inelastic attenuation**  $I_p(\mathbf{x}, \omega)$

Intrinsic attenuation occurs mainly in shear which means that the quality factor for S-waves,  $Q_s$ , is always smaller than for P-waves,  $Q_p$ . I assume a  $Q_p/Q_s$ -ratio of 9/4 which implies that only the shear modulus contributes to Q, and not the bulk modulus (e.g., Lay and Wallace, 1995). After substitution of  $\beta$  by  $\alpha$  (3.28) becomes

$$I_p(\mathbf{x}, \omega) = \exp\left(-\frac{\omega r(\mathbf{x})}{2 Q_p \alpha}\right) \quad \text{with} \quad Q_p = \frac{9}{4} Q_s \quad (3.34)$$

- **Site effects**  $F_p(\mathbf{x}, \omega)$  and  $H_p(\mathbf{x}, \omega)$

For simplicity reasons I assume that site effects on P-waves are equal to effects on S-waves. However, as P-wave velocities in soil are generally higher than S-wave velocities, it follows from (2.31) that the fundamental frequency of P-wave amplification is higher while the amplitude of amplification is lower than those for S-waves. As the water saturation affects P-wave velocities it has significant impact on amplification (Sokolov, 2005, pers. comm.).

Time series for P- ( $a_p^{output}(\mathbf{x}, t)$ ) and S-waves ( $a_s^{output}(\mathbf{x}, t)$ ) are generated separately from each other, and then summed up with the respective time delays due to different propagation velocities. Examples of simulated ground motion time series for earthquakes of  $M_w = 5.0$ ,  $M_w = 6.0$  and  $M_w = 7.0$  at 15 km distance are shown in Figure 3.3, 3.4 and 3.5. Velocity and displacement data are obtained by time-integration and high-pass filtering above 0.2 Hz.

### 3.3 Stochastic Simulation of Ground Motion from Finite Faults in the Marmara Region

Using the modified *FINSIM* code as described in Chapter 3.2.2 a set of synthetic ground motion records for the Marmara region is produced. Similar procedures have been applied to synthesize the



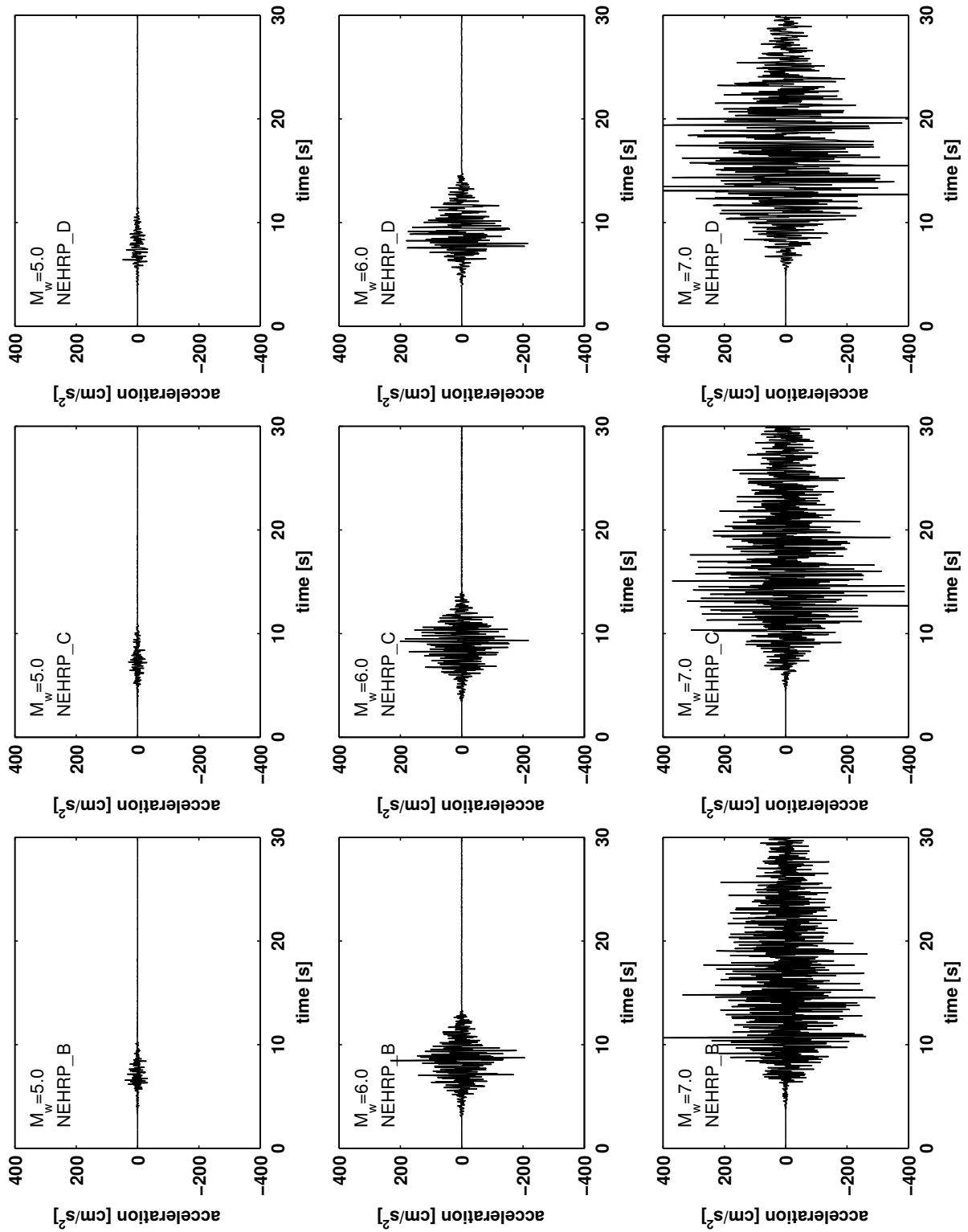
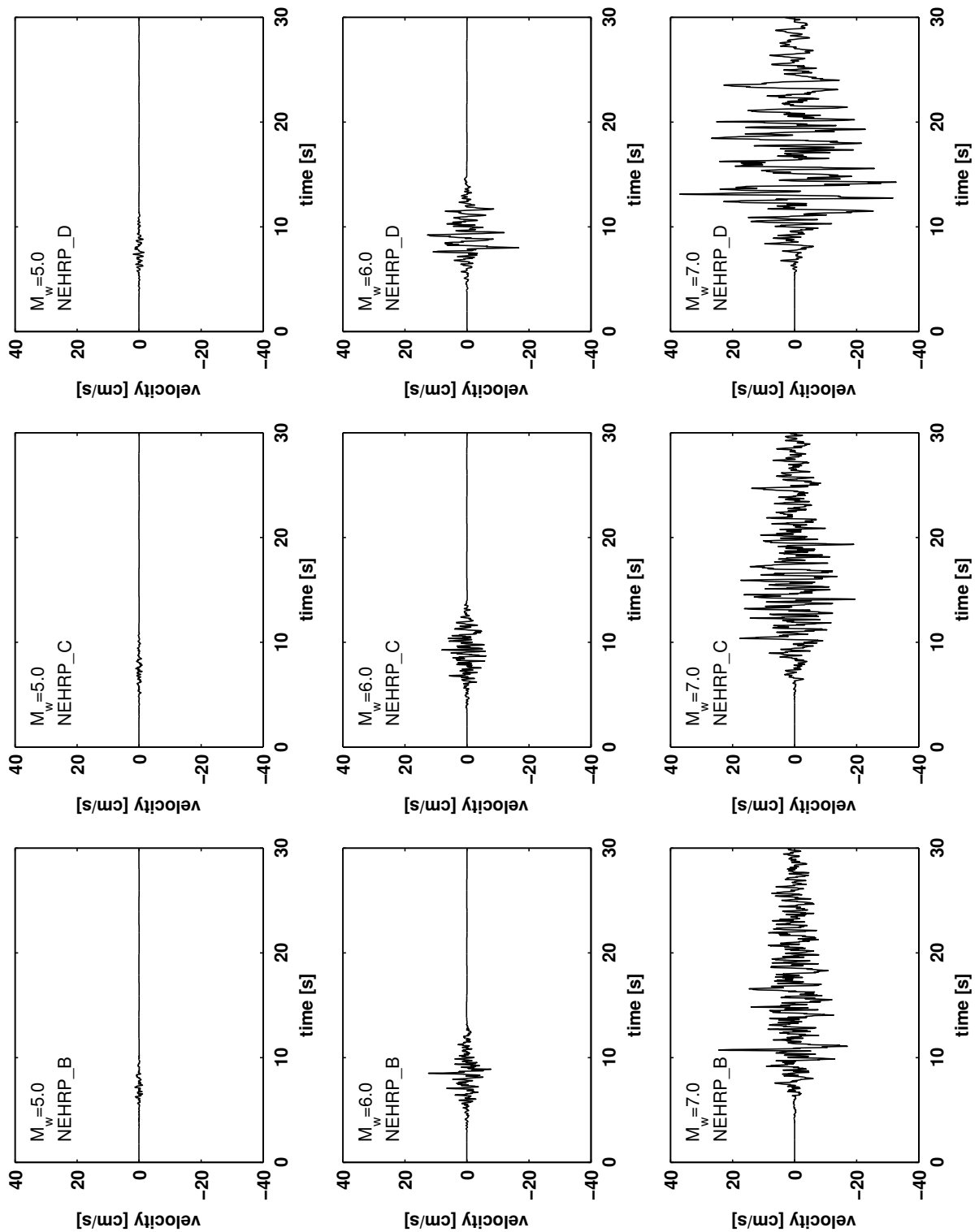
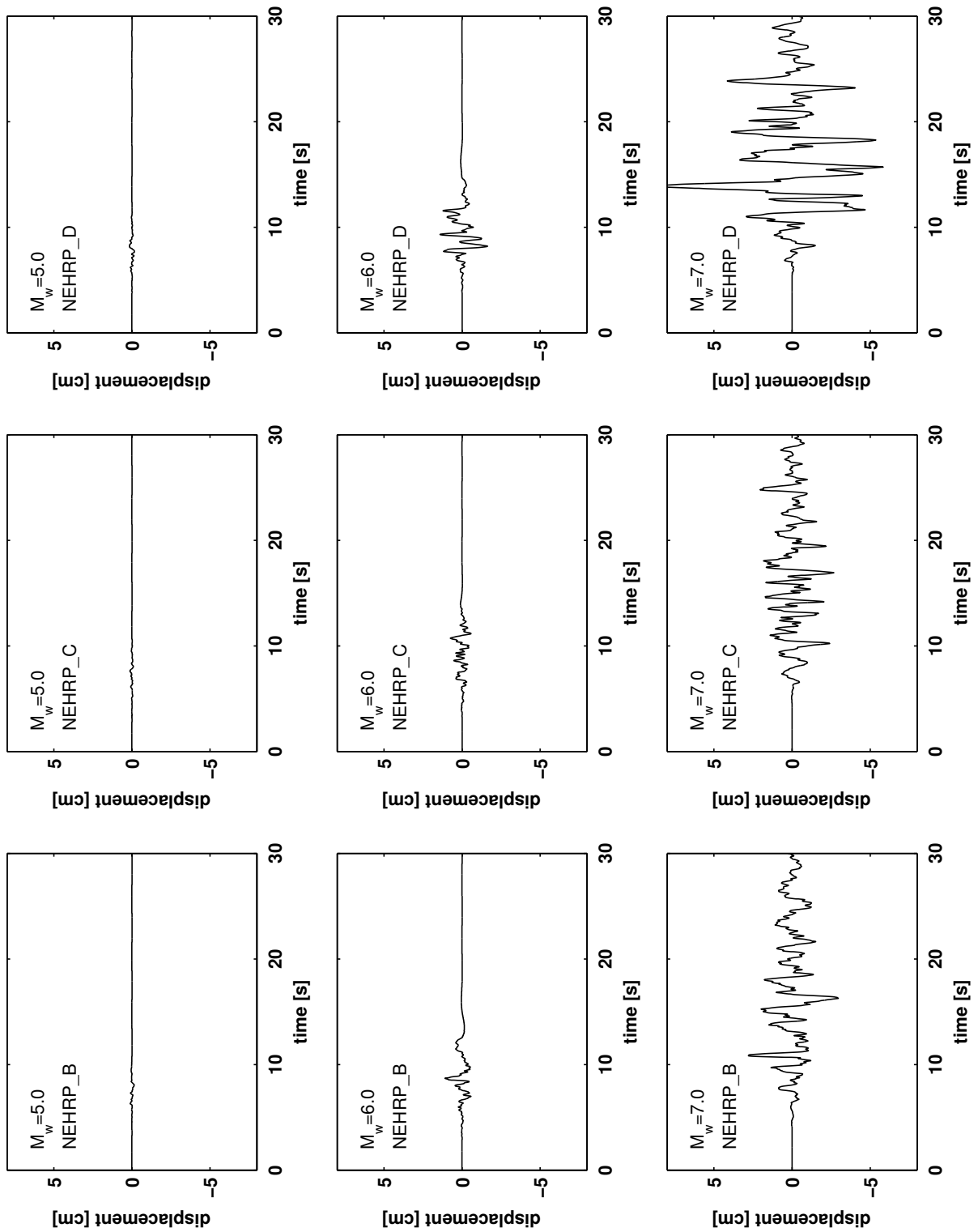


Figure 3.3: Simulated mean horizontal components of acceleration at 15 km distance.



**Figure 3.4:** Mean horizontal components of velocity obtained from time-integration of acceleration records in Figure 3.3.



**Figure 3.5:** Mean horizontal components of displacement obtained from time-integration of velocity records in Figure 3.4.

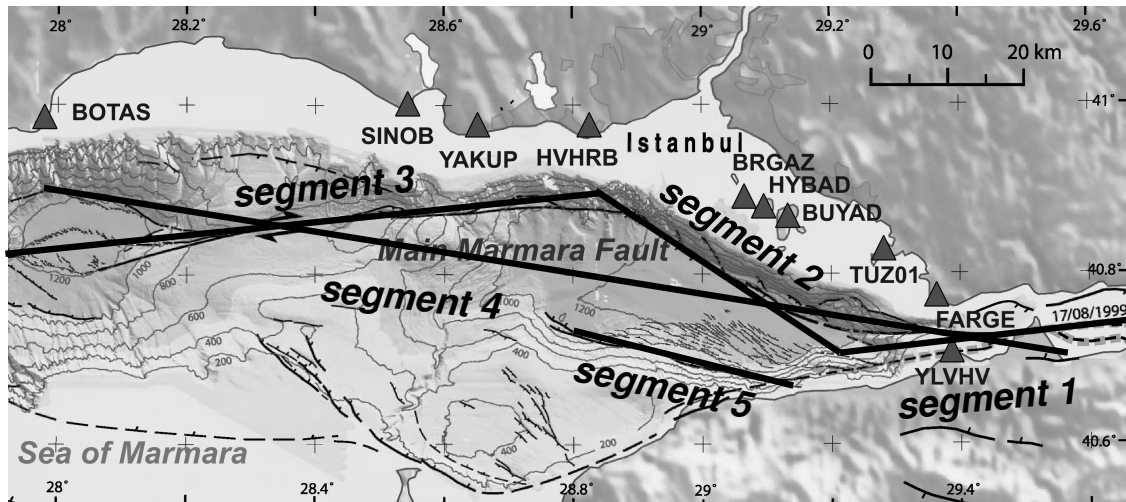


**Figure 3.6:** Fault segments in the Sea of Marmara close to Istanbul used for the simulations of seismic ground motion in this work. SEGMENT 1 corresponds to the *Izmit Fault*, SEGMENT 2 to the *Cinarcik Fault*, and SEGMENT 3 to the *Western Fault* (see Figure 1.3). Fault SEGMENT 4 represents joint ruptures of SEGMENTS 1 to 3 which corresponds to the interpretation by Le Pichon et al. (2003). SEGMENT 5 considers source locations beyond the Main Marmara Fault in the southeastern part of the Sea of Marmara.

1999 Kocaeli earthquake (*Stochastic Method*, Durukal, 2002) or to model different scenario earthquakes for seismic hazard assessment in Istanbul (*Hybrid Method*, Pulido et al., 2004).

The required input parameters for the stochastic simulation are mostly taken from the literature (Table 3.1). These reference values are varied within reasonable limits as indicated in the table to make the database as realistic as possible. Diverse slip distributions are simulated by randomized weight matrices (see (3.21)) and are combined with different directions of rupture propagation, including bi- and unidirectional cases.

The distribution of simulated earthquake hypocenters is constrained by the locations of faults in the Sea of Marmara. As denoted in Chapter 1.3 there is an ongoing debate between Le Pichon et al. (2003) and Armijo et al. (2002) concerning the existence of a single through-going or segmented *Main Marmara Fault*<sup>4</sup> in the Sea of Marmara. In this study both interpretations shall be considered. Five fault segments are introduced as possible source locations of moderate and strong earthquakes (Figure 3.6): SEGMENT 1 corresponds to the *Izmit Fault*, SEGMENT 2 to the *Cinarcik Fault*, and SEGMENT 3 to the *Western Fault* (see Figure 1.3). Fault SEGMENT 4 represents joint ruptures of SEGMENTS 1 to 3 which corresponds to the interpretation by Le Pichon et al. (2003).<sup>5</sup> SEGMENT 5 considers source locations beyond the Main Marmara Fault in the southeastern part of the Sea of Marmara. Locations of the five segments aside from specifications of the maximum possible magnitudes on each segment determined from the Wells-Coppersmith relation (2.22) are compiled in Table 3.2.

Fifty earthquakes are simulated in narrow bands along each fault segment in the magnitude range of  $4.5 \leq M_w \leq 7.5$ . The database is supplemented by 30 additional earthquakes ( $4.5 \leq M_w \leq 5.0$ )

<sup>4</sup>Note that even though using the term *Main Marmara Fault* in this work I do not want to imply that this fault is necessarily through-going.

<sup>5</sup>Note that *FINSIM* can only model plane rupture propagation.

**Modeling parameters**

term	variable	value	reference	
source	rupture depth	: $Z_{rupt}$	5.0 km	
	rupture dip	: $\delta$	90°	
	rupture length	: L	eq.(2.22)	WC94
	rupture width	: W	eq.(2.22)	WC94
	subfault size	: $\Delta l$	eq.(3.26)	AB95
	radiation strength	: sfact	0.9 – 1.3	
	stress drop	: $\Delta\sigma$	$6 - 13 \cdot 10^6$ N/m <sup>2</sup>	HMcG81
	density	: $\rho$	3,000 kg/m <sup>3</sup>	POA04
	S-wave velocity	: $\beta$	3,300 m/s	POA04
	moment magnitude	: $M_w$	$4.5 \leq M_w \leq 7.5$	
geometrical spreading	trilinear model	: rg1	2	SCE97, mod.
	see eq.(3.27)	: rg2	400	
		: pow1	-1.5	
		: pow2	-0.8	
		: pow3	-0.7	
inelastic attenuation	crustal Q model	: $Q_0$	50	HKB98
	see eq.(3.28)	: $\eta$	1.09	
site amplification	frequency-dependent	: NEHRP B	Table 2.2	BJ97
	amplification	: NEHRP C	Table 2.2	
	see eq.(3.29)	: NEHRP D	Table 2.2	
high-frequency diminution	$\kappa$ filter	: $\kappa$ NEHRP B	0.035	BJ97
	see eq.(3.30)	: $\kappa$ NEHRP C	0.040	
		: $\kappa$ NEHRP D	0.045	
duration	trilinear model	: rmin	10	AB95, mod.
	see eq.(3.2)	: rd1	70	
		: rd2	130	
		: durmin (B, C, D)	2.00, 2.20, 2.40	
		: b1 (B, C, D)	0.25, 0.30, 0.40	
		: b2	0.10	
		: b3	0.04	

**References:** AB95 Atkinson and Boore (1995) POA04 Pulido et al. (2004)  
 BJ97 Boore and Joyner (1997) SCE97 Sadigh et al. (1997)  
 HMcG81 Hanks and McGuire (1981) WC94 Wells and Coppersmith (1994)  
 HKB98 Horasan et al. (1998)

**Table 3.1:** Input parameters for the stochastic simulation of seismic ground motion in the Marmara region.

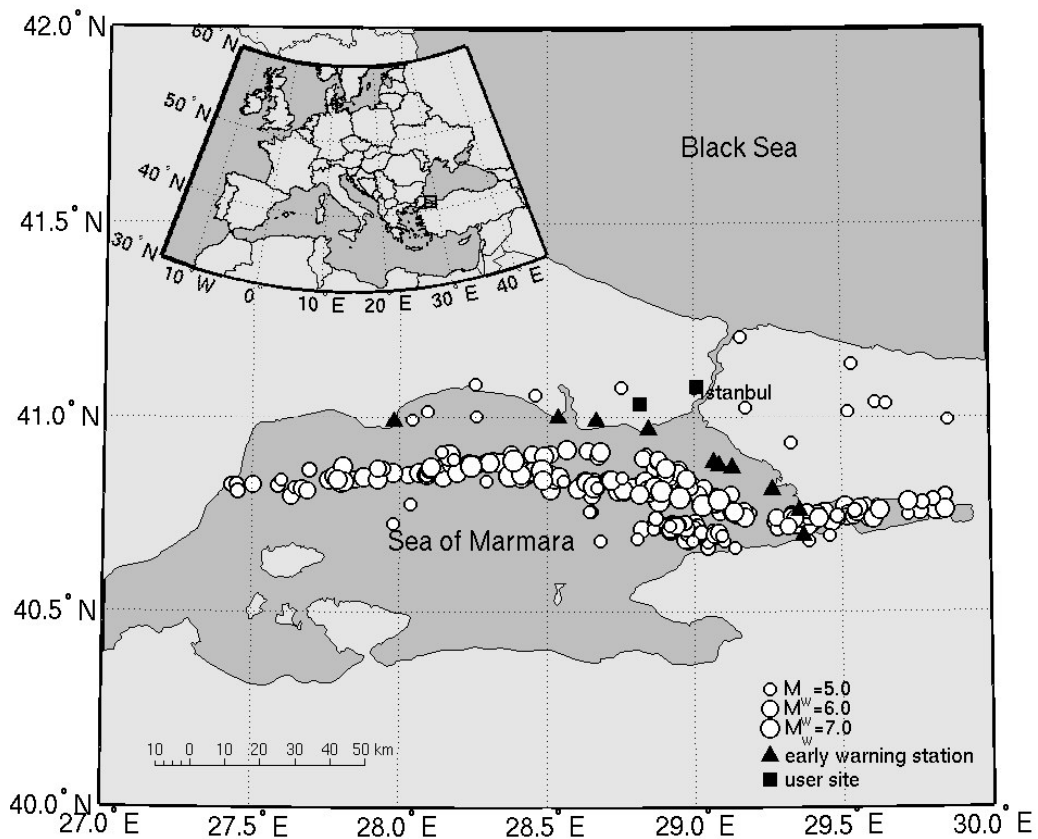


**Figure 3.7:** Epicenters of 250 synthetic earthquakes ( $4.5 \leq M_w \leq 7.5$ ) along the five fault segments in the Sea of Marmara shown in Figure 3.6; further 30 small and moderate events ( $4.5 \leq M_w \leq 5.0$ ) are randomly distributed in the Marmara region. Details on the simulated earthquakes are given in Appendix B.

**Fault segments in the Sea of Marmara**

SEGMENT ID	fault start	fault end	azimuth	fault length	magnitude range
1	[40.77°N; 29.91°E]	[40.73°N; 29.20°E]	265°	60 km	$M_w \leq 7.1$
2	[40.73°N; 29.20°E]	[40.91°N; 28.79°E]	300°	40 km	$M_w \leq 6.8$
3	[40.91°N; 28.79°E]	[40.83°N; 27.61°E]	265°	100 km	$M_w \leq 7.4$
4	[40.71°N; 29.52°E]	[40.90°N; 28.00°E]	280°	130 km	$6.5 \leq M_w \leq 7.6$
5	[40.68°N; 29.15°E]	[40.74°N; 28.80°E]	282°	30 km	$M_w \leq 6.6$

**Table 3.2:** Fault segments in the Sea of Marmara (see Figure 3.6) and assigned maximum possible magnitudes determined from the Wells-Coppersmith relation (2.22) as input for the simulations in this study.

that are independent from the large segments and that are randomly distributed in the Marmara region (Figure 3.7). Source depths of the 280 synthetic earthquakes vary between 5 and 20 km. Tables B.1 to B.6 in Appendix B summarize the locations of epicenters on the fault segments, aside from specifications of source depths, magnitudes and locations of ruptures.

For each earthquake I simulate seismic ground motion at the ten stations of the Istanbul earthquake early warning system (Figure 1.3), at one site in Istanbul (*ISTAN*) and at one industrial settlement close to Istanbul (*UserX*) as potential users of early warnings. Station coordinates and NEHRP classes at the respective sites are compiled in Table 3.3. Studies on site effects at these locations are not available. For the early warning stations and the Istanbul site frequency-dependent amplification functions based on the NEHRP soil classification scheme (Boore and Joyner, 1997) presented in Chapter 2.3.3 are integrated. For the industrial facility site I make use of the amplification spectrum observed at station *TLC* in Tulcea, Romania (see Figure 3.8, Sokolov et al. (2005)), which is installed on metamorphic rock, to demonstrate the impact of realistic site effects. This idea shall be explained in more detail in Chapter 6.

Histograms for magnitudes and depths of the synthetic earthquakes are displayed in Figure 3.9. Figure 3.10 shows the simulated ground motion at the different sites for a  $M_w = 6.5$  earthquake (SEGMENT 2, #25). Rupture directivity can be well observed at station *HVHRB*. At all sites a 3<sup>rd</sup> order Butterworth filter is applied between 0.05 to 12.0 Hz at a sampling rate of 50 samples per second (Erdik et al., 2003b).

### 3.4 Discussions

The principle idea behind the *Stochastic Simulation Method of Seismic Ground Motion* is the combination of the estimated Fourier amplitude spectrum of ground motion with a random phase (Boore, 1983, 2003). The method provides a simple and suitable technique for the simulation of ground shaking time series for moderate and strong earthquakes that cover the frequency band of interest for most

10 early warning stations and 2 user sites

STATION NO.	STATION ID	LAT $\varphi$ ° N	LON $\lambda$ ° E	NEHRP class
1	BOTAS	40.99	27.98	C
2	BRGAZ	40.88	29.07	B
3	BUYAD	40.87	29.13	B
4	FARGE	40.76	29.36	B
5	HVHRB	40.97	28.84	D
6	HYBAD	40.88	29.09	B
7	SINOB	41.00	28.54	C
8	TUZ01	40.81	29.27	D
9	YAKUP	41.00	28.67	C
10	YLVHV	40.70	29.37	C
11	ISTAN	41.08	29.01	C
12	UserX	41.04	28.82	TLC (Figure 3.8)

**Table 3.3:** Coordinates and NEHRP soil classes at the ten early warning stations and two user sites in the Marmara region. *ISTAN* is a site in Istanbul and *UserX* is located at the site of an industrial settlement close to the mega-city. For the simulation of seismic ground motion average amplification values are used to include site effects by near-surface soil deposits as proposed by Boore and Joyner (1997) (see Chapter 2.3.3). At site *UserX* the amplification spectrum observed at station *TLC* in Tulcea, Romania (see Figure 3.8, Sokolov et al. (2005)) is used. *TLC* is installed on metamorphic rock, and is used to demonstrate the possible impact of realistic (non-smoothed) site effects.

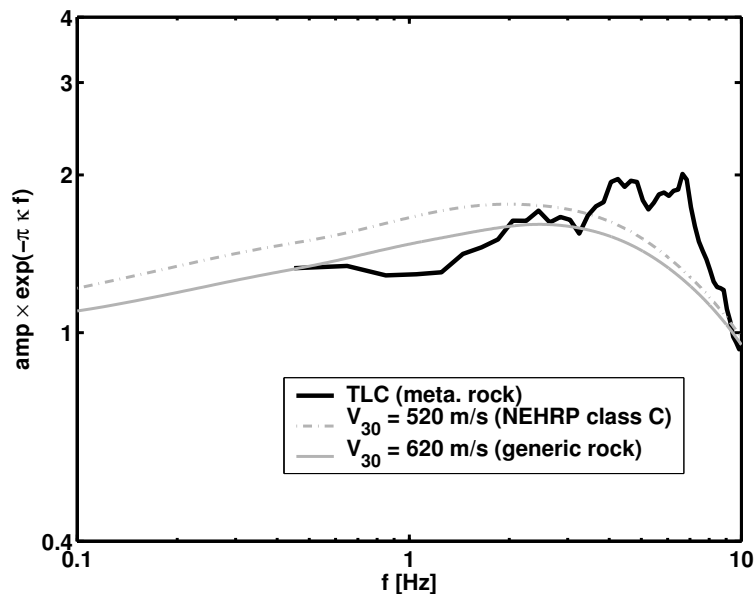


**Figure 3.8:** Comparison of the amplification spectrum at station *TLC* (Tulcea, Romania) deployed on metamorphic rock ( $\kappa = 0.040$  s, Sokolov et al. (2005)) and average amplification functions determined by Boore and Joyner (1997) for NEHRP class C and generic rock.



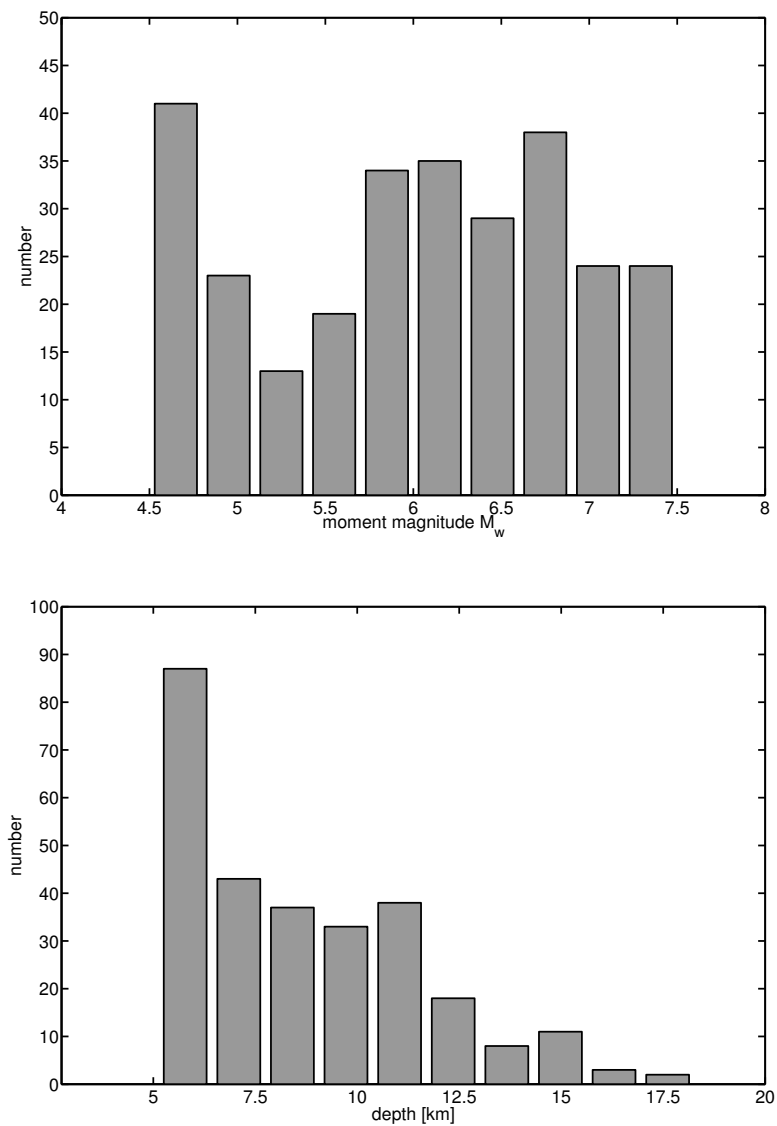


**Figure 3.9:** Histograms of magnitudes and depths for the synthetic database including 280 simulated earthquakes in the Marmara region. Source depths of the modeled earthquakes are in good agreement with observations (see Figure 1.4), while the distribution of earthquake magnitudes is unrealistic as it does not follow the Gutenberg-Richter relation (Gutenberg and Richter, 1956).

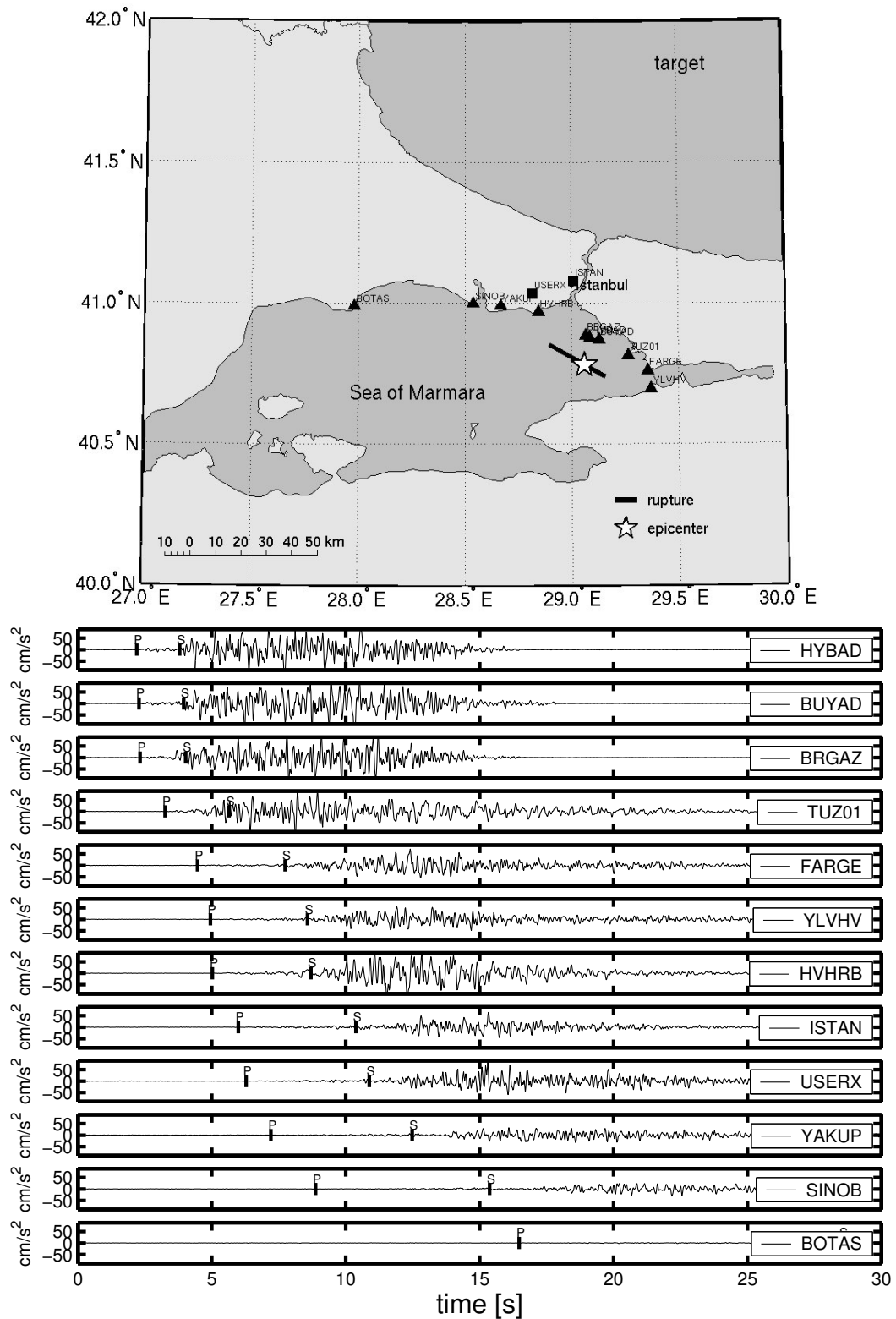


**Figure 3.10:** Seismic scenario: Simulated ground motion for a  $M_w = 6.5$  earthquake on SEGMENT 2 (id.# 25). The rupture length is almost 30 km. Rupture directivity can be well observed at station *HVHRB*.

engineering problems (up to 10 Hz and higher). Its power is that details on earthquake sources and propagation effects on seismic waves are not required. The stochastic simulation procedure is theoretically circumstantiated under the conditions of linear stress-strain relation and time-independence of Green's function (Chapter 2) and is supported by observational data. As a matter of principle the stochastic method, however, can only reflect major characteristics of ground motion, such as mean amplitudes (see Chapter 4), and provides a simplified image of true shaking. Some of the major simplifications of the approach come from the usage of averaged radiation patterns, of constant rupture velocities (here:  $v_r = 0.8 \beta$ ) and the usage of simple models for seismic wave velocities and inelastic attenuation. Crucial are also parameters that describe the form of the shaping window applied to the Gaussian time series to model the random phase (Saragoni and Hart, 1974).

In comparison to the *Stochastic Point Source* approach the *Stochastic Simulation Method for Seismic Ground Motion from Finite Faults* allows for the inclusion of source dimensions: depending on the earthquake magnitude the length of the seismic rupture can be some tens of kilometers which clearly affects the observed ground shaking in the epicentral area. In addition, the method allows for the simulation of effects of *rupture directivity* (see Chapter 2.2.3) as shown Figure 3.10. Source dimensions should be principally considered in seismic hazard analyses. As pointed out in Chapter 3.2.1 subfault size  $\Delta l$ , shear wave velocity  $\beta$  and parameter  $K \approx (3 y \text{ } sfact)$  have to be carefully chosen as they are crucial for the obtained simulation results (3.25). Parameter  $y$  is related to rupture velocity  $v_r$  (3.12), parameter  $sfact$  is related to the maximum slip velocity  $v_{max}$  (3.15). The distribution of seismic wave velocities plays an important role in the level of observed ground motion; however, it has to be extremely simplified in the stochastic modeling procedure. Rectangular rupture planes and the consideration of only one typical asperity size on the fault ( $\Delta l$ ) constitute further limiting assumptions of the modeling procedure.

In this study a modified *FINSIM* code (Beresnev and Atkinson, 1998) is applied to simulate ground motion records at different points of observation in the Marmara region for P- and S-waves. The required input parameters for the simulation procedure are mostly taken from the literature (Table 3.1). In order to obtain a database of synthetic earthquakes that is as realistic as possible variability is assigned to the subfault size  $\Delta l$ , the stress drop  $\Delta\sigma$ , and parameter  $sfact$  within specified limits as indicated in Table 3.1. As a consequence of the random selection of source parameters and the introduction of frequency-dependent site effects, I expect that the synthetic database includes a realistic degree of *inter-* and *intra-event variability*. The quality of the simulated time series will be evaluated on basis of ground motion parameters in the following chapter: I will compare attenuation relationships derived from the synthetic database with observational data from three earthquakes in northwestern Turkey and with attenuation laws determined for other seismic active regions in the world.



## Chapter 4

# Seismic Ground Motion Parameters

To simplify time series and Fourier amplitude spectra of earthquake ground shaking, both quantities are frequently reduced to so-called (*seismic*) *ground motion parameters* that summarize their main characteristics. This chapter will give a short summary of ground motion parameters that are most commonly used in seismic engineering and that will be of interest for the development of PreSEIS in Chapter 6. Comprehensive descriptions of ground motion parameters are given by Kramer (1996) and Stewart et al. (2001).

Based on the stochastically simulated earthquake records presented in Chapter 3.3, I will determine correlations between Fourier amplitudes and nine ground motion parameters, among them peak values, spectral values and seismic intensities. I will determine magnitude- and site-dependent amplification factors and discuss the obtained results with respect to site effects and damage by earthquakes. All these studies will enter into a meaningful parameterization of seismic ground motion required as input information for PreSEIS; the determined amplification factors will be essential for the calculation of shake and alert maps in Chapter 6.

The second part of this chapter is dedicated to *attenuation relationships* of ground motion parameters. Based on the synthetic database I will calculate attenuation laws for nine ground motion parameters, and compare these relations with observational data using records of the 1999 Kocaeli and Düzce earthquakes and of a small event that occurred in the southeastern Sea of Marmara in 2004. In addition, I will compare the obtained results with relations determined for other seismic active regions, and use these findings for a rough frequency-dependent evaluation of the synthetics.

## 4.1 Parameterization of Seismic Ground Motion

### 4.1.1 Amplitude Parameters: PGD, PGV and PGA

The most commonly used ground motion parameters in the time domain are the peak values of acceleration  $a$ , velocity  $v$ , and displacement  $d$  denoted by PGA, PGV and PGD. Peak values give the largest absolute amplitudes of the respective - mostly non-filtered - time series:

$$\text{PGD} \equiv \max\{|u|\} \quad (4.1)$$

$$\text{PGV} \equiv \max\{|v|\} = \max\{|\dot{u}|\} \quad (4.2)$$

$$\text{PGA} \equiv \max\{|a|\} = \max\{|\ddot{u}|\}. \quad (4.3)$$

Peak values can be measured for all three components of shaking, i.e. for the two orthogonal horizontal and the vertical component. Because buildings are generally designed to resist vertically acting forces - such as gravity - the horizontal components usually cause the main damage to structures. Some authors have introduced the terminology PHA, PHV, and PHD in order to emphasize that peak values are taken from the horizontal components. Peak horizontal values can either refer to the maximum peak value of both horizontal components, or to the peak value of the resultant time series after taking the vector sum of both. In this work peak values refer to the mean horizontal component.

Peak ground acceleration (PGA) is related to the peak force induced in very stiff structures and can be correlated to earthquake intensity (e.g., Trifunac and Brady, 1975; Murphy and O'Brien, 1977; Krinitzky and Chang, 1987). The PGA-intensity relationship, however, is rather imprecise and is therefore generally only applied when merely intensity information is available. This, for example, can happen if no strong motion instruments have been installed in the area where a large earthquake occurs. Peak ground velocity (PGV) has been found to correlate well with earthquake damage in structures (Trifunac and Todorovska, 1997; Boatwright and Seekins, 2001). Peak ground displacement (PGD) has not been experienced as useful parameter for engineering purpose yet (Kramer, 1996) but is strongly related to damage within buildings.

Typically, large peak values - in particular of acceleration - indicate destructive ground motions. If peak values, however, last only for a very short period of time or if they occur at very high frequencies, damage to many types of structures may be little. Peak values therefore should be combined with information on duration and frequency content of ground motion (Kramer, 1996; Jennings, 2003).

### 4.1.2 Spectral Parameters

The frequency content of seismic ground motion is usually quantified through spectra, such as the Fourier amplitude spectra (FAS) or response spectra commonly used in earthquake engineering.

#### **Fourier Amplitude Spectra (FAS): $\omega_c$ , $f_{max}$ , $T_p$ , and $v_{max}/a_{max}$**

For the assessment of strong motion characteristics the frequency content of ground motion is usually described by single period parameters instead of complete spectra. A characteristic parameter that can be derived from the FAS is, e.g., the *corner frequency*  $\omega_c$  which is related to the cube square of the seismic moment  $M_0$  (2.19) and therewith to the cube square of the seismic stress drop  $\Delta\sigma$  (2.18). Another spectral parameter is the *cut-off frequency*  $f_{max}$  (2.34) which can be either linked to local site effects or to the earthquake source.

The *predominant period*  $T_p$  is defined as shaking period corresponding to the maximum value of the smoothed FAS<sup>1</sup> (Stewart et al., 2001). Different procedures for the determination of  $T_p$  in the frequency or in the time domain - using the zero-crossing approach for example (Correig, 1996) - have been proposed. Closely related to the predominant period is the  $v_{max}/a_{max}$  ratio which indicates the most significant period of ground motion (e.g., McGuire, 1978; Kramer, 1996). The high correlation between the predominant period of the first vibrations of seismic ground motion (as well as the  $v_{max}/a_{max}$  ratio) and earthquake magnitude turns  $T_p$  into a promising predictive parameter for earthquake early warning (Chapter 5.3).

---

<sup>1</sup>Note that in earthquake engineering the predominant period mostly refers to the maximum value of the response spectrum and not of the FAS.

**Response Spectra:  $S_d$ ,  $S_v$ ,  $S_a$ , PSA, and PSV**

Response spectra describe the peak motion response of a single-degree of freedom elastic structure with a specified level of viscous damping towards a base acceleration  $a(t)$ , that in case of earthquakes corresponds to seismic ground motion at the point of observation. The equation of motion of a simple harmonic oscillator is given by a second order, linear, inhomogeneous differential equation:

$$\ddot{x} + 2\beta\omega\dot{x} + \omega^2x = -a(t), \quad (4.4)$$

whereby  $\beta$  is the fraction of critical damping and  $\omega$  is the natural frequency of the elastic structure. A numerical solution for (4.4) by the approximation of  $a(t)$  by segmentally linear functions has been proposed by Nigam and Jennings (1969) and will be used in this work:

$$-a(t) \approx -a_i - \frac{\Delta a_i}{\Delta t_i}(t - t_i), \quad t_i \leq t \leq t_{i+1}, \quad (4.5)$$

with

$$\begin{aligned} \Delta t_i &= t_{i+1} - t_i, \\ \Delta a_i &= a_{i+1} - a_i. \end{aligned}$$

Displacement  $x$  and velocity  $\dot{x}$  at time  $t = t_{i+1}$  are given by

$$\bar{x}_{i+1} = A(\beta, \omega, \Delta t_i)\bar{x}_i + B(\beta, \omega, \Delta t_i)\bar{a}_i, \quad (4.6)$$

whereby

$$\begin{aligned} \bar{x}_i &= \begin{pmatrix} x_i \\ \dot{x}_i \end{pmatrix} & \bar{a}_i &= \begin{pmatrix} a_i \\ a_{i+1} \end{pmatrix} \\ A &= \begin{pmatrix} a_{11} & a_{12} \\ a_{21} & a_{22} \end{pmatrix} & B &= \begin{pmatrix} b_{11} & b_{12} \\ b_{21} & b_{22} \end{pmatrix}. \end{aligned} \quad (4.7)$$

The elements of matrices  $A$  and  $B$  in (4.7) are specified in Nigam and Jennings (1969). Once  $x$  and  $\dot{x}$  are known at time  $t_i$ , the state of the oscillator can be exactly calculated at all subsequent times. Usually, it is assumed that  $x = \dot{x} = 0$  for  $t = t_1$ . The desired response spectra are obtained from the maximum values of displacement  $x$ , velocity  $\dot{x}$  and acceleration  $\ddot{x}$  for a given excitation at each frequency  $\omega$ :

$$S_d(\omega, \beta) \equiv \max \{|x(\omega, \beta)|\} \quad (4.8)$$

$$S_v(\omega, \beta) \equiv \max \{|\dot{x}(\omega, \beta)|\} \quad (4.9)$$

$$S_a(\omega, \beta) \equiv \max \{|\ddot{x}(\omega, \beta)|\}, \quad (4.10)$$

where  $S_d$ ,  $S_v$  and  $S_a$  are the spectral values of displacement, velocity, and acceleration, respectively, given damping  $\beta$  and natural frequency  $\omega$ . Typical values for the quantified description of structural response to ground shaking caused by an earthquake are  $\beta = 5\%$  and  $T_1 = 0.3$  s,  $T_2 = 1.0$  s and  $T_3 = 2.0$  s; these periods are characteristic for buildings of 3 and 10 stories, and long-period structures such as bridges, respectively (Figure 4.1).<sup>2</sup> I will use these values for subsequent response analyses.

<sup>2</sup>As a rule of thumb, the eigenperiod of a building or structure - which is the reciprocal value of the eigenfrequency - can be estimated as 0.1 s times the number of stories (e.g., Hough, 2004).

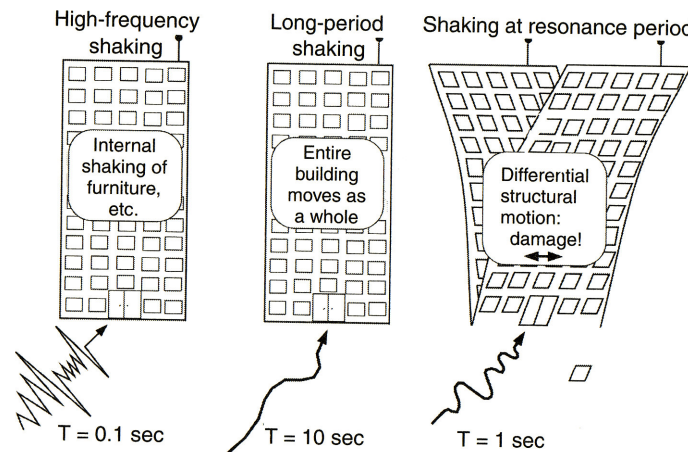


**Figure 4.1:** Response of a building with eigenperiod  $T = 1.0$  s towards ground shaking of different frequency content (Hough, 2004).

Spectral velocity  $S_v$  and spectral acceleration  $S_a$  are generally not calculated directly but are derived from spectral displacement  $S_d$  through

$$\text{PSV} \equiv \omega S_d \approx S_v, \quad (4.11)$$

$$\text{PSA} \equiv \omega^2 S_d \approx S_a, \quad (4.12)$$

whereby the *pseudo spectral velocity* PSV and the *pseudo spectral acceleration* PSA are approximations of the true spectral values (Kramer, 1996; Jennings, 2003). Figure 4.2 shows the calculated PSA derived from the simulated acceleration time series displayed in Figure 3.3 at 5% damping. Response spectra provide neither information on the duration of shaking nor on the inelastic response of structures.

### 4.1.3 Duration Parameters: Bracketed Duration

The duration of seismic ground shaking has generally strong impact on damage to structures caused by earthquakes as the stiffness and therewith resistency of structures towards ground shaking can significantly decrease with duration of seismic demand. Many physical processes, such as the increase of pore water pressures in loose, saturated sands, depends on the number of load or stress cycles that occur during earthquakes. This phenomenon is known as *soil liquefaction* (e.g., Seed and Idriss, 1982; Osinov, 2003). Effects on shaking duration have been discussed in Chapter 2.2.3.

One of the most common measures of duration is the *bracketed duration* (Bolt, 1969), which is the time interval between the first and last exceedance of specified thresholds of ground shaking. Duration measures can be combined with other ground motion parameters such as the cumulative absolute velocity (CAV) as will be shown in the following subsection.



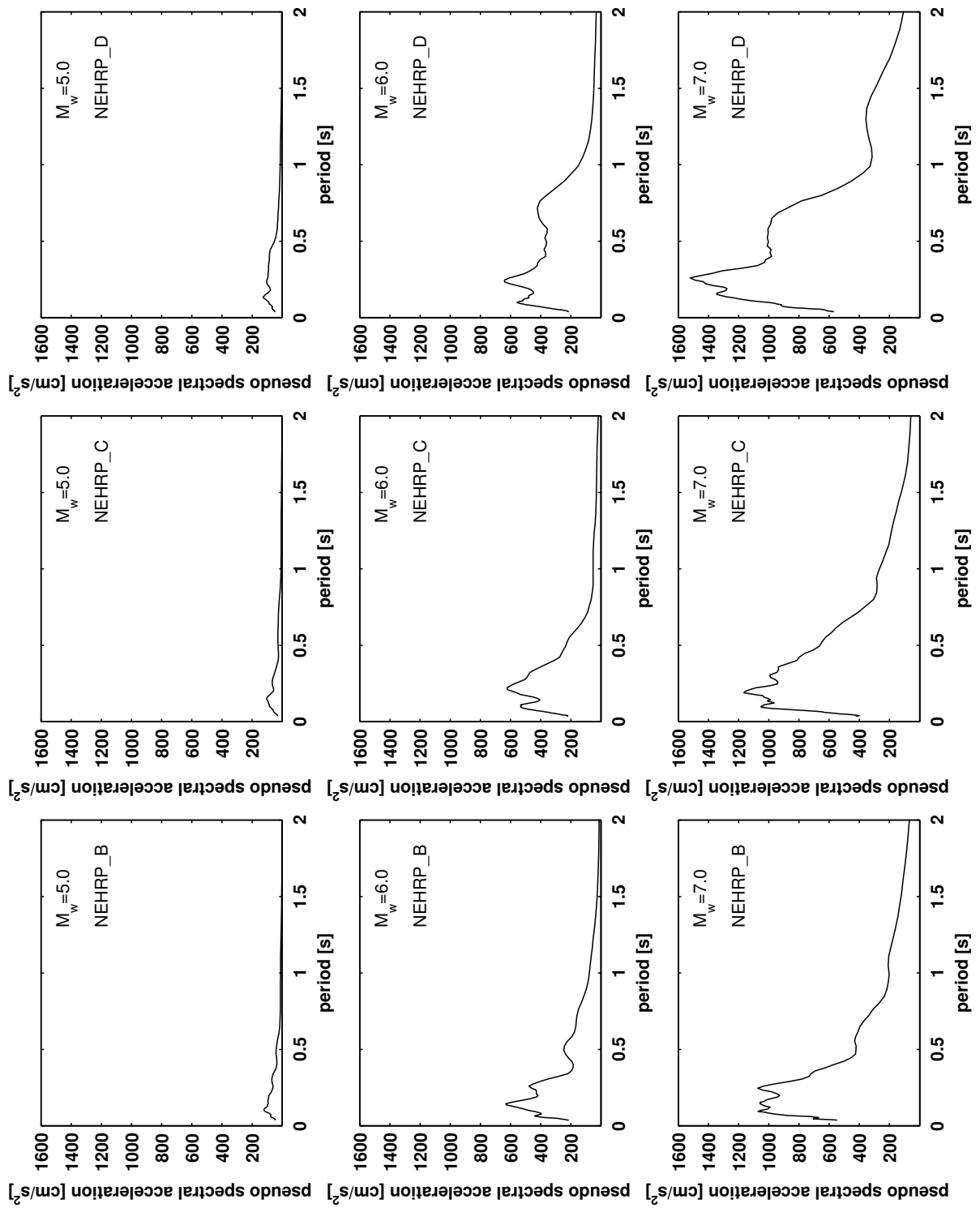


**Figure 4.2:** (Pseudo) spectral acceleration at 5% damping for the simulated acceleration time series displayed in Figure 3.3.

#### 4.1.4 Integrative Parameters: Seismic Intensity, $I_a$ and CAV

##### Seismic Intensity

*Seismic intensity* is a measure of shaking and damage from earthquakes. Most frequently used are the *Modified Mercalli Intensity (MMI)* scale in the USA, Canada, Mexico, and others, the *Medvedev-Sponhauer-Karnik (MSK)* scale in eastern and southeastern Europe, and the *European Macroseismic Scale (EMS)*. As differences are usually less than 0.5 units, the scales are often assumed to be identical (e.g., Murphy and O'Brien, 1977; Chernov and Sokolov, 1988).

*Computed intensity* (or *macroseismic/instrumental intensity*) is derived from instrumental records instead of human descriptions. It can therefore replace common intensity quantifications if descriptions of damage are lacking, e.g., in sparsely populated areas or shortly after earthquake catastrophes. Macroseismic intensity is also useful for the estimation of intensity from simulated earthquake records. Intensity can be empirically estimated from the Fourier amplitude spectra (FAS) of ground acceleration as proposed by Chernov and Sokolov (1988), Sokolov and Chernov (1998), Chernov and Sokolov (1999), and Sokolov (2002). In the following I will summarize the main concept of this approach; the method will be applied for intensity estimates in this work.

From a database of about 1,150 worldwide recorded ground motion time series Sokolov (2002) has determined empirically mean values  $a_{i,j}$  and unit standard deviations  $\sigma_{i,j}$  of the logarithmized acceleration spectral density function  $\log|A_0|$  for intensity levels  $III \leq i \leq IX$  at so-called *representative frequencies*  $f_j$  in the range of 0.4-13.0 Hz (Figure 4.3). Values for lower and higher intensities up to *XII* have been estimated from extrapolation (Sokolov, 2002). The probability that the logarithmized value of the observed spectral amplitude  $x_j$  at frequency  $f_j$  of a given earthquake does not exceed  $a_{i,j}$  is given by

$$P[x_j \leq a_{i,j}] = 1 - \frac{1}{\sqrt{2\pi\sigma_{i,j}^2}} \int_{x_{min}}^{x_j} \exp\left(-\frac{(a_{i,j} - x)^2}{2\sigma_{i,j}^2}\right) dx. \quad (4.13)$$

$x_{min}$  is set to  $x_{min} = a_{i,j} - 5\sigma_{i,j}$ . The (weighted) probability that all observed logarithmic spectral amplitudes  $x$  covering all representative frequencies do not exceed  $a_i$  is given by

$$P[x \leq a_i] = \frac{\sum_{j=1}^{n_f} P[x_j \leq a_{i,j}] \sigma_{i,j}^2}{\sum_{j=1}^{n_f} \sigma_{i,j}^2}, \quad (4.14)$$

where  $n_f$  is the number of considered frequencies. The probability that the intensity level  $I$  of an observed earthquake does not exceed the given value  $i$  can be estimated from

$$P[I \leq i] = \prod_{i=III}^{XII} P[x \leq a_i]. \quad (4.15)$$

Sokolov (2002) propose to determine the intensity level  $I$  of a given earthquake either from the maximum of the first derivative of the probability function  $P$  (4.15) or from the intensity value at  $P = 0.5$ . Unless otherwise noted I will take the mean value of both when specifying intensities in this thesis.

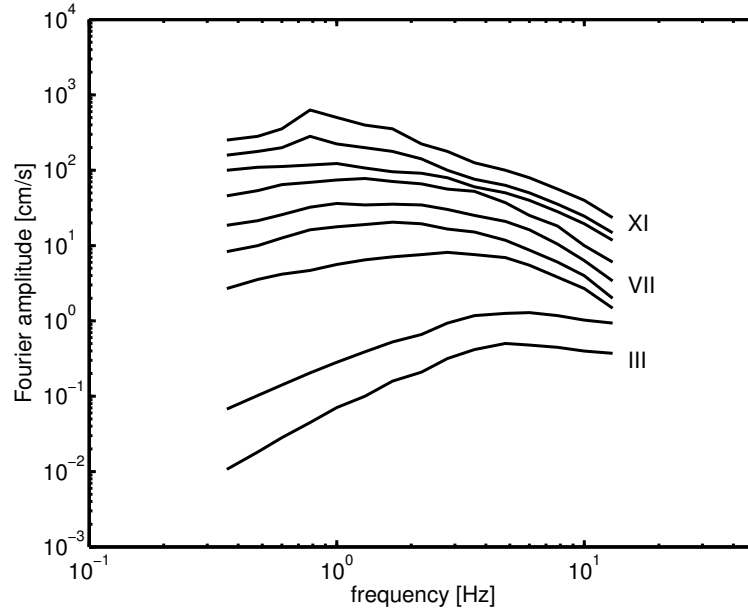


**Figure 4.3:** Mean acceleration spectra of earthquakes with intensities III-XI after Sokolov (2002).

### Arias Intensity $I_a$

The *Arias intensity*  $I_a$  is defined by the integrated squared acceleration  $a(t)$  of seismic ground motion over a time interval  $[0...t_{max}]$  whereby  $t_{max}$  usually corresponds to the duration of the earthquake record (Arias, 1970):

$$I_a \equiv \frac{\pi}{2g} \int_0^{t_{max}} a(t)^2 dt, \quad (4.16)$$

where  $g$  is the acceleration of gravity ( $g = 9.81 \text{ m/s}^2$ ). The Arias intensity quantifies the energy in the accelerogram in units of  $[\text{m/s}]$  (Kramer, 1996). It has its own scale and cannot be directly converted into other intensity scales.

### Cumulative Absolute Velocity (CAV)

The cumulative absolute velocity (CAV) is defined by the integrated absolute velocity over a time interval  $[0...t_{max}]$  whereby  $t_{max}$  usually corresponds to the duration of the earthquake record:

$$\text{CAV}_{t_{max}} \equiv \int_0^{t_{max}} |a(t)| dt. \quad (4.17)$$

The CAV can be taken as the sum of absolute peak-to-valley velocity changes. Figure 4.4 illustrates the increase of CAV with time applied to a stochastically simulated  $M_w = 7.0$  earthquake record. Figure 4.5 shows the course of CAV for the acceleration time series plotted in Figure 3.3: magnitudes as well as local underground appear to have significant impact on the observed CAV level.

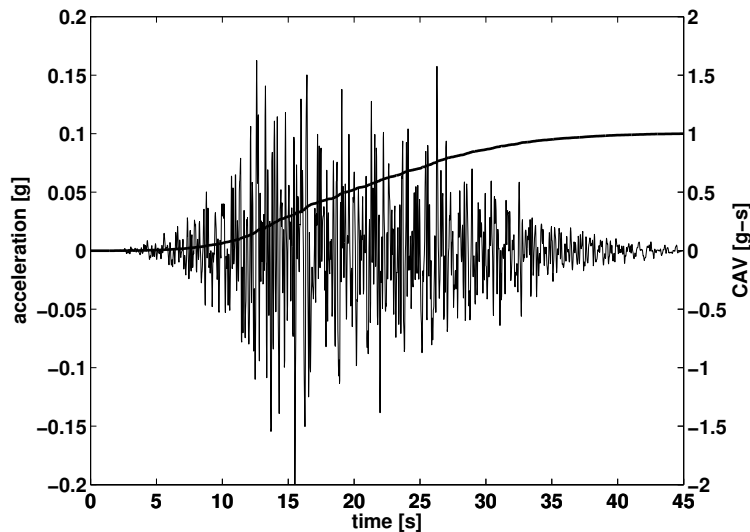


**Figure 4.4:** Bandpass-filtered simulated accelerogram (0.5-10.0 Hz) and cumulative absolute velocity (CAV) of a  $M_w = 7.0$  earthquake at a source-to-site distance of 35 km on stiff soil. The corresponding seismic intensity estimated from the Fourier amplitude spectrum is 7.4.

Based on the study of about 250 observed earthquakes of intensities between I and X Benjamin and Associates (1988) found that spectral accelerations and the cumulative absolute velocity are the two (out of ten) most reliable ground motion parameters to predict damage. Peak ground acceleration (PGA), on the other hand, has come off the worst. In their report on a *Criterion for determining the exceedance of the Operating Basis Earthquake (OBE)*<sup>3</sup> on behalf of the Electric Power Research Institute (EPRI) in Palo Alto, California, Benjamin and Associates (1988) propose the following two-level criterion to avoid unnecessary shutdowns of nuclear power plants in response to earthquakes:

*"The 5% damped spectral accelerations for the earthquake ground motion at the site, at frequencies between 2.0 and 10.0 Hz, must exceed the corresponding OBE design response spectrum or 0.2 g, whichever is greater, and, secondly, the computed CAV value from the earthquake record must exceed 0.3 g s."*

(Benjamin and Associates, 1988)

Figure 4.6 (left) shows the observed correlation between CAV and seismic intensity for 177 earthquakes used by Benjamin and Associates (1988): the introduction of the proposed threshold at 0.3 g s allows for the identification of all damaging events with intensities larger than VI. Figure 4.7 shows that the threshold is also applicable to the simulated earthquake records presented in Chapter 3.3.

The CAV defined after (4.17) clearly depends on duration  $t_{max}$ . To confine the CAV calculation to parts of ground motion that are damaging, the Yankee Atomic Electric Company (1991) suggests a standardization of the parameter. The authors define the *bracketed cumulative absolute velocity* which considers only acceleration values in one-second intervals where at least one value exceeds 0.025 g (see Chapter 4.1.3). Using this definition the Yankee Atomic Electric Company (1991) proposes a new CAV threshold of 0.166 g s to identify damaging earthquakes (Figure 4.6, right).

<sup>3</sup>The Operating Basis Earthquake (OBE) is defined as an earthquake which - considering specific characteristics of the local geology - could reasonably be expected to affect the plant site during the operating life of the system.

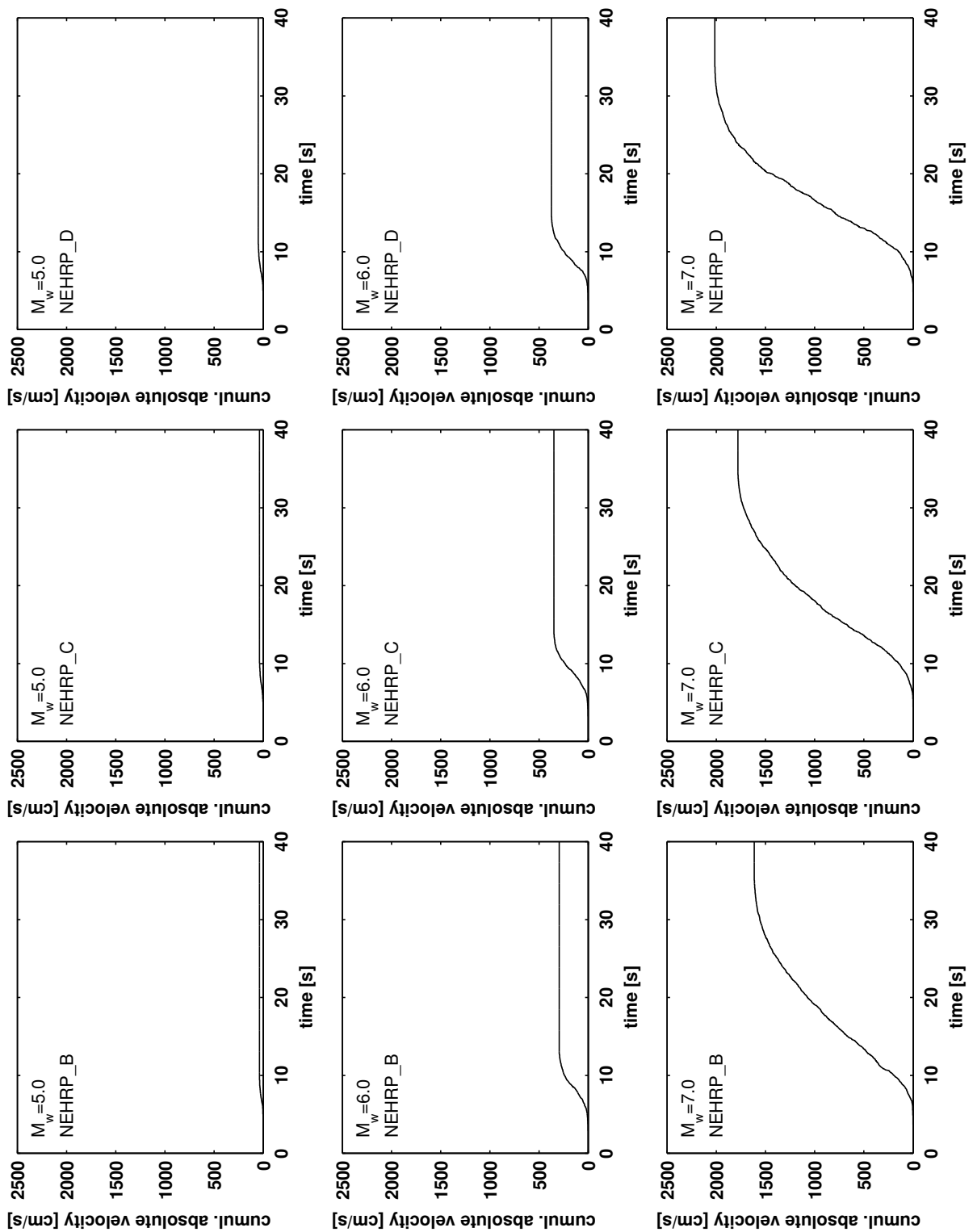


**Figure 4.5:** Cumulative absolute velocity (CAV) for the simulated acceleration time series displayed in Figure 3.3.

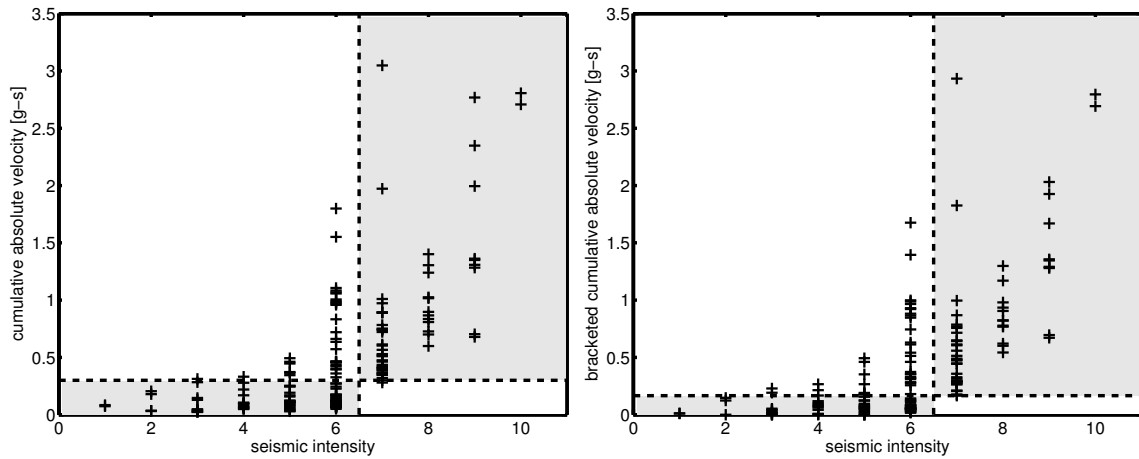


**Figure 4.6:** Correlations between CAV (left) and bracketed CAV (right) and seismic intensity for 177 observed weak and strong earthquakes. Benjamin and Associates (1988) propose thresholds of 0.3 g s and 0.166 g s, respectively, to identify damaging earthquakes with intensities larger than VI. Displayed data is taken from Benjamin and Associates (1988).

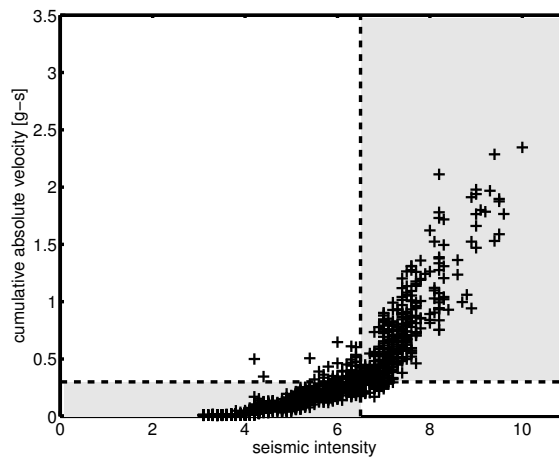


**Figure 4.7:** Correlation between CAV and seismic intensity for synthetic earthquake records. Seismic intensity has been determined from the Fourier amplitude spectrum of acceleration (Sokolov, 2002). The threshold of 0.3 g s as proposed by Benjamin and Associates (1988) to identify damaging earthquakes with intensities larger than VI appears to be also applicable to the simulated data.

## 4.2 Correlating Ground Motion Parameters with Fourier Amplitudes

Figure 4.8 shows the correlations between nine ground motion parameters and Fourier amplitudes of acceleration<sup>4</sup> based on 3,600 stochastically simulated earthquake records ( $4.5 \leq M_w \leq 7.5$ , Chapter 3.3). From top to bottom the figure shows results for three amplitude parameters (PGA, PGV and PGD), three spectral parameters (PSA at 0.3 s, 1.0 s and 2.0 s) and three integrative parameters (seismic intensity derived from FAS, Arias intensity  $I_a$  and CAV). A linear (left column) and a non-linear 3<sup>rd</sup> order (right column) model are tested. Correlations at each frequency  $f$  are quantified through *correlation coefficient*  $R$  defined by

$$R_i(f) \equiv \left( \frac{(y(f) - \overline{y(f)})(\hat{y}_i(f) - \overline{\hat{y}_i(f)})}{\sigma_{y(f)} \sigma_{\hat{y}_i(f)}} \right), \quad i = 1, 2, \quad (4.18)$$

with the two predictive models

$$\begin{aligned} \hat{y}_1(f) &= a_1(f) + b_1(f) (IM), \\ \hat{y}_2(f) &= a_2(f) + b_2(f) (IM) + c_2(f) (IM)^2 + d_2(f) (IM)^3. \end{aligned}$$

The frequency-dependent model parameters  $a_i(f)$ ,  $b_i(f)$ ,  $c_i(f)$ , and  $d_i(f)$  are determined through linear/non-linear least-squares regression from the synthetic database.  $y(f)$  is the Fourier amplitude at frequency  $f$ ,  $IM$  the value of the analyzed ground motion parameter,  $y_i(f)$  and  $\hat{y}_i(f)$  are the mean values of Fourier amplitudes and outputs of model  $i$  at frequency  $f$ , respectively;  $\sigma_{y(f)}$  and  $\sigma_{\hat{y}_i(f)}$  are the unit standard deviations of  $y(f)$  and  $\hat{y}_i(f)$ . The correlation coefficient can take values between -1 and 1.

Figure 4.8 (top) demonstrates that PGA is a high-frequency parameter that is mainly controlled by frequencies above 3.0 Hz; PGD primarily depends on motions with frequencies below 0.5 Hz; the frequency range from 0.5 to 3.0 Hz has strongest impact on parameter PGV. At low frequencies spectral accelerations at 5% damping (Figure 4.8, center) correlate well with the corresponding Fourier amplitudes. At frequencies above 1.5 Hz the correlation pertains to broader frequency bands which comes from the plateau in the FAS of acceleration above corner frequency  $\omega_c$ , i.e. the correlation level is almost constant at frequencies above  $\omega_c$ . This behaviour certainly applies to all studied ground motion parameters. For integrative parameters (Figure 4.8, bottom)<sup>5</sup> it is as expected impossible to identify single frequencies with preferential correlation. Arias and seismic intensities show a non-linear, all other studied ground motion parameters a linear dependency on Fourier amplitudes.

Note that these results are purely empirical; for a more sophisticated analyses of relations between FAS and response spectra, e.g., see Jennings (2003) and references given therein.

## 4.3 Attenuation Relationships for Seismic Ground Motion Parameters

*Attenuation or predictive relationships* describe the mean (or median) and unit standard deviations of probabilistic distributions of ground motion parameters as intensity measures  $IM$  of shaking conditioned on the occurrence of an earthquake of magnitude  $M$  in a source-to-site distance  $r$ ; they

<sup>4</sup>smoothed over 0.5 Hz intervals (moving average)

<sup>5</sup>Since the intensity method developed by Sokolov (2002) is not calibrated for small earthquakes, events with intensities of less than III have been removed from the database prior to the correlation analyses.

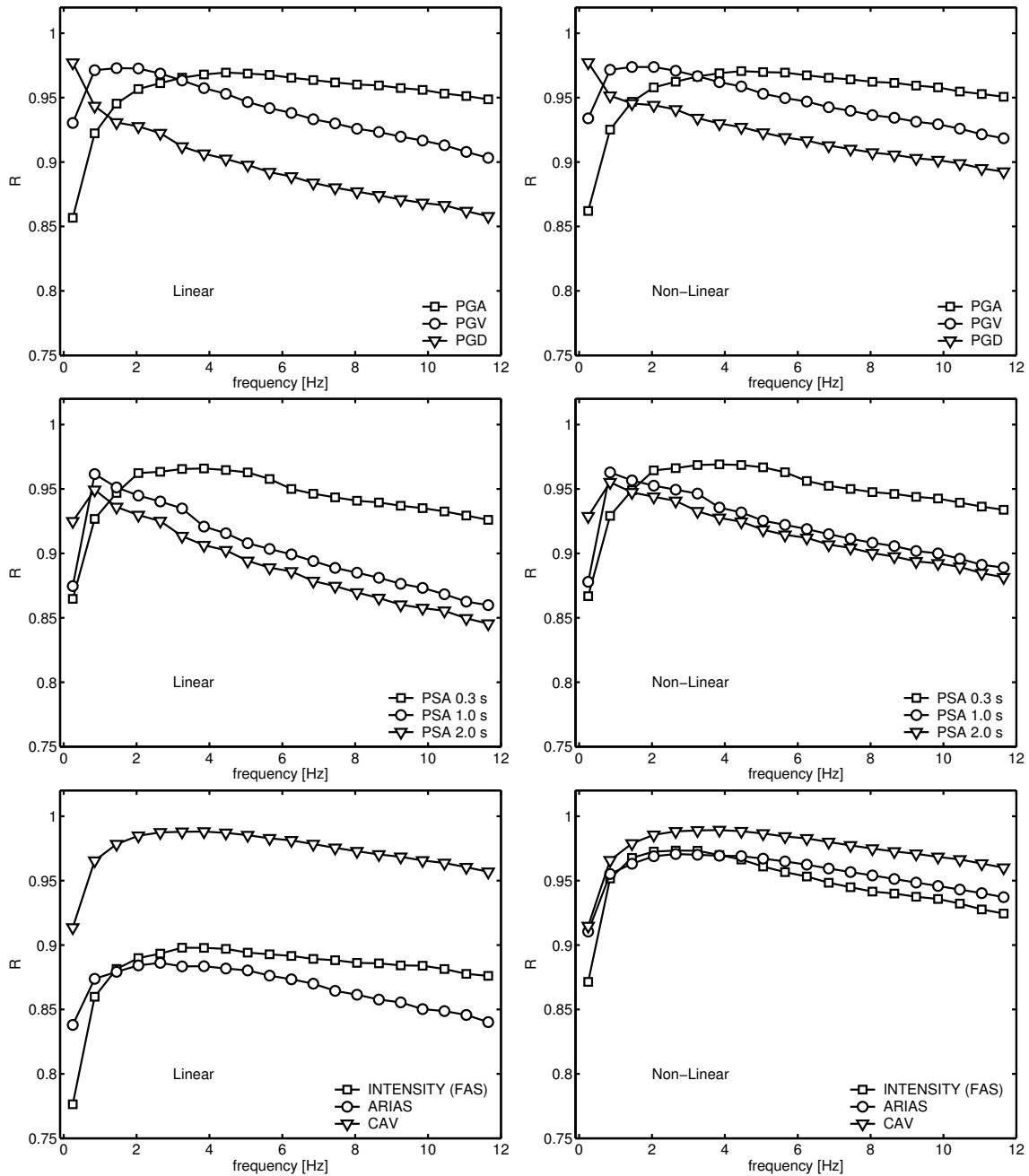


**Figure 4.8:** Correlations between nine ground motion parameters and the smoothed Fourier amplitude spectrum of ground motion determined from 3,600 stochastically simulated earthquake records ( $4.5 \leq M_w \leq 7.5$ ) using a linear (left) and non-linear  $3^{rd}$  order (right) model. All correlations are characterized by correlation coefficient  $R$ . Top: peak values PGA, PGV and PGD depend on distinct frequency bands. Center: at low damping response and Fourier amplitude spectra show a high proportionality for long period shaking. Bottom: for integrative ground motion parameters such as seismic intensity, Arias intensity and CAV single frequencies with preferential correlation cannot be identified. Arias and seismic intensities show a non-linear, all other studied ground motion parameters a linear dependency on Fourier amplitudes.



hence define the statistical moments of the probability density function  $f(IM|M, r, P_1, P_2, \dots, P_n)$  with model parameters  $P_1, P_2, \dots, P_n$  that allow - aside from  $M$  and  $r$  - for additional characterizations of the earthquake source, propagation path and site effects. Attenuation relationships are determined from regression analyses of observational data, sometimes supplemented by synthetic earthquake records.

Non-uniform distributions of observational data with respect to  $M$  and  $r$  often lead to significant *epistemic uncertainties*, i.e. uncertainties about the correct form of attenuation functions. Attenuation relations are mostly based on a few well-recorded events. This allows for a good quantification of *intra-event aleatory variability* of ground motion, i.e. variability from station to station within one single event, while it prevents the evaluation of *inter-event aleatory variability*, i.e. variability across a set of different events. One of the striking challenges in the formulation of attenuation laws is the development of regression procedures that allow for a proper weighting of data points with the objective to find a reasonable quantification of *overall aleatory variability*, i.e. the sum of inter- and intra-event variability (e.g., Joyner and Boore, 1993, 1994; Campbell, 1981; Brillinger and Preisler, 1984, 1985). Simulated earthquake records, usually, do not come along with this problem.

#### 4.4 Attenuation Relationships for the Simulated Seismic Ground Motion in the Marmara Region

Attenuation relationships for the synthetic database described in Chapter 3.3 are established on basis of a functional form similar to a equation proposed by Kramer (1996):

$$\boxed{\ln(IM) = \underbrace{C_1}_{1.} + \underbrace{C_2 M_w}_{2.} + \underbrace{C_3 \ln(r_{jb} + C_4 M_w)}_{3.} + \underbrace{C_5 r_{jb}}_{4.} + \underbrace{C_6 (soil, M_w)}_{5.} \pm \underbrace{\sigma_{\ln(IM)}}_{6.}} \quad (4.19)$$

Source-to-site distances are quantified by the so-called *Joyner-Boore distance*  $r_{jb}$  defined by the closest horizontal distance to the vertical projection of the rupture onto the surface. The free parameters  $C_1$  to  $C_6$  are determined through regression. Following Kramer (1996) the single terms in (4.19) can be explained as follows:

1. Ground motion parameters are usually log-normally distributed. Thus regression should be performed on the natural logarithm of the data, which is normally distributed.
2. Magnitude scales are usually derived from peak values of ground motion. Therewith follows that  $\ln(IM)$  and  $M$  are proportional to each other.
3. Geometrical spreading reduces amplitudes of seismic body waves traveling away from the seismic source by  $1/r$  (2.23). Strictly speaking this is only true in a homogeneous space. The correction term accounts for the expansion of the rupture area with increasing magnitude, i.e. for the *effective distance* which is usually larger than  $r$ : seismic waves causing ground motion at a certain site partly arrive from distance  $r$ , partly from larger distances.
4. Inelastic attenuation leads to an exponential decay of wave amplitudes with increasing source-to-distance  $r$  (2.29).
5. Ground motion parameters are affected by source and site characteristics.

6. The standard deviation  $\sigma_{\ln(IM)}$  of the attenuation relations is assumed to be magnitude- and site-dependent.

Regression analyses on basis of the synthetic data are separately performed for peak ground acceleration (PGA), peak ground velocity (PGV), peak ground displacement (PGD)<sup>6</sup>, spectral acceleration (PSA) at 0.3 s, 1.0 s and 2.0 s, macroseismic intensity derived from the Fourier amplitude spectrum (FAS) of ground motion, Arias intensity, and the cumulative absolute velocity (CAV). Definitions of these parameters have been given in Chapter 4.1.

In order to avoid epistemic uncertainties in the predictive relations due to missing magnitude and distance ranges, an additional dataset of 900 synthetic earthquakes at dense source-to-site intervals from 1 to 100 km with  $M_w = 5.0$ ,  $M_w = 6.0$  and  $M_w = 7.0$  for NEHRP classes B, C, and D (Chapter 2.3.3) is simulated. Simulation parameters are the same as taken for the first database adapted to the Marmara region (Table 3.1). Due to variability of model parameters with respect to the seismic source and site effects, a reasonable degree of overall aleatory variability is considered. A non-linear inversion<sup>7</sup> for coefficients  $C_1, \dots, C_5$  is performed for each of the nine ground motion parameters  $IM$  using all 2,700 records; the magnitude- and site-dependent coefficient  $C_6$  as well as the unit standard deviation  $\sigma_{\ln(IM)}$  are determined from the obtained residuals.

The resulting coefficients for all nine ground motion parameters are compiled in Appendix C. Data and attenuation laws are visualized in Figure 4.9. Note that there is a clear saturation of all ground motion parameters at short distances. Amplification factors relative to NEHRP class B are illustrated in Figure 4.10: there is a clear dependency of amplification on the respective ground motion parameter. In Chapter 2.3 it was demonstrated that with decreasing shear wave velocity in the near-surface layer the peak of strongest amplification moves towards lower frequencies. Using the amplification spectra for NEHRP class D (stiff soil) as proposed by Boore and Joyner (1997), e.g., highest amplification is observed at around 0.5 - 2.0 Hz (Figure 2.2). From Figure 4.8 follows that motions in this frequency band have strongest impact on parameters PGV, PGD, alike on PSA at 1.0 s and 2.0 s. Figure 4.10 shows that these parameters are actually strongly amplified for NEHRP class D. The resultant Fourier amplitude spectrum as product of source and amplification spectra (corrected for propagation effects) clearly depends on corner frequency  $\omega_c$  (of the source spectrum). The underlying assumption of linearity in the simulation of seismic ground motions therewith leads to a stronger amplification of large earthquakes (with low  $\omega_c$ ) relative to small events with higher corner frequencies. This magnitude-dependency of amplification of different ground motion parameters can be well observed in Figure 4.10.

#### 4.4.1 Comparisons with Observational Data and other Attenuation Relationships

Figure 4.11 shows PGA values observed during the strong Kocaeli and Düzce earthquakes in 1999 (Durukal, 2002) and during a small earthquake close to Yalova in 2004. Details on the three earthquakes are given in Table 4.1. The data is overlaid by attenuation laws derived from the synthetic ground motion time series described in Chapter 4.4: mean values are plotted by solid, 95% confidence intervals by dashed lines. Owing to the lack of magnitude conversion schemes for northwestern Turkey I assume for the small earthquake that  $M_w \approx M_l$ .

---

<sup>6</sup>Velocity and displacement data are obtained from the acceleration time series by time-integration and high-pass filtering above 0.2 Hz.

<sup>7</sup>The non-linear least-squares regression is performed by using the Gauss-Newton method in MATLAB Statistics Toolbox, MathWorks Inc., function *nlinfit*.

#### 4.4 Attenuation Relationships for the Simulated Seismic Ground Motion in the Marmara Region

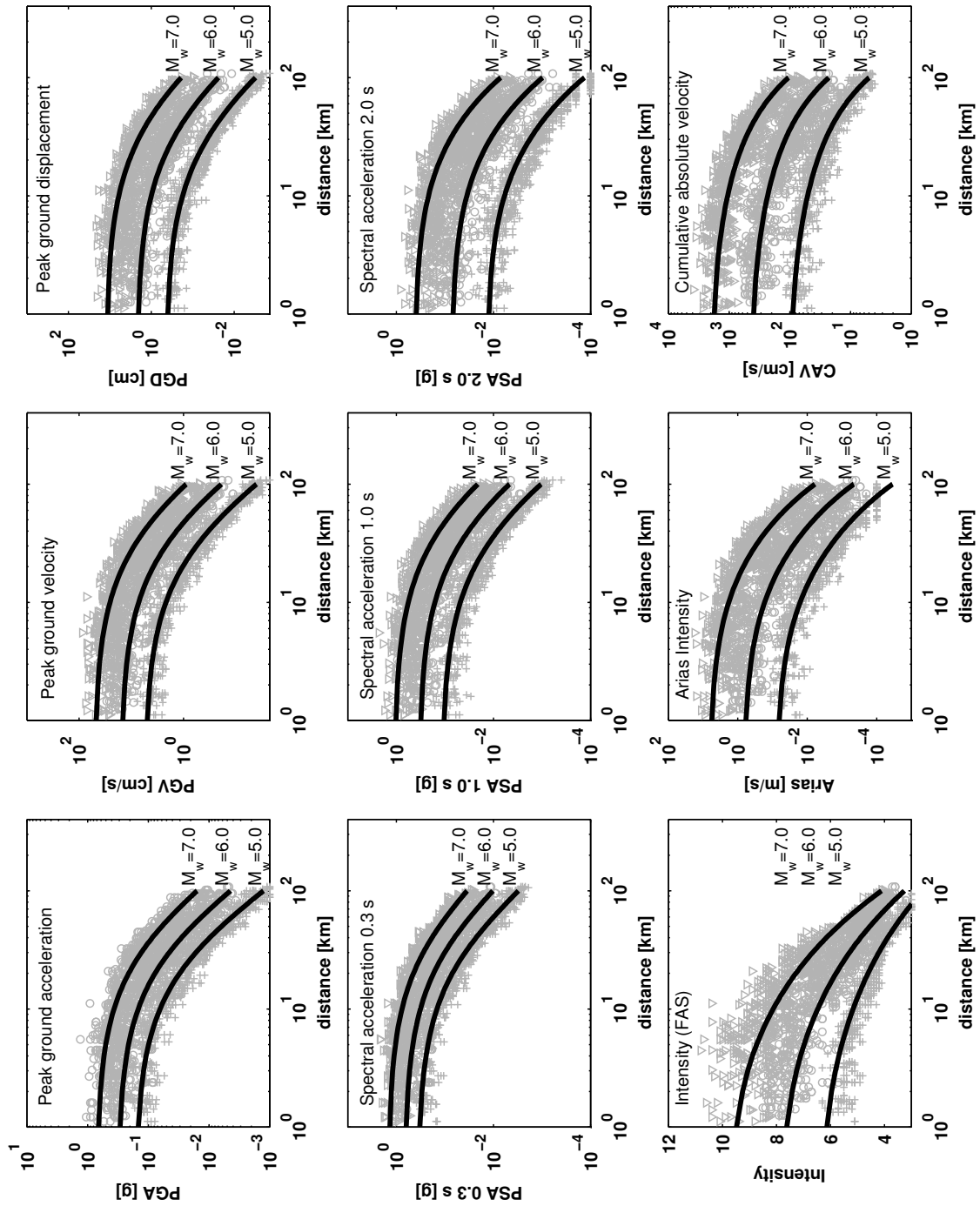


**Figure 4.9:** Attenuation laws for nine ground motion parameters derived from stochastically simulated earthquake records. Coefficients of the relations are compiled in Appendix C.

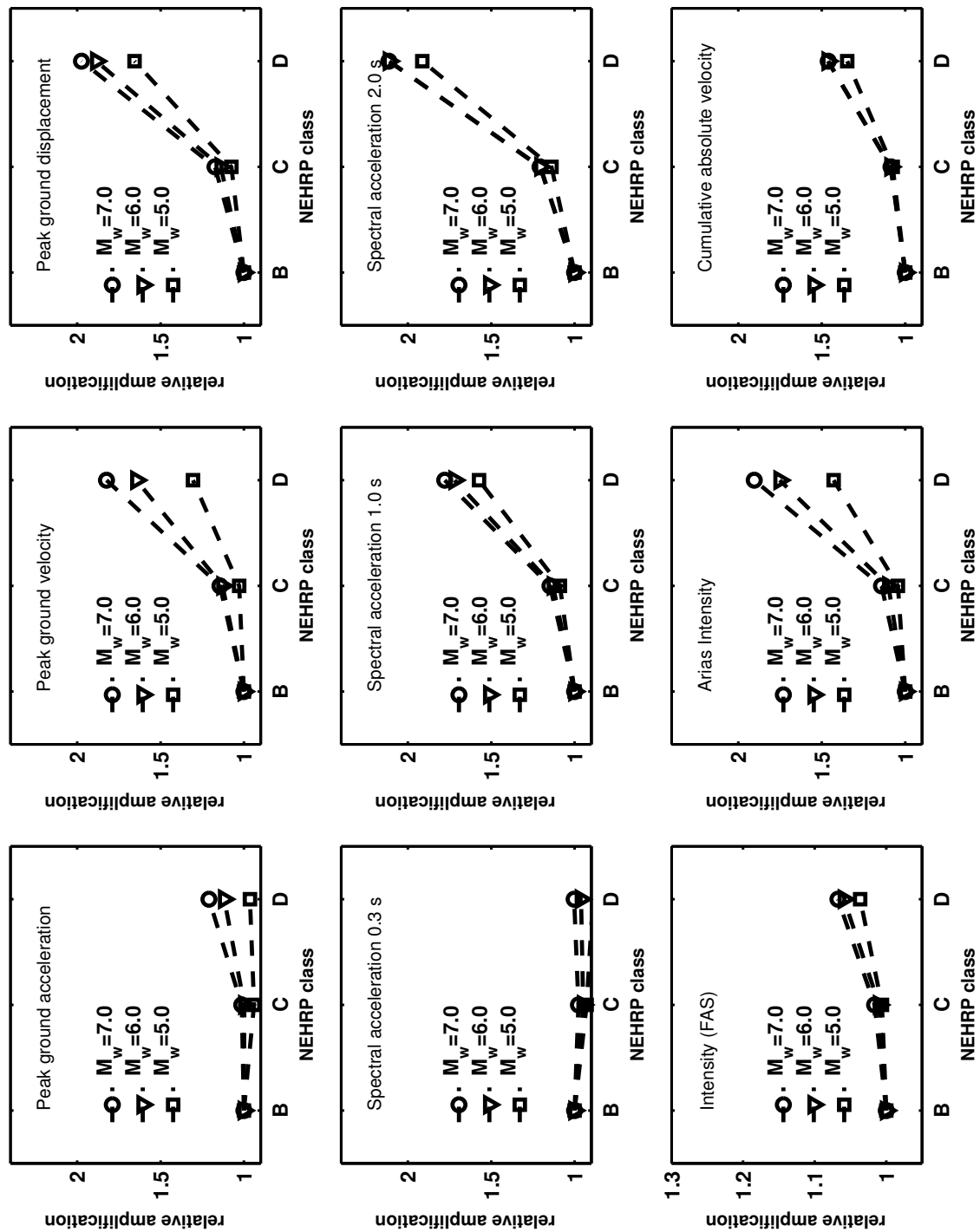


**Figure 4.10:** Magnitude- and site-dependent amplification factors relative to NEHRP class B for nine ground motion parameters. The factors are derived from the stochastically simulated ground motion records.

**Analyzed earthquakes in northwestern Turkey**

name	date	lat [°]	lon [°]	depth [km]	magnitude	reference
Kocaeli	1999/08/17	40.70 N	29.99 E	17	$M_w = 7.4$	USGS
Düzce	1999/11/12	40.93 N	31.25 E	18	$M_w = 7.2$	Harvard
Yalova	2004/05/16	40.70 N	29.32 E	11	$M_l = 4.3$	Kandilli

**Table 4.1:** Locations and magnitudes of three earthquakes used for the comparison of attenuation laws derived from stochastically simulated earthquake records with observational data. See Figure 4.11.

The broadness of the 95% confidence intervals of the predictive relations (Figure 4.11, dashed lines) indicates a strong variance of ground motion parameters derived from the synthetics due to variable source and site characteristics. This behaviour is also observed in the measured PGA data (Figure 4.11, points). PGA values close to the rupturing fault, however, are overestimated through the attenuation laws determined from the simulated ground motion time series. From their 2D FD modeling of the Kocaeli earthquake Miksat et al. (2005) conclude that the recording stations might be unfavorably placed; peak values therefore appear unexpectedly small in the first kilometers from the fault without the indication of a true trend. Peak amplitudes at distances larger than 80 km, on the other hand, are underestimated by the predictive relations. Since the database of observational data contains in this distance range only data recorded on soft soil (NEHRP D) the underestimation is likely due to underestimated site effects caused by the used averaged amplification values proposed by Boore and Joyner (1997) (Figure 2.2). In addition, the misfit of predicted and observed peak amplitudes is likely caused by simplified models for seismic wave propagation (Chapter 3.2.1). The stochastic simulation procedure is principally useful for the simulation of *mean* ground motions for a set of earthquakes having a certain magnitude and source-to-site distance but is less suited for simulating site- and earthquake-specific ground motions (Boore, 2003).

The comparison of attenuation laws derived from the synthetics and other predictive relationships is established on basis of the following references<sup>8</sup>:

#### A) Sadigh et al., 1997: Strong crustal earthquakes in California

Sadigh et al. (1997) have determined attenuation laws for peak ground acceleration and response spectral acceleration of crustal earthquakes. The relations are based on Californian strong motion data and are valid in the range of  $4.0 \leq M_w \leq 8.0$  and distances up to 100 km. For strike-slip faultings the relationships for rock sites are given by

$$\ln(IM) = C_1 + C_2M + C_3(8.5 - M)^{2.5} + C_4 \ln(r_{rup} + \exp(C_5 + C_6M))$$

whereby  $IM$  is the ground motion of interest and  $r_{rup}$  the closest distance to the rupture surface.

<sup>8</sup>Coefficients of all relations are compiled in Appendix C. Peak values and spectral acceleration are given in units of [g], distances in [km], and velocities in [m/s].

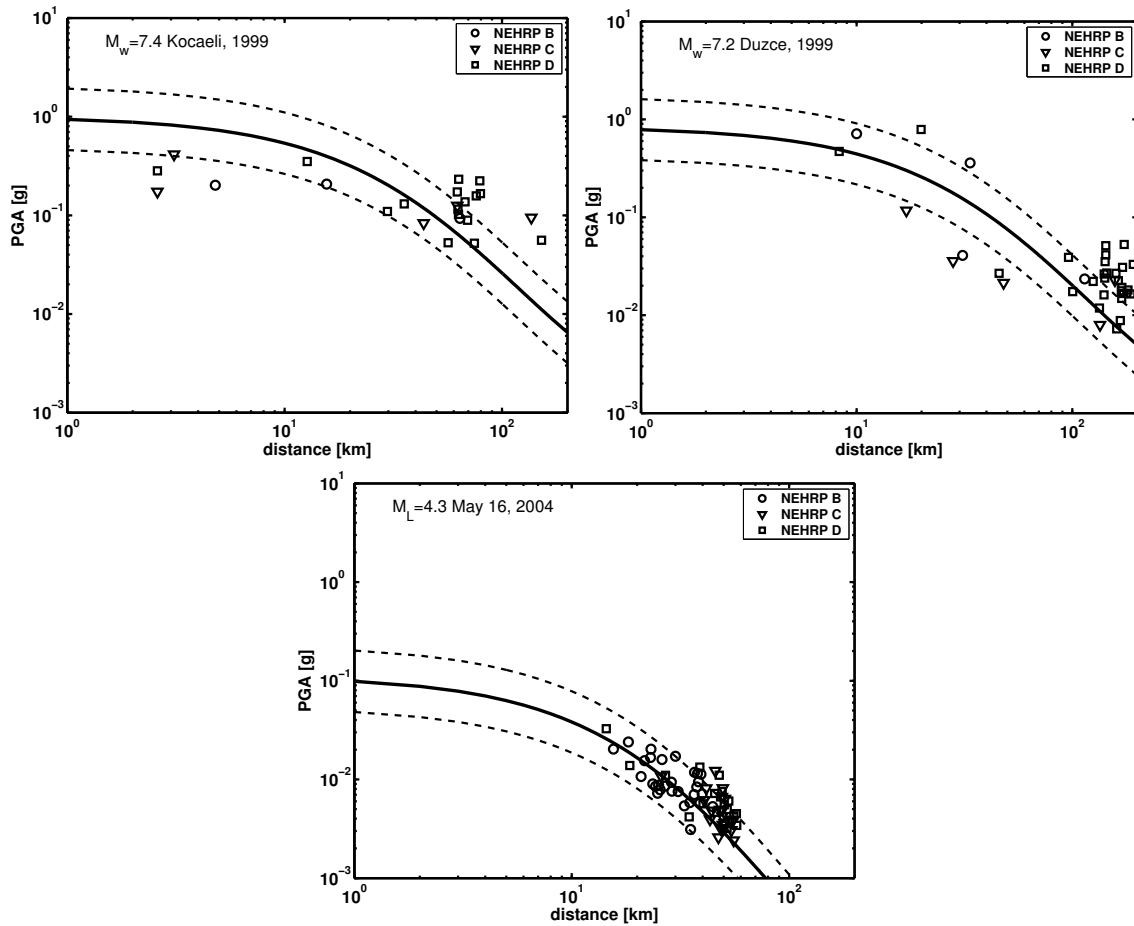


**Figure 4.11:** Attenuation laws for the stochastically simulated data in comparison to three earthquakes in northwestern Turkey: the 1999 Kocaeli and Düzce earthquakes, and a small event that occurred on May 16, 2004, close to Yalova (see Table 4.1). PGA data for both strong events are taken from Durukal (2002). Shown are the mean values of the attenuation laws (solid line) and 95% confidence intervals (dashed lines).

**B) Boore et al., 1997: Earthquakes in western North America**

Boore et al. (1997) have proposed predictive relations for peak acceleration and (horizontal) response spectra derived from recordings of shallow earthquakes in western North America. The laws have the following form:

$$\ln(IM) = C_1 + C_2(M - 6) + C_3(M - 6)^2 + C_4 \ln(r) + C_5 \ln(V_{30}/Va)$$

where

$$r = \sqrt{r_{jb}^2 + h^2},$$

with *Joyner-Boore distance*  $r_{jb}$ . Parameter  $h$  is determined through regression.  $V_{30}$  is the average shear wave velocity of the uppermost 30 m (see Chapter 2.3.3).

**C) Campbell, 1997: Near-source observations**

Campbell (1997) gives empirical near-source attenuation relationships for horizontal and vertical components of peak ground acceleration, peak ground velocity, and pseudo-absolute acceleration response spectra. The relations are considered to be appropriate for the prediction of strong ground motion caused by earthquakes of  $M_w \geq 5$  at distances of  $r_{seis} \leq 60$  km to the seismogenic rupture surface in any active tectonic region in the world. For peak ground acceleration the relation for strike-slip events on soft rock sites is given by

$$\ln(PGA) = -3.512 + 0.904M - 1.328 \ln \sqrt{r_{seis}^2 + (0.149 \exp(0.647M))^2} + 0.440 - 0.171 \ln(r_{seis})$$

and for peak ground velocity

$$\ln(PGV) = \ln(PGA) + 0.26 + 0.29M - 1.44 \ln(r_{seis} + 0.0203 \exp(0.958M)) + 1.89 \ln(r_{seis} + 0.361 \exp(0.576M)) + (0.0001 - 0.000565M)r_{seis} - 0.15 + 0.75 \tanh(0.51D) + f_V(D)$$

with

$$f_V(D) = \begin{cases} 0.0 & D \geq 1\text{km} \\ -0.45 (1 - D) & D < 1\text{km} \end{cases}$$

For spectral acceleration the relation is

$$\ln(IM) = \ln(PGA) + C_1 + C_2 \tanh(C_3(M - 4.7)) + (C_4 + C_5M)r_{seis} + 0.5C_6 + C_7 \tanh(C_8D) + f_{SA}(D)$$

$D$  is the depth to basement rock. It is

$$f_{SA}(D) = \begin{cases} 0.0 & D \geq 1\text{km} \\ 1.5 C_6 (1 - D) & D < 1\text{km} \end{cases}$$

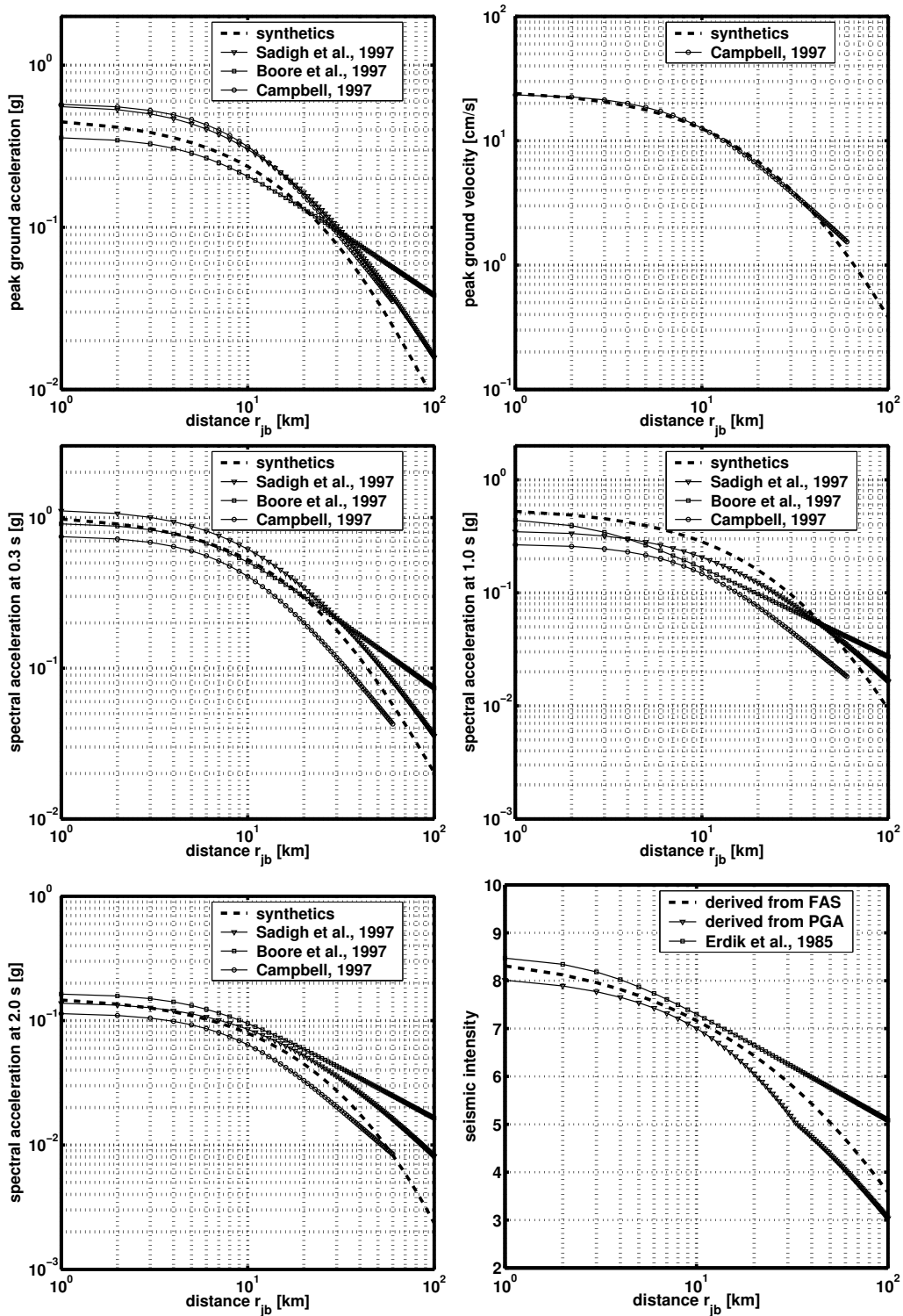


**Figure 4.12:** Comparison of attenuation laws derived from the synthetic data and common relations for peak values, spectral acceleration (5% damping) and seismic intensity for  $M_w = 6.5$ .  $r_{jb}$  is the Joyner-Boore distance.



**D) Erdik et al., 1985: Earthquakes along the North Anatolian fault**

Erdik et al. (1985) have determined an attenuation law for seismic intensity  $I$  for earthquakes along the North Anatolian fault in northern Turkey with

$$I = -3.92 + 2.08M - 0.98 \ln(r_{rup})$$

$r_{rup}$  is the closest distance to the rupture surface. Note that this law has been proposed prior to the strong Kocaeli and Düzce earthquakes in 1999.

**E) Wald et al., 1999: Macroseismic intensity derived from PGA in California**

Wald et al. (1999a) and Wald et al. (1999b) have proposed empirical scaling relations for peak ground acceleration (in  $[cm/s^2]$ ) and seismic intensity  $I$  by

$$I = \begin{cases} 2.20 \log(PGA) + 1.00 & \text{for } I < V \\ 3.66 \log(PGA) - 1.66 & \text{for } V \leq I \leq VIII \end{cases}$$

Note that the atop presented empirical attenuation laws are mostly based on Californian strong motion data. Several studies have repeatedly demonstrated that predictive relations for earthquakes in one region cannot be simply modified for use in other regions. For the 1999 Kocaeli and Düzce earthquakes, e.g., common laws appear to overestimate ground motion for distances up to about 15 km (e.g., Gülkan and Kalkan, 2002). Attenuation laws derived from data of the Kocaeli and Düzce earthquakes alone - as proposed for example by Ozbey et al. (2004) - , on the other hand, should be also considered with caution as these relations are likely biased. (Remember the discussion on this topic at the beginning of the subsection.) Parolai et al. presently work on attenuation relations for western Turkey including data of the two strong motion events as well as on a high number of aftershocks (Parolai, 2005, pers. comm.).

Distinct definitions of source-to-site distances  $r_{rup}$ ,  $r_{jb}$ , and  $r_{seis}$  aggravate a comparison of different attenuation relationships. A scheme for their conversion has been recently developed by Scherbaum et al. (2004). Figure 4.12 compares the discussed attenuation relationships for PGA, PGV, PSA at 0.3 s, 1.0 s and 2.0 s, and seismic intensity with relations derived from the synthetic database at distances of up to 100 km; for clearness only the relation for  $M_w = 6.5$  is plotted, assuming a basement depth of 500 m, a rupture surface depth of 3 km, a seismogenic zone depth of 3.5 km, and a shear wave velocity in the subsurface layer of  $V_{30} = 520$  m/s. The later corresponds to soft rock sites (Table 2.1).

For all ground motion parameters the attenuation laws derived from the synthetics (dashed lines) are in good agreement with the other relations. However, they generally predict lower values at distances of less than 20 km, and the decay of ground motion parameters appears to be more steeply than prognosted by the other relations. Seismic intensity (Figure 4.12, bottom, right column) is compared with values that are (1) determined from FAS and (2) determined from the PGA-intensity relation after Wald et al. (1999a), and (3) obtained from the relation proposed by Erdik et al. (1985). For distances of up to 20 km the predicted intensity matches of all three methods are very high; for larger distances the values can differ in the order of one unit.

## 4.5 Discussions

This chapter gave an overview of different ground motion parameters and described a number of commonly used attenuation laws. Ground motion parameters characterize shaking by earthquakes either in the time or in the frequency domain; they favorably show a high correlation with damage by earthquakes which depends aside from mechanical characteristics and conditions of structures on amplitudes, duration and frequency content of ground shaking (Jennings, 2003). Attenuation relationships describe the decay of seismic ground motion parameters with increasing source-to-site distances.

Based on 3,600 stochastically simulated earthquake records (Chapter 3.3) correlations between nine ground motion parameters and Fourier amplitudes have been analyzed by testing a linear and a non-linear predictive model (Chapter 4.2). The results clearly demonstrate that peak values depend on well separable frequency bands of shaking whereby values of peak ground displacement (PGD) show the highest correlation with motions below 0.5 Hz, peak ground velocity (PGV) with motions between 0.5 to 3.0 Hz, and peak ground acceleration (PGA) mostly depends on motions with frequencies above 3.0 Hz. Bringing to mind that most buildings have eigenfrequencies from 0.5 to 3.0 Hz it appears plausible why the PGV-damage relation is stronger than for the other two peak values (Chapter 4.1.1). However, unlike PGA, peak velocity does not directly give the response of a particular class of structures (Jennings, 2003).

Integrative ground motion parameters, such as seismic intensity derived empirically from the Fourier amplitude spectrum (FAS) of ground motion (Sokolov, 2002), Arias intensity ( $I_a$ ), and the cumulative absolute velocity (CAV), have the advantage that they do not only depend on single amplitudes but on the frequency content and/or duration of shaking. As described in Chapter 4.1.3 the duration of ground motion has generally strong impact on damage to structures caused by earthquakes as their resistency towards ground shaking can significantly decrease with duration of seismic demand; effects such as soil liquefaction can modify the characteristics of the underground. The analyses of correlations with Fourier amplitudes in this chapter revealed that integrative ground motion parameters depend - as expected - on broad frequency bands of seismic ground shaking. Strongest correlations are observed for seismic intensity and CAV for frequencies between 0.2 to 4.0 Hz; this interval has been identified before as from the seismic engineering perspective most relevant part of the FAS. As shown in Figure 4.7 there is a high correlation between seismic intensity derived from FAS and CAV using the simulated data.

The knowledge of frequency bands that are most relevant for the level of different ground motion parameters appears useful for the evaluation of site effects: site effects are clearly frequency-dependent (Chapter 2.3) and will therewith differently affect distinct ground motion parameters. From regression analyses I have determined in this chapter site- and magnitude-dependent amplification factors relative to amplification observed for NEHRP class B using the stochastically simulated ground motion data. Examples that clearly demonstrate these effects are shown in Figure 3.3 for PGA, Figure 3.4 for PGV, Figure 3.5 for PGD, Figure 4.2 for PSA, and Figure 4.5 for CAV. The used amplification spectra (Boore and Joyner, 1997) for the integration of site effects in the stochastic simulations are smooth while observed site effects are much more intricate. Note that the simulations suggest a slight increase of amplification with increasing earthquake magnitude for almost all ground motion parameters (Figure 4.10). Laboratory and numerical experiments suggest that non-linear characteristics of soil response lead to distinct effects on seismic waves depending on the level of ground motion: large strain levels generally decrease the shear modulus and therewith reduce seismic wave velocities. This leads to increased impedance ratios and hence to increased amplification effects. Non-linearities,

however, can also increase intrinsic attenuation and damping of seismic waves in the soil layer which leads to decreased amplification. The reduction of the shear modulus and seismic velocities usually leads to a lengthening of the fundamental response period of the soil layer (Borcherdt, 1994, and references given therein). As a matter of principle the used stochastic simulation method can not reproduce non-linearities in soil response.

It is well known that slip distributions on rupturing faults can be very complex (Chapter 5.1). The highest slip, e.g., does not necessarily occur in the beginning of the rupture (e.g., Kanamori and Brodsky, 2001). Figure 4.13 shows stochastically simulated ground motion time series for different slip distributions with increasing complexity from top to bottom. It appears that inhomogeneous slip distributions generally lead to lower values of ground motion parameters due to the increasing incoherence of seismic waves. There is a significant difference in the level of PGA of factor 1.8 and in seismic intensity derived from FAS of factor 1.1 which corresponds to almost one full intensity unit. Figure 4.14 shows the logarithmized values of PGA (left) and CAV (right) for the six slip distributions in Figure 4.13 at 5 time steps after P-wave onsets: due to the summation of amplitudes over several seconds the CAV values appear smoother than peak values for the different slip histories at the different time steps. The logarithmized CAV is a good indicator for earthquake magnitude for a known source-to-site distance. This is a very important feature that will be used in the later conceptual design of PreSEIS (Chapter 6).

There are further advantageous characteristics of the cumulative absolute velocity (CAV):

- The calculation of CAV is simple (4.17) and suitable for real-time applications.
- The CAV can be standardized: the *bracketed* CAV (Yankee Atomic Electric Company, 1991) considers only damaging parts of the accelerogram (Chapter 4.1.4).<sup>9</sup>
- The CAV is an integrative ground motion parameter that depends on shaking duration but is not strongly affected by details of rupture histories (see above).
- The logarithmized CAV is a good measure of earthquake magnitude (for a fixed or known source-to-site distance), with a reliable convergence towards the true magnitude value (Figure 4.14).
- The CAV is sensitive to directivity effects (not shown here).
- The CAV is closely related to damage by earthquakes as has been shown by Benjamin and Associates (1988) on basis of observational data. The CAV has been suggested as part of the two-level criterion of the Electric Power Research Institute (EPRI) for decision support for shutdowns of nuclear power plants in the U.S. in response to strong earthquakes (Chapter 4.1.4).
- The CAV shows a high correlation with the Fourier amplitude spectrum of seismic ground motion including long-period shaking that is generally most destructive (Chapter 4.2).
- The superiority of the CAV to other ground motion parameters in performance-based liquefaction hazard evaluations has been demonstrated by Kramer et al. (2003)<sup>10</sup>. Because of its high correlation with long-period shaking the authors propose that the CAV might have a close relationship to pore pressure generation.

<sup>9</sup>For the simulated earthquake records used in this work the standardization is irrelevant as the data contains no noise.

<sup>10</sup>For the calculation of CAV the authors apply a threshold acceleration of 5.0 cm/s<sup>2</sup>.

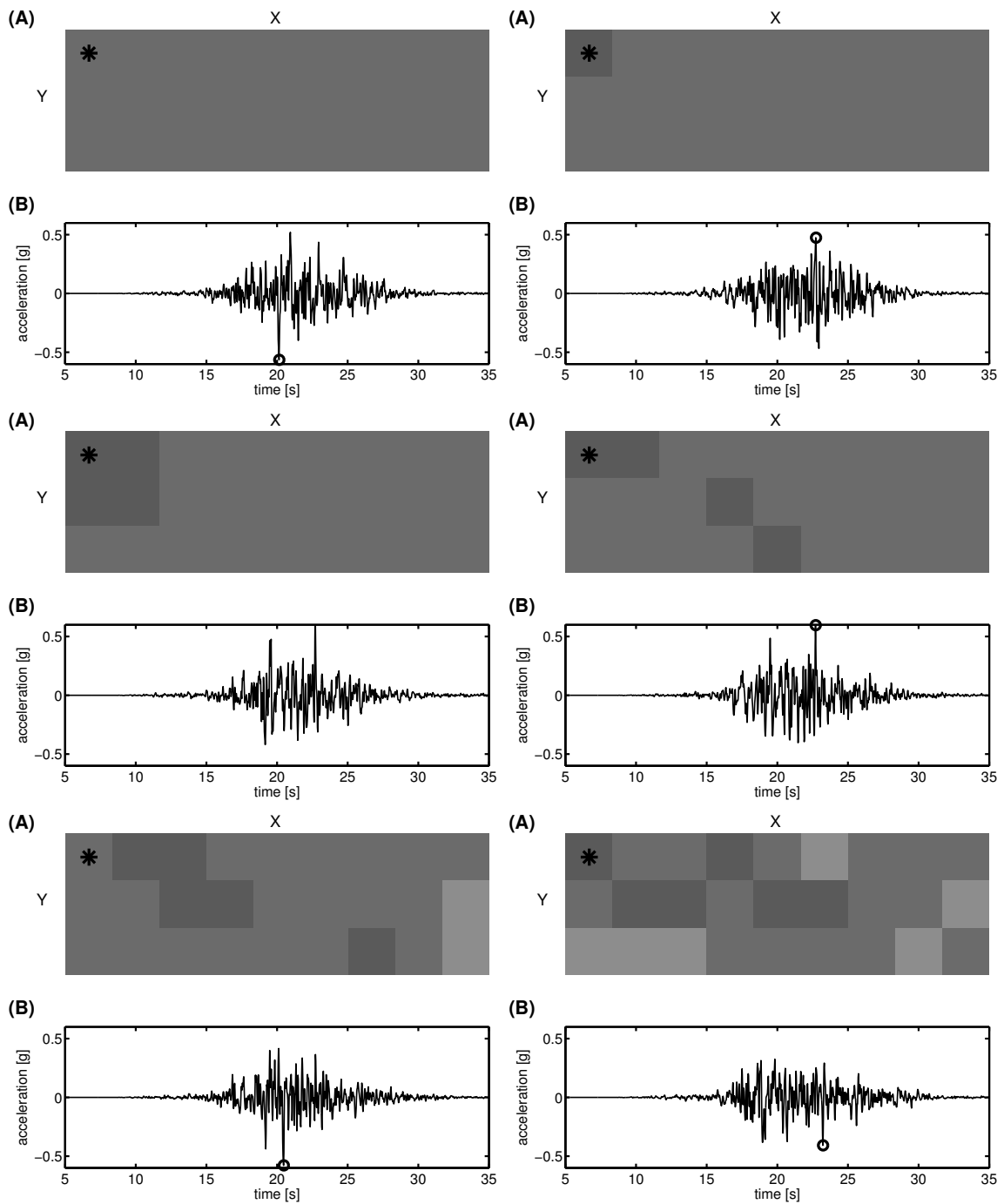


**Figure 4.13:** Impact of slip distributions on the observed level of (simulated) seismic ground motion for six scenarios with  $M_w = 7.0$  and source-to-site distances of 50 km; the rupture size is 53 km x 12 km. Figure (A) shows the distributions of slip on the fault: bright to dark colors indicate dislocations of 0.0 m, 1.9 m, and 3.8 m, respectively. Figure (B) shows the resulting acceleration time series. Due to increasing incoherence of seismic waves amplitudes appear lower in case of inhomogeneous slip distributions. PGA values vary with a factor 1.8, seismic intensity with a factor 1.1 ( $8.5 \leq I \leq 9.4$ ).

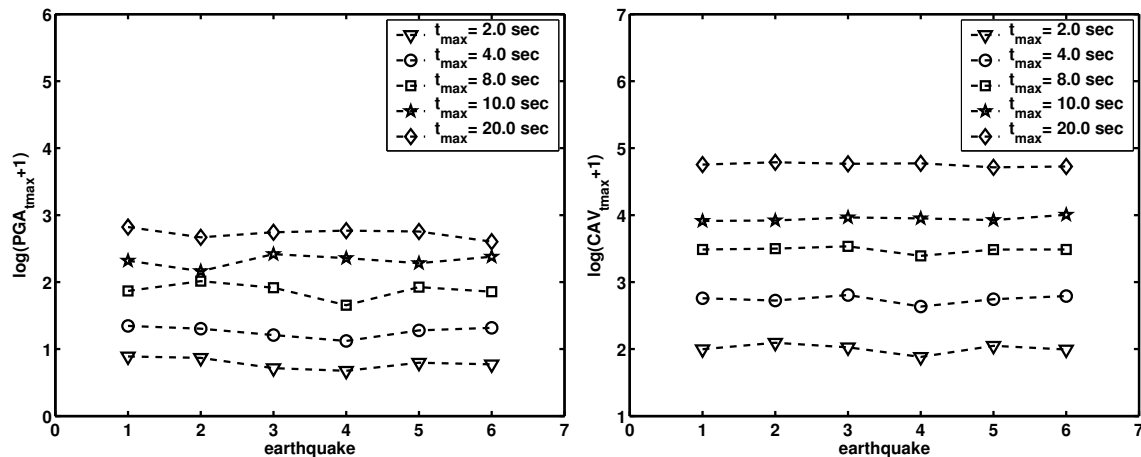


**Figure 4.14:** Impact of slip distributions displayed in Figure 4.13 on logarithmic values of PGA (left) and CAV (right) at different time steps. Note that the CAV values are as a matter of principle smoother at each step and therefore allow for a good estimate of earthquake magnitude with a reliable convergence towards the correct value.

Using records of the synthetic database (Chapter 3.3) attenuation relationships have been developed for ground motion parameters PGA, PGV, PGD, PSA at 0.3 s, 1.0 s and 2.0 s at 5% damping, seismic intensity derived from FAS, Arias intensity  $I_a$  and CAV (Chapter 4.4). The obtained relations are generally in good agreement with observational data in northwestern Turkey and with attenuation laws determined for other seismic active regions in the world (Chapter 4.4.1). At source-to-distances of about 30 km, however, the decay of ground motion parameters derived from the synthetics appears more steeply. Remember that the stochastic modeling procedure is - as a matter of principle - useful for the simulation of *mean* ground motions, but less suited for the simulation of site- or earthquake-specific shaking (Boore, 2003). Comparisons of attenuation laws determined for different seismic active regions rise the question of applicability, and are aggravated by distinct definitions of model parameters such as source-to-site distances (Scherbaum et al., 2004). Deviations between observational data of the Kocaeli and Düzce earthquakes and common attenuation relations are well known in literature (e.g., Gülkan and Kalkan, 2002; Miksat et al., 2005).

Despite of these limitations the comparison of attenuation relations of different ground motion parameters with quantities derived from simulated data can principally allow for a rough frequency-dependent evaluation of synthetic ground motion time series. Using the explored correlation results between ground motion parameters and Fourier amplitudes (Chapter 4.2) it appears that the agreement between synthetics and the different attenuation relationships is significantly higher for parameters that depend on motions above 1.0 Hz (Figure 4.12); among them are PGV, PGA and PSA at 0.3 s. On the other hand, there is a significant difference for spectral acceleration at 1.0 s and 2.0 s that is strongly dependent on motions of 1.0 Hz and less. These findings indicate that the stochastic simulations in Chapter 3.3 have problems in reproducing long-period motions, which, however, is not necessarily a matter of principle but can be also due to inappropriate models of seismic wave propagation including effects of attenuation and geometrical spreading (e.g., Bindi et al., 2006).



## Chapter 5

# Earthquake Early Warning

Almost 140 years ago the basic idea of earthquake early warning came up in California: Cooper (1868) describes the main concept of a seismic early warning system in the *San Francisco Daily Evening Bulletin* based on the observation of the different propagation speed of seismic and electromagnetic waves. Activated by an electronic current an alarm bell installed in San Francisco, California, should almost instantaneously ring once seismic detectors set up near Hollister were triggered by a strong earthquake; Hollister is located about 120 km southeast of San Francisco and is considered as a region with high seismic potential. Cooper's concept of an earthquake early warning system was never implemented. It even took more than one century until the first seismic early warning system was set up at all, and not in California but in Japan. The progress in earthquake early warning over the last few years with respect to instrumentation and real-time communication technologies, as well as to the development of fast algorithms for the real-time processing of seismic data is impressive. Yet, the problem of early warning in general is far from being solved (see Chapter 1): the majority of early warning systems is today still operated for research purpose, i.e. they do not trigger any actions.

In this chapter general design paradigms for earthquake early warning systems will be discussed. The state-of-the-art in implementation will be presented - firstly with respect to instrumentation, later with respect to algorithms. The objective of this chapter is to give an overview of earthquake early warning and to provide a basis for subsequent discussions. Special attention will be turned towards the Romanian early warning system; novel scaling relations derived in the frame of this thesis will be presented at the end of the chapter.

### 5.1 Design Paradigms for Earthquake Early Warning Systems

A classification of earthquake early warning (EEW) systems can be based on the type of tectonic environment in that the system is embedded: tectonic settings frequently predetermine the technological implementation. For example, in regions with a well-defined zone of seismic activity the EEW system can be realized by the installation of seismic devices as close as possible to this zone to maximize possible warning times. This design is called *front-detection*. Front-detection is mainly possible in areas of subducting lithospheric plates, mostly offshore (e.g., Mexico, Japan, Taiwan), sometimes onshore (e.g., Romania). The more frequent case, however, is that a single seismic hazardous zone can not be identified, i.e. locations of strong earthquakes are not known in advance. In these settings the

conceptual design of EEW systems needs much more sophisticated strategies and requires expanded networks of seismic instruments for earthquake detection and source localization.

Early warning systems can also be classified with respect to the underlying design paradigm (see Chapter 1): *regional* warning systems, as a matter of principle, have more warning time available which allows for the integration of ground shaking measurements at several seismic stations of a local or regional network; the entire seismic signal including different types of seismic phases can be analyzed. On the other hand, *on-site* warning systems are capable to give warnings to sites close to the triggered device. The available warning time is thus significantly reduced compared with the regional approach. To maximize warning times on-site warning systems use data from single seismic stations, mostly only information extracted from the faster P-waves, following the idea: the P-wave carries the information, the S-wave carries the energy of the earthquake (Kanamori, 2005).

The feasibility of the on-site method strongly depends on the physics behind the rupture process. Do the beginnings of small and large earthquakes differ? How does the starting earthquake *know* that the following rupture along the fault will grow to a certain size? Our today's knowledge about rupture initiation and evolution is still fragmentary and diverse - partly controversial - theories coexist (see, e.g., Olson and Allen, 2005, and references given therein). In the *cascade model*, e.g., the earthquake begins abruptly whereby there is no difference between a small and a large event. In the *pre-slip model*, on the other hand, the earthquake rupture is preceded by an aseismically episode of slow stable slidings over a limited area of the fault zone, the so-called *pre-slip zone*. The size of the pre-slip zone and the slip within this zone increase gradually until a critical size is reached at which the process can become unstable and the rupture starts to propagate away.

Ellsworth and Beroza (1995) observe a scaling relation between source parameters for the so-called *nucleation phase*<sup>1</sup> and source parameters for the entire earthquake such as size and duration of the nucleation phase. In the *cascade* model the nucleation phase results from a cascade of a number of small to the largest sub-event. The *breakaway phase*<sup>2</sup> then could represent the first large slip event. The observed scaling could arise if the earthquake rupture occurs over a hierarchy of sub-event sizes whereby the last jump (in sub-event size) determines the size of the entire earthquake (Beroza and Ellsworth, 1996). In the *pre-slip* model the last stages of failure in the pre-slip zone correspond to the nucleation phase while the breakaway phase is marked by the begin of rupture propagation. In the pre-slip model the observed scaling between nucleation and entire earthquake can be explained by the pre-slip zone: in case of a large slip amplitude within the nucleation zone, the dynamic rupture would be difficult to stop (Kanamori, 2005) and the likelihood for a large earthquake is very high (Beroza and Ellsworth, 1996). The pre-slip model therewith implicates a difference between small and large earthquakes in the beginning. Even if the scaling relations by Ellsworth and Beroza (1995) only refer to the nucleation phase they demonstrate that it might be feasible to already recognize a strong earthquake in the beginning of the seismic signal. For further discussions see Kanamori (2005).

## 5.2 Earthquake Early Warning Systems in Operation

The following enumeration and short description of existing earthquake early warning systems is limited to the most prominent systems and reflects the state-of-the-art in mid-2005. The realization

---

<sup>1</sup>The *nucleation phase* defines the weak initial phase of the seismogram characterized by a low moment rate.

<sup>2</sup>The *breakaway phase* is the very seismic rupture and is characterized by a linear increase in ground velocity.



strategies of the diverse systems depend on the tectonic backgrounds as well as on the available budgets. Though seismic alarm and early warning systems are low-cost investments in comparison to expensive measures for seismic enforcement, the financial expense for their design, implementation and operation, however, is considerable (see Chapter 1).

### 5.2.1 Alert and Early Warning Systems in Japan

Japan is exposed to an extremely high seismic hazard caused by the subduction of the Pacific and Philippine Sea Plates under the Eurasian Plate. The January 17, 1995 Kobe earthquake ( $M_w = 6.9$ ), with more than 5,000 casualties and about USD  $10^{11}$  in damage goes down in history as the most expensive natural disaster worldwide. However, an even more scaring scenario is a strong earthquake hitting the mega-city Tokyo. As a consequence of complex social and economic integration, experts reckon that such a strike would have fatal impact on national as well as international level.

Japan has experience with EEW since more than twenty years. Today, there exist several early warning systems in Japan, with the *Urgent Earthquake Detection and Alarm System (UrEDAS)* as the most prominent one. The development of *UrEDAS* started with the *Ordinary Alarm System* built up by the *Japanese National Railways (JNR)* in the mid-sixties. The *Ordinary Alarm System* was designed to avoid derailment of high-speed trains such as the *Tokaido Shinkansen* during strong shaking (Nakamura and Tucker, 1988). Using the definitions of Chapter 1 this system was clearly no early warning in a narrower sense rather than alert system. Alarm seismometers were installed every 20 to 25 km along the railway lines adjusted to issue alarms if preset levels of horizontal ground acceleration were exceeded. The threshold of  $40 \text{ cm/s}^2$  was determined as the level where earthquakes are assumed to be destructive, i.e. the system was insusceptible to small earthquakes or noise caused by passing trains or environment.

The next step towards EEW was realized by *JNR* with the construction of the *Coastline Detection System* for the *Tohoku Shinkansen Line* in the eighties. In contrast to the *Ordinary Alarm System*, stations of this front-detection system were installed along the coastline at the Tohoku area where the likelihood of strong earthquakes is very high. The *Tohoku Shinkansen Line* runs about 70 km inland from this coastline. Thus the configuration provided a certain time for early warning. Based on the P-wave, the *Coastline Detection System* could detect earthquakes and estimate their effect on the railroad. The first on-site warning system was established.

The contemporary *Urgent Earthquake Detection and Alarm System (UrEDAS)* (e.g., Nakamura, 1989; Saita and Nakamura, 2003) is the further development of the *Coastline Detection System*. Each of the 30 *UrEDAS* stations is capable to detect the initial P-wave onset of an earthquake and to estimate its location and magnitude within about 3 seconds; the newest device *Fast Response Equipment against Quake Load (FREQL)* by *System and Data Research* (URL: <http://www.sdr.co.jp>) needs only one second after P-wave detection (Nakamura, 2005a).

Since 1996 the *Ordinary Alarm System* and *UrEDAS* are combined in the *Compact UrEDAS*. This system can issue both, ordinary (threshold-based) and P-wave alarms; the later is based on the so-called *PI value* (Nakamura, 1998, 2004). Further *UrEDAS* systems are currently installed in Berkeley and Pasadena, California (Nakamura, 2005a).

During the 2003 Miyagi ken-Oki ( $M_w = 7.0$ ) and Niigata ken-Chuetsu earthquakes ( $M_w = 6.6$ ) *Compact UrEDAS* successfully issued warnings. In the first case, eight *Shinkansen* trains in the alarmed region between Sendai and Morioka could be de-accelerated or stopped; no derailments occurred. In

the second case, four trains were within the alarm area between Muikamachi and Nagaoka. One of these trains was only a few kilometers from the epicenter and derailed without loss of lives though having received a warning (Nakamura, 2005b). All other trains could be stopped without damage.

In 2003 the *National Research Project on Earthquake Early Warning System and its Application* started as a joint project of the *National Research Institute for Earth Science and Disaster Prevention (NIED)*, the *Japan Meteorological Agency (JMA)* and other agencies in Japan (Hayama et al., 2005). The project has the objective to develop and enhance early warning technologies with a prototype for practical application. The regional warning system uses data from about 800 seismometers of the *Hi-net*, covering Japan with an average spacing of approximately 25 km. The system will implement algorithms developed by Horiuchi et al. (2005) and build on experience with early warning gained from the *JMA Nowcast* system.

### 5.2.2 Seismic Alert Systems in Mexico

The Mexican *Seismic Alert System (SAS)* is a typical front-detection system: it is primarily designed to issue warnings to users in Mexico City if strong earthquakes occur along the Guerrero subduction zone, around 320 km away. Despite of the large distance, the seismic threat by Guerrero earthquakes is considered as very high due to the enormous amplification of seismic waves at the lake bed sites below the capital. It is expected that the impact of a strong earthquake ( $M > 7$ ) on Mexico City could be of the same or even higher order than the destructive Michoacan earthquake of September 19, 1985 ( $M_w = 8.0$ ). The large distance towards Mexico City provides a warning time of about 60 seconds for all earthquakes occurring in the Guerrero subduction zone.

*SAS* consists of 12 digital strong motion stations with a 100 Hz sampling rate; they are installed at about 25 km intervals along the Guerrero Coast (Espinosa-Aranda et al., 1995). Each single station is capable to detect moderate and strong earthquakes and to determine certain parameters of the seismic signals; this information is transmitted to the central control system at the *Centro de Instrumentacion y Registro Sismico (CIRES)* in Mexico City where the parameters are compared with data derived from past earthquakes to estimate the magnitude of the event. For redundancy a warning is only issued if the estimation of magnitude is confirmed by at least one further station. To ensure reliability, *SAS* uses two independent communication paths through two different radio frequencies.

*SAS* provides *universal alerts* for Guerrero earthquakes with magnitudes  $M \geq 6$  and *limited alerts* for earthquakes with  $M \geq 5$ . Recipients of limited alerts are elementary schools, offices of Civil and Mexican government agencies, universities, public services, and housing complexes. Alerts are broadcasted via UHF radio receivers installed in the respective buildings. Universal alerts are broadcasted via commercial radio stations to reach a larger community. Public preparedness in terms of effective response to warnings plays an important role in the Mexican strategy for earthquake risk mitigation (Espinosa-Aranda et al., 1995).

During operation from August 1991 to May 2005 the *Seismic Alert System* successfully detected 1,783 earthquakes with  $2.5 < M < 7.3$  and issued 11 universal and 46 limited alerts; one false alert was given in 1993 (Espinosa-Aranda et al., 2005).

Also Oaxaca City has suffered severe damage by earthquakes in the Guerrero subduction zone in the past. The *Seismic Alert System Oaxaca (SASO)* is designed to warn of earthquakes along the Guerrero Coast, the Tehuacan-Huajuapán de León region, and the Tehuantepec and Orizaba areas. The system consists of 29 seismic sensor stations installed in the seismic active regions around Oaxaca City.

Between November 2003 and July 2005 *SASO* issued five warnings (Espinosa-Aranda et al., 2005).  
URL: [http://www.cires.org.mx/in\\_index.php4](http://www.cires.org.mx/in_index.php4)

### 5.2.3 Rapid Reporting and Early Warning System in Taiwan

Located on the western circum-Pacific belt, Taiwan has been repeatedly hit by damaging earthquakes in the past, e.g. on 17 March 1906 in Chiayi ( $M = 7.1$ ), in 1935 in the Hsinchu-Taichung area ( $M = 7.1$ ), or in 1999 in Nantou Country ( $M_w = 7.5$ ), known as the *Chi-Chi* earthquake.

Since 1995 the *Taiwan Weather Bureau* (CWB) makes use of its *Rapid Earthquake Information Release System* (RTD) to develop a *Rapid Reporting System* (RRS) and an *Early Warning System* (EWS) for earthquakes in Taiwan (Wu et al., 1997, 1998). RTD consists of 79 telemetered strong motion stations which are distributed across Taiwan over an area of  $100 \text{ km} \times 300 \text{ km}$ . The sensors are three-component, force-balanced accelerometers with  $\pm 2g$  full recording dynamic range, 50 Hz sampling rate and 16-bit resolution. RRS is capable to provide reporting information within about one minute after the occurrence of any significant earthquake (Teng et al., 1997; Wu et al., 2001).

For the EWS a *Virtual Subnetwork* (VSN) of RTD stations is used (Wu and Teng, 2002). The respective subset is automatically configured by a monitoring software. Usually a VSN consists of about a dozen stations, which are located in a 60-km-radius centered on the event. By the limitation of seismic stations for the EWS the reporting time for an earthquake can be shortened to an average of about 22 seconds after the origin time. This reporting time offers more than 20 seconds of early warning to cities at distances greater than 145 km from the source. The *Virtual Subnetwork* was put into operation from December 2000 to June 2001. In this period 54 earthquakes were detected and mostly correctly processed (Wu and Teng, 2002).

Recently, Wu and Kanamori (2005a,b) have proposed to combine the existing regional EWS with an on-site approach to expand the possible warning area. The used algorithm will be described in the following section.

### 5.2.4 Real-time Seismology and Seismic Early Warning in California and Central U.S.

Despite of important progress in earthquake research and real-time seismology in the last decades (Noda and Meguro, 1995; Kanamori et al., 1997), the problem of earthquake early warning for California and Central U.S. has not been solved yet (Holden et al., 1989). The complexity and seismic danger of fault systems - such as the prominent *San Andreas Fault* - aggravate the realization of an early warning system. The quick detection of earthquakes and the estimation of seismic parameters require the installation of expanded networks of telemetered seismic stations which is in contrast to front-detection systems such as in Mexico.

One of the objectives of the *TriNet Project* (1997-2001) of the *California Institute of Technology* (Caltech), the *U.S. Geological Survey* (USGS), and the *California Division of Mines and Geology* was to develop a prototype earthquake early warning system for southern California, called *Seismic Computerized Alert Network* (SCAN) (Heaton, 1985). SCAN could never be put into operation because of reasons summarized in Chapter 1 (Goltz, 2002).

Of course, developments in real-time seismology are directly linked to progress in seismic instrumentation. The following enumeration shall provide an overview of seismic networks and projects associated with real-time seismology in California and Central U.S. over the last decades:

- **Southern California Seismic Network (SCSN):**  
Since the 1960's the *Caltech Seismological Laboratory* and the *USGS Pasadena* operate the *Southern California Seismic Network (SCSN)* with more than 200 seismic analog stations. The *SCSN* catalogue starts in 1932 and is with more than 344,000 events one of the most complete in the world.
- **National Strong Motion Program (NSMP) network:**  
Within the *National Strong Motion Program (NSMP)* the *USGS* operates nationwide 571 strong motion stations.
- **California Strong Motion Instrumentation Program (CSMIP) network:**  
The *California Geological Survey (CGS)* operates within the *California Strong Motion Instrumentation Program (CSMIP)* network 400 analog strong motion sensors.
- **TERRAscope network:**  
The *TERRAscope* project started in 1987 with 19 digital stations installed in southern California, allowing a real-time distribution of earthquake data. It was extended into the *CUBE project* in 1990 (Kanamori et al., 1991) and led to the foundation of the *Southern California Earthquake Center (SCEC)* at *Caltech*. URL: <http://www.gps.caltech.edu/bryant/cube.html>
- **Automated Strong Motion Monitoring Program (AMOES):**  
In 1994 *Caltech* and *Kinematics Inc.* started the joint development and installation of 16 digital *K2* instruments in the greater Los Angeles region.
- **Rapid Earthquake Data Integration (REDI):**  
In 1996 the *USGS Menlo Park* and the *Berkeley Seismological Laboratory (BSL)* combined their earthquake reporting operations, the *Northern California Seismic Network (NCSN)* and the *Berkeley Digital Seismic Network (BDSN)*, into a joint notification system, the *Rapid Earthquake Data Integration (REDI)* (Gee et al., 1996, 2000). URL: <http://www.seismo.berkeley.edu/seismo/redi/>
- **TriNet project:**  
The *TriNet* project triggered the upgrade of the existing seismic networks of *SCSN*, *CSMIP*, and *NSMP* with 635 digital accelerometers and broad-band seismometers, as well as real-time processing capabilities. For telemetry digital phone lines, radios, microwave links, and internet accesses were installed. The automatic analyses of data includes the determination of earthquake locations, magnitudes, and types of faulting. Aside from *ShakeMaps* (see Chapter 1) the information is made public through internet and sent directly to cost-sharing partners through a commercial paging system and intranet within minutes after the earthquake (Goltz, 2003). URL: <http://www.trinet.org/>
- **California Integrated Seismic Network (CISN):**  
The collaboration of *BSL* and *USGS Menlo Park* in northern California, and of *Caltech* and *USGS Pasadena* in southern California together with the *California Division of Mines and Geology* forms the *California Integrated Seismic Network (CISN)* with 155 seismic stations. *ElarmS* (Allen and Kanamori, 2003), the *Virtual Seismologist* (Cua, 2004) and the  $\tau_c$  method (Kanamori, 2005; Wu et al., 2005) are current studies to address the problem of earthquake early warning in California on basis of the *CISN* instrumentation. URL: <http://www.cisn.org/>

- **Rapid Earthquake Information System (REIS)**

The *Center of Earthquake Research and Information (CERI)* at the University of Memphis, *Saint Louis University Earthquake Center*, *South Carolina Seismic Network*, and the *U.S. National Seismic Network* build up the *New Madrid Rapid Earthquake Information System (REIS)* for the central and Eastern U.S. (Withers et al., 2000a,b). URL: <http://www.ceri.memphis.edu/reis/>

### 5.2.5 Istanbul Earthquake Rapid Response and Early Warning System (IERREWS) in Turkey

Considering the enormous seismic risk in the Marmara region (see Chapter 1) and pushed by the 1999 Kocaeli and Düzce earthquakes, a Real-Time Earthquake Information System for Istanbul has been designed and implemented in the *Istanbul Earthquake Rapid Response and Early Warning System (IERREWS)*. The installation of *IERREWS* by the *Bogazici University* with logistical support by the *Governorate of Istanbul*, *First Army Headquarters* and *Istanbul Metropolitan Municipality* could be finished in fall 2002. The system consists of 152 tri-axial strong motion stations, two data centers and several end-use nodes. The accelerometers have a dynamic range of  $\pm 2g$  at 18-24 bit resolution (Erdik et al., 2003b). *IERREWS* is operated by the *Kandilli Observatory* of the *Bogazici University* in Istanbul.

One hundred of the 152 accelerometers have been installed in the metropolitan area of Istanbul; they are operated in dial-up mode for the generation of rapid response information, such as shake maps. Ten further seismic stations are sited along the coast of the Marmara Sea and are part of the early warning (front-detection) system within *IERREWS* (see Figure 1.3). These stations are operated in online transmission mode. The continuous telemetry of 50 Hz data is realized by a digital 2.4 GHz spread spectrum radio modem system using two repeater stations. Communication services are provided by *ARIA GSM*. The warning time is assumed to be in the order of 10 seconds, depending on the point of rupture initiation and the location of the recipient facility (Erdik et al., 2003b). The remaining 40 stations are sited on critical engineering structures in Istanbul such as on the Bosphorus Bridge. So far, *IERREWS* is operated for research purpose. URL: <http://www.koeri.boun.edu.tr/deprenmmuh/EWRR/EWRRMain.htm>

### 5.2.6 Earthquake Early Warning in Romania

Within the last century Romania has experienced four strong earthquakes on Nov. 10, 1940 ( $M_w = 7.7$ ), on March 4, 1977 ( $M_w = 7.4$ ), on August 30, 1986 ( $M_w = 7.1$ ), and on May 30, 1990 ( $M_w = 6.9$ ) (Oncescu and Bonjer, 1997). The 1977 event was most damaging and caused 1,570 fatalities, more than 11,300 injured people - 90% of them in the Romanian capital Bucharest - , and USD 2 billion direct damage costs. All strong earthquakes aside from several small to moderate size events occurred at depths between 70 to 180 km in a well-defined volume of about 40 km  $\times$  80 km  $\times$  190 km size in the Vrancea zone, SE Carpathians. This intermediate-depth seismicity coincides with the location of a lithospheric slab segment whose subduction took place 22 to 10 million years ago (Sperner and the CRC 461 team, 2005).

The favorable geometry formed by the seismogenetic Vrancea zone and Bucharest, accompanied by consistent source mechanisms of all strong Vrancea earthquakes (Plenefisch, 1996), allows for the design of a simple, cheap and robust earthquake front-detection system for the Romanian capital as

proposed by Wenzel et al. (1999, 2001). The average epicentral distance of 130 km towards Bucharest provides a warning time of about 25 seconds for all intermediate-depth events, defined by the time difference between P-wave detection in Vrancea and S-wave arrival in Bucharest.

The *National Institute for Earth Physics (NIEP)* in Bucharest and the *Collaborative Research Center (CRC) 461: Strong Earthquakes: a Challenge for Geosciences and Civil Engineering* (1996 to 2007) at the *University of Karlsruhe* (Germany) have designed and installed key components of a prototype front-detection system for Bucharest. The system consists of three tri-axial strong motion sensors deployed in the epicentral area and a satellite communication link to the *Romanian Data Center* at *NIEP* in Bucharest. The seismic sensors are installed in Vrancea (VRI) and in Plostina, about 8 km away. One of the Plostina stations (PL1), a FBA-23 sensor, is deployed in a 50 m deep borehole in order to minimize accidental triggerings of the system; the other instrument (PL2) is an *Episensor* that is installed on top of the borehole.

The prediction of the level of ground shaking, that Bucharest will experience during moderate to strong earthquakes, can be based on simple scaling relations as shown by Wenzel et al. (1999). The Romanian earthquake early warning system is now in a test phase with a sterilization facility working with a nuclear source as a test user (Ionescu and Marmureanu, 2005).

### 5.3 Algorithms for Earthquake Early Warning

Aside from seismic instrumentation with real-time data transmission capability as described above, a further key component of seismic real-time systems is a software for the automatic processing of seismic data streams to extract information from the earthquake signals. Basic tasks of this software encompass the detection of earthquakes, preferably a discrimination from other sources such as quarry blasts, and a rapid determination of seismic source parameters. Once the location and magnitude of the earthquake are known, it is possible to estimate seismic ground motion at any site from empirical attenuation laws as described in Chapter 4 of this work.

The three fundamental tasks of *earthquake detection*, *earthquake localization* and *estimation of earthquake magnitude* are common for most seismic early warning systems. However, there are significant differences in the realization: *regional* warning systems (see Chapter 1) have more time available before parameters have to be determined. Therefore, regional warning systems can process data from a network of seismic instruments and estimate the parameters using (traditional) *network approaches*. Results of such network procedures are certainly much more reliable than if obtained from *single stations*. The later is mostly used for *on-site* warning systems (see Chapter 1). On-site warning systems have to make information much more rapidly available in order to effectively warn potential users within some tens of kilometers away from the earthquake epicenter. In many on-site warning systems, seismic parameters are estimated from the faster (direct) P-wave to save valuable warning time. The following subsections will present different procedures for the estimation of earthquake location and magnitude using network and single station approaches applied to earthquake early warning.

#### 5.3.1 Earthquake Detection

Seismic detection describes the distinction between ambient noise and earthquake registrations. Earthquake early warning alike other seismic monitoring systems have automatic detectors to decide whether an earthquake has occurred or not.

Standard detectors in geophysical data processing are based on short-term average to long-term average (STA-LTA) values (Vanderkulk et al., 1965). Alternative approaches based on data-driven reasoning and pattern recognition, respectively, have been proposed by Chiaruttini and Salemi (1993) and Joswig (1990). Further algorithms are given by Allen (1978) and Magotra et al. (1987). The interested reader is additionally referred to literature that is published in the context of the *Comprehensive Test Ban Treaty*, e.g., Walter and Hartse (2002). The possible discrimination between natural earthquakes and other sources of ground motion, such as quarry blasts or nuclear explosions, is described, e.g., by Dowla et al. (1990).

### 5.3.2 Earthquake Localization

Common procedures for the localization of earthquake hypocenters are based on measurements of arrival times of seismic waves, mainly P- and S-waves, by at least three seismic sensors distributed around the epicenter. Graphical approaches encompass circle and hyperbola methods (e.g., Mohorovicic, 1915; Pujol, 2004). The inverse problem can be also solved by numerical approaches (e.g., Lahr, 1999). The applicability of graphical procedures for earthquake early warning systems is studied by Rydelek and Pujol (2004) in the U.S. and by Horiuchi et al. (2005) in Japan.

Based on the decay of ground motion amplitude with distance from the seismic source, Kanamori (1993) proposes an alternative concept for earthquake localization using amplitude data instead of travel times: starting from a given empirical attenuation law, the model space of magnitude and location parameters is scanned to find a (global) minimum of the error function given by the observed and computed data. Using these results as first approximation, the final solution is determined with the method of least-squares. Because amplitude is affected not only by distance but also by specific source and site characteristics, earthquake localization by amplitude is mostly inaccurate. Nevertheless, the method has two important advantages over travel time based approaches: first, the exact knowledge of the point of rupture initiation is irrelevant for post-earthquake emergency services which rather need the rapid information of spatial distribution of ground motion parameters. Second, amplitudes are usually easier to determine than phase onsets.

Once the earthquake magnitude is determined, e.g., by methods presented in the following subsection, the hypocentral distance can be approximated from a single station using attenuation laws (Nakamura, 1998). Alternatively, it is possible to estimate the hypocentral distance from a single seismic broadband station by the identification of individual seismic phases or by matching the observed waveforms with synthetics generated for an appropriate crustal model (e.g., Dreger and Helmberger, 1993). Odaka et al. (2003) present a method for the quick estimation of the epicentral distance by fitting an exponential function  $f$  defined by

$$f(t) = B t \exp(-A t) \quad (5.1)$$

to the initial parts of the waveform envelope of single seismic records;  $t$  denotes the time and  $A$  and  $B$  are free parameters that are determined through regression from previous events. Using data of the Japanese *K-Net*, Odaka et al. (2003) find an inverse proportionality between  $\log B$  to  $\log \Delta$ , where  $\Delta$  is the epicentral distance. The authors claim that this relation is hardly affected by earthquake magnitude.

Signal polarization allows the determination of station-source backazimuth using the eigenvalues and eigenvectors of the covariance matrix of two or three signal components of a single station. Path effects - such as scattering or anisotropy - lead to uncertainties in the estimated azimuth. Typical errors are in

the order of  $15^\circ$ . To reduce instabilities, Nakamura and Saito (1983) propose a smoothing procedure for seismic real-time data streams. Focal depth is constrained by relative times of large-amplitude surface-reflected arrivals in the P-coda, and by the relative amplitudes of surface- and body-wave groups.

A comprehensive review on methods for earthquake localization using single three-component seismic sensors - including Neural Network and Artificial Intelligence approaches - is given by Frohlich and Pullim (1999) in the context of the *Comprehensive Test Ban Treaty (CTBT)*.<sup>3</sup>

### 5.3.3 Determination of Earthquake Magnitude

Seismic ground motion caused by strong earthquakes generally contains lower frequencies than if generated by small events. Thus, it should be possible to approximate the magnitude of an earthquake from the *predominant frequency*  $f^P$  of the seismic signal. Several methods to estimate  $f^P$  of the initial parts of seismic recordings have been developed in the past. For real-time applications  $f^P$  is generally approximated in the time domain from the ratios of ground motion amplitudes based on *Parseval's theorem*, which states that the power of a signal represented by a function  $s(t)$  is the same whether computed in time or in the frequency domain:

$$\int_{-\infty}^{+\infty} s^2(t) dt = \int_{-\infty}^{+\infty} |S(f)|^2 df. \quad (5.2)$$

Thus the predominant frequency  $f^P$  can be calculated from

$$f^P \equiv \sqrt{\langle f^2 \rangle} = \frac{\sqrt{\int_0^{\infty} f^2 |U(f)|^2 df}}{\sqrt{\int_0^{\infty} |U(f)|^2 df}} = \frac{1}{2\pi} \frac{\sqrt{\int_0^{\infty} \dot{u}^2(t) dt}}{\sqrt{\int_0^{\infty} u^2(t) dt}}, \quad (5.3)$$

where  $U(f)$  is the Fourier transform of the seismic displacement time series  $u(t)$ . Kanamori (2005) modifies (5.3) by keeping the upper limit of the integrals fixed to  $\tau_0 \approx 3$  s

$$f_{Kanamori}^P \approx \frac{1}{2\pi} \frac{\sqrt{\int_0^{\tau_0} \dot{u}^2(t) dt}}{\sqrt{\int_0^{\tau_0} u^2(t) dt}} \equiv \frac{1}{\tau_c}. \quad (5.4)$$

After Kanamori (2005) it is possible to decide whether an earthquake is  $M_w \leq 6.5$  or  $M_w > 6.5$  using only information of the first three seconds of the seismic signal. The applicability of the so-called  $\tau_c$  *method* for on-site earthquake early warning has been studied by Wu and Kanamori (2005b) in Taiwan and by Wu et al. (2005) in California. The authors find that the magnitude- $\tau_c$  relation can be expressed by

$$M = a \log \tau_c + b, \quad (5.5)$$

<sup>3</sup>Single station approaches are not unusual in the context of *CTBT*, because only 18% of the Earth's surface is covered by three or more stations within  $10^\circ$  (which can be used by the *CTBT* organization) - the minimum number of instruments for the localization of earthquakes or nuclear explosions (Frohlich and Pullim, 1999).



whereby  $a$  and  $b$  are free parameters. Strong earthquakes of  $M > 6$  generally have  $\tau_c > 1$  s (Wu et al., 2005), whereby the scattering of values, however, is partly very high.

The original idea to estimate the predominant period  $T_p$ , i.e. the reciprocal value of the predominant frequency  $f^p$ , from ratios of ground motion of continuous seismic signals was proposed by Nakamura (1985):

$$T_{Nakamura,i}^P \approx 2\pi \sqrt{\frac{\dot{U}_i}{\ddot{U}_i}} = 2\pi \sqrt{\frac{\alpha \dot{U}_{i-1} + \dot{u}_i^2}{\alpha \ddot{U}_{i-1} + \ddot{u}_i^2}}. \quad (5.6)$$

The smoothing constant  $\alpha$  takes values between 0.95 to 0.99. Note that Nakamura (1985) uses the ratios of velocity and acceleration amplitudes (on the vertical component), whereas Kanamori (2005) uses velocity and displacement data. The recursive algorithm given by (5.6) is implemented in the Japanese *UrEDAS*. The fluctuations of magnitude that are estimated by *UrEDAS* are almost within  $\pm 0.5$  units relative to magnitudes estimated by the *Japanese Meteorological Agency (JMA)* (Saita and Nakamura, 2003). Allen and Kanamori (2003) use Nakamura's method (1985) to estimate the predominant period in the conceptual early warning system *ElarmS* in California. Since the higher frequency content of small earthquakes ( $M < 5.0$ ) is measured in a shorter time window, the magnitude of these events can be determined more rapidly than the magnitude of large events: magnitude estimations are available 1 s after the P-wave arrival in case of small earthquakes and after 1 to 4 s in case of large earthquakes.<sup>4</sup> Lockman and Allen (2003) show the existence of similar scaling relationships for earthquakes in the circum-Pacific belt.

Cua and Heaton (2003) and Cua (2004) address the problem of magnitude and distance trade-off in their *Virtual Seismologist* using a Bayesian approach: the most likely values of magnitude and location are those, whose expected amplitudes, ratios of different components of ground motion (acceleration-displacement ratio once again as indicator for the earthquake magnitude) and envelope parameters are most consistent with the observations. With additional data from the ongoing earthquake rupture, the estimations of magnitude and distance are updated. Background knowledge derived from earlier observations - such as fault locations or the relative frequency of earthquake magnitudes (*Gutenberg-Richter law*) - can be incorporated as Bayesian prior, i.e. as a priori probability. Yamada and Heaton (2005) currently work on an extension of the *Virtual Seismologist* to finite faults.

Grecksch and Kümpel (1997) analyze strong-motion records of 244 earthquakes that occurred in North and Central America between 1940 and 1986 to determine the correlation between peak acceleration, predominant frequency (obtained from the Fourier amplitude spectrum), spectral amplitude, and rise time on the one hand, and epicentral distance and magnitude on the other hand. The authors find that the magnitude can be predicted from the first second of a single accelerogram within  $\pm 1.36$  magnitude units. Using eight or more accelerograms of the same earthquake, the uncertainty can be reduced to  $\pm 0.5$  magnitude units. A similar positive effect of averaging over estimations by several stations was observed by Wu and Kanamori (2005b) and Wu et al. (2005) using the  $\tau_c$  method.

Tsuboi et al. (2002) use the duration of the initial P-wave pulse  $\tau$  to estimate the seismic moment  $M_0$  of earthquakes by using the seismic moment-duration relation (see section 2.1.2)

$$M_0 \propto \tau^3. \quad (5.7)$$

The authors assume that the vertical component of displacement of a broadband recorded P-wave can be taken for the far-field source time function of the respective earthquake. Tsuboi et al. (2002) find

<sup>4</sup>For small earthquakes, Allen and Kanamori (2003) apply a low-pass filter at 10 Hz, for large earthquakes at 3 Hz.

that earthquakes with  $M > 6$  are identifiable within three seconds after the P-wave arrival - the same value that was also found by Kanamori (2005).

Another approach to predict magnitude levels on the basis of the sum of squared acceleration is implemented in the Mexican SAS. In order to ensure that the incoming signal comes from the expected distance range, a certain time window between P- and S-wave arrival has to be obeyed (Espinosa-Aranda et al., 1992).

In contrast to the approaches for magnitude and location estimations presented so far, Scrivner and Helmberger (1995) propose a method for single broadband station inversion to approximate source parameters such as strike, rake, dip and seismic moment (Zhao and Helmberger, 1994). Together with a library of Green's functions - that are calculated for an average southern California crustal model or derived from regional weak motion data - Scrivner and Helmberger (1995) develop a procedure to predict the whole time series of ground motion for an arbitrary site of interest. The inversion uses only that data that is available at each time step.

### 5.3.4 Other Approaches

Leach and Dowla (1996) analyze 434 three-component records of regional earthquake ( $2.5 \leq M_L \leq 4.6$ ) with epicentral distances of 20 to 300 km recorded by instruments maintained by the *Lawrence Livermore National Laboratory* in southern California from 1988 to 1992. For each record the authors determine 30 parameters - that are not specified in more detail - at six different window sizes; these values are used as input for two *Two-Layer Feed-Forward* Neural Networks (Chapter 6.1.3): the first network is trained to predict the earthquake scale (in terms of peak ground acceleration), the second to estimate the record profile expressed by envelope and duration parameters. The first prediction is available 0.3 s after the arrival of the direct P-wave; estimates are updated at each new sample.

*P-wave alarms* issued by *Compact UrEDAS* are based on the so-called *PI value* intensity index (Nakamura, 1998, 2004). The *PI value* is defined as the maximum value of the logarithmic product of acceleration and velocity amplitudes. There is a strong relationship between the *PI value* and seismic intensity.

Wu and Kanamori (2005b) propose to make use of the correlation between the peak initial displacement amplitude  $P_d$  and the peak ground velocity (PGV) at the same site to estimate ground shaking for on-site warning systems. This approach has been successfully tested by Wu and Kanamori (2005b) in Taiwan and by Wu et al. (2005) in southern California.

More simple are threshold based approaches as applied in the Turkish *IERREWS*: whenever a certain threshold of filtered acceleration at two or three stations is exceeded, the early warning system issues an alarm. Currently, the system works with three alarm levels associated with thresholds of 0.02 g, 0.05 g and 0.1 g. As these thresholds can be exceeded by the P-wave, the level of ground shaking in Istanbul can be significantly higher.

The Romanian earthquake early warning system as designed by Wenzel et al. (1999) is based on simple scaling relations between the maximum filtered P-wave amplitude  $P_{epi}$ , recorded on the vertical component of an accelerometer that is deployed in the epicentral area, and filtered peak horizontal acceleration in Bucharest  $PGA_{filt}$ . A 3<sup>rd</sup> order Butterworth-filter is applied between 1 to 2 seconds because site effects in Bucharest show a significant amplification in this period range (Bonjer et al., 1999); in addition, this band covers the range of eigenperiods of medium to high-rise structures in

Bucharest and is therefore meaningful for engineering problems (Wenzel et al., 1999). Secondly, the filtering reduces the probability of false alarms caused by small earthquakes with high-frequency motions that might occur closely to the seismic device or by site effects in the epicentral area. Based on data of

- 18 weak motion records, FBA23, S13/SH-1, S13, and
- 2 strong motion records, digitized from SMA-1 film recorders,

Wenzel et al. (1999) find for the epicentral station *MLR* in Montuele-Rosu and station *BUC* in Bucharest the following relation:

$$PGA_{filt} \approx 10 \cdot P_{epi}. \quad (5.8)$$

Within this thesis, the scaling relation given by (5.8) is revised on the basis of additional weak motion data obtained from the *Kinematics K2* strong motion network installed in Romania since 1997. Installation and maintenance of the network are achieved in joint efforts of the Romanian *National Institute for Earth Physics (NIEP)* and the *Geophysical Institute at Karlsruhe University (GIK)*. Moreover, two strong motion records of the 1986 and 1990 Vrancea earthquakes and additional synthetic records obtained from *Empirical Green's Functions (EGF)* after Irikura (1983) and simulated by Wirth (2004) are integrated into the analyses. The dataset therewith is composed of

- 19 weak motion records ( $3.7 \leq M_w \leq 5.3$ ), *Kinematics K2*;
- 2 strong motion records (1986  $M_w = 7.2$ , 1990  $M_w = 6.9$ ), SMA-1;
- 36 synthetic records ( $5.6 \leq M_w \leq 8.0$ ) obtained from *Empirical Green's Functions*.

The new scaling relations will be determined for the epicentral station *VRI* in Vranceioia<sup>5</sup> and the Bucharest station Incerc *INC* (later renamed *RBA*) (Figure 5.1). For earthquake early warning two stations with real-time capability (*PL1* and *PL2*) were installed in Plostina during spring 2004. Despite of a distance of approximately 8 km between the sensors deployed in Plostina and station *VRI* in Vranceioia, the P-wave amplitudes on the vertical components of all sensors are almost equal after filtering (Figure 5.2). Scaling laws that will be derived for station *VRI* are therefore assumed to be also applicable to the early warning sites *PL1* and *PL2*. Moreover, the data used by Wenzel et al. (1999) that was recorded by station *MLR* will be also included in the database here. This is possible as only long-period shaking is assessed that is hardly affected by attenuation at the short distances between the epicentral stations.

Figure 5.3 shows the time window defined by the arrivals of the direct P-wave at station *PL1* (vertical component) and the high-amplitude S-wave at station *RBA* in Bucharest (EW component) using the example of the October 27, 2004  $M_w = 5.9$  Vrancea earthquake; the maximum possible warning time for Bucharest therewith is - as described before - in the order of 25 seconds.

Additional scaling relations for peak ground acceleration *PGA*, spectral response at different periods ( $PSA_{0.3s}$ ,  $PSA_{1.0s}$ ,  $PSA_{2.0s}$  at 5% damping), and seismic intensity *I* will be determined. Input parameter is  $P_{epi}$ . For the validation of the new scaling relations, data of the October 27, 2004 Vrancea earthquake ( $M_w = 5.9$ ) will be used. (Instrumental) seismic intensity *I* will be derived from the Fourier

<sup>5</sup>For the recordings of the strong motion events station Surduc (*SUR*) is used as records from station *VRI* are not available.



**Figure 5.1:** Distributions of accelerometers used for the Romanian earthquake early warning system and additional stations used for the definition of scaling relations.

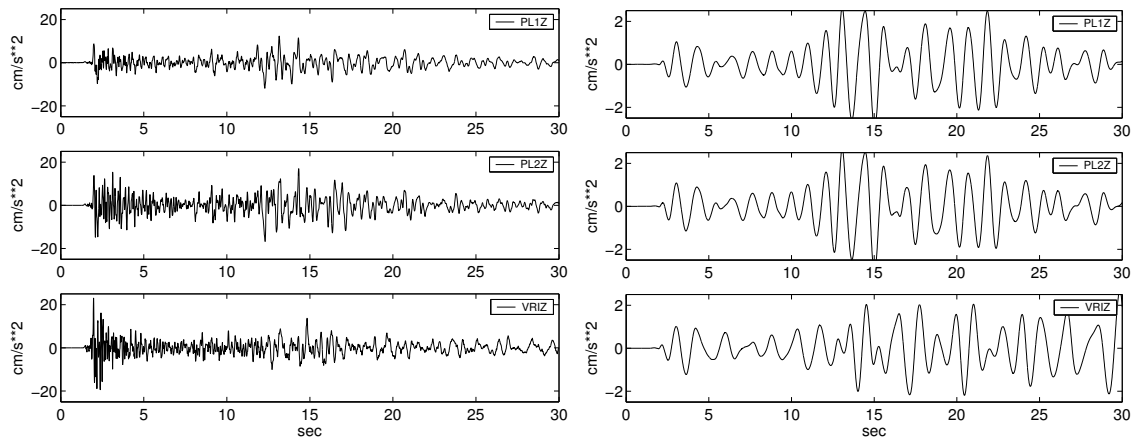


**Figure 5.2:** Vertical components of recorded ground acceleration of the October 27, 2004, Vrancea earthquake ( $M_w = 5.9$ ) at station *PL1* (borehole sensor) and *PL2* in Plostina, and at station *VRI* in Vrancea, from top to bottom. Left: unfiltered records. Right: filtered records after application of a 3<sup>rd</sup> order Butterworth-filter between 1 to 2 seconds. The levels of P-wave amplitudes are almost equal at all three sensors implying the applicability of the same scaling relations to all epicentral sites.

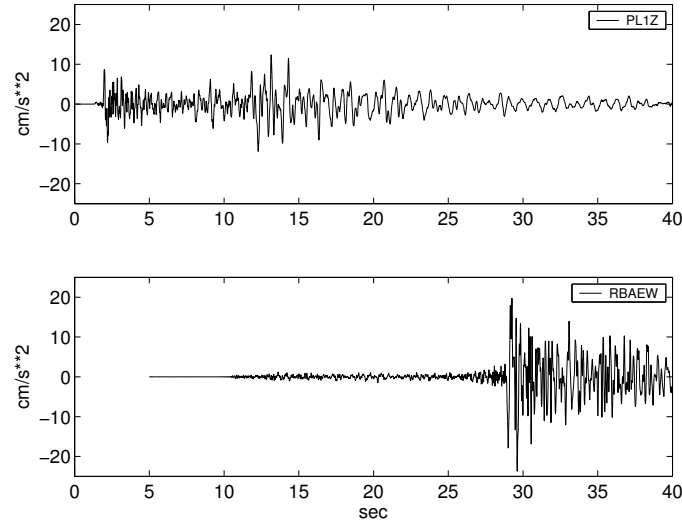


**Figure 5.3:** Vertical component of ground acceleration at epicentral station *PLI* (top) and horizontal component at station *RBA* in Bucharest (bottom) for the October 27, 2004, Vrancea earthquake ( $M_w = 5.9$ ). The maximum warning time for Bucharest is defined by the time window between the arrival of the direct P-wave at the detecting EWS station and the S-wave arrival in Bucharest. The theoretical warning time for Vrancea earthquakes is about 25 seconds.

amplitude spectra of acceleration applying a method proposed by Chernov and Sokolov (1988) as described in Chapter 4.

The underlying scaling relations for  $PGA$ ,  $PGA_{filt}$ ,  $PSA_{0.3s}$ ,  $PSA_{1.0s}$ , and  $PSA_{2.0s}$  are assumed to be given by a logarithmic dependency of form

$$\log IM = a + b \log P_{epi} \pm \sigma, \quad (5.9)$$

and for  $I$  of form

$$I = a + b \log P_{epi} \pm \sigma. \quad (5.10)$$

$P_{epi}$  is the maximum filtered epicentral P-wave amplitude of acceleration on the vertical component (in  $[cm/s^2]$ ),  $IM$  is the ground motion parameter of interest in  $[cm/s^2]$  (for  $PGA$  and  $PSA$ ), referring to the larger value of both horizontal components of acceleration in Bucharest. Coefficients  $a$  and  $b$  are to be determined from the database by regression. The inversion results for  $a$ ,  $b$  and  $\sigma$  are summarized in Table 5.1 and visualized in Figure 5.4; reliabilities of scaling relations are quantified by determination coefficients  $R^2$  (Table 5.1).

Note that for seismic intensity the majority of weak motion events had to be excluded from the database because the method applied for the determination of seismic intensity from the Fourier amplitude spectrum of acceleration is only calibrated for earthquakes with intensities  $I \gtrsim 3.5$  (Chernov and Sokolov, 1988). This leads to a dominance of synthetic records in the database. On the other hand, the *EGF* simulations seem to generally overestimate seismic intensity. This can be clearly seen for the two strong motion SMA-1 events in Figure 5.1: the corresponding intensities are one to two units lower than the average values determined for the entire dataset ( $I_1$ ). I recalculated the scaling relations after excluding all *EGF* synthetics and found a significant lower increase of intensity with P-wave amplitude. The corresponding coefficients for the new scaling relation for seismic intensity  $I_2$  are shown in Tab. 5.1.

Scaling coefficients				
$IM$	a	b	$\sigma$	$R^2$
$PGA_{filt}$	0.6643	0.9929	0.1618	0.98
$PGA$	1.4331	0.6310	0.1508	0.92
$PSA_{0.3s}$	1.5966	0.6286	0.1660	0.89
$PSA_{1.0s}$	1.3889	0.9696	0.1469	0.96
$PSA_{2.0s}$	0.8914	1.0301	0.2025	0.93
$I_1$	6.3375	2.7169	0.4468	0.87
$I_2$	1.6435	5.2626	0.1452	0.92

**Table 5.1:** Coefficients for scaling relations in (5.9) and (5.10) for different ground motion parameters for the Romanian earthquake early warning system.  $\sigma$  is the unit standard deviation,  $R^2$  is determination coefficient.

The revised scaling relation for filtered PGA after (5.9) with coefficients specified in Table 5.1 gives in rearranged form

$$PGA_{filt} \approx 5 \cdot P_{epi}. \quad (5.11)$$

That is, the estimated values are two times smaller than if determined from the relation proposed by Wenzel et al. (1999) (see (5.8)). Note, however, that the uncertainty of the scaling relation (5.11) is of the same order; both relations are therewith not mutually exclusive.

For the validation of the proposed scaling relations, the October 27, 2004, ( $M_w = 5.9$ ) Vrancea earthquake will be used as a test scenario. The maximum filtered P-wave amplitude of the event at station  $VRI$  is  $P_{epi} \approx 1.2 \text{ cm/s}^2$ . Inserting this value into (5.9) and (5.10) with coefficients taken from Table 5.1 allows predicting ground motion in Bucharest in terms of different  $IM$ . Observed levels of ground shaking  $IM_{obs}$  and prognostics  $IM_{est}$  for the scenario earthquake are compared in Table 5.2: in general, the ground motion parameters are well-predicted by the scaling laws, whereby most parameters are slightly overestimated. Considering the 95% confidence intervals to reflect the expected level of scattering in the data, all predictions give satisfying results; that is, ground motion in Bucharest can be well approximated by the given relations. Slight discrepancies are given in case of seismic intensity that is overestimated by one to two units using the first relation ( $I_1$ ), and half to one unit using the second relation ( $I_2$ ).

## 5.4 Discussions

Substantial progress in real-time seismology has been made over the past few years. This holds for improvements in real-time acquisition and communication technologies alike for developments of new seismic processing software: numerous algorithms have been designed to educe information from seismic real-time data - a basic requirement for earthquake early warning systems. The general tendency in the conceptual design and implementation of early warning systems goes towards an extension of warning times and therewith to an expansion of areas that can be effectively warned of approaching seismic waves. While hitherto existing *regional* warning systems have mostly focused on potential users in epicentral distances of some hundreds of kilometers, *on-site* warning systems are supposed to serve a broader user community on local scale. *On-site* systems save warning time by decentralized processing and restriction on information derived from single stations instead of station

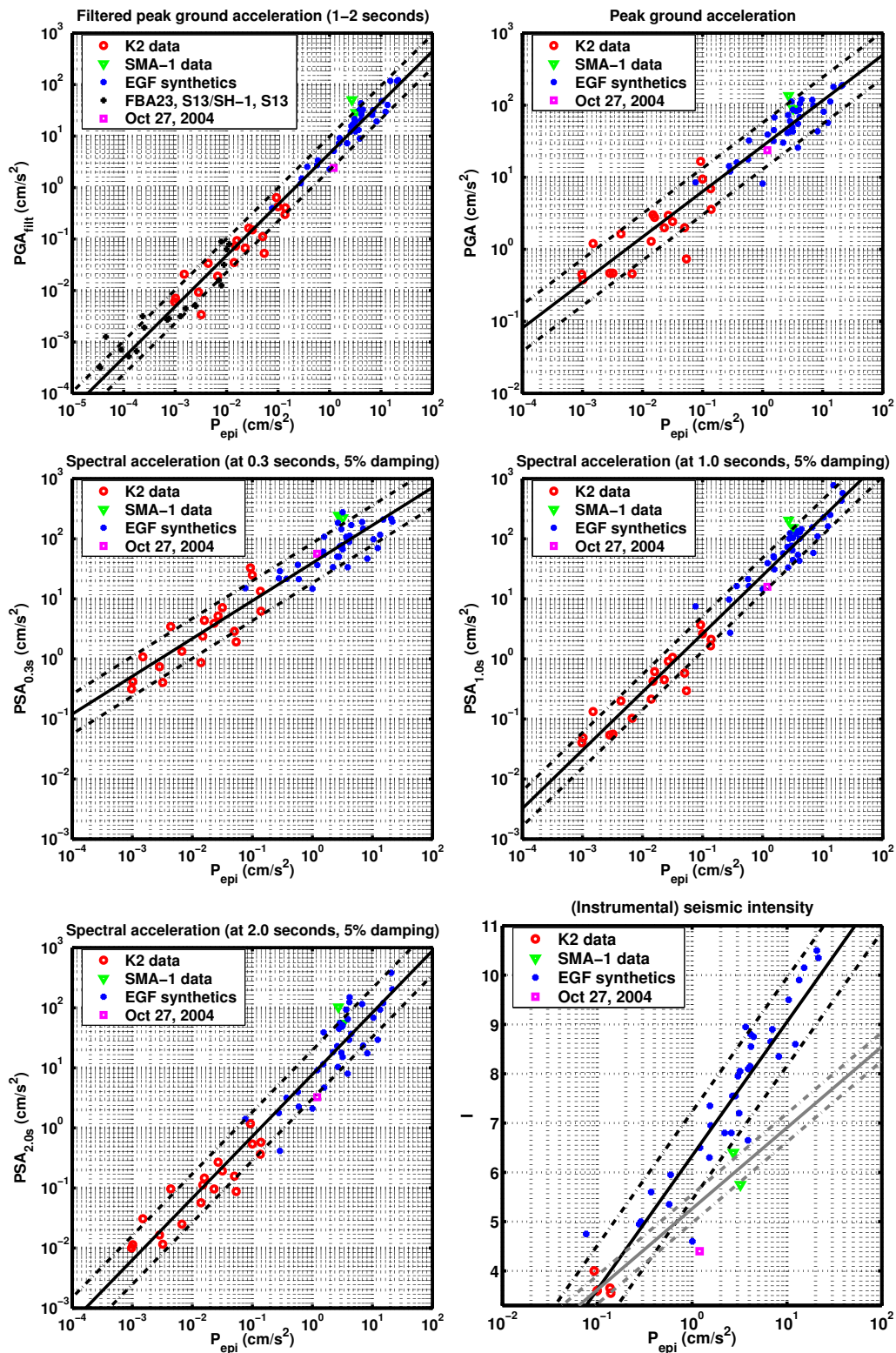


**Figure 5.4:** Correlations between maximum filtered epicentral P-amplitude  $P_{epi}$  and different ground motion parameters in Bucharest : filtered peak ground acceleration ( $PGA_{filt}$ ), peak ground acceleration ( $PGA$ ), spectral response ( $PSA$ ) at 0.3 s, 1.0 s and 2.0 s (5% damping), and instrumental intensity  $I$ . The solid lines show the determined scaling relations, the dashed lines define the 95% confidence intervals. The relations are derived from different datasets as indicated in the legends.

$IM$	$IM_{est}$	$2\sigma$	$IM_{obs}$
$PGA_{filt}$	5.5 ±	2.9	2.4
$PGA$	30.4 ±	15.2	23.7
$PSA_{0.3s}$	44.3 ±	23.7	56.3
$PSA_{1.0s}$	29.2 ±	14.4	15.8
$PSA_{2.0s}$	9.4 ±	5.7	3.2
$I_1$	6.6 ±	0.9	4.4
$I_2$	5.4 ±	0.3	4.4

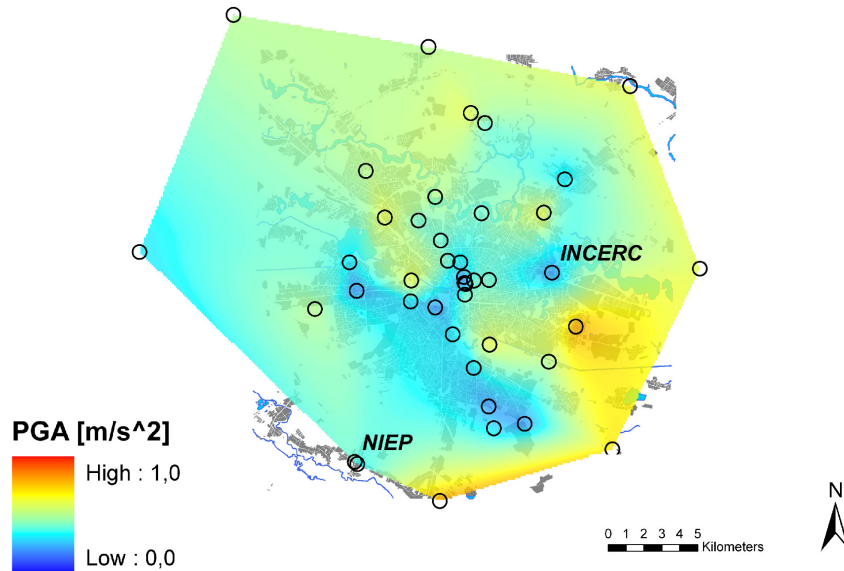
**Table 5.2:** Validation of scaling relations by usage of the Oct. 27, 2004 Vrancea earthquake ( $M_w = 5.9$ );  $IM_{est}$  are estimated values of ground shaking,  $IM_{obs}$  observed values (in [ $cm/s^2$ ]). Using 95% confidence intervals - approximated by  $2\sigma$  - almost all parameters are well predicted; intensity is overestimated by both intensity relations  $I_1$  and  $I_2$ .

networks; generally, only the initial parts of the seismic signals - the P-waves - are analyzed. Despite of their rapidness, the scattering of estimations using single stations can be extremely high; frequently, the uncertainties can be only balanced by averaging over estimates of a fairly high number of stations (e.g., Lockman and Allen, 2005); this procedure, however, is clearly in conflict with the initial idea behind *on-site* warnings.

The favorable geometry of the seismogenetic Vrancea zone in the SE-Carpathians and Bucharest allows for the design of a simple and robust earthquake front-detection warning system for the Romanian capital with a stable warning time of about 25 seconds. In this chapter, I have established scaling relations for six commonly used ground motion parameters with associated uncertainties for the prediction of ground motion that Bucharest will experience. The relations are validated by the usage of the October 27, 2004 Vrancea earthquake ( $M_w = 5.9$ ) as a test scenario. All relations give satisfying estimates of the level of ground shaking based on information of the epicentral P-wave amplitude. For the discrimination of intermediate-depth Vrancea earthquakes and local crustal events, as well as for the avoidance of accidental triggerings, redundancy is essential for the early warning system. The planned integration of further stations, such as of *MLR* in Montuele-Rosu (Figure 5.1), will increase the desired reliability of the system in future. Figure 5.5 demonstrates the feasibility to link the output of the Romanian earthquake early warning system (here: the estimated PGA value at station INC for the October 27, 2004 ( $M_w = 5.9$ ) Vrancea earthquake) to the *Urban Shakemap Methodology for Bucharest* proposed by Wirth (2004) and Bartlakowski et al. (2006). The shake maps at the bottom in Figure 5.5 are predicted from the estimated PGA values at stations INC (mean, mean-2 std) by scaling relations developed for early warning in this thesis (see Table 5.2) and ground motion ratios at phantom sites determined by Wirth (2004) and Bartlakowski et al. (2006). For the center of Bucharest there is a good fit with the shake map determined from observational data and phantom sites (top) while there is a strong overestimation to the west. Note, however, that in this area phantom sites are very sparse and uncertainties in ground motion ratios therewith very high.



## Shakemap Bucharest, October 27, 2004, $M_w=5.9$ Observational and Phantom Sites



## Estimated from Early Warning System

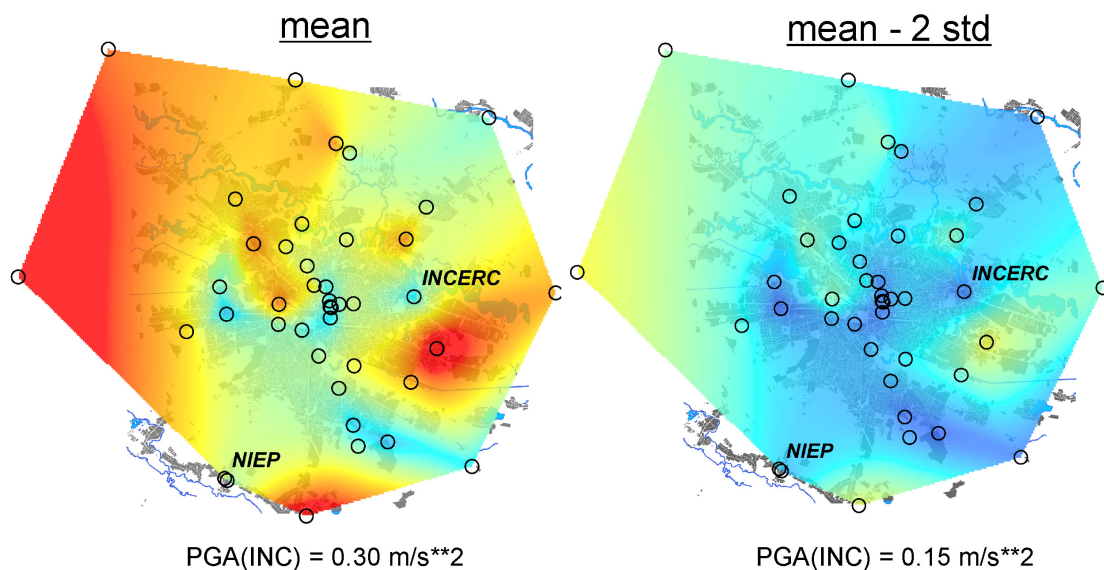


**Figure 5.5:** Linking the output of the Romanian Earthquake Early warning system to the *Urban Shakemap Methodology for Bucharest* for the October 27, 2004 ( $M_w = 5.9$ ) Vrancea earthquake. Shown are shake maps for peak ground acceleration (PGA). Top: Urban Shakemap interpolated from 11 observational and 31 phantom sites (circles) using a method proposed by Wirth (2004) and Bartlakowski et al. (2006). Bottom: Shake maps predicted from the estimated level of ground shaking at station INCERC as output of the Early Warning System and ground motion ratios at the phantom sites relative to INCERC. Shake maps are calculated from the mean estimated PGA value at INCERC ( $0.30 \text{ m/s}^2$ , left) and the mean value minus the double standard deviation ( $0.15 \text{ m/s}^2$ , right). These maps can be made available around 25 s before seismic waves arrive in Bucharest. There is a good fit of shake maps for the center of Bucharest while PGA is strongly overestimated to the west.



## Chapter 6

# PreSEIS: Earthquake Early Warning through Artificial Neural Networks

Earthquake early warning systems generally follow either the *regional* or the *on-site* warning paradigm (Chapter 5.1). The former require dense networks of seismic sensors with real-time communication link to a central processing unit, whereas the latter systems are single station based and therewith much faster at the expense of robustness.

In this chapter I will develop a methodology for earthquake early warning that takes advantage of both, regional and on-site warning strategies: PreSEIS (Pre-SEISmic shaking) combines information derived from seismic observations at several sites without requiring that earthquake waves have reached all sensors before warnings are issued. Even non-triggered stations provide important information on likely source locations of earthquakes as they confine the space of possible solutions. PreSEIS issues estimates on source locations, magnitudes and rupture expansions only 0.5 s after P-wave detection at the first seismic sensor. With ongoing time longer time series of ground motion at more and more stations become available and allow to infer improved details on the earthquake; consequently, estimates of seismic source parameters are continuously updated in the PreSEIS methodology. This is in particular important in case of highly complex rupture histories with inhomogeneous slip distributions. The PreSEIS methodology is as fast as the on-site warning method at a concurrent higher stability due to a larger number of involved stations. The link between time-dependent input information at the different sensors and predicted source parameters is established by so-called *Artificial Neural Networks* (ANNs). The first part of this chapter will focus on the general architecture of ANNs and suitable learning algorithms. The second part will describe the PreSEIS methodology developed in this thesis. The required database is provided by the simulated earthquake time series presented in Chapter 3.3.

### 6.1 Artificial Neural Networks (ANNs)

Artificial Neural Networks (ANNs) are used as statistical models of systems and processes with a large variety of applications. Their massively parallel structure with a high number of simple interconnected processing units - the so-called *neurons* - allows the ANNs to be used for complex, linear as well as non-linear input-output mappings. Each neuron works autonomously on local information in signals received from other neurons. The importance of a link between one processing unit to another is

controlled by a *weight* parameter. *Weights* are iteratively adapted by learning from a set of example patterns through appropriate *training algorithms* (see Chapter 6.1.2). Training iterations are called *epochs*.

The tuning of free parameters is always a balancing of the trade-off between network *accuracy* and *generalization capability* (see Chapter 6.1.5). Once training is accomplished, ANNs are capable to process unknown data that follows the same statistical process as the training examples. In comparison to procedures of conventional computations, ANNs have the advantage that they do not need formulations of explicit algorithms or rules (*if-then* structures) that often cannot be provided. It is not necessary to make prior assumptions on the statistical model of the input data. In summary, ANNs are non-linear mapping functions with a high capability to generalize and a high tolerance to noisy input data (Swingler, 1996).

ANNs are mostly applied for classification, that is for discrete mapping, or for tasks requiring continuous mapping, such as functional approximations. They are typically applied in signal processing, e.g., as neural filters, for time series prediction, or process modeling and management, such as the control of robotic systems (Swingler, 1996). In geophysics, ANNs are mainly applied in exploration seismology and reservoir characterization. Examples are given in Sandham and Leggett (2003).

In the following subsections, I will give an overview of ANNs and different learning algorithms with special attention to so-called *Multi-Layer Neural Networks* that will be applied within the PreSEIS method. Derivations will mainly follow Bishop (1995), Rojas (1993), Swingler (1996), and Zell (1994), as well as references given in the text.

### 6.1.1 General Architecture of Artificial Neural Networks

Artificial Neural Networks are inspired by biological neural systems like the mammalian brain. Alike their biological counterpart, the main characteristic of ANNs is their massive parallelism. Yet biological systems are much more complex than ANNs: the human brain, e.g., consists of more than 100 billions ( $10^{11}$ ) neural cells while the most generous ANNs consist of  $10^2$  to  $10^4$  neurons.

Artificial Neural Networks are composed of (Zell, 1994)

1. *neurons* (neural cells, units); at time  $t$  each neuron  $j$  is associated with
  - a *state of activation*  $z_j(t)$ ;
  - an *activation function*  $g(\cdot)$  that determines the relation between a new state of activation of the neuron  $z_j(t+1)$ , its previous state  $z_j(t)$ , a net *input*  $a_j(t)$ , and some *threshold* (*bias*)  $\theta_j$ , i.e.  $z_j(t+1) = g(z_j(t), a_j(t), \theta_j)$ ;  $g(\cdot)$  is usually a non-linear *sigmoid function* (logistic function or hyperbolic tangent, see Figure 6.1, top);
  - an *output function*  $f(\cdot)$  that describes the dependency of cell *output*  $y_j(t)$  on the activation state  $z_j(t)$ , i.e.  $y_j(t) = f(z_j(t))$ ;  $f(\cdot)$  is generally the *identity function*, i.e.  $y_j(t) = z_j(t)$ ;
2. a *network of connections* between different neurons associated with certain *weights*  $w_{ji}$ ; depending on the direction of the flow of information one distinguishes between *feed-forward* and *feed-back networks*;
3. a *propagation function* that defines the computation of net *input*  $a_j$  from *outputs* of previous neurons and *weights*;

4. a *learning rule* that determines the iterative update of weights during Neural Network training; learning paradigms include *supervised*, *reinforcement* and *unsupervised learning* rules.

### 6.1.2 Teaching Artificial Neural Networks: Parameter Optimization Algorithms

The aim of *supervised* teaching (or training) of Artificial Neural Networks is the minimization of the error  $E$  between observed network outputs  $\mathbf{y}^n$  and target values  $\mathbf{t}^n$  for a given input vector  $\mathbf{x}^n$  in the training set  $\{\mathbf{x}^n, \mathbf{t}^n \mid n = 1, 2, \dots, N\}$ , i.e. the determination of the set of weights  $\mathbf{w}^* = (w_1^*, \dots, w_d^*)$  at which

$$\nabla E|_{\mathbf{w}^*} = \left( \frac{\partial E}{\partial w_1}, \dots, \frac{\partial E}{\partial w_d} \right)^T |_{\mathbf{w}^*} = \mathbf{0}. \quad (6.1)$$

Typically,  $E = E(\mathbf{w})$  is a highly non-linear *error* or *cost function* in weight space with a global and several local minima.

One of the simplest algorithms for the optimization of network parameters is *Gradient* or *Steepest Descent*. This algorithm starts with some initial guess of the weight vector  $\mathbf{w}^{(\tau=0)}$  that is iteratively updated by a factor  $\Delta \mathbf{w}$  by moving at each training step  $\tau$  a certain distance  $\eta$  in the direction of largest decrease of the error function  $E(\mathbf{w})$ , i.e. following the negative gradient  $\nabla E$  at  $\mathbf{w}^{(\tau)}$ :

$$\Delta \mathbf{w}^{(\tau)} = \mathbf{w}^{(\tau+1)} - \mathbf{w}^{(\tau)} = -\eta \nabla E|_{\mathbf{w}^{(\tau)}}. \quad (6.2)$$

Because  $E(\mathbf{w})$  refers to the entire dataset of training patterns, (6.2) is called *batch* version of *Gradient Descent*, whereas in the *online* version of the algorithm the gradient is evaluated for only one pattern at a time and weights are updated using

$$\Delta \mathbf{w}^{(\tau)} = -\eta \nabla E^n|_{\mathbf{w}^{(\tau)}}, \text{ with } E = \sum_{n=1}^N E^n. \quad (6.3)$$

The *learning rate*  $\eta$  controls the speed of learning: if  $\eta$  is very small then the search for  $\mathbf{w}^*$  will proceed extremely slowly and computational times become very long. If  $\eta$ , on the other hand, is inappropriately large then the algorithm might overshoot the wanted minimum in the error function.

Several modifications of *Gradient Descent* have been developed to reduce this problem. One of these methods makes use of an additional *momentum term*  $\mu$  that is included into the primary *Gradient Descent* rule in (6.2):

$$\Delta \mathbf{w}^{(\tau)} = -\eta \nabla E|_{\mathbf{w}^{(\tau)}} + \mu \Delta \mathbf{w}^{(\tau-1)}, \quad (6.4)$$

with  $0 \leq \mu \leq 1$  (Plaut et al., 1986). For error surfaces with little curvature  $\mu$  reduces the *effective learning rate*. Conversely, if the error function shows a high curvature the pure *Gradient Descent* algorithm is oscillatory; successive contributions from  $\mu$  will tend to cancel, and the effective learning rate is close to  $\eta$  (Bishop, 1995). The introduction of a momentum term generally improves *Gradient Descent* though at the expense of a second parameter  $\mu$  that has to be specified aside from learning rate  $\eta$ .

In addition to *Gradient Descent with Momentum Term*, I will test two further parameter optimization algorithms in PreSEIS: *Resilient Propagation* and the *Levenberg-Marquardt* algorithm. *Resilient Propagation (RPROP)* (Riedmiller and Braun, 1993) is a so-called *adaptive* learning algorithm that allows for the adaption of parameters *during* learning, controlled by the observed behavior of the error

function. Unlike other adaptive learning algorithms, *RPROP* thereby does not consider the size of the partial derivatives  $\partial E/\partial w_i$  but only their signs: oscillating signs indicate that the last update of the learning rate was too large and the algorithm has jumped over the minimum. *RPROP* then decreases the update value  $\Delta w_i$  by a certain factor. Stable signs of the partial derivative, on the other hand, indicate little curvature of the local error surface and the update value will be increased.

*Second order methods* make use of information on the shape of the error function  $E(\mathbf{w})$ . The Taylor expansion of  $E(\mathbf{w})$  around some point  $\hat{\mathbf{w}}$  in weight space is given by

$$E(\mathbf{w}) = E(\hat{\mathbf{w}}) + (\mathbf{w} - \hat{\mathbf{w}})^T \nabla E|_{\hat{\mathbf{w}}} + \frac{1}{2} (\mathbf{w} - \hat{\mathbf{w}})^T \mathbf{H}|_{\hat{\mathbf{w}}} (\mathbf{w} - \hat{\mathbf{w}}) + \dots \quad (6.5)$$

where the Hessian matrix  $\mathbf{H}$  at  $\hat{\mathbf{w}}$  is defined by

$$\mathbf{H}|_{\hat{\mathbf{w}}} \equiv \frac{\partial^2 E}{\partial w_i \partial w_j} |_{\hat{\mathbf{w}}}. \quad (6.6)$$

The local approximation of the gradient of  $E$  in (6.5) at point  $\hat{\mathbf{w}}$  is

$$\nabla E = \nabla E|_{\hat{\mathbf{w}}} + \mathbf{H}|_{\hat{\mathbf{w}}} (\mathbf{w} - \hat{\mathbf{w}}). \quad (6.7)$$

*Newton's Method* determines the desired weight vector  $\mathbf{w}^*$  from

$$\mathbf{w}^* = \mathbf{w} - \mathbf{H}^{-1} \nabla E. \quad (6.8)$$

For a quadratic error surface the so-called *Newton Step*  $\mathbf{H}^{-1} \nabla E$ , evaluated at any  $\mathbf{w}$ , points directly at the minimum. As the quadratic approximation is generally not exact, it is necessary to apply (6.8) iteratively and to re-evaluate the Hessian  $\mathbf{H}$  at each new search point. This, however, is in praxis extremely time consuming. *Quasi-Newton Methods* try to overcome this problem by building up an approximation to the inverse Hessian over several iterations (e.g., Bishop, 1995).

The *Levenberg-Marquardt* algorithm (Levenberg, 1944; Marquardt, 1963), that - as said before - will be tested in PreSEIS, combines *Steepest Descent* with *Newton's Method*. The algorithm has been developed specifically for minimizing the sum-of-squares errors (SSE)

$$E_{sse}(\mathbf{w}) = E(\mathbf{w}) = \sum_{n=1}^N E^n(\mathbf{w}), \text{ with } E^n(\mathbf{w}) = \sum_{k=1}^K (t_k^n - y_k^n(\mathbf{x}^n))^2. \quad (6.9)$$

Using the SSE function has the advantage that the Hessian can be estimated from the gradients (Bishop, 1995):

$$(\mathbf{H})_{ik} = \frac{\partial^2 E}{\partial w_i \partial w_k} = \sum_n \left( \frac{\partial E^n}{\partial w_i} \frac{\partial E^n}{\partial w_k} + E^n \frac{\partial^2 E^n}{\partial w_i \partial w_k} \right) \quad (6.10)$$

$$\approx \sum_n \left( \frac{\partial E^n}{\partial w_i} \frac{\partial E^n}{\partial w_k} \right), \quad (6.11)$$

i.e. the Hessian matrix  $\mathbf{H}$  can be approximated by

$$\mathbf{H} \approx \mathbf{Z}^T \mathbf{Z}, \text{ with } (\mathbf{Z})_{ni} \equiv \frac{\partial E^n}{\partial w_i}. \quad (6.12)$$

For a linear network (6.12) is exact, otherwise it is an approximation of the true matrix. The *Levenberg-Marquardt* algorithm makes use of the following update rule

$$\Delta \mathbf{w}^{(\tau)} = \mathbf{w}^{(\tau+1)} - \mathbf{w}^{(\tau)} = - \left[ \mathbf{Z}^T \mathbf{Z} + \lambda \mathbf{I} \right]^{-1} \mathbf{Z}^T E \left( \mathbf{w}^{(\tau)} \right). \quad (6.13)$$

For small  $\lambda$  (6.13) is equivalent to *Newton's Method* using the approximated Hessian matrix in (6.12). For large  $\lambda$ , on the other hand, (6.13) becomes *Gradient Descent* with a small step size. Because *Newton's Method* is faster and more accurate close to the error minimum, the shift towards *Newton's Method* should favorably occur as soon as possible. This means,  $\lambda$  should be decreased after each successful step at that the error is reduced, and increased when a step would increase the error. Details on the different optimization algorithms are given, e.g., in Bishop (1995).

### 6.1.3 Multi-Layer Feed-Forward (MLFF) Neural Networks

The most commonly applied class of ANNs are the so-called *Multi-Layer Feed-Forward* (MLFF) Neural Networks. MLFF are composed of two or more layers of neurons, whereby each neuron is connected to all neurons in the subsequent layer. Layers that do not give the total output of the network are called *hidden* layers. MLFF provide a general framework for the representation of non-linear functional mappings between a set of input and output variables (Bishop, 1995). Because *Two-Layer Feed-Forward* networks have no feed-back loops, outputs can be calculated as explicit functions of input values and weight parameters.

In the following, I will describe the main processing steps within a *Two-Layer Feed-Forward*<sup>1</sup> Neural Network as illustrated in Figure 6.1, bottom: the network is assumed to be composed of  $I$  input,  $J$  hidden, and  $K$  output units. The input  $a_j$  of the  $j$ th hidden neuron ( $j = 1, 2, \dots, J$ ) is given by a linear combination of input values  $x_i$  with weights  $w_{ji}^{(1)}$  in the first layer ( $i = 1, 2, \dots, I$ )

$$a_j = \sum_{i=1}^I w_{ji}^{(1)} x_i + w_{j0}^{(1)} = \sum_{i=0}^I w_{ji}^{(1)} x_i, \quad (6.14)$$

whereby  $x_0 = 1$ . Parameter  $w_{j0}^{(1)}$  is called *threshold* or *bias* and is equivalent to  $\theta_j$  introduced in Chapter 6.1.1.

The activation  $z_j$  of neuron  $j$  is obtained by the application of an *activation function*  $g(\cdot)$  to (6.14), i.e.

$$z_j = g(a_j) = g \left( \sum_{i=0}^I w_{ji}^{(1)} x_i \right). \quad (6.15)$$

A commonly used activation function  $g(\cdot)$  is the *logistic function* defined by

$$g(x) \equiv \frac{1}{1 + \exp(-x)}. \quad (6.16)$$

Other activation functions are the hyperbolic tangent or the linear (identity) functions (Figure 6.1, top). Note that the activation in (6.15) is independent of previous activation states, unlike in the general formulation in Chapter 6.1.1.

<sup>1</sup>Since there is no processing of data in the input units, the input layer is generally not numbered.

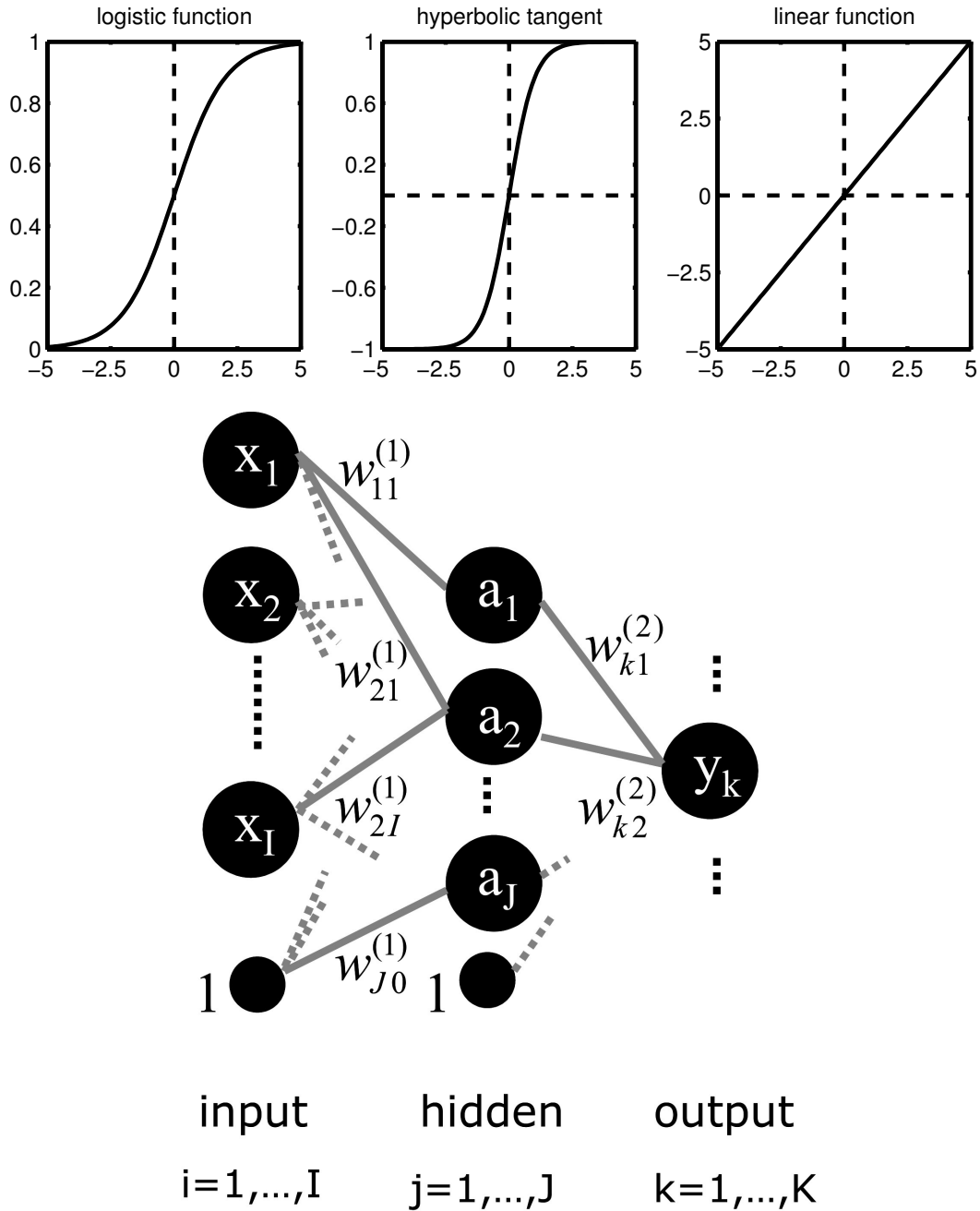


**Figure 6.1:** Top: From left to right logistic, hyperbolic and linear activation functions commonly used in Multi-Layer Feed-Forward Neural Networks. Bottom: Scheme of a Two-Layer Feed-Forward Neural Network composed of one input, one hidden and one output layer.



For each output unit  $k$  ( $k = 1, 2, \dots, K$ ), input  $a_k$  is calculated from linear combinations of outputs of neurons in the hidden layer with weights  $w_{kj}^{(2)}$ , i.e.

$$a_k = \sum_{j=1}^J w_{kj}^{(2)} z_j + w_{k0}^{(2)} = \sum_{j=0}^J w_{kj}^{(2)} z_j, \quad (6.17)$$

with  $z_0 = 1$  and threshold parameter  $w_{k0}^{(2)}$ . The activation and output<sup>2</sup>  $y_k$  of the  $k$ th output unit is obtained by application of a second activation function  $\tilde{g}(\cdot)$  to (6.17)

$$y_k = \tilde{g}(a_k) = \tilde{g}\left(\sum_{j=0}^J w_{kj}^{(2)} z_j\right). \quad (6.18)$$

Hidden and output units play different roles within the network and might require different activation functions (Bishop, 1995). While the most common activation function applied to the hidden layer to encompass non-linear behavior of the network is the sigmoid logistic activation function, the activation function applied to the output units is mostly linear for functional approximations and non-linear for classifications.

Inserting (6.15) into (6.18) gives the complete transfer function of the Two-Layer Feed-Forward Neural Network with

$$y_k = \tilde{g}\left(\sum_{j=0}^J w_{kj}^{(2)} g\left(\sum_{i=0}^I w_{ji}^{(1)} x_i\right)\right). \quad (6.19)$$

Networks with only two layers of processing units are capable to approximate any continuous non-linear function (Bishop, 1995). The principle processing steps of a Two-Layer Feed-Forward Neural Network with two input, two hidden and one output neuron are summarized in Figure 6.2.

#### 6.1.4 Teaching MLFF Networks: The Backpropagation Algorithm

Learning algorithms as discussed in Chapter 6.1.2 cannot be used to determine the weights  $w_{ji}^{(1)}$  between input and hidden layer of MLFF networks because there is no procedure for assigning target values to their outputs (*credit assignment problem*). A simple way to solve this problem is the usage of the *Backpropagation* algorithm (Rumelhart et al., 1986). In the following, I will demonstrate *Backpropagation for Gradient Descent*. Yet, the algorithm can be applied to any other type of optimization, e.g. to *Resilient Propagation* or *Levenberg-Marquardt*.

For on-line *Steepest Descent* after (6.3) the update rule of network weights at iteration step  $\tau$  is given by

$$\Delta \mathbf{w}^{(\tau)} = -\eta \nabla E^n(\mathbf{w}^{(\tau)}) = -\eta \frac{\partial E^n}{\partial \mathbf{w}} \Big|_{\mathbf{w}^{(\tau)}}, \quad (6.20)$$

i.e. the derivatives of the error function  $E^n$  for pattern  $n$  are determined separately from each other.

Using the input  $a_k$  of output neuron  $k$  given in (6.17), the partial derivatives of  $E^n$  w.r.t. the hidden-to-output weights  $w_{kj}^{(2)}$  are calculated by application of the chain rule:

$$\frac{\partial E^n}{\partial w_{kj}^{(2)}} = \frac{\partial E^n}{\partial a_k} \frac{\partial a_k}{\partial w_{kj}^{(2)}} = -\delta_k \frac{\partial a_k}{\partial w_{kj}^{(2)}}, \quad \text{where } \delta_k \equiv -\frac{\partial E^n}{\partial a_k}. \quad (6.21)$$

<sup>2</sup>It is assumed that output function  $f(\cdot)$  is the *identity function*, see Chapter 6.1.1

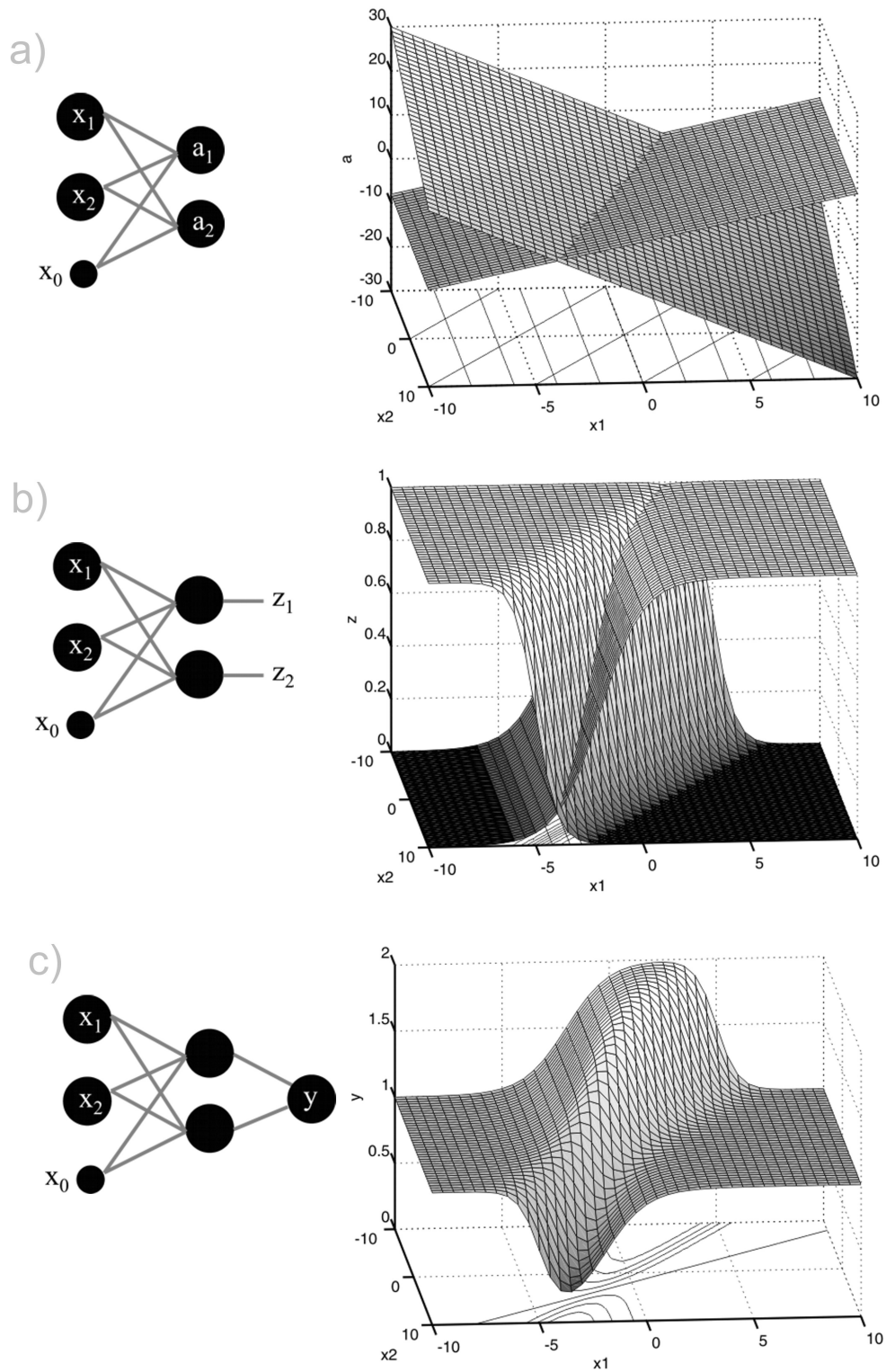


**Figure 6.2:** Processing steps in a Two-Layer Feed-Forward Neural Network with two input, two hidden and one output unit; a) linear combination of input values; b) logistic transformation of the linear combination; c) summation of both logistic functions.

Presuming that the activation function  $\tilde{g}(\cdot)$  is differentiable and the sum-of-squares errors (SSE) function defined in (6.9) is chosen, it follows from (6.18) that

$$\delta_k \equiv -\frac{\partial E^n}{\partial a_k} = -\frac{\partial E^n}{\partial y_k} \frac{\partial y_k}{\partial a_k} = (t_k^n - y_k^n) \tilde{g}'(a_k), \quad (6.22)$$

where  $t_k^n$  is the target and  $y_k^n$  the observed network output.  $\delta_k$  is called *sensitivity* or *error* of output neuron  $k$ . The resulting update rule for hidden-to-output weights  $w_{kj}^{(2)}$  for *Gradient Descent* after (6.20) therewith is

$$\Delta w_{kj}^{(2)} = \eta \delta_k z_j, \text{ with } z_j = \frac{\partial a_k}{\partial w_{kj}^{(2)}}. \quad (6.23)$$

The partial derivatives of  $E^n$  w.r.t. the input-to-hidden weights  $w_{ji}^{(1)}$  are determined by application of the chain rule using (6.15)

$$\frac{\partial E^n}{\partial w_{ji}^{(1)}} = \frac{\partial E^n}{\partial z_j} \frac{\partial z_j}{\partial a_j} \frac{\partial a_j}{\partial w_{ji}^{(1)}}, \quad (6.24)$$

whereby

$$\frac{\partial E^n}{\partial z_j} = \sum_{k=1}^K \frac{\partial E^n}{\partial a_k} \frac{\partial a_k}{\partial z_j} = - \sum_{k=1}^K \delta_k \frac{\partial a_k}{\partial z_j} = - \sum_{k=1}^K \delta_k w_{kj}^{(2)}, \quad (6.25)$$

$$\frac{\partial z_j}{\partial a_j} \frac{\partial a_j}{\partial w_{ji}^{(1)}} = g'(a_j) x_i. \quad (6.26)$$

Analog to (6.22) the *sensitivity* or *error*  $\delta_j$  of hidden neuron  $j$  is defined by

$$\delta_j \equiv -\frac{\partial E^n}{\partial a_j} = g'(a_j) \sum_{k=1}^K w_{kj}^{(2)} \delta_k. \quad (6.27)$$

The resulting update rule for input-to-hidden weights  $w_{ji}^{(1)}$  for *Gradient Descent* after (6.20) therewith is

$$\Delta w_{ji}^{(1)} = \eta g'(a_j) \sum_{k=1}^K w_{kj}^{(2)} \delta_k x_i = \eta \delta_j x_i. \quad (6.28)$$

The evaluations of (6.22) and (6.27) are called *backpropagation of errors*.

Sigmoid activation functions - such as the logistic function - satisfy the requirement of differentiability of the resulting error function. The derivative of the logistic activation function ( $x$ ) defined by (6.16) with respect to argument  $x$  is

$$g'(x) = g(x) (1 - g(x)), \quad (6.29)$$

i.e. is itself a logistic function. Because according to (6.19) Multi-Layer Feed-Forward Neural Networks calculate a sequence of functional compositions, the error function itself becomes continuous and differentiable if a sigmoid activation with these properties is chosen. The smoothing effect of sigmoid activation supports the feasibility of *Gradient Descent*.

### 6.1.5 Accuracy versus Generalization Capability

The objective of Neural Network learning is rather to build a statistical model of the underlying process than to find an exact representation of the training data itself. This leads to a trade-off between *mapping accuracy* and *generalization capability* of Neural Networks. Insight into this trade-off comes from the decomposition of the error into *bias* and *variance* components: the bias is a measure of the averaged difference between target and observed network outputs, while the variance describes the sensitivity of the network function to the particular choice of data (e.g., Bishop, 1995).

A balance between variance and bias is obtained through methods that allow for controlling the *effective complexity* of Neural Networks. Complexity of Two-Layer Feed-Forward Neural Networks is mainly governed by the number of hidden units. In praxis, the available dataset is usually divided into a *training* subset that is used for *model selection*, and two independent *validation* and *test* subsets that are used for the evaluation of network performances *during* and *after* training (*model validation*). The validation data is used to define an *early stopping* criteria that determines the transition at which the network becomes over-fitted to the training data at the expense of generalization capability. At this epoch the iterative update of weight parameters should be stopped. The number of hidden units can be determined from a systematic testing of different network architectures: optimum networks perform well for both, training and test patterns.

The splitting of data into training, validation and test subsets usually occurs on basis of a random selection: in k-fold *cross-validation* the available dataset is divided into k subsets of approximately equal size. The network then is trained k times, at each time omitting one of the subsets from training. In *bootstrapping*, by contrast, the model is tested with randomly determined subsamples omitted from the training set.

## 6.2 PreSEIS: Estimates of Seismic Parameters Pre-SEISmic Shaking

PreSEIS is a methodology for earthquake early warning that is based on Artificial Neural Networks. More strictly speaking, PreSEIS makes use of *Two-Layer Feed-Forward* Neural Networks with processing units arranged in an input, a hidden and an output layer that are interconnected to each other (Chapter 6.1.3). The most important features of PreSEIS are:

- PreSEIS is a *dynamic* method for the inversion for seismic source parameters from time-dependent ground motion measurements at different sensors that are combined within a sensor network. First estimates are available only 0.5 s after P-wave detection at the first sensor - called *triggering* of PreSEIS - with a continuous update of predictions every half second. Within the first few seconds after rupture initiation the P-wave will generally have arrived at a minor subset of sensors in the network, implying that the inversion problem for seismic parameters will be underdetermined. Significant improvement of estimates can be achieved through the integration of information on non-triggered sensors since this allows confining the space of possible solutions as shown, e.g., by Rydelek and Pujol (2004) and Horiuchi et al. (2005). From example patterns in the training database, PreSEIS learns in addition *a priori* information on likely source locations associated with the major faults in the region where PreSEIS is applied. With ongoing time longer time series of ground motion at more and more sensors become available and allow inferring improved information on the earthquake.

- PreSEIS utilizes amplitude information on earthquakes in terms of the cumulative absolute velocity (CAV) for the estimation of earthquake magnitudes. The merit of CAV in comparison to other ground motion parameters has been described in Chapter 4.1.4 and 4.5.
- Seismic ground motion at a specific site can be predicted from the combination of (estimated) magnitudes and source locations with empirical attenuation laws for the given region. Maps visualizing distributions of ground shaking on urban or regional scale are called *shake maps*; if they are calculated from *estimated* magnitudes and source locations these maps are usually called *alert maps*. It is important to note that the level of ground motion thereby is not controlled by hypocentral distances but by the closest distance from a site to the rupture surface. PreSEIS cannot only predict magnitudes and hypocenter locations of earthquakes but also the positions and expansions of evolving ruptures along the faults. From above considerations it follows that the prediction of rupture expansions leads to a significant improvement of *alert maps*. Furthermore, finite faults show dynamic effects such as rupture directivity (see Chapter 2.2.3) that can be more easily integrated into alert maps when rupture locations and expansions are known. A demonstration of the effect of rupture directivity on the distribution of seismic ground motion in term of intensity is given in Figure 6.29.
- Combining *estimated* source parameters with *estimated* empirical attenuation laws rises the problem of joining quantities that are each associated with uncertainties. As Allen (2005) points out, the largest errors in ground motion prediction mostly do not come from incorrectly predicted magnitudes and source locations but from uncertainties in the attenuation laws. To exclude this unstableness, PreSEIS is capable to estimate ground motion directly in terms of the Fourier amplitude spectrum of ground motion at a given site without requiring specifications of attenuation laws. In this case, the ANNs themselves have to learn the specific attenuation characteristics for the given region.

### 6.2.1 Database and Data Pre-Processing

PreSEIS has been developed and tested using a database of 280 stochastically simulated earthquake scenarios in the Marmara region. The database comprises finite-fault earthquakes covering the moment magnitude range from 4.5 to 7.5 with randomized slip distributions and variable source parameters including, e.g., static and dynamic stress drops. Earthquake records have been simulated at the ten online stations of the *Istanbul Earthquake Rapid Response and Early Warning System (IERREWS, Chapter 5.2.5)* and at an additional user site (*UserX*) to the west of Istanbul. A detailed description of the synthetic database is given in Chapter 3.3.

Pre-warning times are a crucial issue in any early warning system. Pre-warning times for earthquakes are generally defined by the time window between P-wave detection by at least one early warning station and the arrival of high-amplitude S- (and surface) waves at a potential user site (see (1.1)). For the constant velocity model with  $\alpha = 5.7$  km/s and  $\beta = 3.3$  km/s used for the stochastic modeling of ground motion records in the Marmara region and for the present station configuration of *IERREWS*, warning times for Istanbul city vary between zero (no warning possible) and thirty seconds with an average pre-warning time of 8 to 15 seconds (Figure 6.3, left). For a potential user at site *UserX* warning times are of the same order (Figure 6.3, right). From Figure 6.4 follows that on average the first sensor detects the P-wave 2.5 s after rupture initiation. Within the first few seconds that are relevant for earthquake early warning - in the Marmara region this is approximately 4.0 s - between

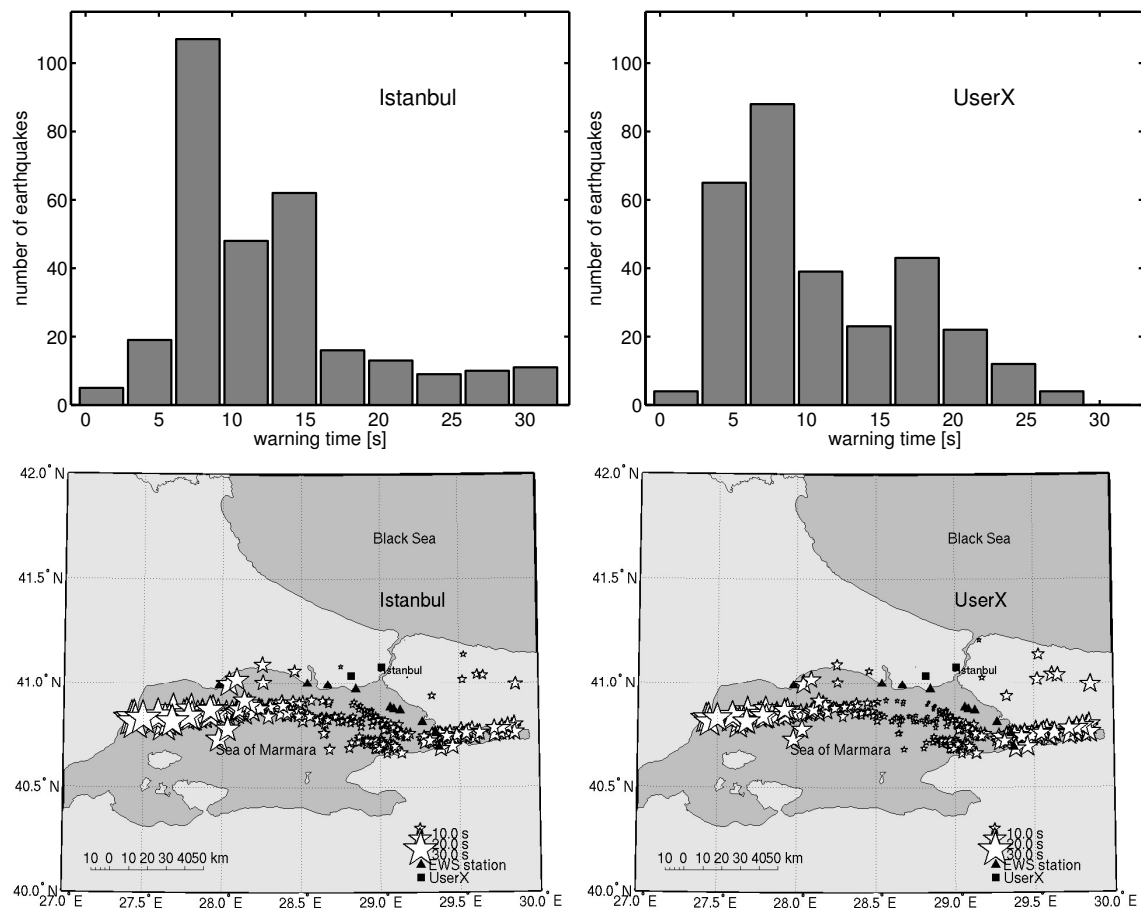


**Figure 6.3:** Pre-warning times for 280 simulated earthquake scenarios (Chapter 3.3) defined by the time window between P-wave arrival at the first early warning station of *IERREWS* and S-wave arrival in Istanbul (left) or at user site *UserX* (right). Pre-warning times range up to 30 s with an average value of 8 to 15 s. The available warning times of course depend on respective source locations as visualized in the maps at the bottom; the markersize of the different earthquake epicenters characterizes the amount of available time for each event.

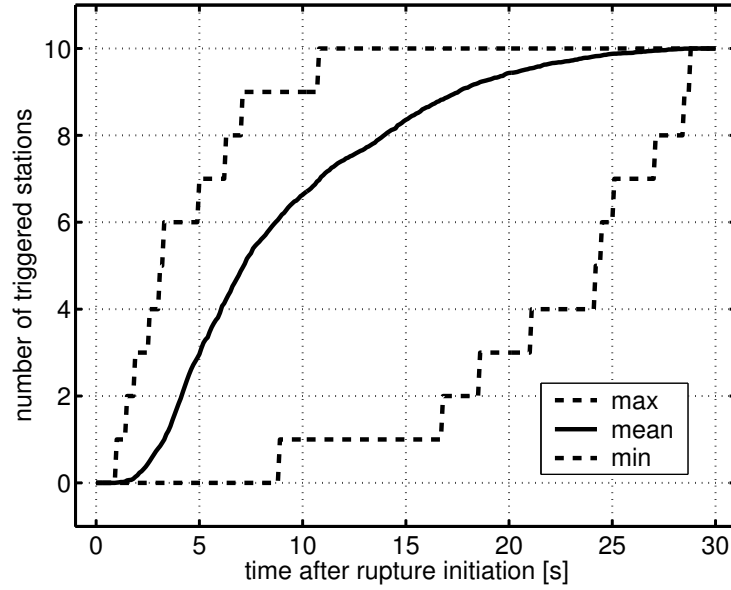


**Figure 6.4:** Number of triggered early warning stations in the Marmara region as a function of time after rupture initiation calculated on basis of the synthetic database in Figure 3.7. Plotted are the average, minimum and maximum number of stations at which the direct P-wave has arrived at each time step after rupture initiation. On average, the P-wave needs 2.5 s to reach the first sensor. Due to the extremely little pre-warning times in the Marmara region (see Figure 6.3) only the first few seconds ( $\approx 4.0$  s) after detection are relevant for earthquake early warning. This means that the P-wave will have arrived at five stations on average.

zero and eight stations will be triggered by the propagating P-wave, with an average value of five stations. Note that all these estimates are based on the distribution of hypocenters of the simulated earthquakes in the database.

Data pre-processing is likely the most difficult and most essential step in neural computations. Following the data processing flow of the *IERREWS* system (Chapter 5.2.5) all records in the database are bandpass-filtered between 0.05 and 12.0 Hz. The filtered acceleration time series are parameterized to extract information on traveltimes differences and amplitudes. These parameter sets will be used as input for the inversion for source parameters, such as hypocenter locations and moment magnitudes.

### 1. (Relative) P-wave arrivals

The first parameter set comprises P-wave arrival times  $t_{i,n}^{trigg}$  at sensor  $i$  for the  $n$ th earthquake.<sup>3</sup> Because earthquake origin times are unknown during real-time operation of the early warning system, only the *relative onset times*  $\Delta t_{i,n}^{trigg} = (t_{i,n}^{trigg} - t_{i_0,n}^{trigg})$  can be quantified;  $t_{i_0,n}^{trigg}$  is the onset time at the first sensor  $i_0$  in the network, i.e.  $t_{i_0,n}^{trigg} \leq t_{i,n}^{trigg}$ . Information on P-wave arrivals at the different sensors will become available only step by step. At a given time  $t_m$ , onset times can of course be only specified for stations at which the P-wave has already arrived, i.e.  $t_m \geq t_{i,n}^{trigg}$ . If - on the other hand - a station is not triggered at time  $t_m$ , it follows that  $t_{i,n}^{trigg} > t_m$ . The known or estimated relative onset times that

<sup>3</sup>A break down of station numbers and names is given in Table 3.3.

are available at time  $t_m$  can be therewith determined from the following relations:

$$\Delta t_{i,m,n}^{trigg} = \begin{cases} t_m & -t_{i_0,n}^{trigg}, t_m < t_{i,n}^{trigg} \\ t_{i,n}^{trigg} & -t_{i_0,n}^{trigg}, t_m \geq t_{i,n}^{trigg} \end{cases}, \quad (6.30)$$

whereby the first equation gives the minimum value of the expected time interval for a non-triggered station at time  $t_m$  relative to sensor  $i_0$ .

Using information that the P-wave has not arrived at certain sensors in the network at time  $t_m$  confines the space of possible source locations as demonstrated in Figure 6.6: in this example it is assumed that information on seismic ground motion is available at two sensors, whereby the first sensor (here: *FARGE*) has detected the P-wave, while the other sensor (here: *TUZ01*) has not. It is presumed that both sensors work properly. In case of a homogeneous velocity distribution it follows that the earthquake hypocenter will be closer to the first sensor than to the second. The boundary between possible and impossible positions is indicated by the hyperbolic curve. With ongoing time the area enclosed by the hyperbola shrinks. The additional *a priori* information on likely source locations derived from the distribution of previous earthquakes (Figure 6.5) - that enters the PreSEIS system in form of the training database for the Artificial Neural Networks - leads to a further confinement of the space of solutions, indicated by the contour lines. As demonstrated for the example in Figure 6.6, the combined information on non-triggered stations and the *a priori* knowledge on fault segments allows for a good prediction of source locations with a clear and fast convergence of estimated (dark point) towards correct solutions (bright star).

Figure 6.7 demonstrates the possible reduction of localization errors as a function of time using information in terms of (6.30) for two (*FARGE*, *TUZ01*), three (*FARGE*, *TUZ01*, *YLVHV*), and four (*FARGE*, *TUZ01*, *YLVHV*, *BUYAD*) stations for all 31 scenario earthquakes shown in Figure 6.5. The location errors are quantified through the 25th, 50th, 75th and the 95th percentiles; the 50th percentile is better known as the *median* that divides the lower half from the higher half of a statistical distribution. The other percentiles can be interpreted in a same way, e.g., 95% of the earthquake scenarios have location errors smaller than indicated by the 95th percentile, while 5% show larger failures. Once again note, that also the information on non-triggered stations enters the predictions. For the analyzed subset of earthquakes in the synthetic database, the average location error can be reduced in the first 3.5 s after triggering from 6.0 km to 2.5 km for two stations, from 3.5 km to 1.5 km for three stations, and from 3.0 km to 1.0 km for four stations.

## 2. Cumulative absolute velocity (CAV)

The second parameter set derived from the synthetic database is the time-dependent cumulative absolute velocity ( $CAV_{i,m,n}$ ) determined from the ground motion times series at sensor  $i$  for earthquake  $n$  at time step  $m$ . The most important characteristics of the CAV have been discussed in Chapter 4.1.4 and 4.5. In order to stress the prominence of the faster (low-amplitude) P-waves in the early warning system, CAV values are logarithmized; this leads to a faster convergence of the parameter to final values taken over the entire record length. Linear and logarithmized CAV values for scenario #25, SEGMENT 2 at the ten online sensors of *IERREWS* are visualized in Figure 6.8 (c.w. Figure 3.10).

Alike the parameter set of P-wave arrival times described above, the CAV is considered as time-dependent parameter. At a non-triggered station the CAV is set to zero [cm/s]; because the logarithm,



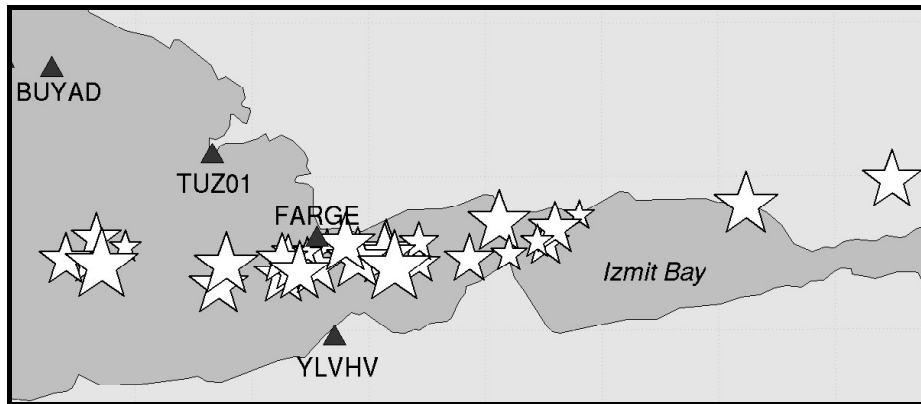


**Figure 6.5:** Subset of simulated earthquake scenarios in the Marmara region. The stars show the distribution of 31 epicenters in the Izmit Bay area. Four *IERREWS* early warning stations (*FARGE*, *TUZ01*, *YLVHV*, and *BUYAD*) are used for first tests on a possible design of PreSEIS. Details are given in the text.

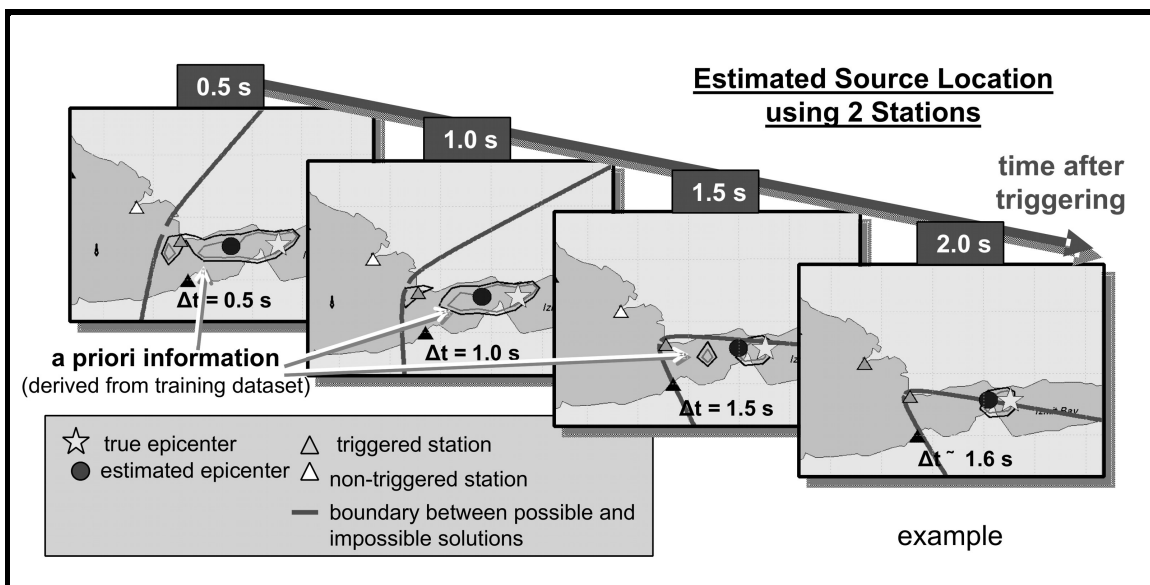


**Figure 6.6:** Using information of non-triggered stations (hyperbolic curve) and *a priori* information on likely source locations (contour lines) confines the space of possible hypocenter positions with ongoing time. The four maps demonstrate the enhancement of estimated source locations by the ANNs and a possible interpretation of their outputs. For the distribution of earthquake epicenters see Figure 6.5.

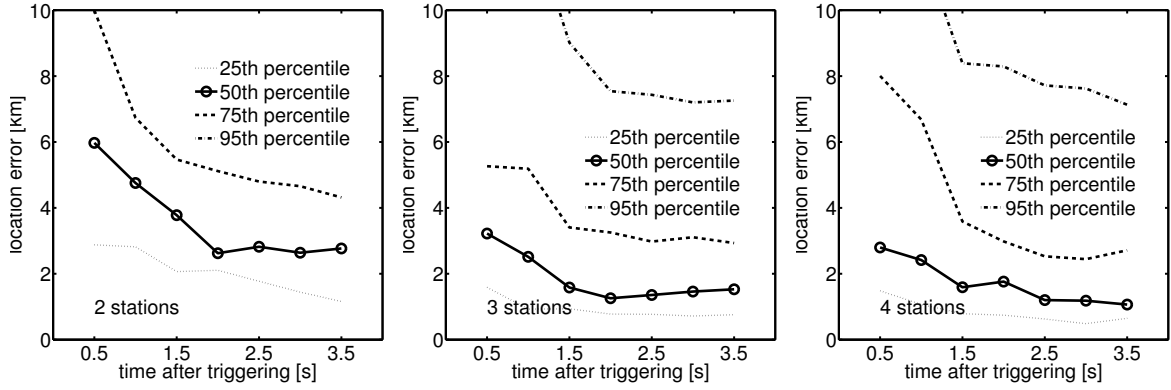


**Figure 6.7:** Reduction of localization errors with time after triggering combining information at two, three and four sensors. The 50th percentile is better known as the *median*. For the distribution of earthquake epicenters see Figure 6.5.

however, is not defined at zero, a constant value of one [cm/s] is added to the velocity sum:

$$\log (CAV_{i,m,n} + 1) = \begin{cases} 0 & , t_m < t_{i,n}^{trigg} \\ \log \left( \int_{t_{i,n}^{trigg}}^{t_m} |a_{i,n}(t)| dt + 1 \right) & , t_m \geq t_{i,n}^{trigg} \end{cases} \quad (6.31)$$

where  $|a_{i,n}(t)|$  is the absolute ground acceleration in [cm/s<sup>2</sup>] at station  $i$  for earthquake  $n$ ;  $dt$  is the sampling interval of the acceleration time series (here:  $dt = 0.02$  s; Chapter 5.2.5).

The increasing reliability of estimated earthquake magnitudes with time after triggering from amplitude information in terms of (6.31) at two (*FARGE*, *TUZ01*), three (*FARGE*, *TUZ01*, *YLVHV*) and four (*FARGE*, *TUZ01*, *YLVHV*, *BUYAD*) sensors is shown in Figure 6.9 using the 31 scenario earthquakes in Figure 6.5. There is a very clear enhancement of reliability of estimates with ongoing time from 0.5 to 3.5 s and with the number of involved stations quantified through the correlation coefficient  $R$  and the unit standard deviation  $\sigma$ . While the prediction at 0.5 s after triggering of the first sensor - based on information from two stations - is fairly poor ( $R=0.35$ ), it can be significantly improved if one ( $R=0.64$ ) or two further stations ( $R=0.77$ ) are involved. At 3.5 s after triggering prediction results are very satisfying using two ( $R=0.65$ ), three ( $R=0.94$ ) and four stations ( $R=0.96$ ), respectively. Note from the histograms in Figure 6.10 that also information of non-triggered stations is used.

## 6.2.2 Design of the Artificial Neural Networks in PreSEIS

Using the available input information at the early warning stations of *IERREWS* at each time step  $m$ , PreSEIS is capable to estimate

1. the earthquake hypocenter location characterized by the geographical latitude  $\varphi^{hypo}$  [°], the geographical longitude  $\lambda^{hypo}$  [°], and source depth  $h$  [km],
2. the earthquake (moment) magnitude  $M_w$ ,

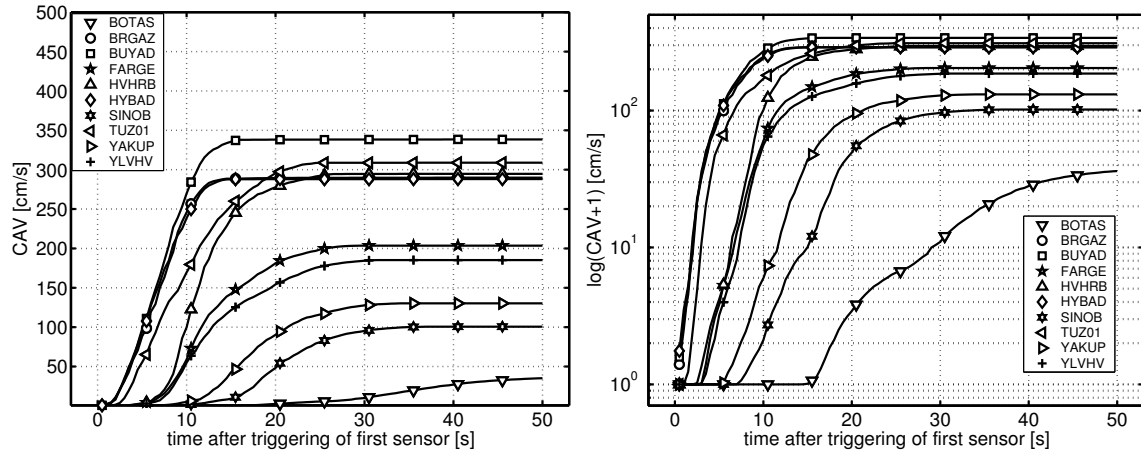


**Figure 6.8:** Linear cumulative absolute velocity (CAV, left) and logarithmized values of CAV (right) calculated from the acceleration time series for earthquake scenario # 25 on SEGMENT 2. Records are displayed in Figure 3.10. Using the logarithmized CAV instead of linear values assigns higher priority to small ground motion amplitudes in the faster P-wave phase in comparison to the S-phase - a favorable characteristic for early warning.

3. the rupture location and expansion characterized by the geographical coordinates of the start and end points of the rupture projected onto the Earth surface,  $\varphi_{start}^{rupt}$  [°],  $\lambda_{start}^{rupt}$  [°],  $\varphi_{end}^{rupt}$  [°],  $\lambda_{end}^{rupt}$  [°], and
4. the smoothed Fourier amplitude spectrum (FAS) of acceleration from 0.25 to 11.25 Hz at site *UserX*.

Each of these four tasks is solved by a Two-Layer Feed-Forward Neural Network with a certain design, named *Hypo*, *M<sub>w</sub>*, *Rupt* and *Spec*. The Neural Networks are trained on data that is available at time steps between 0.5 and 15.0 s after triggering with intervals of 0.5 s. This means that for each task PreSEIS makes use of 30 subnetworks, that are identified through index  $m = 1, \dots, 30$ . In the following, I will discuss at first the general design *Net(m)* that is common for *Hypo(m)*, *M<sub>w</sub>(m)*, *Rupt(m)* and *Spec(m)*; the second part of the subsection will focus on the specifics of each of the networks and discuss their interconnections; this is because inputs and outputs of the different nets are of course not independent from each other.

### I. General Design of *Net(m)*

Following the general design description of a Two-Layer Feed-Forward Neural Network in Chapter 6.1.3, *Net(m)* is built up by neurons arranged in one input layer ( $i = 0, \dots, I^{net}$ ), one hidden layer ( $j = 0, \dots, J^{net}$ ), and one output layer ( $k = 1, \dots, K^{net}$ ) as shown in Figure 6.11. The argument  $m$  indicates that the network operates only on data that is available at time step  $m$ .

The vector of *unscaled input* information  $\mathbf{X}_{m,n}^{net}$  that is available for earthquake  $n$  ( $n = 1, \dots, N^{set}$ ) at time step  $m$  ( $m = 1, \dots, M$ ) is

$$\mathbf{X}_{m,n}^{net} = \{x_{0,m,n}^{net}, x_{1,m,n}^{net}, x_{2,m,n}^{net}, \dots, x_{I^{net},m,n}^{net}\}, \quad (6.32)$$

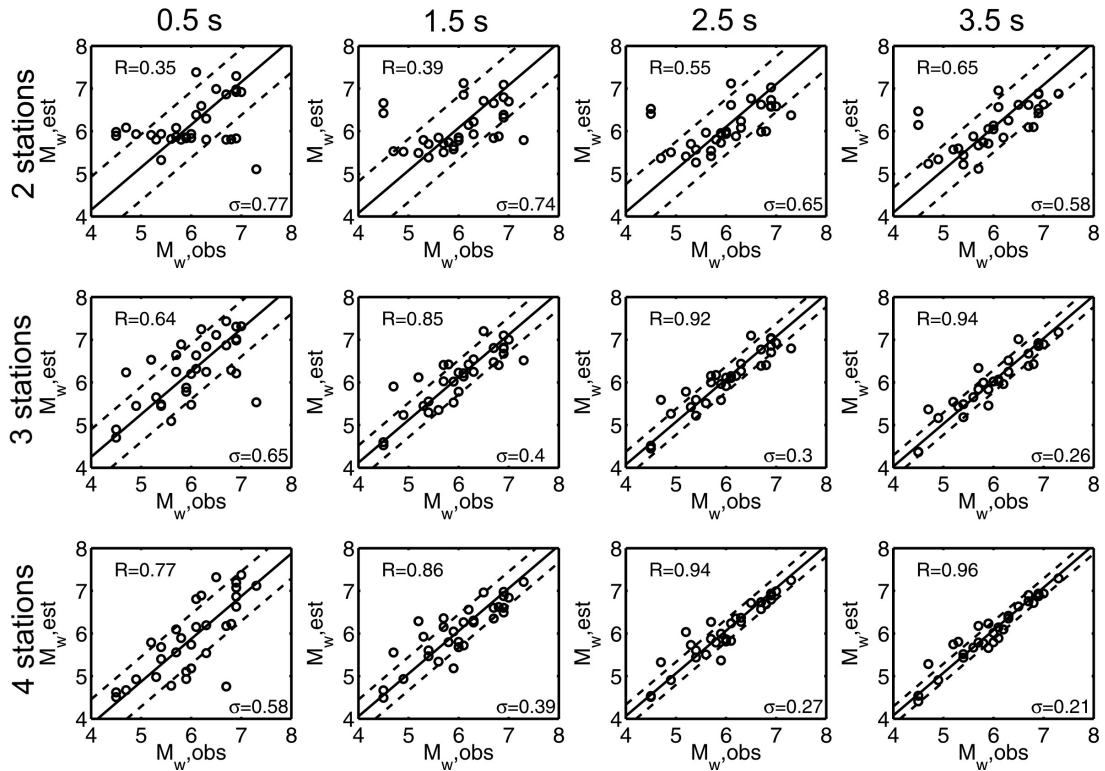


**Figure 6.9:** Accuracies of predicted magnitudes 0.5, 1.5, 2.5, and 3.5 s after triggering of the first sensor (from left to right) using information on CAV measurements at two (*FARGE*, *TUZ01*), three (*FARGE*, *TUZ01*, *YLVHV*) and four (*FARGE*, *TUZ01*, *YLVHV*, *BUYAD*) stations (from top to bottom). The distribution of epicenters of the 31 analyzed earthquakes is shown in Figure 6.5.  $M_{w,obs}$  is the observed,  $M_{w,est}$  the moment magnitude estimated by the ANNs. There is a very clear enhancement of estimates with ongoing time and the number of involved stations quantified through correlation coefficient  $R$  and unit standard deviation  $\sigma$ . Note from Figure 6.10 that also information on non-triggered stations is used.

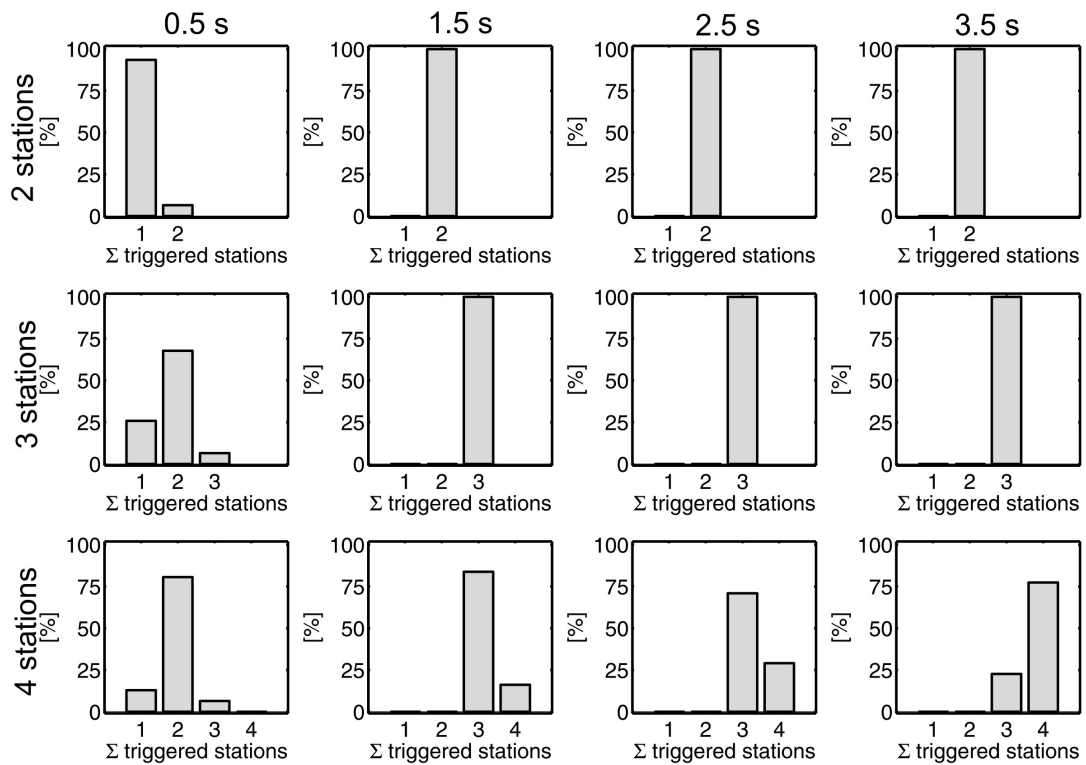


**Figure 6.10:** Histograms showing the number of triggered stations at different time steps (from left to right) for two, three and four sensors (from top to bottom). See Figure 6.9.

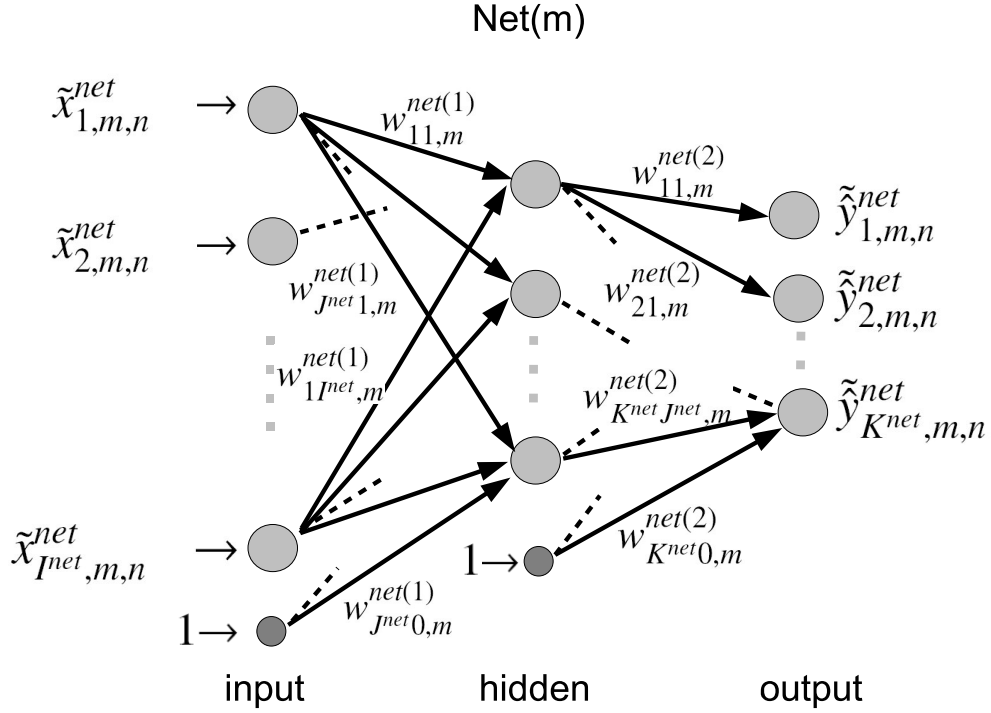


**Figure 6.11:** Design of Two-Layer Feed-Forward network  $Net(m)$  with  $(I^{net} + 1)$  input,  $(J^{net} + 1)$  hidden and  $K^{net}$  output neurons.

whereby  $m \cdot 0.5$  s are lapsed after triggering of the first sensor in the network, and  $x_{0,m,n}^{net} = 1$ .

The input data is linearly scaled so that all data points fall into the range from  $-1$  to  $+1$ . The *scaled input* then is

$$\begin{aligned} \tilde{\mathbf{X}}_{m,n}^{net} &= \{\tilde{x}_{0,m,n}^{net}, \tilde{x}_{1,m,n}^{net}, \tilde{x}_{2,m,n}^{net}, \dots, \tilde{x}_{I^{net},m,n}^{net}\}, \text{ with} & (6.33) \\ \tilde{x}_{i,m,n}^{net} &= 2 \frac{x_{i,m,n}^{net} - \min(\{x_{i,m,1}^{net}, x_{i,m,2}^{net}, \dots, x_{i,m,N^{set}}^{net}\})}{\max(\{x_{i,m,1}^{net}, x_{i,m,2}^{net}, \dots, x_{i,m,N^{set}}^{net}\}) - \min(\{x_{i,m,1}^{net}, x_{i,m,2}^{net}, \dots, x_{i,m,N^{set}}^{net}\})} - 1, \quad i = 0, \dots, I^{net} \end{aligned}$$

Scaling is an essential step in data pre-processing prior to neural computations. It ensures that all variables cover more or less the same value range; this is recommended because higher parameter values will have a stronger impact on the error function  $E(\mathbf{w})$  (e.g. defined by (6.9)) during learning than small values. Moreover, through data scaling it is often possible to reduce the required duration of network training (Swingler, 1996). With respect to the output data, scaling is needed to ensure that target values and network outputs are in the same range after the application of the chosen output activation function.

Using (6.19) the *scaled output* of  $Net(m)$  for earthquake  $n$  at time step  $m$  can be written as:

$$\begin{aligned} \tilde{\mathbf{Y}}_{m,n}^{net} &= \{\tilde{y}_{1,m,n}^{net}, \tilde{y}_{2,m,n}^{net}, \dots, \tilde{y}_{K^{net},m,n}^{net}\}, \text{ with} & (6.34) \\ \tilde{y}_{k,m,n}^{net} &= \tilde{g} \left( \sum_{j=0}^{J^{net}} w_{kj,m}^{net(2)} g \left( \sum_{i=0}^{I^{net}} w_{ji,m}^{net(1)} \tilde{x}_{i,m,n}^{net} \right) \right), \end{aligned}$$

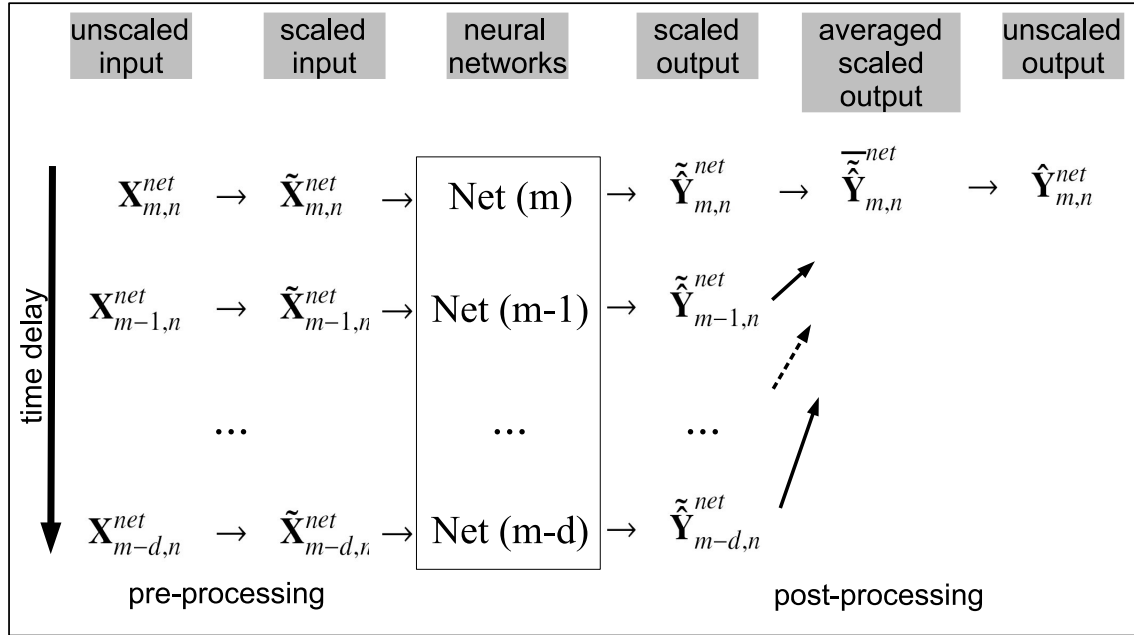


**Figure 6.12:** Moving average architecture in PreSEIS for the smoothing of network outputs over  $(d + 1)$  time steps.

whereby  $g(\cdot)$  and  $\tilde{g}(\cdot)$  are the activation functions of the hidden and output layer, respectively. PreSEIS uses for  $g(\cdot)$  the sigmoid logistic (6.16) and for  $\tilde{g}(\cdot)$  a linear function (see Figure 6.1, top).

The final output of network  $Net(m)$  is obtained from the moving average of network outputs over  $d + 1$  time steps. The *averaged scaled output* is

$$\begin{aligned} \bar{\tilde{Y}}_{m,n}^{net} &= \{\bar{\tilde{y}}_{1,m,n}^{net}, \bar{\tilde{y}}_{2,m,n}^{net}, \dots, \bar{\tilde{y}}_{K^{net},m,n}^{net}\}, \text{ with} \\ \bar{\tilde{y}}_{k,m,n}^{net} &= \frac{1}{d+1} (\tilde{y}_{k,m,n}^{net} + \tilde{y}_{k,m-1,n}^{net} + \tilde{y}_{k,m-2,n}^{net} + \dots + \tilde{y}_{k,m-d,n}^{net} + \tilde{y}_{k,m-d,n}^{net}). \end{aligned} \quad (6.35)$$

The link between the different time steps leads to a smoothing of outputs, i.e. to a removal of possible outliers. The described time delay architecture is illustrated in Figure 6.12. In principle it is possible to incorporate time delays directly into the ANNs, e.g. by so-called *Time-Delay Neural Networks (TDNN)* (Lang and Hinton, 1988; Waibel et al., 1989). A separation in different networks operating on information available at each time step  $m$ , yet, has the advantage that errors of single networks, e.g. caused by adverse weight initialization in the beginning of the learning stage that may lead to a trapping in a local minimum of  $E$ , can be smoothed; this effect is similar to the so-called *committee machines* that combine different networks trained on the same task (e.g., Bishop, 1995).

Finally, the *unscalled output* of  $Net(m)$  is obtained from (6.35) by

$$\begin{aligned} \hat{Y}_{m,n}^{net} &= \{\hat{y}_{1,m,n}^{net}, \hat{y}_{2,m,n}^{net}, \dots, \hat{y}_{K^{net},m,n}^{net}\}, \text{ with} \\ \hat{y}_{k,m,n}^{net} &= \frac{1}{2} \left( \bar{\tilde{y}}_{k,m,n}^{net} + 1 \right) \left[ \max(\{y_{1,m,n}^{net}, y_{2,m,n}^{net}, \dots, y_{K^{set},m,n}^{net}\}) - \min(\{y_{1,m,n}^{net}, y_{2,m,n}^{net}, \dots, y_{K^{set},m,n}^{net}\}) \right] \\ &\quad + \min(\{y_{1,m,n}^{net}, y_{2,m,n}^{net}, \dots, y_{K^{set},m,n}^{net}\}), \end{aligned} \quad (6.36)$$

whereby  $y_{k,m,n}^{net} = y_{k,n}^{net}$  are the target and  $\hat{y}_{k,m,n}^{net}$  the observed network outputs of  $Net(m)$  for earthquake  $n$  at time step  $m$ . During the training phase, network weights of  $Net(m)$  are tried to be determined

such that the error between targets  $y_{k,m,n}^{net}$  and outputs  $\hat{y}_{k,m,n}^{net}$ , here defined by the sum-of-squares errors (SSE)

$$E_m^{net} = \sum_{n=1}^{N^{set}} \sum_{k=1}^{K^{net}} \left( \hat{y}_{k,m,n}^{net} - y_{k,m,n}^{net} \right)^2, \quad (6.37)$$

is minimized. Details on the applied training procedure will be given below.

## II. Specific Designs of $Hypo(m)$ , $M_w(m)$ , $Rupt(m)$ , and $Spec(m)$

So far, only the common design of Artificial Neural Networks in PreSEIS - denoted by  $Net(m)$  - has been presented. This paragraph now will identify the specifics of each of the networks  $Hypo$ ,  $M_w$ ,  $Rupt$ , and  $Spec$  that will be used to solve the different inversion tasks described above. These tasks are not independent from each other which leads to an interconnection of the different nets. Figure 6.13 visualizes the linkage between the four networks schematically.

### II.1 Network $Hypo(m)$

Network  $Hypo$  estimates the hypocenter location of the  $n$ th earthquake defined by  $(\varphi_n^{hypo}, \lambda_n^{hypo}, h_n^{hypo})$ . The predicted hypocenter location at time step  $m$   $(\hat{\varphi}_{m,n}^{hypo}, \hat{\lambda}_{m,n}^{hypo}, \hat{h}_{m,n}^{hypo})$  is based on information on the relative P-wave onset times  $\Delta t_{i,m,n}^{trigg}$  at the different sensors defined by (6.30):

$$\begin{aligned} \text{Training input: } \mathbf{X}_{m,n}^{hypo} &= \{x_{1,m,n}^{hypo}, x_{2,m,n}^{hypo}, \dots, x_{10,m,n}^{hypo}\} \\ &= \{\Delta t_{1,m,n}^{trigg}, \Delta t_{2,m,n}^{trigg}, \dots, \Delta t_{10,m,n}^{trigg}\} \end{aligned} \quad (6.38)$$

$$\begin{aligned} \text{Target output: } \mathbf{Y}_{m,n}^{hypo} &= \{y_{1,m,n}^{hypo}, y_{2,m,n}^{hypo}, y_{3,m,n}^{hypo}\} \\ &= \{\varphi_n^{hypo}, \lambda_n^{hypo}, h_n^{hypo}\} \end{aligned} \quad (6.39)$$

$$\begin{aligned} \text{Network input: } \mathbf{X}_{m,n}^{hypo} &= \{x_{1,m,n}^{hypo}, x_{2,m,n}^{hypo}, \dots, x_{10,m,n}^{hypo}\} \\ &= \{\Delta t_{1,m,n}^{trigg}, \Delta t_{2,m,n}^{trigg}, \dots, \Delta t_{10,m,n}^{trigg}\} \end{aligned} \quad (6.40)$$

$$\begin{aligned} \text{Network output: } \hat{\mathbf{Y}}_{m,n}^{hypo} &= \{\hat{y}_{1,m,n}^{hypo}, \hat{y}_{2,m,n}^{hypo}, \hat{y}_{3,m,n}^{hypo}\} \\ &= \{\hat{\varphi}_{m,n}^{hypo}, \hat{\lambda}_{m,n}^{hypo}, \hat{h}_{m,n}^{hypo}\} \end{aligned} \quad (6.41)$$

### II.2 Network $M_w(m)$

Network  $M_w$  estimates the moment magnitude  $M_{w,n}$  of the  $n$ th earthquake. The predicted magnitude at time step  $m$   $\hat{M}_{w,m,n}$  is based on information on the logarithmized CAV  $\log(CAV_{i,m,n} + 1)$  at the different sensors defined by (6.31) and, secondly, on the true hypocenter location  $(\varphi_n^{hypo}, \lambda_n^{hypo}, h_n^{hypo})$ , or the estimated hypocenter location  $(\hat{\varphi}_{m,n}^{hypo}, \hat{\lambda}_{m,n}^{hypo}, \hat{h}_{m,n}^{hypo})$  predicted by  $Hypo(m)$ , respectively:



$$\begin{aligned}
 \text{Training input: } \mathbf{X}_{m,n}^{M_w} &= \{x_{1,m,n}^{M_w}, x_{2,m,n}^{M_w}, \dots, x_{13,m,n}^{M_w}\} \\
 &= \{\log(\text{CAV}_{1,m,n} + 1), \log(\text{CAV}_{2,m,n} + 1), \dots, \log(\text{CAV}_{10,m,n} + 1), \\
 &\quad \varphi_n^{\text{hypo}}, \lambda_n^{\text{hypo}}, h_n^{\text{hypo}}\} \tag{6.42}
 \end{aligned}$$

$$\begin{aligned}
 \text{Target output: } \mathbf{Y}_n^{M_w} &= \{y_{1,m,n}^{M_w}\} \\
 &= M_{w,n} \tag{6.43}
 \end{aligned}$$

$$\begin{aligned}
 \text{Network input: } \mathbf{X}_{m,n}^{M_w} &= \{x_{1,m,n}^{M_w}, x_{2,m,n}^{M_w}, \dots, x_{13,m,n}^{M_w}\} \\
 &= \{\log(\text{CAV}_{1,m,n} + 1), \log(\text{CAV}_{2,m,n} + 1), \dots, \log(\text{CAV}_{10,m,n} + 1), \\
 &\quad \hat{\varphi}_{m,n}^{\text{hypo}}, \hat{\lambda}_{m,n}^{\text{hypo}}, \hat{h}_{m,n}^{\text{hypo}}\} \tag{6.44}
 \end{aligned}$$

$$\begin{aligned}
 \text{Network output: } \hat{\mathbf{Y}}_{m,n}^{M_w} &= \{\hat{y}_{1,m,n}^{M_w}\} \\
 &= \hat{M}_{w,m,n} \tag{6.45}
 \end{aligned}$$

### II.3 Network *Rupt(m)*

Network *Rupt* estimates the start and end points of the evolving rupture of the  $n$ th earthquake defined by the geographical coordinates  $(\varphi_n^{\text{rupt } 1}, \lambda_n^{\text{rupt } 1}, \varphi_n^{\text{rupt } 2}, \lambda_n^{\text{rupt } 2})$ . The predicted coordinates at time step  $m$   $(\hat{\varphi}_{m,n}^{\text{rupt } 1}, \hat{\lambda}_{m,n}^{\text{rupt } 1}, \hat{\varphi}_{m,n}^{\text{rupt } 2}, \hat{\lambda}_{m,n}^{\text{rupt } 2})$  are based on information on the logarithmized CAV  $\log(\text{CAV}_{i,m,n} + 1)$  at the different sensors defined by (6.31), on the true hypocenter location  $(\varphi_n^{\text{hypo}}, \lambda_n^{\text{hypo}}, h_n^{\text{hypo}})$  or the estimated hypocenter location  $(\hat{\varphi}_{m,n}^{\text{hypo}}, \hat{\lambda}_{m,n}^{\text{hypo}}, \hat{h}_{m,n}^{\text{hypo}})$  predicted by *Hypo(m)*, respectively, and finally on the true moment magnitude  $M_{w,n}$  or the estimated magnitude  $\hat{M}_{w,m,n}$  predicted by  $M_w(m)$ , respectively:

$$\begin{aligned}
 \text{Training input: } \mathbf{X}_{m,n}^{\text{rupt}} &= \{x_{1,m,n}^{\text{rupt}}, x_{2,m,n}^{\text{rupt}}, \dots, x_{14,m,n}^{\text{rupt}}\} \\
 &= \{\log(\text{CAV}_{1,m,n} + 1), \log(\text{CAV}_{2,m,n} + 1), \dots, \log(\text{CAV}_{10,m,n} + 1), \\
 &\quad \varphi_n^{\text{hypo}}, \lambda_n^{\text{hypo}}, h_n^{\text{hypo}}, M_{w,n}\} \tag{6.46}
 \end{aligned}$$

$$\begin{aligned}
 \text{Target output: } \mathbf{Y}_n^{\text{rupt}} &= \{y_{1,m,n}^{\text{rupt}}, y_{2,m,n}^{\text{rupt}}, y_{3,m,n}^{\text{rupt}}, y_{4,m,n}^{\text{rupt}}\} \\
 &= \{\varphi_n^{\text{rupt } 1}, \lambda_n^{\text{rupt } 1}, \varphi_n^{\text{rupt } 2}, \lambda_n^{\text{rupt } 2}\} \tag{6.47}
 \end{aligned}$$

$$\begin{aligned}
 \text{Network input: } \mathbf{X}_{m,n}^{\text{rupt}} &= \{x_{1,m,n}^{\text{rupt}}, x_{2,m,n}^{\text{rupt}}, \dots, x_{14,m,n}^{\text{rupt}}\} \\
 &= \{\log(\text{CAV}_{1,m,n} + 1), \log(\text{CAV}_{2,m,n} + 1), \dots, \log(\text{CAV}_{10,m,n} + 1), \\
 &\quad \hat{\varphi}_{m,n}^{\text{hypo}}, \hat{\lambda}_{m,n}^{\text{hypo}}, \hat{h}_{m,n}^{\text{hypo}}, \hat{M}_{w,m,n}\} \tag{6.48}
 \end{aligned}$$

$$\begin{aligned}
 \text{Network output: } \hat{\mathbf{Y}}_{m,n}^{\text{rupt}} &= \{\hat{y}_{1,m,n}^{\text{rupt}}, \hat{y}_{2,m,n}^{\text{rupt}}, \hat{y}_{3,m,n}^{\text{rupt}}, \hat{y}_{4,m,n}^{\text{rupt}}\} \\
 &= \{\hat{\varphi}_{m,n}^{\text{rupt } 1}, \hat{\lambda}_{m,n}^{\text{rupt } 1}, \hat{\varphi}_{m,n}^{\text{rupt } 2}, \hat{\lambda}_{m,n}^{\text{rupt } 2}\} \tag{6.49}
 \end{aligned}$$

### II.4 Network *Spec(m, f)*

Network *Spec(f)* is used to estimate the Fourier amplitude spectrum (FAS) of acceleration at frequency identified by index  $f$  at site *UserX* of the  $n$ th earthquake defined by  $a_{n,f}$ . The predicted FAS at time step  $m$   $\hat{a}_{m,n,f}$  is based on information on the logarithmized CAV  $\log(\text{CAV}_{i,m,n} + 1)$  at the different sensors defined by (6.31), on the true hypocenter location  $(\varphi_n^{\text{hypo}}, \lambda_n^{\text{hypo}}, h_n^{\text{hypo}})$  or the estimated

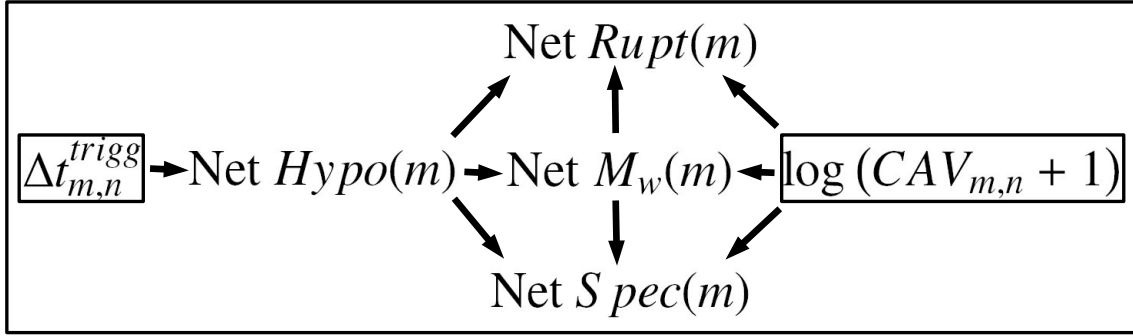


**Figure 6.13:** Link between the four Neural Networks  $Hypo(m)$ ,  $M_w(m)$ ,  $Rupt(m)$ , and  $Spec(m)$  in PreSEIS and the two used parameter sets  $\Delta t_{m,n}^{trigg}$  (6.30) and  $\log(CAV_{m,n} + 1)$  (6.31) at time step  $m$  for earthquake  $n$ .

hypocenter location  $(\hat{\varphi}_{m,n}^{hypo}, \hat{\lambda}_{m,n}^{hypo}, \hat{h}_{m,n}^{hypo})$  predicted by  $Hypo(m)$ , respectively, and finally on the true moment magnitude  $M_{w,n}$  or the estimated magnitude  $\hat{M}_{w,m,n}$  predicted by  $M_w(m)$ , respectively:

$$\begin{aligned}
 \text{Training input: } \mathbf{X}_{m,n}^{spec} &= \{x_{1,m,n}^{spec}, x_{2,m,n}^{spec}, \dots, x_{14,m,n}^{spec}\} \\
 &= \{\log(CAV_{1,m,n} + 1), \log(CAV_{2,m,n} + 1), \dots, \log(CAV_{10,m,n} + 1), \\
 &\quad \varphi_n^{hypo}, \lambda_n^{hypo}, h_n^{hypo}, M_{w,n}\} \quad (6.50)
 \end{aligned}$$

$$\begin{aligned}
 \text{Target output: } \mathbf{Y}_{n,f}^{spec} &= \{y_{1,m,n,f}^{spec}\} \\
 &= \{a_{n,f}\} \quad (6.51)
 \end{aligned}$$

$$\begin{aligned}
 \text{Network input: } \mathbf{X}_{m,n}^{spec} &= \{x_{1,m,n}^{spec}, x_{2,m,n}^{spec}, \dots, x_{14,m,n}^{spec}\} \\
 &= \{\log(CAV_{1,m,n} + 1), \log(CAV_{2,m,n} + 1), \dots, \log(CAV_{10,m,n} + 1), \\
 &\quad \hat{\varphi}_{m,n}^{hypo}, \hat{\lambda}_{m,n}^{hypo}, \hat{h}_{m,n}^{hypo}, \hat{M}_{w,m,n}\} \quad (6.52)
 \end{aligned}$$

$$\begin{aligned}
 \text{Network output: } \hat{\mathbf{Y}}_{m,n,f}^{spec} &= \{\hat{y}_{1,m,n,f}^{spec}\} \\
 &= \{\hat{a}_{m,n,f}\} \quad (6.53)
 \end{aligned}$$

whereby  $f=1$  identifies frequency 0.25 Hz,  $f=2$  identifies frequency 1.25 Hz and  $f=12$  identifies frequency 11.25 Hz. Table 6.1 summarizes the specific designs of  $Hypo(m)$ ,  $M_w(m)$ ,  $Rupt(m)$ , and  $Spec(m)$ .

### 6.2.3 Training of the Artificial Neural Networks

PreSEIS is developed on basis of 280 simulated earthquake scenarios in the Marmara region (Chapter 3.3). This database is split randomly into one subset with 196 training events (70%), one subset with 56 test events (20%), and one subset with 28 validation events (10%). The role of the different sets was discussed in Chapter 6.1.5.

#### Artificial Enlargement of the Training Database

As a rule of thumb a training database with 196 example patterns allows to train a network with

**Neural Network Designs in PreSEIS**

Net	no. input units $J^{net}$ (without bias)	no. hidden units $J^{net}$ (without bias)	no. output units $K^{net}$	total number of weights (with bias)
<i>Hypo</i>	10 eq.(6.38)	4, 6, 8, 10	3 eq.(6.39)	59, 87, 115, 143
$M_w$	14 eq.(6.42)	4, 6, 8, 10	1 eq.(6.43)	65, 97, 129, 161
<i>Rupt</i>	14 eq.(6.46)	4, 6, 8, 10	4 eq.(6.47)	80, 118, 156, 194
<i>Spec</i>	14 eq.(6.50)	4, 6, 8, 10	1 (per frequency) eq.(6.51)	65, 97, 129, 161

**Table 6.1:** Number of input, hidden and output units in the four Two-Layer Neural Networks *Hypo* for earthquake localization,  $M_w$  for magnitude determination, *Rupt* for the estimation of rupture location and dimensions, and finally *Spec* for the prediction of the Fourier amplitude spectrum of acceleration (FAS) at site *UserX*. The total number of weights (right column) are free parameters within the networks and have to be adapted to the given tasks through learning from examples. Note that the total number of weights includes the two bias terms  $w_{j0}^{(1)}$  and  $w_{k0}^{(2)}$ .

approximately 20 weight parameters; that is, each free parameter requires around 10 example patterns<sup>4</sup> (e.g., Swingler, 1996). From Table 6.1 follows that the Neural Networks trained on the inversion for seismic source parameters in PreSEIS are of much larger complexities. For increased stability of the inversion routine, the available database of scenario earthquakes is artificially enlarged by the manipulation of the existing data: PreSEIS is allowed to make small errors when picking the P-wave onsets at the different sensors. By this, additional training patterns are obtained. A similar approach has been proposed by Swingler (1996). Furthermore, the described procedure has the advantage that it allows building a robust statistical model with a high degree of generalization capability that is strongly required for real-time operation of PreSEIS because seismic wave-onsets will of course never be perfectly picked. For each of the 280 scenario patterns in the original database, five additional patterns with incorrectly picked onsets are determined and integrated into the updated set. The new database therewith encompasses  $6 \times 196 = 1,176$  training examples,  $6 \times 56 = 336$  test, and  $6 \times 28 = 168$  validation patterns. The distribution of picking errors of the patterns in the new database is shown in the histogram in Figure 6.14.

The Artificial Neural Networks are successively optimized through three different training algorithms: (1) *Gradient Descent with Momentum Term*, (2) *Resilient Propagation (RPROP)*, and (3) *Levenberg-Marquardt*. A short description of these algorithms was given in Chapter 6.1.2.

### The Optimum Number of Hidden Units and Learning Epochs

As pointed out before, one of the most crucial issues in neural computations is the determination of model complexity, that is the optimum number of hidden units. For that purpose the database of

<sup>4</sup>The number of required training patterns depends on the acceptable error of the ANNs as well as on the intrinsic dimension of the inversion problem (e.g., Swingler, 1996).

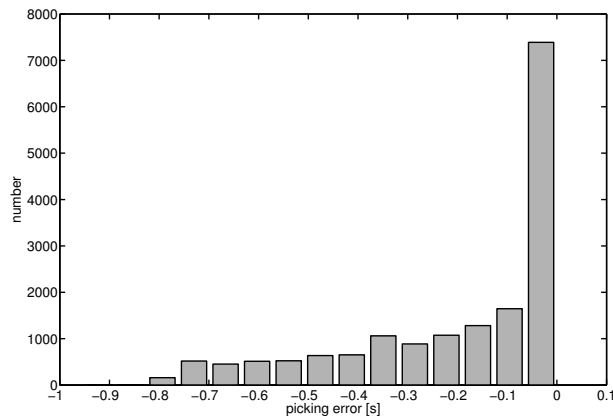


**Figure 6.14:** Histogram of picking errors of P-wave onsets at the ten early warning stations for 280 simulated earthquake scenarios in the database. A picking error of zero means that the onset is perfectly recognized. Through the manipulation of the available data the original dataset (without picking errors) is artificially enlarged.

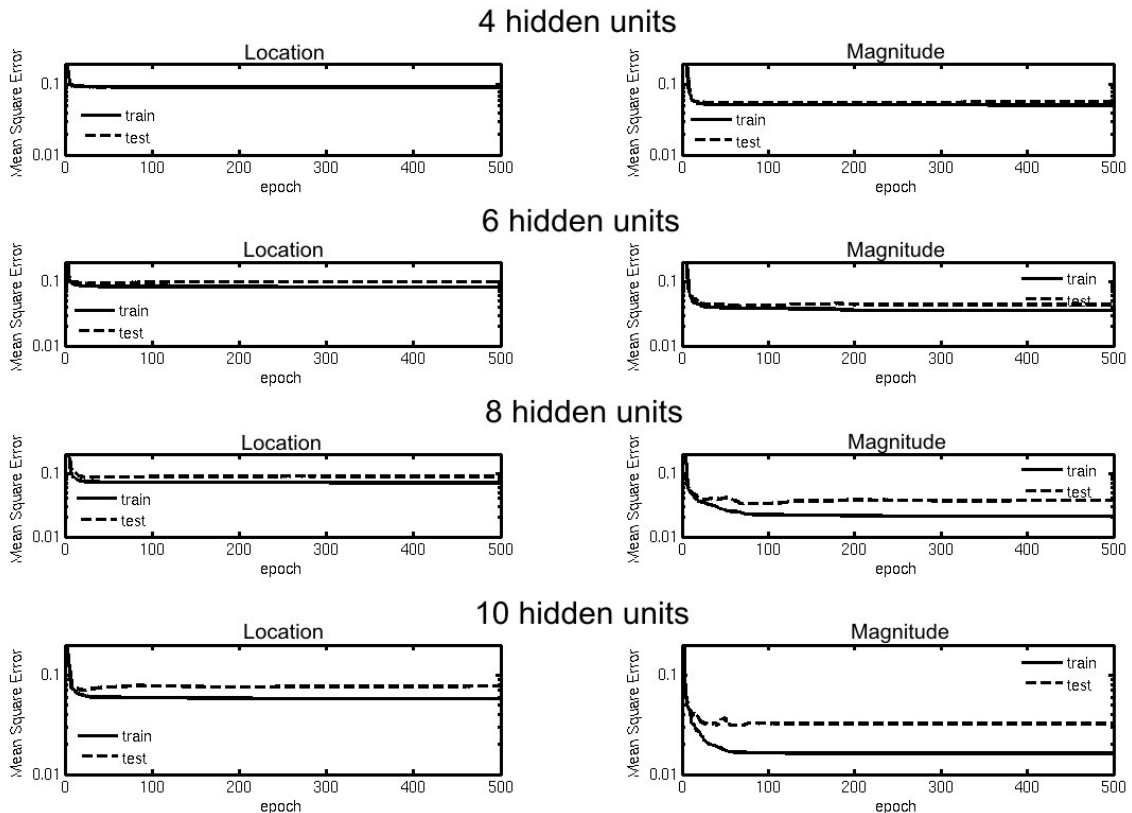


**Figure 6.15:** Location (left) and magnitude (right) prediction errors (MSE) as a function of training epochs for four, six, eight and ten neurons in the hidden layer. One half of the available patterns in the database is used for training of  $Hypo$  and  $M_w$  (solid lines), the remaining patterns are used for validation (dashed lines). The figures demonstrate the trade-off between network accuracy and generalization capability of the different nets. Wanted is a network that has low errors for both, training and test datasets. For the tasks presented here six neurons in the hidden layer appear to be appropriate.

correctly and incorrectly picked ground motion time series is subdivided into two equally sized subsets: the first set is used for training (*model selection*), the second set for *model validation*. Location and magnitude prediction errors as a function of learning epochs are calculated for four, six, eight and ten hidden units and are plotted in Figure 6.15: the solid lines indicate the temporal evolution of the mean-square-error (MSE) for the training set, the dashed lines the development of MSE for the test set.

A well-balanced Artificial Neural Network performs well on *known* training alike on *unknown* test data provided of course that they are subject to the same statistical process. Wanted is the network with the smallest overall failure rate. As illustrated in Figure 6.15, six neurons in the hidden layer appear to be appropriate in the presented inversion problems. This means that the applied networks *Hypo* and  $M_w$  in PreSEIS have 87 or 97 weights, respectively (see Table 6.1). These weights have to be optimized through learning from a database of 1,176 example patterns. Analyses for the other two networks *Rupt* and *Spec* give similar results. To confirm robustness of the findings above, this study was repeated several times with changing training and test sets as well as with different weight initializations at the beginning of the learning phase.

The optimum number of learning epochs is determined through *early stopping* (see Chapter 6.1.5), i.e. training is terminated once the error for the independent validation set increases. This allows for determining the transition point at which the Artificial Neural Networks start to reproduce the training data at the expense of generalization capability. For the tasks presented here, *Levenberg-Marquardt* optimization usually requires less than 40 training epochs. For the other optimization algorithms the number of required epochs is significantly higher and ranges between some hundred to some thousands iterations for *Gradient Descent with Momentum Term* and *Resilient Propagation*.

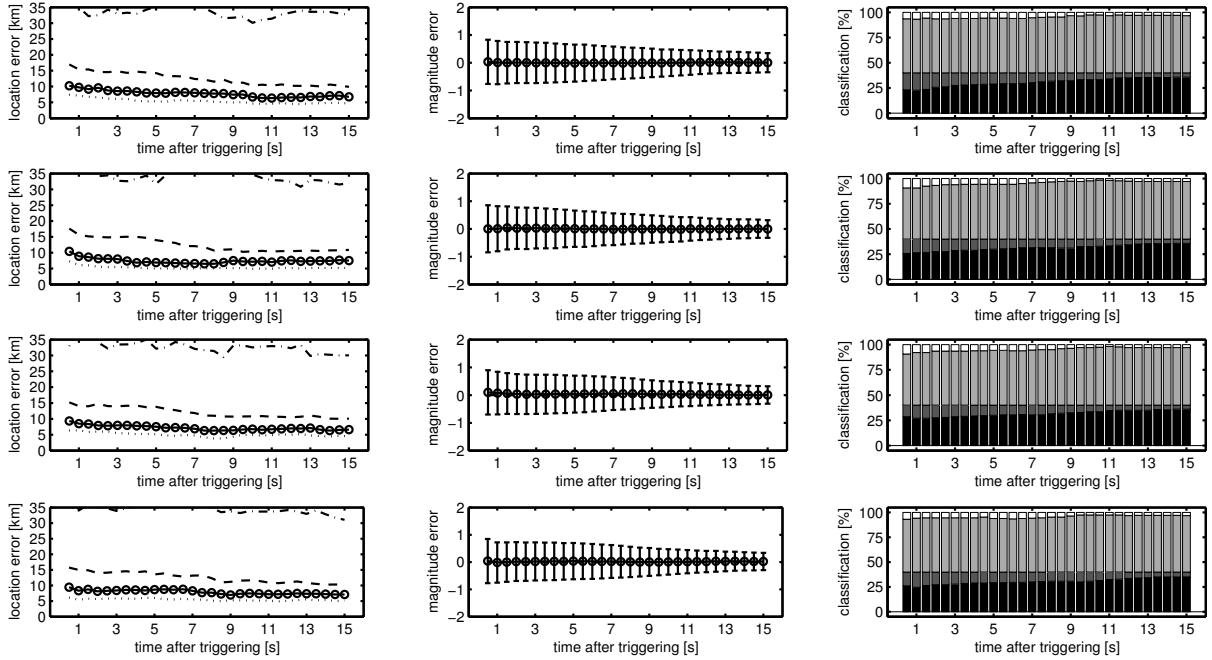
## 6.2.4 Performance Analyses

### I. Comparing Neural Network Outputs for Different Optimization Algorithms

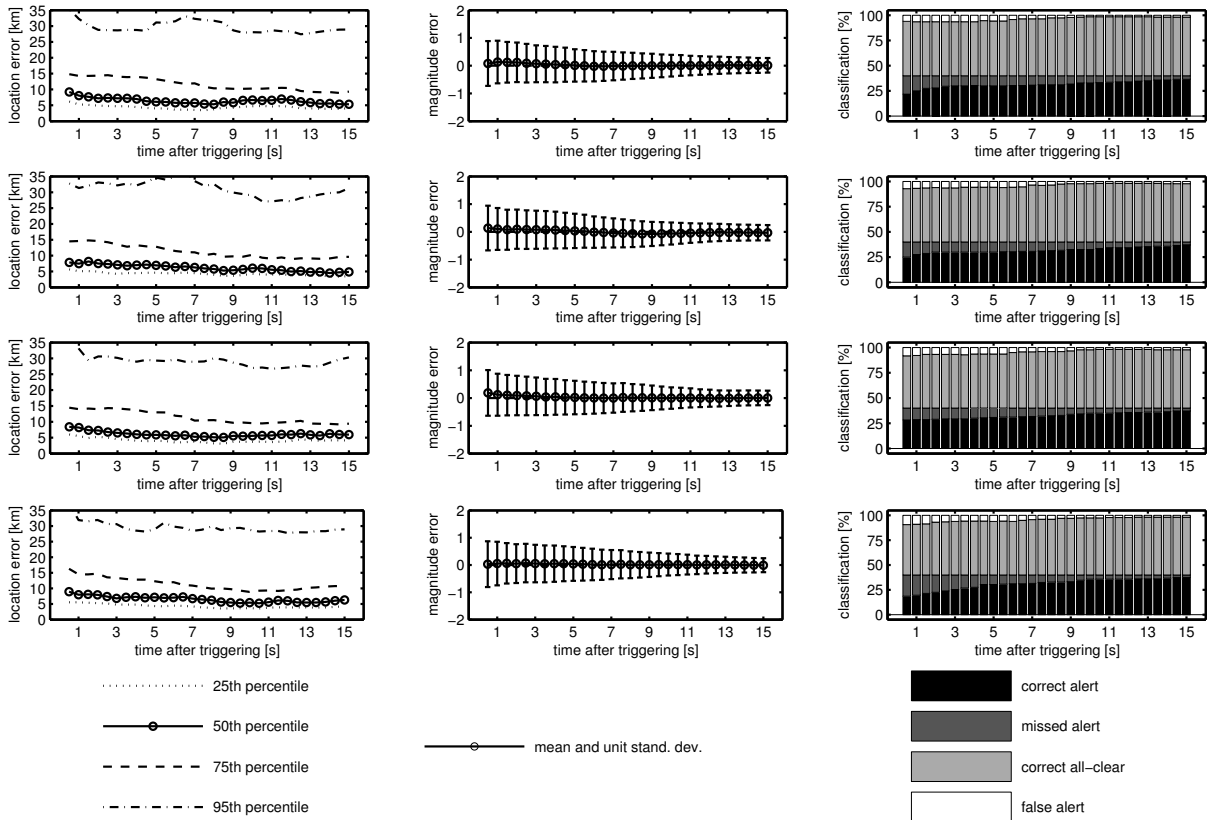
Network performances after training through the three algorithms - (1) *Gradient Descent with Momentum Term*, (2) *Resilient Propagation (RPROP)*, and (3) *Levenberg-Marquardt* - are visualized in Figure 6.16. The statistics summarize the results for both - training and test patterns - as a function of time after triggering of the first sensor. (A separate analysis for training and test sets is shown in Figure 6.17.) For each optimization algorithm, training and evaluation is repeated four times with changing training, test, and validation sets (*bootstrapping*, see Chapter 6.1.5), as well as with different weight initializations at the beginning of the training procedure.

Absolute location errors (Figure 6.16, left column) are quantified through the 25th, 50th, 75th and the 95th percentiles; the 50th percentile is better known as the *median* that divides the lower half from the higher half of a statistical distribution. Absolute magnitude errors for training and test earthquakes (Figure 6.16, middle column) are quantified at each time step through the mean prediction error and its unit standard deviation. For all three optimization algorithms there is a clear increase of reliability of predictions of earthquake hypocenter locations and moment magnitudes with ongoing time. The average location error (median) is less than 10 km after only 0.5 s after triggering and can be reduced to approximately 5 km during the following 15 s. This high accuracy is due to the advantage that the ANNs have learned the *a priori* information, that earthquakes usually cluster along the major fault segments in the Sea of Marmara (Figure 3.6). The 95th percentile of the location errors generally starts with 35 km and falls to a value between 25 to 30 km. These higher errors are usually linked to earthquakes that occur beyond the fault segments or in the border areas of the sensor network. With

Gradient Descent with Momentum Term



Resilient Propagation (RPROP)



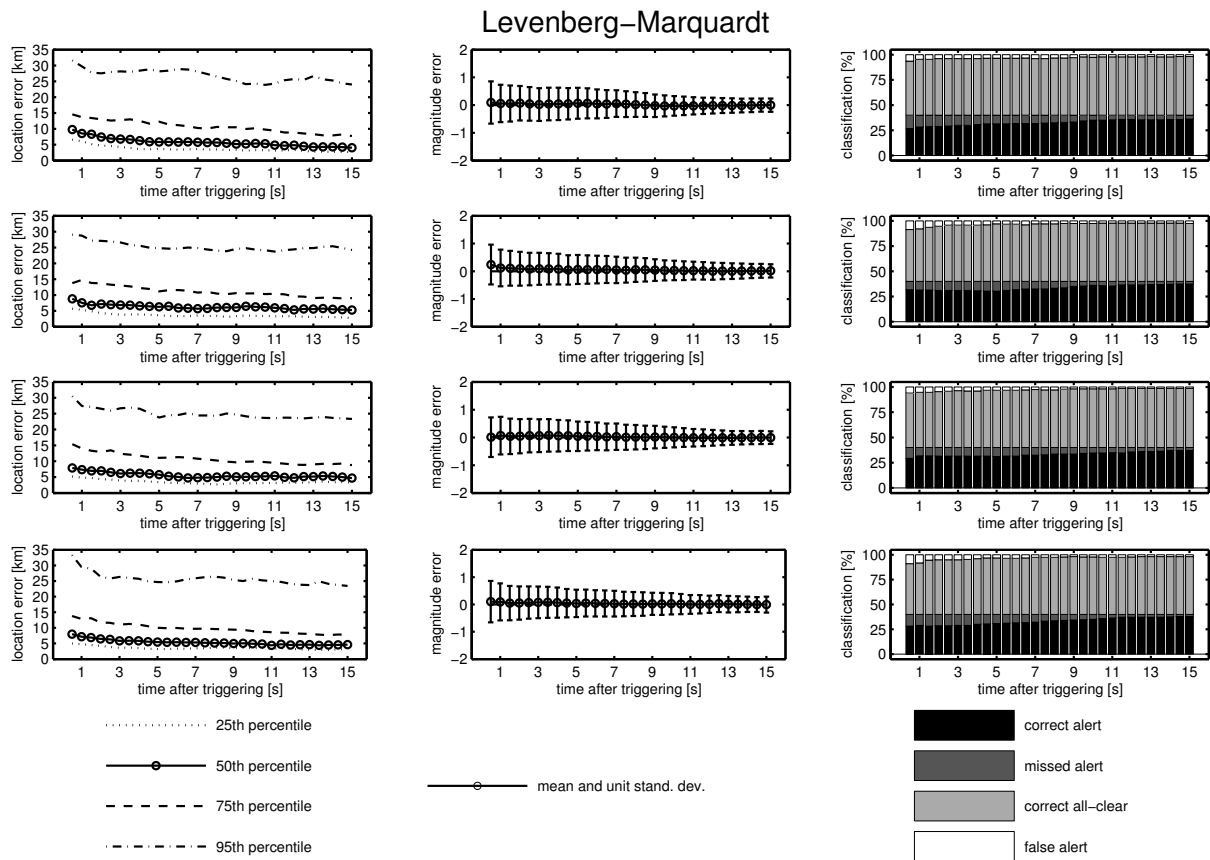


**Figure 6.16:** Performance analyses for (1) *Gradient Descent with Momentum Term*, (2) *Resilient Propagation (RPROP)*, and (3) *Levenberg-Marquardt* optimization. For each optimization method the ANNs are trained and evaluated four times with randomly changing training, validation and test subsets (*bootstrapping*), as well as with different weight initializations at the beginning of the training procedure. The errors refer to the entire database of 280 earthquake scenarios, i.e. they are determined for training, validation and test patterns. Figures in the left column show the (hypocentral) location errors as a function of time after P-wave arrival at the first early warning station. The plots visualize the 25th, 50th, 75th, and 95th percentiles of the error distributions. The 50th percentile is better known as the *median* value. For all three optimization methods 50% of the scenarios have localization errors of less than 10 km 0.5 seconds after triggering and less than 5 km after 10 seconds. The figures in the middle column visualize the average magnitude errors for the same time span. The mean error at each time step is zero, the unit standard deviation is 0.7 units after 0.5 seconds and 0.3 after 15 seconds for *Levenberg-Marquardt* optimization. Estimated source locations and magnitudes are combined with empirical attenuation laws to predict ground motion at site *UserX*. PreSEIS issues a warning whenever a certain threshold of ground shaking will be likely exceeded. The figures in the right column show the classification results after introduction of a threshold of 5.5 seismic intensity units. The error analyses demonstrate a clear enhancement of reliability with ongoing time, and, secondly, show a clear superiority of the *Levenberg-Marquardt* algorithm compared to *Gradient Descent* and *Resilient Propagation*. Details in the text.

respect to moment magnitudes the mean error is zero at all time steps with a clear decrease of the unit standard deviation from 0.7 to 0.3 magnitude units in the analyzed 15 s interval for *Levenberg-Marquardt* optimization. For the other two optimization methods the errors are somewhat higher.

Note that location and magnitude errors are not strongly linked to each other because  $M_w(m)$  receives aside from the estimated hypocenter location by  $Hypo(m)$  additional amplitude information in terms of the cumulative absolute velocity (CAV) that itself is affected by source-to-site distances<sup>5</sup>. All results turn out to be very stable and hardly affected by the selected data as well as weight initialization. The best performance is achieved for *Levenberg-Marquardt* optimization.

From the combination of (estimated) source locations and (estimated) magnitudes with empirical attenuation laws, seismic ground motion can be estimated at any given site. Based on the stochastically simulated ground motion time series for the Marmara region, attenuation relations for different ground motion parameters have been determined in Chapter 4.4. Figure 6.16 (right column) shows the performance of the different Neural Networks when translating location and magnitude information into estimates of seismic intensity (Chapter 4.1.4) at site *UserX* after the introduction of a certain threshold. Whenever the expected seismic intensity at the site exceeds 5.5 units, PreSEIS issues a warning. Note that intensity 5.5 earthquakes are generally non-destructive. However, this fairly low threshold has been introduced here to assure a well-balanced distribution of alarm and non-alarm events. Remember that the attenuation laws determined in Chapter 4.4 are rather conservative with a rapid decrease of seismic intensity with increasing source-to-site distances. The actual intensity level might be a half to a full unit higher than predicted from the data-consistent attenuation laws.

After the introduction of the alarm threshold at  $I = 5.5$  intensity units, the database comprises 112 alarm events (40%) and 168 (60%) non-alarm events. Outputs of PreSEIS are classified as follows: (1) a *correct alert* means recognition of an earthquake with  $I \geq 5.5$ , (2) a *missed alert* means that an earthquake with  $I \geq 5.5$  is not recognized, (3) a *correct all-clear* means recognition of a non-destructive earthquake, and (4) a *false alert* means an erroneous warning in case of a non-destructive earthquake. The classification results of the different Neural Networks are shown in Figure 6.16, right column. Note, that the applied attenuation laws for seismic intensity described in Chapter 4.4 quantify source-to-site distances through the *Joyner-Boore distance*  $r_{jb}$  that is defined by the closest horizontal distance to the vertical projection of the rupture onto the surface. The required information on rupture expansion for the study described above is provided through network  $Rupt(m)$  instead of network  $Hypo(m)$ . Once again, there is a clear improvement of predictions with ongoing time.

The best performance with lowest errors in location, magnitude and ground motion prediction is obtained for *Levenberg-Marquardt* optimization. At the same time *Levenberg-Marquardt* requires only a fractional amount of training time in comparison to *RPROP* and *Gradient Descent with Momentum Term* and therewith is the most suitable optimization algorithm here.

A separate error analyses for training and test data is visualized in Figure 6.17. Note that there are only minor differences between performances for both sets demonstrating the high generalization capability of the Neural Networks as a consequence of the *early stopping* procedure (Chapter 6.1.5).

## II. Detailed Analyses of Two Scenario Earthquakes

Two earthquake scenarios will be studied in more detail. Scenario A is a magnitude  $M_w = 6.9$  earthquake, approximately 55 km far from Istanbul and 40 km from *UserX*, accompanied by a 45 km long

---

<sup>5</sup>The possibility to use amplitude data in terms of PGA and CAV for source localization in terms of the *strong motion centroid* has been studied by Kanamori (1993) (see Chapter 5.3).



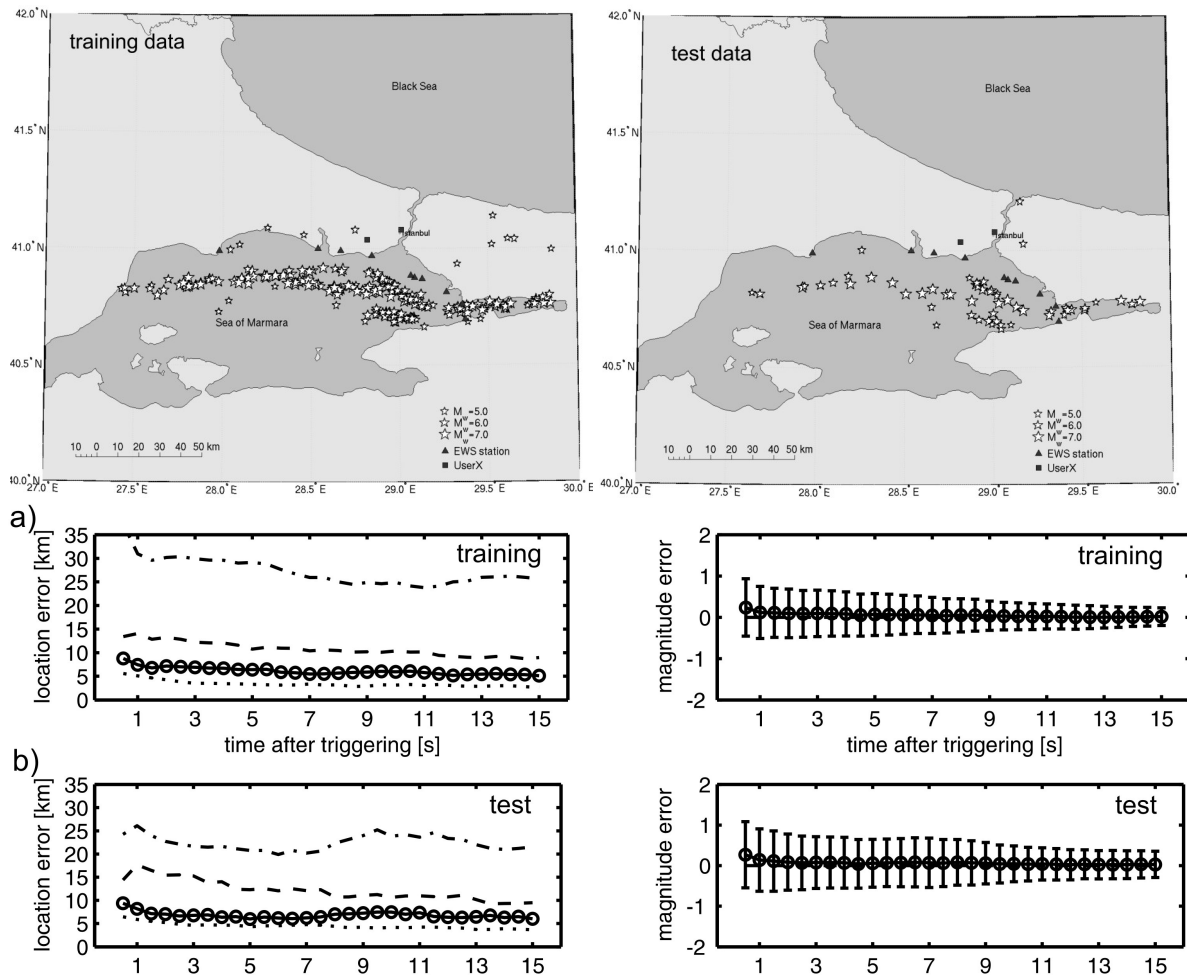


**Figure 6.17:** Separate performance analyses for training and test subsets for *Levenberg-Marquardt* optimization. Top: Epicenter distribution of training (left) and test earthquakes (right). Bottom: a) Location and magnitude errors for the training data, b) Location and magnitude errors for the test data. For further explanation see caption of Figure 6.16. The statistics demonstrate the high generalization capability of the Artificial Neural Networks in PreSEIS as a consequence of the *early stopping* procedure.

rupture of fault SEGMENT 4 (#8, see Appendix B); Scenario B is a magnitude  $M_w = 6.3$  earthquake, approximately 60 km far from Istanbul and 75 km from *UserX*, accompanied by a 20 km long rupture of fault SEGMENT 1 (#30, see Appendix B). The choice of these two scenario earthquakes is due to the consideration that PreSEIS should be demonstrated for two scenarios with different source locations and different magnitudes. A  $M_w = 7.5$  earthquake as, e.g., proposed by Parsons et al. (2000) and Erdik et al. (2003a) as a possible worst case scenario for Istanbul, would be accompanied - following the Wells-Coppersmith relation in (2.22) - by a rupture of approximately 120 km length. This expansion, however, requires joint ruptures of two to three fault segments in the Sea of Marmara. The joint rupture of SEGMENTS 1 to 3 has been made possible in the synthetic database by the introduction of the artificial SEGMENT 4 (see Figure 3.6; remember that the applied *Stochastic Simulation Method for Finite Faults* (Chapter 3.2) can only model plane rupture propagation.) The simulation of strong earthquakes along the artificial fault SEGMENT 4, however, can cause misleading distributions of ground motion along the rupture with completely different shapes of shake maps than, e.g., predicted by Erdik et al. (2003a). To obtain more realistic distributions, I have decided to show only results for scenarios that are linked to ruptures of single fault segments even if this restricts the modeling to lower magnitudes.

### II.1 Simulated Acceleration Time Series and Pre-Warning Times in the Marmara Region

The stochastically simulated mean horizontal components of ground motion at the early warning stations and at sites *UserX* and *ISTAN* are shown in Figure 6.18 (top) for Scenario A and in Figure 6.19 (top) for Scenario B. The time series are sorted according to P-wave arrivals. The Scenario A earthquake is detected by station *SINOB*, approximately 4.0 s after rupture initiation. The Scenario B earthquake is detected by station *FARGE*, approximately 3.5 s after rupture initiation. The maps on the bottom left in both figures illustrate the maximum available pre-warning times defined by the time window between the P-wave detection at the first sensor and S-wave arrivals at the different sites in the Marmara region (see eq.(1.1)). Warning times for *UserX* are less than 10.0 s for the Scenario A and less than 20.0 s for the Scenario B earthquake.

### II.2 Shake Maps of Seismic Intensity

Figures 6.18 and 6.19, bottom right, show for both scenario earthquakes shake maps of seismic intensity. The upper figures visualize the distribution of seismic (instrumental) intensity in the Marmara region for rock condition (NEHRP B, see Chapter 2.3.3), the lower figures show shake maps for Istanbul metropolitan area including mean site amplifications for different soil types. (The expansion of the latter shake map is indicated by a square in the upper figures.) All shake maps have been determined from attenuation laws and site- and magnitude-dependent amplification factors derived from the stochastic simulated database as described in Chapter 4.4. Once again notice that these attenuation relations are rather conservative (see Figure 4.12) with a steeper decay at large source-to-site distances in comparison to other laws: in distances of more than 60 km seismic intensity might be a full unit lower than predicted by the attenuation relation proposed by Erdik et al. (1985).

The shake map procedure applied here can only reflect average amplification values at the different sites. Considering site effects, however, is a significant enhancement of shake maps that are based on the assumption of rock conditions. A further enhancement of shake maps is obtained from the integration of dynamic features of rupture propagation - such as rupture directivity - that have been neglected so far. Examples of shake maps modified by directivity effects are shown in Figure 6.29.

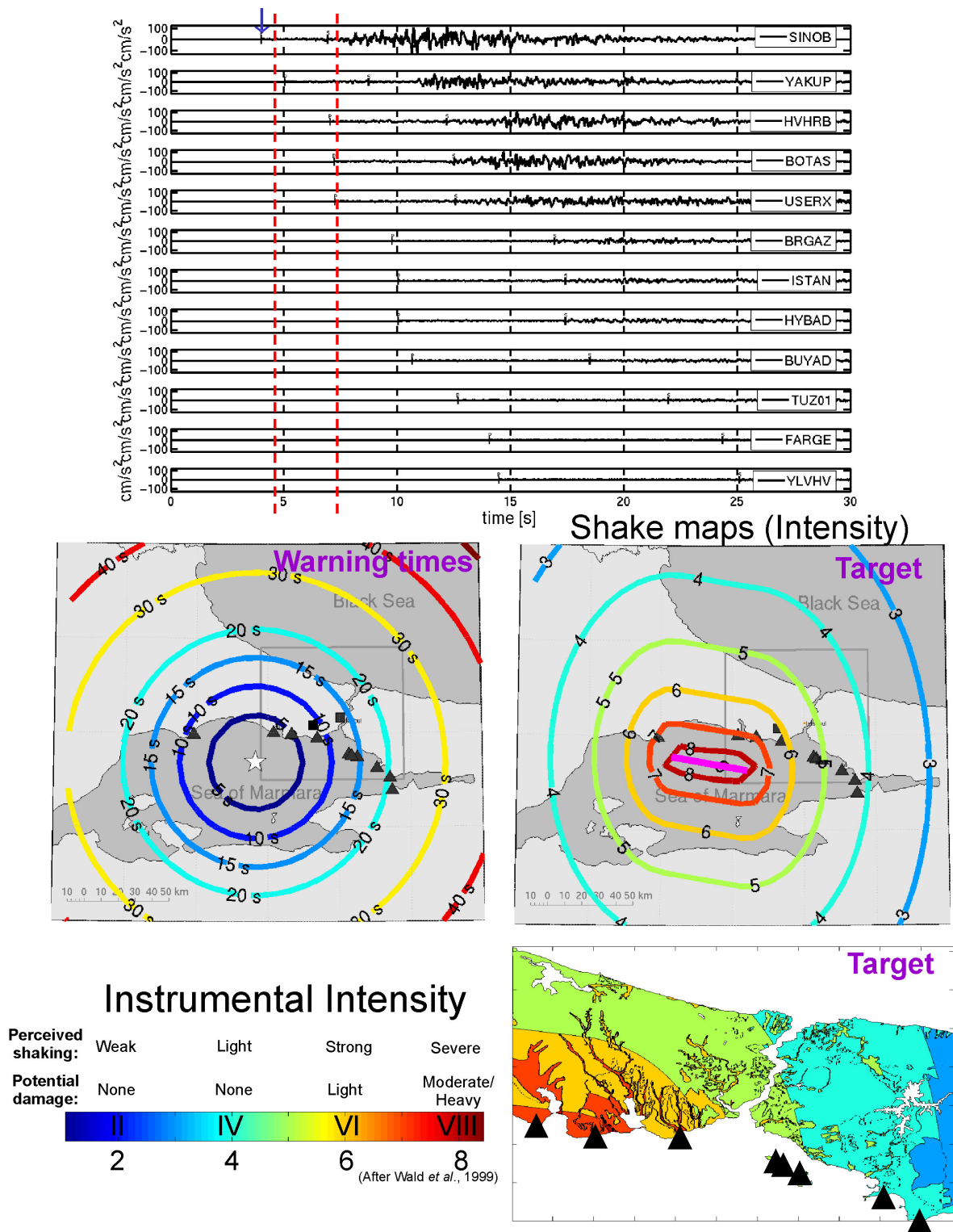


**Figure 6.18: Scenario A ( $M_w = 6.9$ ).** Top: Stochastically simulated mean horizontal components of acceleration at the early warning stations of *IERREWS* and at sites *ISTAN* and *UserX* (see Figure 1.3). Bottom, left: Warning times in the Marmara region defined by the time window between P-wave detection at station *SINOB* and S-wave arrivals. Bottom, right: Shake maps of seismic intensity in the Marmara region for rock condition and, beneath, with simplified site effects in Istanbul metropolitan area.

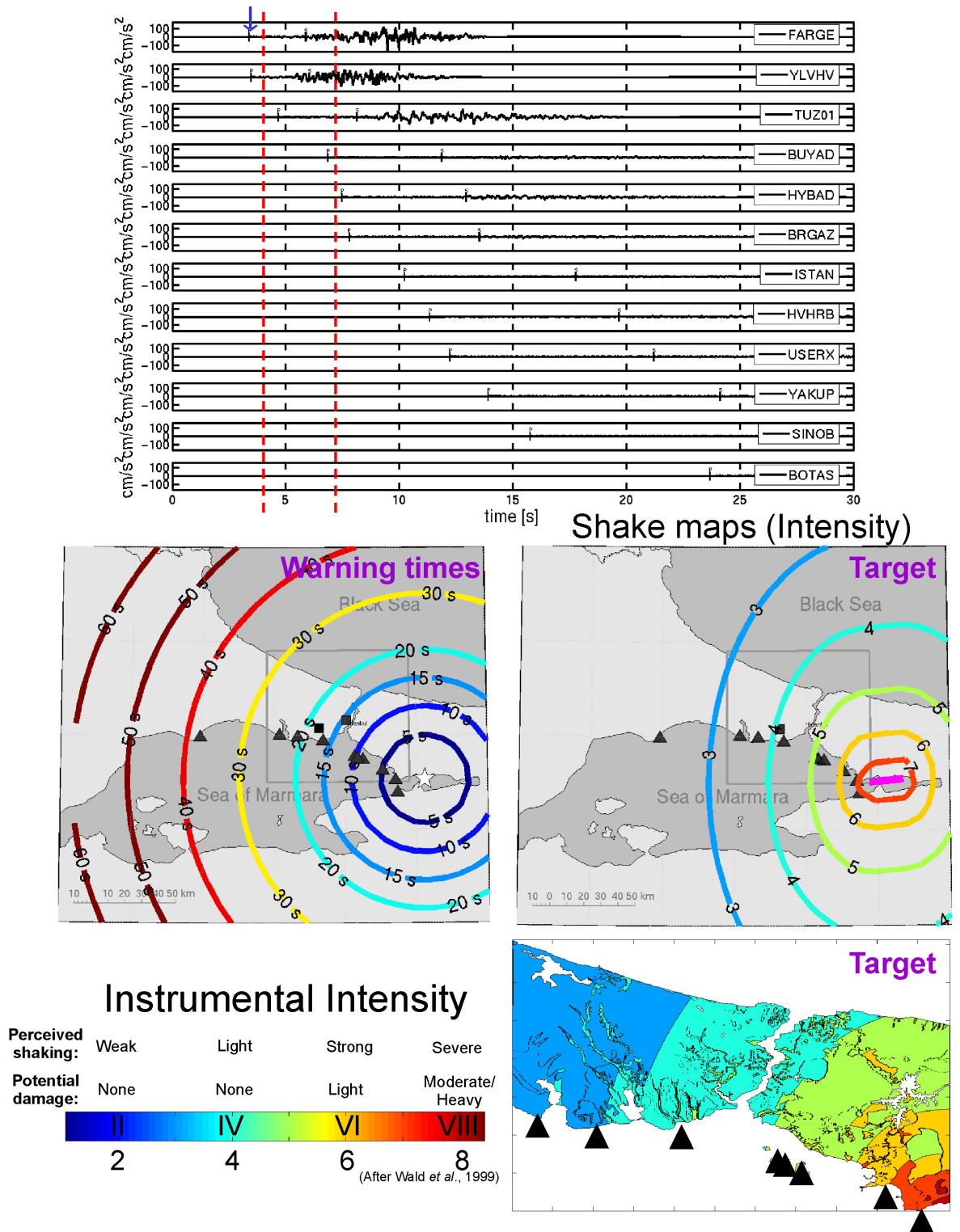


**Figure 6.19: Scenario B** ( $M_w = 6.3$ ). Top: Stochastically simulated mean horizontal components of acceleration at the early warning stations of *IERREWS* and at sites *ISTAN* and *UserX* (see Figure 1.3). Bottom, left: Warning times in the Marmara region defined by the time window between P-wave detection at station *FARGE* and S-wave arrivals. Bottom, right: Shake maps of seismic intensity in the Marmara region for rock condition and, beneath, with site effects in Istanbul metropolitan area.

A conversion scheme for the different intensity levels into simple descriptions of perceived shaking and potential damage is provided by the scales on the lower left in Figures 6.18 and 6.19. This scheme follows the Californian ShakeMap classification proposed by Wald et al. (1999b) and is only restrictively applicable to northwestern Turkey. Translations like this have the advantage that even unskilled persons rapidly understand information provided by shake maps and might respond appropriately to seismic warnings.

Shake maps for the Scenario A earthquake for further ground motion parameters (aside from intensity) are shown in Figure 6.20. Peak ground acceleration (PGA), peak ground velocity (PGV), peak ground displacement (PGD), pseudo-spectral acceleration (PSA) at 1.0 s and 2.0 s at 5% damping, and the cumulative absolute velocity (CAV) are calculated from the attenuation relations determined in Chapter 4.4. For the interpretation of the different parameters with respect to damage potential see Chapter 4.1.

### II.3 Location and Magnitude Estimates by PreSEIS: $Hypo(m)$ and $M_w(m)$

Absolute prediction errors of hypocenter locations and estimates of moment magnitudes for Scenario A and Scenario B by networks  $Hypo$  and  $M_w$  - each as a function of time after triggering of the first sensor - are visualized in Figure 6.21. For the results shown here,  $Hypo$  and  $M_w$  are optimized through the *Levenberg-Marquardt* algorithm. Estimates by PreSEIS are indicated by solid lines. The results are overlaid by the 25th to 95th percentiles and confidence intervals of one standard deviation that have been determined from the entire dataset shown in Figure 6.16. Bars at the bottom line mark the P-wave arrivals at the different early warning sensors of *IERREWS*. Predictions are smoothed over 3.5 s intervals which means that  $d = 6$  in (6.35).

Even if the reliabilities of predictions for the entire dataset clearly increase with time (Figure 6.16), there is not necessarily such a clear convergence towards correct source parameters for single events (Figure 6.21). This behavior is likely due to the fact that the training database contains correctly as well as incorrectly picked events which forces the Neural Networks to stronger generalization and averaging over similar input-output patterns. Figure 6.22 shows the network performances for both scenarios under the assumption that P-wave onsets cannot be picked perfectly. P-wave onsets are once again indicated by the bars at the bottom lines.

### II.4 Ground Motion Prediction by PreSEIS: $Hypo(m)$ , $M_w(m)$ and $Rupt(m)$

Estimates of hypocenter locations and magnitudes alone are not directly meaningful for seismic risk and damage assessment. Only in combination with empirical attenuation laws it is possible to quantify the expected level of ground shaking at potential user sites.

Figures 6.23 and 6.24 show the prediction errors for seismic ground motion at site *UserX* based on estimates of magnitudes and rupture locations provided through  $M_w$  and  $Rupt$ : the solid lines show the predicted level of ground motion at site *UserX* in terms of parameters PGA, PGV, PGD, PSA at 0.3 s, 1.0 s and 2.0 s at 5% damping, seismic intensity, Arias intensity, and CAV as a function of time. In addition, the figures show the level of ground shaking for the true magnitude and true rupture location in combination with the empirical attenuation laws derived in Chapter 4.4 (dashed lines); finally, the plots also illustrate the correct levels of ground motion derived directly from the stochastically simulated data at site *UserX* (dashdot lines).

While the fit between the estimated, the calculated (from attenuation laws), and the observed level of ground motion at site *UserX* is very satisfying for the Scenario B earthquake (Figure 6.24), ground

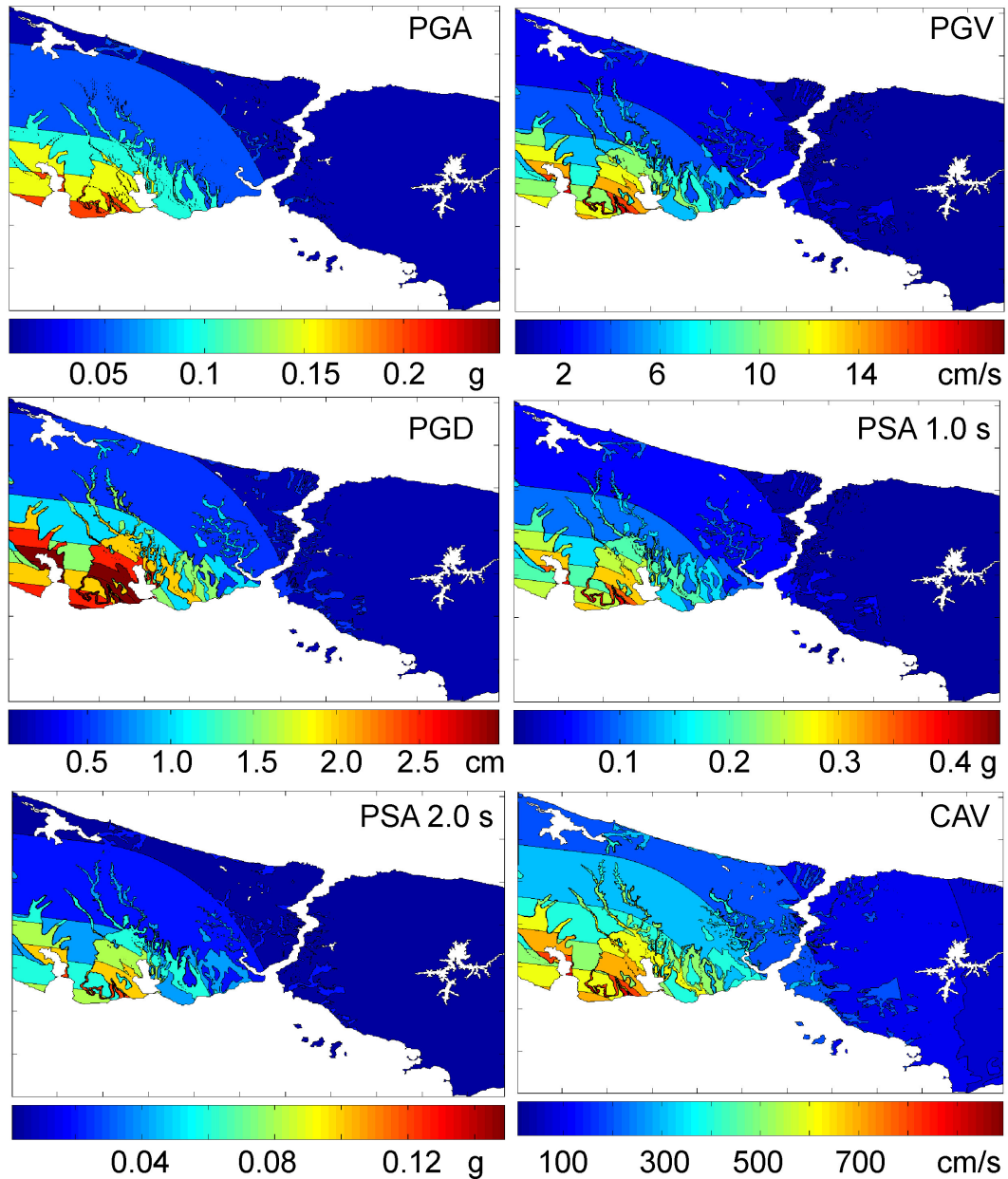


**Figure 6.20: Scenario A** ( $M_w = 6.9$ ). Shake maps for Istanbul metropolitan area for different ground motion parameters calculated from the attenuation relations determined in Chapter 4.4. From top left to bottom right: peak ground acceleration (PGA), peak ground velocity (PGV), peak ground displacement (PGD), pseudo-spectral acceleration (PSA) at 1.0 s and 2.0 s at 5% damping, and cumulative absolute velocity (CAV).

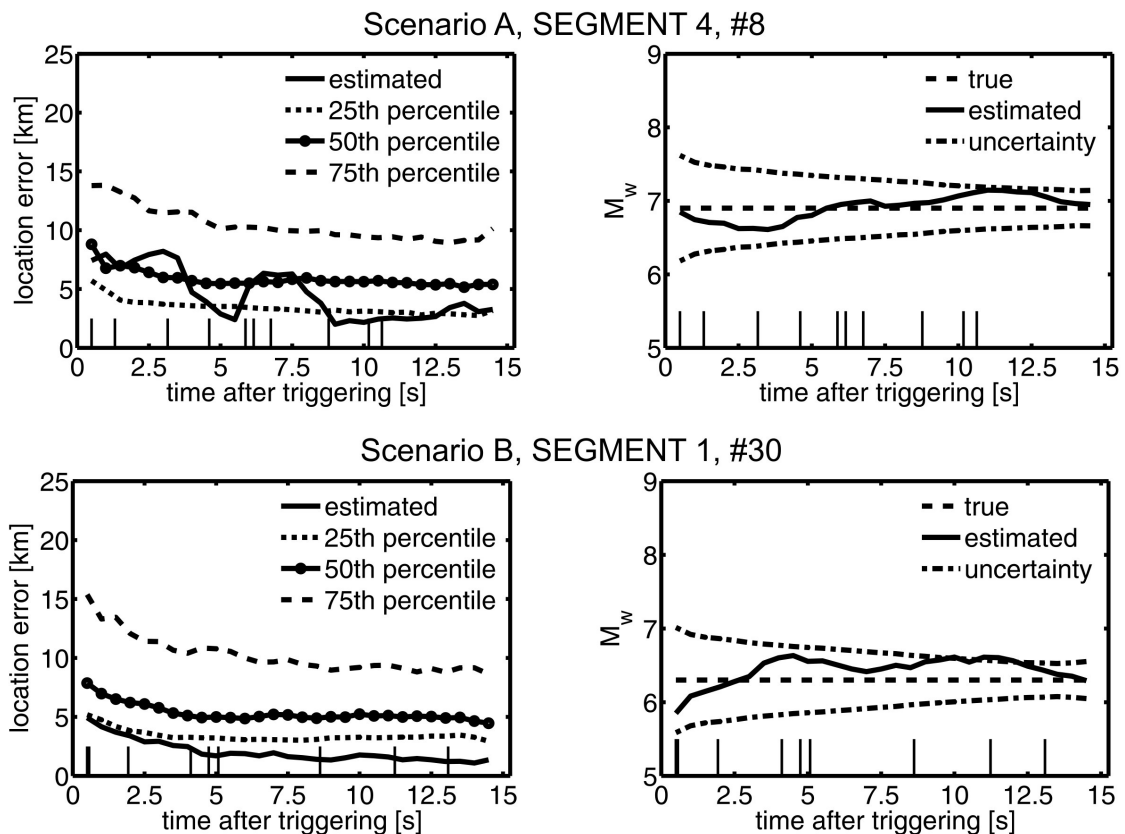


**Figure 6.21: Scenario A (top) and B (bottom).** Performance analyses with location errors (left) and predicted magnitudes (right) as a function of time after P-wave detection at the first sensor presuming the ideal condition that P-wave onsets are perfectly picked. Percentiles and confidence intervals refer to results obtained for the entire database (Figure 6.16). Bars at the bottom lines indicate P-wave arrivals at the different sensors; for the identification of the different stations see Figures 6.18 and 6.19, top. Even if there is a clear enhancement in estimates of source locations and magnitudes with ongoing time for the entire database (Figure 6.16), for single events there is not necessarily such a clear convergence towards correct source parameters. Remember that for earthquake early warning only the first few seconds ( $\approx 4.0$  s) are of interest.

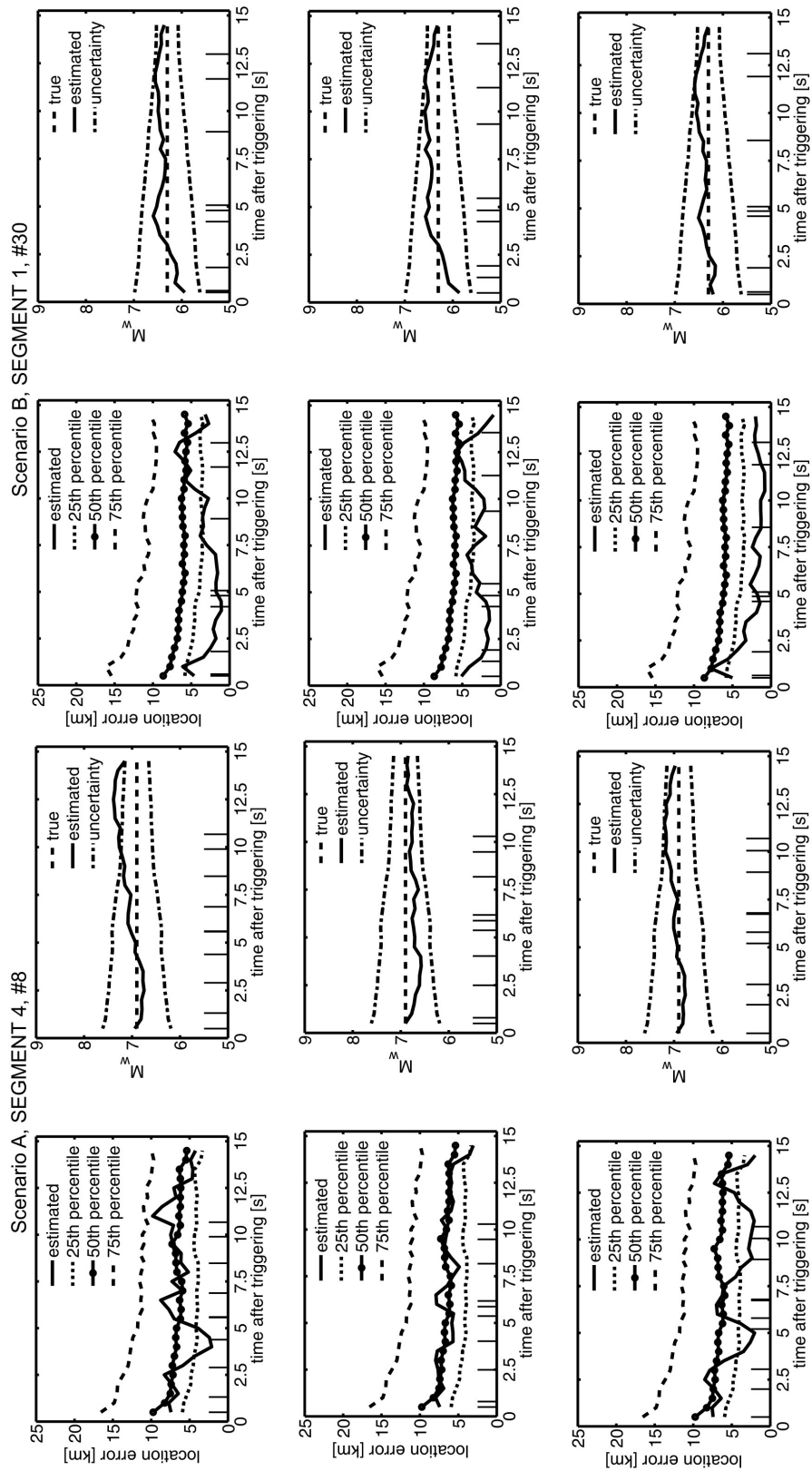


**Figure 6.22: Scenario A (left) and B (right).** Performance analyses for three examples of incorrectly picked P-wave onsets at the different stations. For further explanations see caption of Figure 6.21.



motion estimated by PreSEIS in case of the Scenario A earthquake is partly two times higher than observed (Figure 6.23). Largest errors occur between 10.0 and 15.0 s after triggering. Remember, however, that due to the very small pre-warning times in the Marmara region only the first few seconds ( $\approx 4.0$  s) might be relevant for earthquake early warning. Large errors in ground motion prediction are mainly a consequence of failures in estimates of rupture expansions: *UserX* is only 30 km far from the rupture; even small errors in estimated rupture locations have strong impact on the level of predicted ground motion.

Note also in Figure 6.23 the fairly high differences between ground motion calculated from empirical attenuation laws and observed shaking, e.g. for PGD and PSA at 1.0 s. For real data this effect is expected to be even stronger (in particular caused by site effects). The greatest uncertainty in ground motion prediction is usually not due to errors in magnitude and hypocenter estimates but is a consequence of inaccuracies in empirical attenuation laws (Allen, 2005). This means that the accuracy of predicted locations and magnitudes is less important than the reliability of attenuation laws.

### II.5 Alert Maps of Seismic Intensity by PreSEIS: $Hypo(m)$ , $M_w(m)$ , and $Rupt(m)$

*Shake maps* that are solely based on *estimated* source locations and magnitudes are called *alert maps*. Alert maps are, in particular, for users of interest that operate or rely on networks of lifelines and infrastructures, such as for communication, water supply, electricity, or transportation. Information provided by shake and alert maps enables the rapid identification of network nodes that will most likely suffer damage; the maintenance of lifelines might be ensured by rapid reconfiguration of affected networks. With ongoing time alert maps can gradually transform into shake maps once seismic waves have arrived at stations deployed within the shake map area. Shake maps are required for the assistance of rapid response measures taken *after* earthquake catastrophes (see Chapter 1.1).

Figure 6.25 shows the estimated alert maps for seismic intensity for Scenario A, and Figure 6.26 for Scenario B at 0.5, 1.5, 2.5 and 3.5 s after P-wave arrival at the first sensor. The top figures indicate the location of the wavefronts of direct P- and S-waves, as well as the estimated and true epicenter locations. Alert maps for rock condition are shown in the middle, with site effects in the Istanbul metropolitan area at the bottom. Target shake maps are shown in Figures 6.18 and 6.19. In Scenario A intensity is at first slightly overestimated, in Scenario B underestimated. Rupture expansions estimated through *Rupt* are indicated by solid lines.

### II.6 Estimates of Fourier Amplitude Spectra by PreSEIS: $Spec(m,f)$

Aside from magnitudes, hypocenter locations and rupture expansions, PreSEIS is capable to estimate the smoothed Fourier amplitude spectrum (FAS) of acceleration from 0.25 to 11.25 Hz through the Neural Network *Spec*. Figure 6.27 and Figure 6.28 show the estimated spectra for Scenario A and B 0.5 to 3.5 seconds after triggering. Note that this procedure is different from the ground motion prediction described atop: the FAS is estimated directly and is not determined from attenuation laws. This has the advantage that not two sources of uncertainties are combined with each other: uncertainties of estimated magnitudes and distances and uncertainties of the empirical attenuation laws. The ANNs themselves have learned the local attenuation characteristics affecting seismic wave propagation. This is a very promising approach with good results as demonstrated here for the two scenarios.

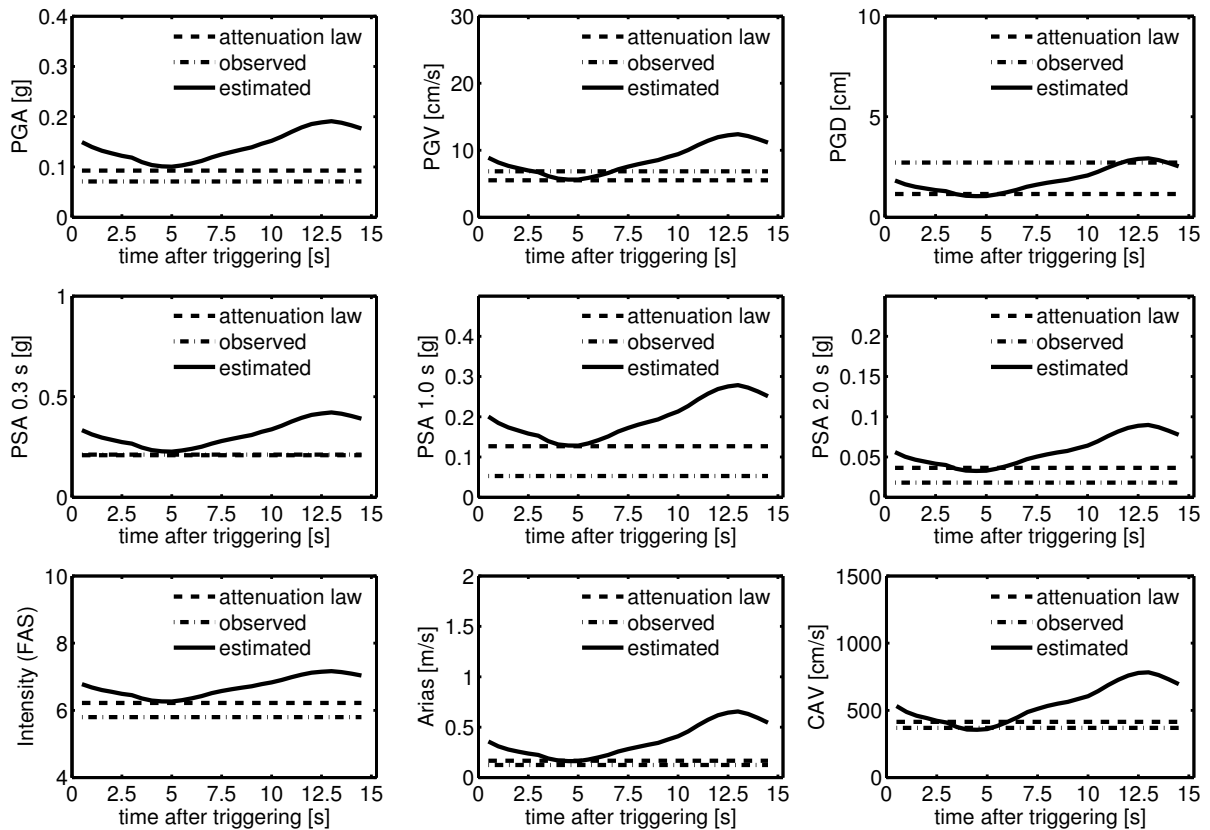


**Figure 6.23: Scenario A** ( $M_w = 6.9$ ). Level of shaking at site *UserX* quantified through different ground motion parameters. Solid lines: ground motion from estimated rupture location and magnitude combined with empirical attenuation laws; dashed lines: ground motion from true rupture location and magnitude combined with attenuation laws; dashdot lines: determined from simulated acceleration time series at site *UserX*. Ground motion is partly two times overestimated by PreSEIS, in particular between 10.0 and 15.0 s after triggering. For early warning, however, only the first 4.0 s are relevant. Note the significant differences between ground motion calculated from empirical attenuation laws (Chapter 4.4) and the observed ground shaking, e.g. for PGD and PSA at 1.0 s. These errors are mainly caused by failures in predictions of rupture expansions. Uncertainties in the empirical attenuation laws have very strong impact on the predicted ground motion and are more relevant than accuracies in estimated hypocenter locations and magnitudes (Allen, 2005).

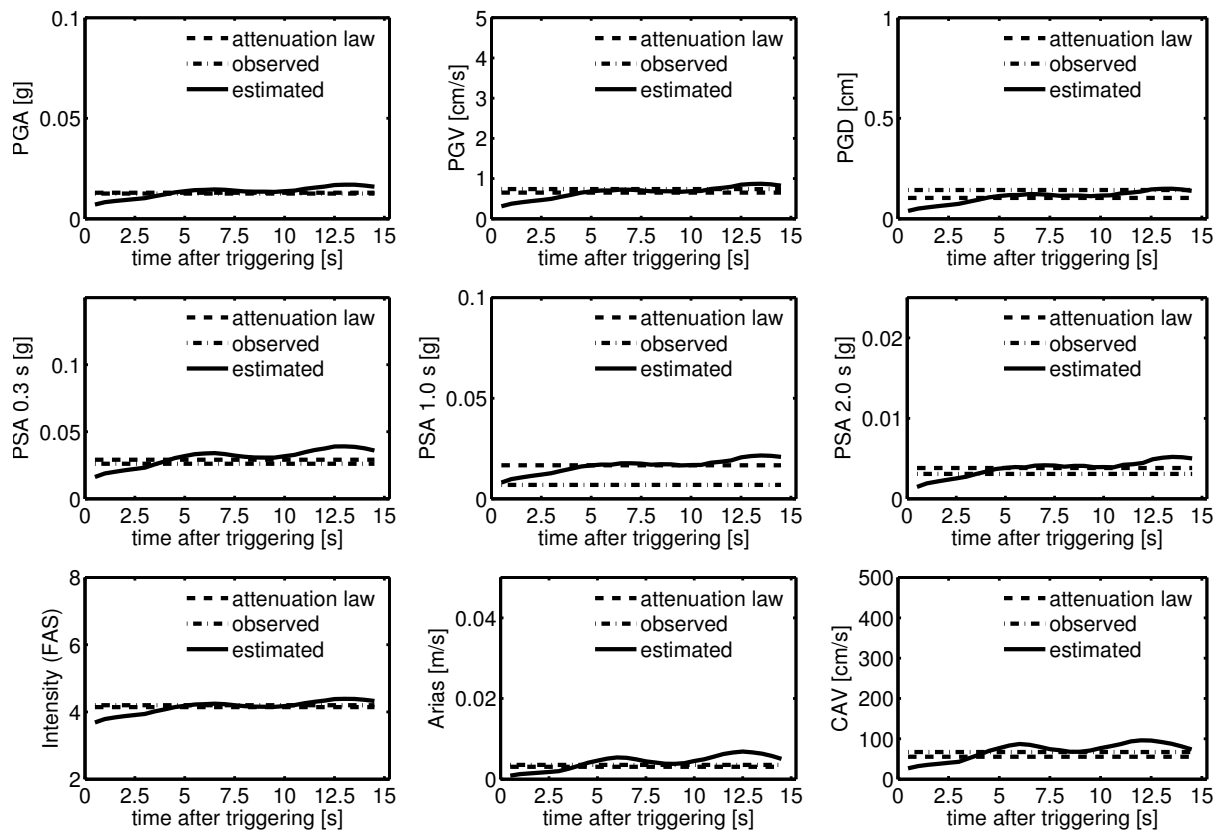


**Figure 6.24: Scenario B** ( $M_w = 6.3$ ). See caption of Figure 6.23. The estimated (by PreSEIS), the calculated (from attenuation laws) and the observed level of ground shaking at site *UserX* fit very well.

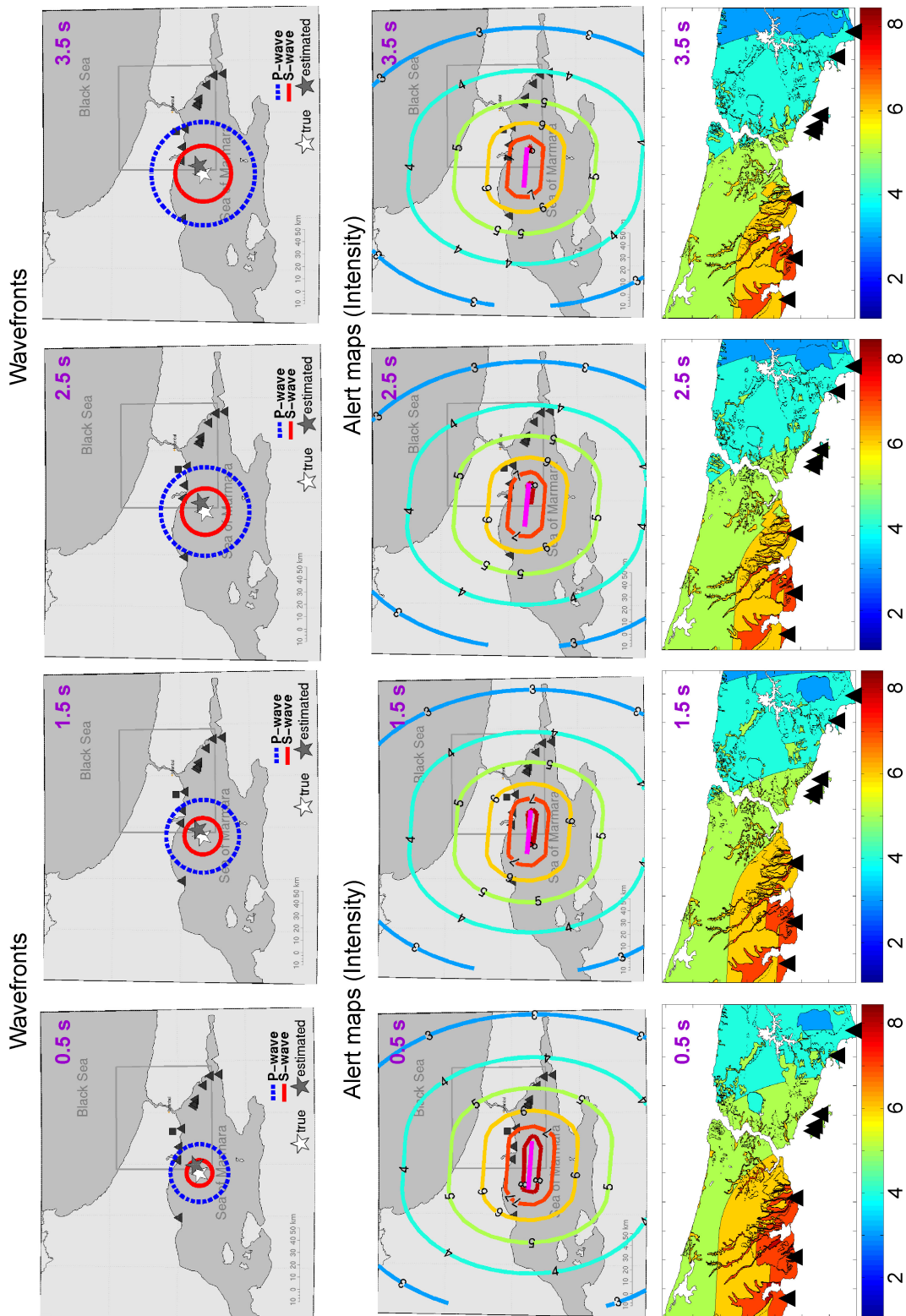


**Figure 6.25: Scenario A** ( $M_w = 6.9$ ). Real-time estimates of seismic intensity at 0.5, 1.5, 2.5 and 3.5 s after P-wave arrival at station *SINOB*. Top: P- and S-wavefronts, as well as true and estimated epicenter locations. Middle: Alert maps of seismic intensity for rock condition. Bottom: Alert maps of seismic intensity with site effects in Istanbul metropolitan area. For target maps see Figure 6.18.

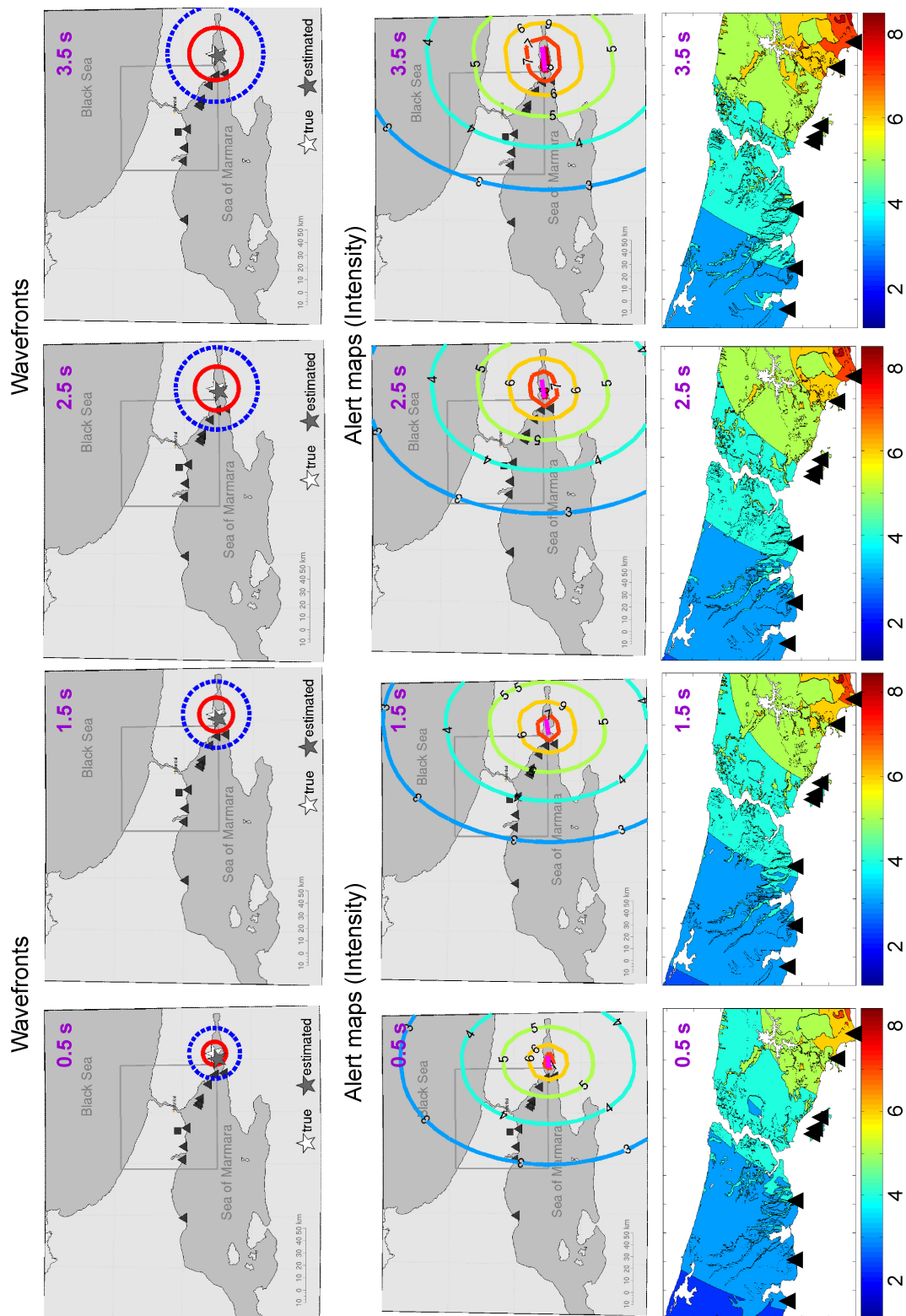


**Figure 6.26: Scenario B** ( $M_w = 6.3$ ). Real-time estimates of seismic intensity at 0.5, 1.5, 2.5 and 3.5 s after P-wave arrival at station *FARGE*. Top: P- and S-wavefronts as well as true and estimated epicenter locations. Middle: Alert maps of seismic intensity for rock condition. Bottom: Alert maps of seismic intensity with site effects in Istanbul metropolitan area. For target maps see Figure 6.19.

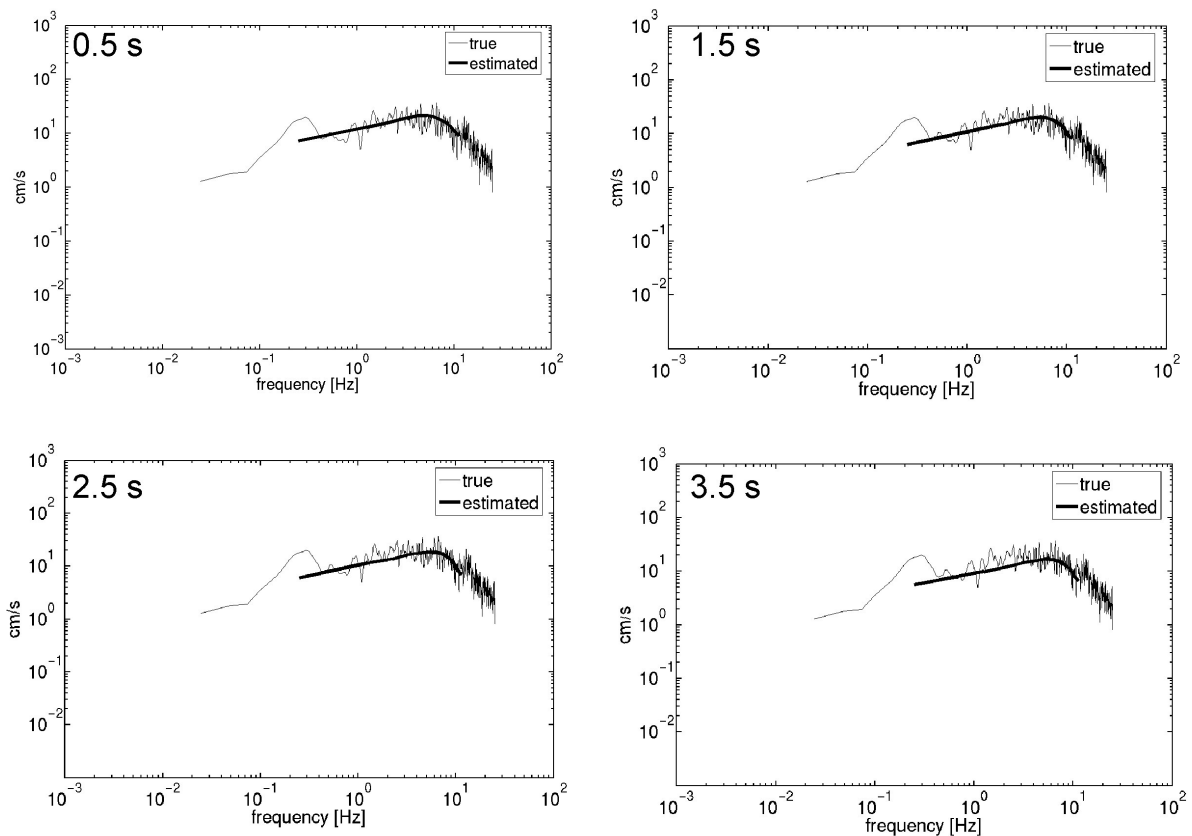


**Figure 6.27: Scenario A** ( $M_w = 6.9$ ). True (thin line) and estimated (thick line) Fourier amplitude spectra (FAS) at site *UserX* at 0.5, 1.5, 2.5, and 3.5 seconds after P-wave arrival at station *SINOB*. The ANNs themselves have learned the local attenuation characteristics of the crust; no empirical attenuation laws are required.

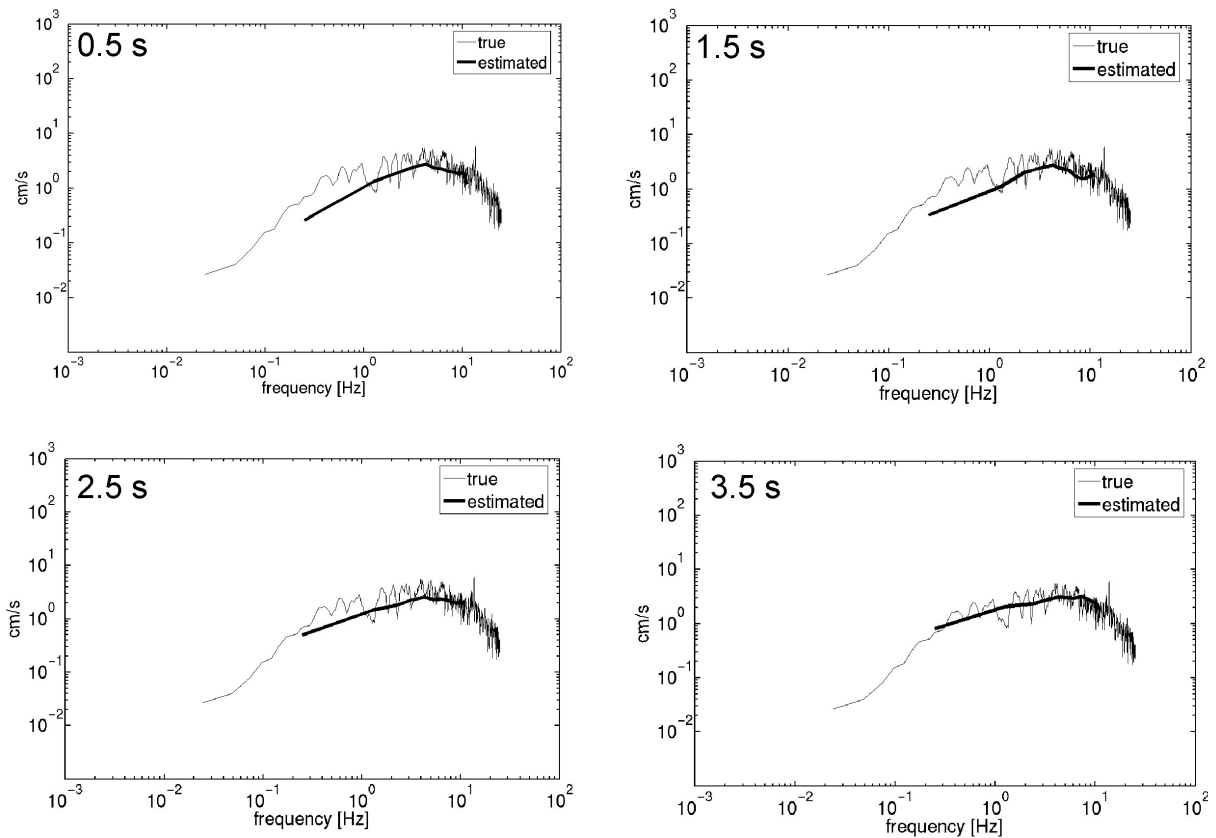


**Figure 6.28: Scenario B** ( $M_w = 6.3$ ). True (thin line) and estimated (thick line) Fourier amplitude spectra (FAS) at site *UserX* at 0.5, 1.5, 2.5, and 3.5 seconds after P-wave arrival at station *FARGE*. See caption of Figure 6.27.

### 6.3 Discussions

PreSEIS (Pre-SEISmic shaking) is a methodology for the non-linear inversion for seismic source parameters from time-dependent input information on ground motion at several sensors that are combined within a seismic network with real-time data transmission. The inversion for source locations and magnitudes is based on Two-Layer Feed-Forward Neural Networks (Chapter 6.1.3). Network weight parameters are iteratively updated during a training phase until appropriate statistical models of the data are found. As described in this chapter, I have tested three parameter optimization methods and found a clear superiority of the *Levenberg-Marquardt* algorithm to *Gradient Descent with Momentum Term* and *Resilient Propagation (RPROP)* with respect to error rates of the resulting models as well as to the number of required training iterations.

With ongoing time more and more sensors will detect the propagating seismic waves and longer time series of ground motion will become available at the different sites. For the entire dataset of 280 simulated scenario earthquakes in the Marmara region it is clearly possible to enhance estimates of seismic parameters with time. This implies that at each time step after triggering of the first sensor, estimates can be provided with assignable uncertainties. The trade-off between reliabilities of warnings and remaining warning and response times can be only solved in consideration of user-specific needs and costs in case of possible missed and false alerts. Note that for single event scenarios there is not necessarily such a clear convergence towards correct source parameters with ongoing time and small interim deterioration can be observed. This behavior might be a result of the high tolerance of PreSEIS towards missed P-wave onsets on which the Neural Networks have been trained.

In combination with empirical attenuation laws estimated source locations and magnitudes can be used to predict the level of ground motion either at a specific site or in expanded maps, called *alert maps*. Alert maps provide meaningful information for users that operate or depend on infrastructure or lifeline networks, including, e.g., communication, electricity, water supply and transportation. Neural Networks in PreSEIS are not only trained to estimate positions of earthquake hypocenters but also to predict likely locations and expansions of evolving ruptures, i.e. of finite sources. Predictions of ground motion can benefit from this information because shaking generally rather depends on closest distance between the rupture and a given site than on the hypocentral distance. In addition, effects of rupture directivity can be more easily integrated after the assessment of rupture expansions. Examples of the effect of rupture directivity are schematically illustrated in Figure 6.29.

One outcome of the performance studies of PreSEIS in this chapter is that not the accuracy of magnitude and location is most essential but uncertainties in attenuation laws. In particular, site effects and non-linear effects in case of real strong motion data might be crucial. Also source effects have strong impact on ground motion as follows from the attenuation laws determined in Chapter 4.4. A possible way to solve the problem of uncertainties in attenuation laws has been demonstrated in this chapter using the example of predicting the Fourier amplitude spectrum (FAS) of ground shaking at a given site from ground motion measurements at the early warning sensors: PreSEIS is trained to estimate the FAS without the indirect combination of estimated source parameters with empirical attenuation relations. As a consequence, the Neural Networks themselves have to learn the local attenuation characteristics affecting the propagating seismic waves. Performance analyses in this chapter reveal very good results of this approach. For further discussions see Chapter 7.



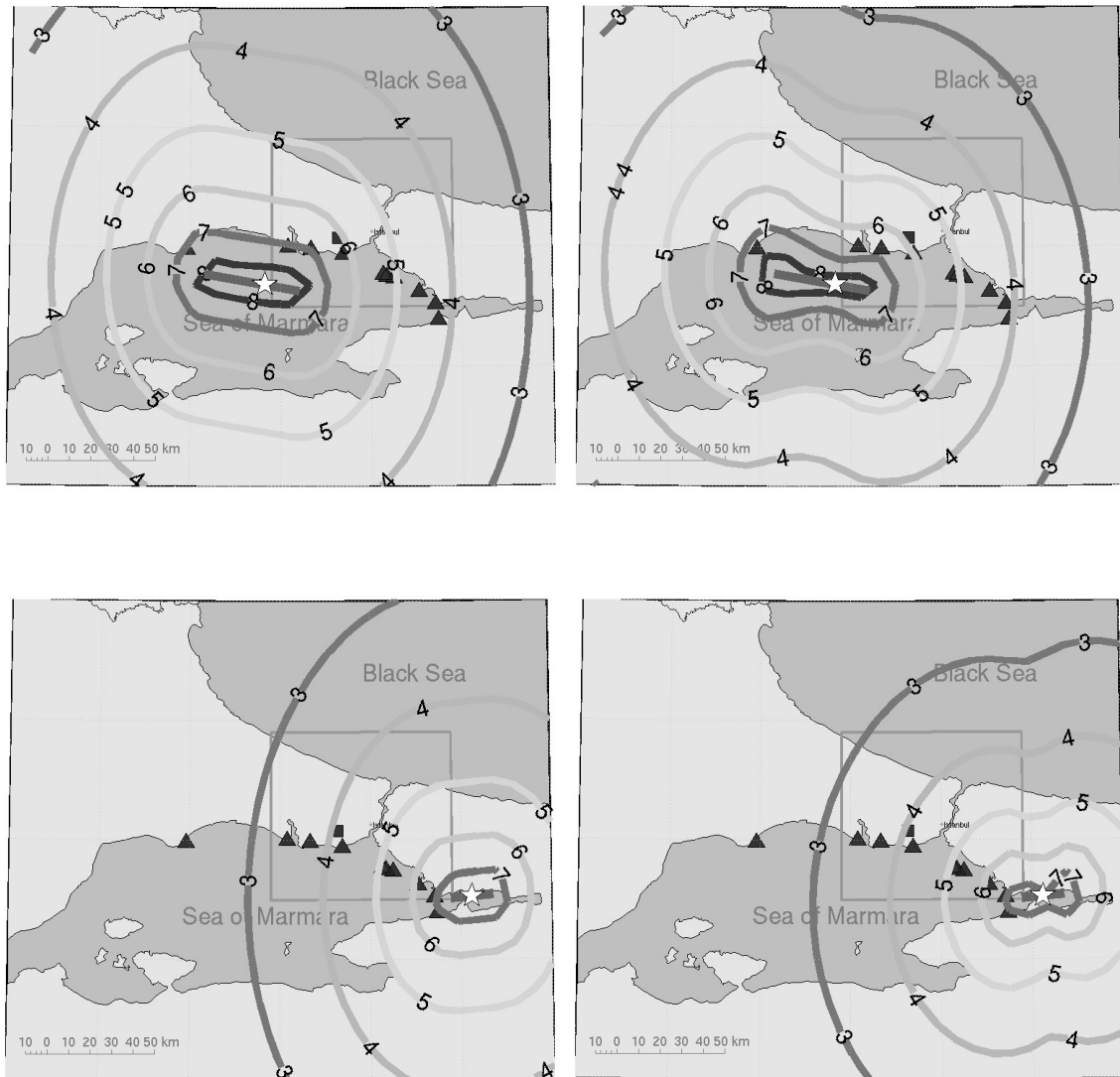


**Figure 6.29: Scenario A (top) and B (bottom).** Shake maps for seismic intensity for rock condition without (left) and with (estimated) directivity effects (right). The maps rather demonstrate the principle idea than true effects.



## Chapter 7

# Summary and Outlook

This chapter will summarize the most important results linked to the PreSEIS (Pre-SEISmic shaking) methodology for earthquake early warning developed in this thesis. For a more detailed description of the single statements I will give references to the respective chapters in this work. Aside from the stochastic simulation of seismic ground motion and the development of PreSEIS described in this summary, this thesis makes an important contribution to earthquake early warning in Romania: Scaling relations with assigned confidence intervals allow for a rapid estimation of the expected level of ground shaking in the Romanian capital Bucharest using the maximum P-wave amplitude in the epicentral Vrancea region (Chapter 5.3.4). These estimates are available approximately 25 s before high-amplitude shear waves arrive in Bucharest. The feasibility to link the output of the early warning system to the *Urban Shakemap for Bucharest* (Wirth, 2004; Bartlakowski et al., 2006) is demonstrated using the example of the October 27, 2004 ( $M_w = 5.9$ ) Vrancea earthquake.

### 7.1 Summary

Either embedded in a Real-Time Earthquake Information System or as stand-alone, earthquake early warning systems can make a highly beneficial contribution to *co-seismic* risk reduction. Early warning systems make basically use of differences in the propagation speed of seismic and electromagnetic waves; if necessary they issue warnings to potential users before seismic waves arrive. Pre-warning times thereby are very little compared to other natural hazards such as tsunamis, volcanic eruptions, or floods: within only a few seconds the systems must recognize the severity of impending ground shaking and trigger automatisms to reduce likely damage to structures and equipment by the approaching seismic waves (Chapter 1.1). Despite of significant progress in seismic real-time data processing and communication technologies in the last years, there are only a few earthquake early warning systems in operation now (Chapter 5.2). The main obstacle for the realization of warning systems is the claim of extremely high reliability together with the need to issue warnings as soon as possible. Earthquake magnitudes are favorably estimated from the initial parts (P-wave) of seismic recordings at single stations. This *on-site* warning approach is very quick, however, less robust than the traditional *regional* warning approach that is based on station networks (Chapter 5.1). Empirical studies (e.g., Kanamori, 2005) support the principle feasibility of this approach, or at least the possibility to specify a lower boundary of earthquake magnitudes within the first three seconds (Chapter 5.3). High scatter in estimates, though, often requires averaging over predictions at several on-site warning sensors, which is in contradiction to the original idea of on-site warning.

In this thesis, I have developed a methodology for earthquake early warning - called PreSEIS (Pre-SEISmic shaking) - that takes advantage of both, *regional* and *on-site* warning paradigms. PreSEIS integrates all available information from a small network of seismic sensors - similar to the regional warning approach (Chapter 6.2). In contrast to *regional* warning, however, PreSEIS does not require that seismic waves have arrived at all sensors before warnings are issued because also non-triggered stations provide important information on the location of the seismic source and help to confine the space of possible solutions. First estimates are available only 0.5 s after triggering of the first early warning sensor. PreSEIS therewith is as quick as the on-site warning approach that is based on single stations at a concurrent higher stability due to a higher number of involved stations.

PreSEIS has been developed using the example of the Turkish mega-city Istanbul. Istanbul is exposed to an extremely high seismic risk due to its closeness to seismic fault segments in the Sea of Marmara and the high concentration of human and industrial settlements in the Marmara region (Chapter 1.3). These fault segments form the western continuation of the North Anatolian Fault and partly run only 15 to 20 km south of Istanbul. From previous earthquakes in the Sea of Marmara and from the stress transfer of the 1999 Kocaeli earthquake ( $M_w = 7.4$ ) Parsons et al. (2000) determine a  $62 \pm 15\%$  probability of strong shaking in Istanbul metropolitan area during the next 30 years and  $32 \pm 12\%$  during the next decade. Erdik et al. (2003a) estimate that in case of a  $M_w = 7.5$  earthquake in the Sea of Marmara destructions might amount to about USD  $1.1 \cdot 10^{10}$  losses, with 40,000 to 50,000 deaths, and between 430,000 to 600,000 destroyed households. Since autumn 2002 the Kandilli-Observatory of the Bogazici University operates ten strong motion sensors with real-time communication link to two datacenters in Istanbul. These early warning stations are part of the *Istanbul Earthquake Rapid Response and Early Warning System (IERREWS)*, Chapter 5.2). Pre-warning times are a crucial issue when designing early warning systems. They are generally defined by the time window between P-wave detection at the first early warning station and the arrival of high-amplitude S-waves at the user site. In case of Istanbul average pre-warning times are expected to range between 8 to 15 s (Chapter 6.2). This short time span implies that an earthquake early warning system in the Marmara region should be capable to estimate the severity of impending ground shaking in less than 4.0 s after detection.

The low seismicity rate in the Marmara region (Chapter 1.3) aggravates the development and verification of algorithms for earthquake early warning. Many other regions in the world are affected by the same problem, in particular with respect to missing strong motion data. For the development and evaluation of PreSEIS in this thesis I use simulated ground shaking time series obtained from the *Stochastic Simulation Method for Finite Faults* (Beresnev and Atkinson, 1997, see Chapter 3.2). This approach provides a simple and suitable technique for the simulation of ground shaking time series for moderate and strong earthquakes that cover the frequency band of up to about 10 Hz. Its power is that detailed specifications of earthquake sources and propagation effects on seismic waves are not required. In contrast to the *Stochastic Point Source Approach* (Boore, 1983) the *Stochastic Simulation Method for Finite Faults* (Beresnev and Atkinson, 1997) allows for the inclusion of source dimensions. This is a strongly required extension of the initial approach since source-to-site distances in the Marmara region are extremely short so that source finiteness must be considered. The principle idea behind the stochastic simulation of seismic acceleration is the combination of the estimated Fourier amplitude spectrum of ground motion at a given site with a random phase (Boore, 1983, 2003). In case of the *Stochastic Simulation Method for Finite Faults* the seismic rupture is considered to be composed of numerous point sources. The final seismogram is obtained from summation of contributions of all subfault elements considering respective time delays due to rupture propagation. Compressional waves are due to their high speed essential for early warning. The *Stochastic Simu-*

*lation Method for Finite Faults* for shear waves is therefore extended to compressional waves so that both, P- and S-waves, can be modeled in this thesis (Chapter 3.2.2).

The source spectrum for finite faults is highly sensitive to seismic wave speed ( $\alpha$ ,  $\beta$ ), as well as to maximum slip and rupture velocities ( $v_{max}$  and  $v_r$ ) (Chapter 3.2). For seismic simulations in this work a simple 1D velocity model with  $\alpha = 5.7$  km/s,  $\beta = 3.3$  km/s, and  $v_r = 0.8 \beta$  is used (Table 3.1). Source parameters, such as the maximum slip velocity controlled by the dynamic stress drop of the earthquake, are kept variable within physically reasonable limits (Chapter 3.3). Bi- and unidirectional ruptures are modeled. For the integration of site effects at the sensor and user sites, I make use of mean amplification spectra empirically determined by Boore and Joyner (1997) for different soil types following the NEHRP soil classification scheme (Building Seismic Safety Council, 1995); the missing amplification function for NEHRP class B thereby is determined from non-linear interpolation (Chapter 2.3.3). With adequate input parameters for the Marmara region taken from the literature, a set of synthetic ground motion records for 280 scenarios with  $4.5 \leq M_w \leq 7.5$  is generated (Chapter 3.3). Amplitude parameters, such as peak ground acceleration (PGA), derived from this database have a variability in the order of factor two due to varied source parameters, different amplification spectra for distinct soil types, and the Gaussian noise as basis for the stochastically simulated phase.

Chapter 4.4 describes the determination of attenuation relations for nine ground motion parameters from the database of simulated acceleration time series, including peak values, spectral parameters, and intensity measures. Data-consistent attenuation laws play an important role in the later described procedure for the calculation of shake and alert maps in the Marmara region. They can be also used for a rough evaluation of the synthetics by comparison with observational data in northwestern Turkey (Chapter 4.4.1) and with relations proposed for other seismic active regions in the world (Sadigh et al., 1997; Boore et al., 1997; Campbell, 1997; Erdik et al., 1985; Wald et al., 1999a). It turns out that the fit is generally very good, whereby the decay of ground motion parameters in the simulated data is somewhat larger at *Joyner-Boore distances* of about 30 km. Correlation analyses with Fourier amplitudes (Chapter 4.2) reveal that ground parameters rely - as expected - on distinct frequency bands. For example, peak ground acceleration (PGA) is mainly controlled by frequencies  $> 3.0$  Hz, whereas peak ground displacement (PGD) generally depends on frequencies  $< 0.5$  Hz. The afore described fit and misfit of the attenuation relations of the different parameters therefore can be used for a rough quality assessment of the synthetics in different frequency bands. It turns out that the stochastic simulation method is less reliable in reproducing long-period motions (Chapter 4.5).

PreSEIS considers earthquake early warning as a problem of time-dependent non-linear inversion for source parameters from the available information at different sensors. With ongoing time more and more stations will be triggered by the propagating seismic waves and longer time series at the single sites will become available. Thus, the estimates of source locations and magnitudes (and others) are continuously updated every 0.5 s. PreSEIS is based on Artificial Neural Networks (ANNs), more strictly speaking on *Two-Layer Feed-Forward* Neural Networks (Chapter 6.1.3). ANNs are generally used as statistical models of processes and systems. They are composed of a high number of simple interconnected processing units called *neurons*. The importance of a link between one neuron to another is controlled by a *weight* parameter. Weights are iteratively adapted to a given inversion problem from a set of example patterns using appropriate optimization algorithms (*supervised learning*). Neurons in a *Two-Layer Feed-Forward* Neural Network are arranged in one input, one hidden, and one output layer (Chapter 6.1.3).

PreSEIS uses Artificial Neural Networks for the mapping of seismic observations onto likely source parameters, including hypocenter locations, earthquake magnitudes, rupture expansions and the

Fourier amplitude spectrum of ground motion at a specified user site. PreSEIS uses parameterized seismic observations at the sensors at subsequent time steps as basis for time-dependent predictions of source parameters. In this thesis the PreSEIS approach is demonstrated for relative P-wave onset times and logarithmic values of the time-dependent cumulative absolute velocity (CAV) as input information (Chapter 6.2). The CAV has several advantages in comparison to other ground motion parameters (Chapter 4.1.4), e.g., it shows a high correlation with seismic intensity. In case of noisy input data the usage of the *bracketed* CAV with a dynamic adaption to the present noise level is recommended (Chapter 4.1.4). The PreSEIS methodology is expected to be not only applicable to CAV but also to other parameterizations of seismic ground motions such as to the predominant period (Chapters 4.1.2 and 5.3).

The Two-Layer Feed-Forward Neural Networks (more strictly speaking the network weights) are adjusted to the inversion problem by usage of the stochastically simulated acceleration data: 70% of the afore described scenario earthquakes are used as example patterns for the underlying input-output relations. From the training database, PreSEIS learns among others the *a priori* information on likely source locations in terms of earthquake clusters along the fault segments. Three parameter optimization methods for the iterative update of network weights are tested: (1) *Gradient Descent with Momentum Term*, (2) *Resilient Propagation (RPROP)*, and (3) *Levenberg-Marquardt* optimization (Chapter 6.1.2). Gradients of the error function, that describes the difference between desired and observed network outputs for each example pattern in dependence on network weights, are determined through the application of the *Backpropagation* algorithm (Chapter 6.1.4). The weight update is terminated once the prediction error for an independent validation subset increases. The validation subset contains 10% of the simulated scenarios. This *early stopping* rule accounts for the desired generalization capability of the Neural Networks (Chapter 6.1.5). The number of required neurons in the hidden layer of the Two-Layer Neural Networks controls the complexity of the statistical models. Systematic tests of different architectures are used in this thesis to find the optimum network (here with six hidden neurons) that is characterized by low errors for both, *known* training and *unknown* test subsets. In order to exclude possible dependencies of the obtained statistical models on start values of the inversion, performance tests are repeated four times, each time with a different weight initialization and randomly changed training, validation and test subsets (*bootstrapping*). As a rule of thumb each weight parameter in the Neural Network requires ten example patterns in the training subset. Through the inclusion of patterns with incorrectly picked P-wave onsets, the database of simulated scenarios for the Marmara region is artificially enlarged. This procedure has the additional advantage that PreSEIS can now be more easily applied to observational data where onsets can be hardly picked without errors.

Performance analyses of the PreSEIS methodology are carried out for (1) the entire database and (2) two separate scenario earthquakes. They demonstrate a clear increase of reliability of predictions with ongoing time after triggering of the first sensor (Chapter 6.2). Largest errors usually occur at the boundary of the sensor network and for earthquakes that occur beyond the large fault segments in the Sea of Marmara. From the three analyzed optimization techniques the *Levenberg-Marquardt* algorithm produces the best models with lowest errors at each time step: the average hypocenter location error is 8.8 km (median) 0.5 s after triggering of the first sensor and can be reduced to 5.9 km in the following 3.5 s. In the same time interval the magnitude error is reduced from  $\pm 0.7$  to  $\pm 0.5$  magnitude units (unit standard deviations). Furthermore, *Levenberg-Marquardt* requires the lowest number of training iterations. For single events the convergence towards correct source parameters can show interim deterioration; however, once again performances are generally satisfying.

Estimated hypocenter locations and magnitudes alone are not directly meaningful for seismic risk

and damage assessment. In combination with empirical attenuation relations, however, they can be used to predict the level of ground motion either at a specific site or in expanded maps, called *alert maps* (Chapter 6.2). The required magnitude-dependent amplification factors at different soil types are estimated from the stochastically simulated time series (Chapter 4.4). Alert maps provide meaningful information to users that operate or depend on infrastructure or lifeline networks, including, e.g., communication, electricity, water supply and transportation networks. Furthermore, alert maps can be considered as first order shake maps that start with estimated source parameters and empirical attenuation laws and then gradually transform into shake maps once observational data is available. Observational data could in case of the *IERREWS* system come from the 100 off-line stations (Chapter 5.2.5). PreSEIS is not only capable to estimate positions of earthquake hypocenters but also to predict in real-time likely locations and expansions of evolving ruptures. Predictions of seismic ground motion can benefit from this information because shaking generally depends rather on closest distances between the rupture and a given site than on hypocentral distances. In addition, directivity effects of the propagating rupture can be more easily integrated after the assessment of rupture expansions.

An important outcome of the performance studies of PreSEIS is that not accuracy of magnitudes and locations are the most essential factors in seismic ground motion predictions, but uncertainties in attenuation laws (Chapter 6.2). In particular, site effects and non-linear effects of seismic waves for observational data are crucial. Remember that also source effects - such as slip distributions - have strong impact on the level of ground motion with a variability in the order of a factor two. The problem of uncertainties in attenuation laws can be solved as demonstrated in this thesis: the Artificial Neural Networks in PreSEIS can be trained to predict the Fourier amplitude spectrum (FAS) of ground motion at a given user site directly, i.e. without the combination with empirical attenuation relations (Chapter 6.2). In this case, the ANNs themselves learn the local attenuation characteristics affecting the seismic waves. This approach gives very promising results.

The developed PreSEIS methodology demonstrates the reasonability to combine seismic observations at a network of ground motion sensors for a rapid and reliable estimate of seismic source parameters suitable for earthquake early warning.

## 7.2 Outlook

The present PreSEIS version has two problems: first, the localization procedure is based on *relative* P-wave arrivals and is therewith fairly sensitive to the P-wave onset detection at the first triggered sensors. It is reasonable to design and train Neural Networks for different subsets of early warning sensors that can be used if one (or more) of the sensors fail. Second, the method requires a large training database so that the Artificial Neural Networks (ANNs) can learn the desired input-output relations including, e.g., local ground motion characteristics at the sensor sites. For the application of the approach to real data PreSEIS has to be modified to allow an open architecture of the network with possibly relocated sensors. For the adjustment of weight parameters ANNs require many training examples that are, however, in many endangered areas in the world not available. A possible solution to this problem is the combination of (1) worldwide recorded weak and strong motion data with information on general characteristics of seismic wave propagation; (2) local data with information on local features, such as on fault locations, seismic wave velocities, crustal attenuation, and local site effects at the sensors; and (3) simulated ground motion time series, e.g. generated by the Stochastic Simulation method, the Empirical Green's Functions approach, or Finite Difference (FD) models (Chapter 3.1). With each new local earthquake or at regular time intervals the Neural Networks

should be updated using the newly available records. Aside from the Two-Layer Feed-Forward Neural Networks applied in this thesis there are many other classes of ANNs that appear useful for inversion problems in earthquake early warning, e.g. networks with feed-back loops (e.g., Rojas, 1993). Other methods - such as *decision tree approaches* - have the advantage that they provide more insight into the inversion than ANNs which are generally considered as *black boxes*.

The Geophysical Institute at Karlsruhe University will participate in two successive projects on earthquake early warning in that the PreSEIS methodology will be tested and modified. Within the *Seismic eArly warning For EuRope (SAFER)* (FP6-2005-Global-4) project it is intended to apply PreSEIS to real weak and strong motion data recorded in Europe and California. The consideration of three-component measurements at the different sensors will require modifications of the present PreSEIS version. Other parameterizations of seismic input data aside from CAV will be explored. In the scope of the *BMBF/DFG-Sonderprogramm Geotechnologien - Frühwarnsysteme im Erdmanagement* the present *Istanbul Earthquake Rapid Response and Early Warning System (IERREWS)* will be expanded to a *Earthquake Disaster Information System for the Marmara Region, Turkey (EDIM)* with additional stations and communication links through satellites. Earthquake early warning will be stronger integrated into the rapid response systems with shake map and damage estimation tools.



## Appendix A

# Response to Earthquake Early Warnings

Examples for response to early warnings with 10 and 50 s warning time after Goltz (2002):

---

10 s Warning Time	50 s Warning Time
<hr/> <hr/>	
<b>1. Education:</b>	
notify teachers with walkie-talkies	shut off gas
have custodian shut off gas	send out/gather emergency supplies
alert custodial staff to secure building	contact fire department, district office, police
shut off machines, move from lab equipment	secure lab equipment / evacuate lab
notify security to be on alert	sound alarms
get walkie-talkies	turn off computers
move clear of falling objects	evacuate to outside area
	contact plant manager
	protection for students in the hallways, ...
	get walkie-talkies, cell phones
	initiate emergency response plan
	notify security to be on alert
	focus on protecting smallest children
<hr/>	
<b>2. Health care:</b>	
shut off equipment	secure equipment (beds etc.)
secure supplies	better meet needs of critical patients
secure patients	shut down labs
shut off gas	stop surgeries, procedures
stop cutting in the emergency room	some evacuation

shut off water  
stop elevators

turn off gas, water  
secure patients with pillows, blankets  
secure hazardous materials  
save work on computer  
get people out of pool  
secure elevator  
secure / shut down operating room  
evacuate lobby, emergency room  
get patients dressed  
thorough job of alerting people

---

**3. Emergency services:**

turn off computer  
send alert to fire department command center  
warn community  
make sure everyone is out of elevators  
start moving equipment out of building  
activate backup  
alert field workers  
shut down equipment  
evacuate bottom floor  
stop hazardous work  
secure equipment

turn off computers  
signal buildings to open automatic doors  
notify schools, hospitals  
prisoner relocation  
move vehicles/equipment out  
notify field workers  
siren for community/broadcast to community  
evacuate elevator  
turn generator on/switch to generators  
clear fire stations  
shut down gas, electricity  
shut down hazardous material  
direct traffic away from underpasses  
use mobile data terminals  
notify watch deputy/jailer

---

**4. Utilities and transportation:**

start making calls  
shut down computers  
notify field  
shut down gas  
alert drivers  
control traffic signals  
put information on the computer

open circuit breakers  
drop customer services  
turn on generator  
notify field workers  
alert fuel workers  
notify police and fire departments  
secure equipment  
stop traffic  
prevent hazardous spills  
inform public works  
get vehicles out of garage  
possibly evacuate  
notify drivers/operators  
shut down computers  
broadcast warning  
stabilize power  
notify air traffic controller, floor wardens, fire station  
stop elevators  
shed load

---

## Appendix B

# Simulated Earthquakes in the Marmara Region

The following six tables compile the details of 280 simulated earthquakes in the Marmara region obtained from the *Stochastic Simulation Method for Finite Faults* (Beresnev and Atkinson, 1997) (Chapter 3). The simulated time series of seismic ground motions are the basis for the development and verification of the PreSEIS methodology in this thesis.

The earthquakes are simulated along the five major fault segments in the Sea of Marmara. For each segment I have synthesized 50 earthquakes (Table B.1 to B.5). The database is supplemented by 30 additional earthquakes which are randomly distributed in the Marmara region (Table B.6). Earthquakes along each segment are identified by serial numbers from 1 to 50 (or 30). Geographical coordinates and depths of the earthquake hypocenters are compiled in columns two, three and four. Moment magnitudes  $M_w$  are shown in column five. The remaining four columns specify the geographical coordinates of the start and end points of fault ruptures projected onto the surface. The distribution of epicenters is shown in Figure 3.7. Histograms for magnitudes and depths are given in Figure 3.9.

**Synthetics SEGMENT 1**

id. #	epi lat ° N	epi lon ° E	depth [km]	$M_w$	start lat ° N	start lon ° E	end lat ° N	end lon ° E
1	40.77	29.51	10.5	6.9	40.79	29.77	40.75	29.25
2	40.72	29.40	5.4	5.1	40.72	29.43	40.72	29.39
3	40.75	29.52	6.2	6.2	40.76	29.70	40.75	29.50
4	40.74	29.52	7.3	6.0	40.75	29.65	40.74	29.51
5	40.74	29.44	7.1	6.5	40.76	29.66	40.74	29.37
6	40.74	29.54	5.8	6.0	40.75	29.67	40.74	29.53
7	40.75	29.60	9.1	6.4	40.76	29.81	40.74	29.54
8	40.74	29.48	10.1	6.1	40.74	29.57	40.73	29.40
9	40.76	29.62	7.6	6.8	40.77	29.79	40.74	29.31
10	40.76	29.76	5.5	5.1	40.76	29.78	40.76	29.74
11	40.73	29.47	13.4	6.9	40.75	29.78	40.72	29.23
12	40.74	29.59	7.0	6.4	40.75	29.75	40.73	29.48
13	40.77	29.79	9.6	6.0	40.77	29.87	40.76	29.73
14	40.76	29.73	5.8	5.0	40.76	29.74	40.76	29.72
15	40.75	29.33	5.6	5.6	40.75	29.37	40.75	29.29
16	40.77	29.77	6.6	6.0	40.78	29.88	40.77	29.72
17	40.74	29.33	9.8	6.7	40.76	29.68	40.73	29.30
18	40.72	29.38	6.9	7.0	40.75	29.80	40.71	29.23
19	40.78	29.83	8.0	5.6	40.78	29.89	40.78	29.81
20	40.76	29.55	7.9	7.0	40.78	29.88	40.74	29.30
21	40.74	29.61	12.3	6.7	40.75	29.75	40.72	29.35
22	40.73	29.27	9.8	5.8	40.74	29.37	40.73	29.26
23	40.76	29.36	5.1	4.5	40.76	29.37	40.76	29.36
24	40.75	29.42	10.5	6.1	40.76	29.56	40.75	29.40
25	40.77	29.58	5.2	4.7	40.77	29.59	40.77	29.58
26	40.78	29.83	10.4	6.9	40.78	29.86	40.74	29.36
27	40.76	29.82	7.0	7.0	40.76	29.85	40.72	29.23
28	40.72	29.34	6.8	6.2	40.72	29.40	40.71	29.21
29	40.74	29.33	6.0	5.9	40.74	29.37	40.73	29.24
30	40.77	29.56	8.9	6.3	40.77	29.68	40.76	29.44
31	40.76	29.76	9.7	6.3	40.76	29.88	40.75	29.67
32	40.76	29.44	6.7	6.1	40.76	29.53	40.75	29.36
33	40.75	29.49	8.3	5.7	40.75	29.53	40.74	29.44
34	40.80	29.85	9.6	5.7	40.80	29.90	40.79	29.80
35	40.76	29.63	13.5	6.9	40.77	29.81	40.73	29.24
36	40.71	29.28	7.5	5.3	40.72	29.33	40.71	29.28
37	40.74	29.28	10.6	6.3	40.76	29.47	40.74	29.26
38	40.75	29.41	10.4	6.9	40.78	29.88	40.75	29.38
39	40.76	29.85	11.2	7.1	40.76	29.90	40.72	29.22
40	40.74	29.36	10.3	6.8	40.76	29.69	40.73	29.21
41	40.75	29.73	5.8	4.6	40.75	29.73	40.75	29.72
42	40.75	29.35	5.2	4.5	40.75	29.36	40.75	29.35
43	40.79	29.81	7.0	5.7	40.79	29.86	40.78	29.76
44	40.75	29.39	10.4	6.9	40.78	29.85	40.74	29.36
45	40.78	29.77	7.9	5.9	40.78	29.81	40.77	29.69
46	40.76	29.38	9.8	5.9	40.76	29.44	40.75	29.32
47	40.75	29.33	8.5	5.3	40.75	29.35	40.74	29.29
48	40.76	29.55	5.6	5.2	40.76	29.55	40.76	29.51
49	40.74	29.34	10.3	6.0	40.74	29.42	40.73	29.27
50	40.78	29.72	10.6	6.9	40.79	29.84	40.75	29.30

**Table B.1:**

**Synthetics SEGMENT 2**

id. #	epi lat ° N	epi lon ° E	depth [km]	$M_w$	start lat ° N	start lon ° E	end lat ° N	end lon ° E
1	40.80	29.07	5.2	4.5	40.80	29.07	40.81	29.06
2	40.86	28.91	6.7	6.2	40.84	28.96	40.91	28.80
3	40.83	28.99	6.3	6.3	40.80	29.06	40.88	28.87
4	40.74	29.16	6.6	5.4	40.73	29.19	40.75	29.13
5	40.77	29.03	8.8	6.8	40.71	29.18	40.87	28.81
6	40.78	29.10	10.4	6.2	40.77	29.11	40.85	28.94
7	40.78	29.04	10.9	6.2	40.72	29.19	40.79	29.02
8	40.83	28.96	8.5	6.2	40.82	28.97	40.89	28.81
9	40.80	29.01	6.8	6.2	40.79	29.03	40.86	28.87
10	40.76	29.09	6.1	6.1	40.74	29.12	40.81	28.97
11	40.83	28.94	11.5	6.3	40.75	29.13	40.84	28.93
12	40.83	28.89	8.0	5.9	40.81	28.92	40.86	28.81
13	40.81	29.02	8.4	5.2	40.80	29.03	40.82	28.99
14	40.80	29.12	11.7	6.6	40.79	29.14	40.91	28.86
15	40.75	29.19	5.5	4.9	40.75	29.20	40.76	29.19
16	40.84	28.95	10.8	6.3	40.79	29.06	40.88	28.87
17	40.83	28.96	7.3	5.9	40.82	28.99	40.87	28.88
18	40.88	28.87	5.2	4.5	40.88	28.88	40.88	28.87
19	40.91	28.84	5.8	4.6	40.90	28.84	40.91	28.83
20	40.86	28.93	7.1	5.4	40.84	28.98	40.86	28.93
21	40.87	28.87	5.8	6.1	40.83	28.96	40.89	28.82
22	40.77	29.11	5.5	4.8	40.77	29.12	40.77	29.11
23	40.86	28.90	5.8	4.9	40.86	28.91	40.86	28.90
24	40.82	28.99	5.6	5.7	40.81	29.01	40.85	28.93
25	40.78	29.06	6.4	6.5	40.74	29.16	40.85	28.90
26	40.75	29.13	7.8	5.5	40.73	29.18	40.75	29.12
27	40.83	28.98	5.2	4.6	40.83	28.98	40.83	28.97
28	40.82	29.03	5.2	4.5	40.82	29.03	40.82	29.02
29	40.89	28.83	11.5	6.3	40.81	29.02	40.90	28.81
30	40.83	28.94	6.7	5.4	40.83	28.94	40.86	28.89
31	40.77	29.07	5.6	5.7	40.76	29.10	40.80	29.02
32	40.85	28.92	10.9	6.4	40.79	29.04	40.89	28.83
33	40.89	28.87	7.3	5.5	40.87	28.91	40.90	28.85
34	40.86	28.91	10.3	5.9	40.82	29.00	40.87	28.88
35	40.76	29.17	8.2	6.0	40.75	29.20	40.80	29.07
36	40.85	28.97	8.1	5.4	40.84	28.99	40.86	28.93
37	40.77	29.04	11.0	6.4	40.75	29.10	40.84	28.88
38	40.81	29.02	5.5	4.6	40.81	29.02	40.82	29.01
39	40.82	29.03	6.2	6.2	40.76	29.16	40.84	28.99
40	40.80	29.01	6.8	6.0	40.79	29.04	40.84	28.92
41	40.81	28.96	9.6	5.8	40.81	28.97	40.85	28.88
42	40.87	28.95	10.7	6.1	40.83	29.04	40.89	28.89
43	40.86	28.92	10.0	5.9	40.84	28.98	40.89	28.87
44	40.86	28.95	10.3	6.2	40.82	29.03	40.89	28.86
45	40.75	29.14	8.9	5.4	40.74	29.15	40.77	29.09
46	40.85	28.90	10.5	6.0	40.83	28.96	40.88	28.83
47	40.82	28.99	9.6	5.9	40.80	29.03	40.85	28.92
48	40.89	28.88	11.8	6.6	40.77	29.15	40.90	28.86
49	40.84	28.98	10.2	6.8	40.74	29.20	40.91	28.81
50	40.87	28.90	7.4	6.7	40.74	29.21	40.88	28.88

**Table B.2:**

**Synthetics SEGMENT 3**

id. #	epi lat ° N	epi lon ° E	depth [km]	$M_w$	start lat ° N	start lon ° E	end lat ° N	end lon ° E
1	40.86	27.69	6.0	5.9	40.87	27.73	40.86	27.61
2	40.89	28.32	10.2	6.8	40.90	28.51	40.87	28.05
3	40.84	27.76	8.1	7.1	40.87	28.23	40.82	27.55
4	40.87	28.15	10.6	6.3	40.89	28.34	40.87	28.13
5	40.82	27.43	8.7	5.6	40.83	27.50	40.82	27.42
6	40.91	28.51	5.9	6.2	40.91	28.63	40.90	28.45
7	40.86	28.44	12.0	6.6	40.86	28.46	40.84	28.10
8	40.83	27.45	8.6	5.9	40.83	27.55	40.83	27.44
9	40.80	27.63	11.1	6.4	40.80	27.70	40.78	27.43
10	40.82	27.64	5.1	4.6	40.82	27.64	40.82	27.63
11	40.85	28.15	14.5	7.1	40.87	28.43	40.82	27.71
12	40.90	28.38	8.5	6.2	40.92	28.55	40.90	28.36
13	40.85	27.78	8.0	7.1	40.87	28.15	40.83	27.49
14	40.86	27.93	6.6	6.1	40.86	27.94	40.85	27.78
15	40.83	27.80	10.8	7.0	40.87	28.37	40.83	27.77
16	40.85	28.03	8.7	6.2	40.86	28.16	40.85	27.96
17	40.87	27.81	7.5	6.8	40.89	28.03	40.86	27.59
18	40.86	28.07	10.3	6.8	40.89	28.50	40.85	28.03
19	40.85	27.88	11.2	6.4	40.86	28.08	40.84	27.81
20	40.84	27.85	10.5	6.3	40.84	27.90	40.83	27.69
21	40.88	28.25	14.7	7.2	40.90	28.64	40.85	27.87
22	40.85	27.94	7.2	5.1	40.85	27.95	40.84	27.92
23	40.84	27.88	10.5	6.9	40.87	28.25	40.83	27.73
24	40.88	28.30	15.3	7.2	40.91	28.63	40.85	27.77
25	40.82	27.59	8.5	5.4	40.83	27.60	40.82	27.54
26	40.90	28.45	5.9	6.3	40.92	28.62	40.90	28.41
27	40.87	28.14	5.2	4.7	40.87	28.15	40.87	28.13
28	40.92	28.57	11.0	7.0	40.92	28.61	40.87	27.96
29	40.88	28.34	7.2	7.2	40.89	28.38	40.83	27.57
30	40.85	28.09	7.3	7.3	40.88	28.48	40.82	27.61
31	40.86	27.98	12.2	6.7	40.88	28.28	40.85	27.90
32	40.84	27.81	11.1	7.1	40.87	28.33	40.83	27.67
33	40.85	28.09	7.5	5.6	40.86	28.16	40.85	28.07
34	40.91	28.64	10.4	6.2	40.92	28.70	40.90	28.50
35	40.86	28.10	8.4	5.7	40.87	28.17	40.86	28.07
36	40.84	27.93	14.4	7.1	40.86	28.28	40.82	27.57
37	40.86	28.38	5.8	4.5	40.86	28.38	40.86	28.37
38	40.90	28.68	9.0	6.4	40.90	28.70	40.88	28.44
39	40.90	28.49	14.2	7.1	40.91	28.70	40.87	28.03
40	40.81	27.45	6.5	5.9	40.81	27.50	40.80	27.38
41	40.87	28.11	11.3	7.1	40.91	28.69	40.86	27.97
42	40.82	27.67	7.0	6.3	40.82	27.77	40.81	27.53
43	40.84	27.60	5.2	4.5	40.84	27.61	40.84	27.60
44	40.87	27.94	8.8	5.4	40.87	27.99	40.87	27.93
45	40.84	27.79	9.9	6.7	40.86	28.15	40.84	27.76
46	40.81	27.69	9.7	6.0	40.82	27.77	40.81	27.63
47	40.87	27.93	11.3	6.5	40.88	28.09	40.86	27.81
48	40.88	28.18	15.4	7.1	40.91	28.56	40.86	27.86
49	40.83	27.50	7.1	6.5	40.84	27.72	40.82	27.43
50	40.91	28.68	15.6	7.3	40.91	28.73	40.85	27.80

**Table B.3:**

**Synthetics SEGMENT 4**

id. #	epi lat ° N	epi lon ° E	depth [km]	$M_w$	start lat ° N	start lon ° E	end lat ° N	end lon ° E
1	40.74	29.17	12.1	7.3	40.74	29.22	40.86	28.29
2	40.88	28.24	7.3	7.3	40.79	28.91	40.91	28.01
3	40.85	28.44	6.5	6.5	40.83	28.63	40.87	28.33
4	40.83	28.82	10.9	7.0	40.81	28.95	40.89	28.34
5	40.83	28.74	7.9	7.0	40.77	29.22	40.85	28.62
6	40.85	28.51	14.5	7.1	40.78	29.03	40.88	28.31
7	40.86	28.20	10.6	6.9	40.80	28.61	40.87	28.08
8	40.84	28.41	10.5	6.9	40.82	28.60	40.89	28.08
9	40.81	28.74	10.6	6.9	40.80	28.83	40.87	28.30
10	40.80	28.65	6.1	6.6	40.79	28.75	40.83	28.41
11	40.84	28.63	8.4	7.2	40.78	29.04	40.89	28.22
12	40.82	28.61	6.7	6.8	40.81	28.63	40.87	28.20
13	40.86	28.43	10.3	6.8	40.86	28.47	40.92	28.00
14	40.81	28.76	14.4	7.1	40.80	28.88	40.89	28.18
15	40.83	28.62	13.2	6.7	40.80	28.84	40.85	28.45
16	40.83	28.66	10.6	6.9	40.82	28.78	40.89	28.24
17	40.85	28.37	16.9	7.5	40.73	29.27	40.89	28.07
18	40.79	28.88	12.7	7.4	40.74	29.20	40.89	28.07
19	40.82	28.79	8.0	7.0	40.78	29.07	40.86	28.44
20	40.72	29.32	6.5	6.6	40.71	29.38	40.75	29.06
21	40.88	28.30	10.4	6.9	40.82	28.76	40.89	28.27
22	40.76	29.13	8.2	7.1	40.72	29.41	40.81	28.68
23	40.76	29.13	14.5	6.9	40.74	29.23	40.82	28.67
24	40.81	28.51	7.8	6.9	40.78	28.74	40.85	28.22
25	40.77	29.03	8.8	7.4	40.72	29.40	40.86	28.33
26	40.82	28.60	12.2	7.3	40.75	29.08	40.88	28.12
27	40.84	28.53	12.9	6.7	40.81	28.78	40.86	28.41
28	40.84	28.83	7.5	6.7	40.80	29.09	40.86	28.69
29	40.88	28.24	16.4	7.4	40.76	29.17	40.90	28.08
30	40.83	28.63	11.6	7.2	40.78	29.02	40.88	28.24
31	40.81	28.84	12.5	7.4	40.73	29.50	40.86	28.43
32	40.82	28.87	13.2	7.5	40.74	29.46	40.91	28.15
33	40.83	28.67	15.6	7.3	40.77	29.13	40.88	28.21
34	40.82	28.66	12.6	7.4	40.76	29.14	40.90	28.04
35	40.81	28.89	12.4	7.4	40.73	29.51	40.86	28.49
36	40.85	28.54	10.0	6.7	40.81	28.78	40.87	28.37
37	40.74	29.42	12.2	6.7	40.74	29.45	40.79	29.07
38	40.81	28.76	7.9	7.0	40.80	28.87	40.88	28.29
39	40.84	28.71	7.6	6.8	40.84	28.75	40.90	28.28
40	40.80	28.81	15.3	7.1	40.74	29.30	40.83	28.63
41	40.86	28.46	14.1	7.0	40.80	28.91	40.89	28.26
42	40.86	28.45	7.8	6.9	40.83	28.69	40.90	28.15
43	40.84	28.72	14.0	7.0	40.78	29.15	40.86	28.52
44	40.79	29.09	18.3	7.5	40.74	29.47	40.89	28.26
45	40.90	28.17	16.1	7.4	40.78	29.14	40.91	28.12
46	40.86	28.48	17.0	7.5	40.73	29.52	40.89	28.30
47	40.84	28.49	10.5	6.9	40.84	28.52	40.90	28.02
48	40.85	28.41	8.7	6.7	40.83	28.57	40.89	28.16
49	40.79	28.95	14.3	7.4	40.73	29.42	40.86	28.39
50	40.89	28.39	12.7	7.4	40.78	29.20	40.93	28.07

**Table B.4:**

**Synthetics SEGMENT 5**

id. #	epi lat ° N	epi lon ° E	depth [km]	$M_w$	start lat ° N	start lon ° E	end lat ° N	end lon ° E
1	40.73	29.00	5.8	6.0	40.71	29.11	40.74	28.97
2	40.71	28.87	5.8	4.9	40.71	28.87	40.72	28.86
3	40.72	29.00	5.8	4.5	40.72	29.00	40.72	28.99
4	40.70	28.98	11.8	6.6	40.68	29.14	40.73	28.81
5	40.69	29.05	9.9	6.0	40.69	29.07	40.71	28.92
6	40.72	29.01	5.8	5.6	40.72	29.02	40.73	28.95
7	40.68	28.98	10.1	6.1	40.67	29.03	40.70	28.86
8	40.70	29.02	5.8	5.0	40.70	29.03	40.70	29.02
9	40.66	29.05	5.6	5.6	40.66	29.07	40.67	28.99
10	40.70	28.98	11.9	6.4	40.67	29.11	40.72	28.84
11	40.71	28.82	6.9	6.3	40.68	29.03	40.72	28.80
12	40.72	28.91	7.9	5.9	40.71	28.97	40.73	28.85
13	40.70	29.04	5.8	4.8	40.70	29.05	40.70	29.04
14	40.71	28.92	8.3	6.6	40.67	29.13	40.72	28.82
15	40.72	29.01	9.1	6.4	40.71	29.09	40.75	28.83
16	40.70	28.97	9.6	6.0	40.70	28.99	40.72	28.86
17	40.72	28.96	5.6	5.2	40.71	29.00	40.72	28.96
18	40.70	29.07	7.2	5.4	40.70	29.10	40.71	29.03
19	40.70	29.07	12.3	6.5	40.69	29.09	40.74	28.82
20	40.73	28.93	9.4	5.9	40.73	28.94	40.75	28.82
21	40.73	28.87	9.0	5.5	40.73	28.89	40.74	28.82
22	40.69	29.02	11.8	6.6	40.67	29.14	40.73	28.81
23	40.73	28.97	6.6	6.0	40.71	29.06	40.73	28.92
24	40.70	28.97	10.2	5.9	40.69	29.08	40.71	28.96
25	40.68	29.05	5.2	4.9	40.68	29.05	40.68	29.04
26	40.71	29.00	6.3	6.3	40.69	29.11	40.73	28.89
27	40.70	29.07	5.8	4.9	40.70	29.07	40.71	29.06
28	40.71	29.06	5.8	4.6	40.71	29.07	40.71	29.05
29	40.70	29.02	5.2	4.9	40.70	29.03	40.70	29.02
30	40.69	29.00	6.9	5.6	40.68	29.08	40.70	29.00
31	40.72	28.88	5.6	6.0	40.70	29.00	40.72	28.87
32	40.68	28.97	6.1	6.0	40.68	28.98	40.71	28.83
33	40.70	29.02	5.8	4.9	40.70	29.03	40.70	29.02
34	40.70	28.98	9.0	5.6	40.70	29.00	40.71	28.93
35	40.72	28.92	7.1	6.5	40.69	29.14	40.73	28.85
36	40.68	29.10	5.5	4.5	40.68	29.11	40.68	29.09
37	40.72	28.97	6.3	6.3	40.69	29.15	40.72	28.92
38	40.73	28.97	9.9	5.8	40.71	29.07	40.73	28.96
39	40.70	29.02	6.7	5.5	40.70	29.03	40.71	28.96
40	40.71	28.86	5.8	4.9	40.71	28.87	40.72	28.85
41	40.70	28.92	7.3	5.5	40.69	28.98	40.71	28.91
42	40.71	28.92	10.1	5.8	40.70	28.98	40.71	28.87
43	40.72	28.95	11.5	6.5	40.70	29.12	40.74	28.82
44	40.68	29.00	5.8	4.7	40.68	29.00	40.68	28.99
45	40.71	28.92	9.3	6.5	40.68	29.12	40.73	28.83
46	40.72	28.94	11.3	6.5	40.69	29.15	40.73	28.87
47	40.70	29.07	9.2	6.5	40.69	29.15	40.73	28.88
48	40.70	29.08	11.4	6.5	40.70	29.11	40.75	28.82
49	40.74	28.87	7.2	5.9	40.73	28.95	40.75	28.82
50	40.72	28.92	5.5	5.0	40.72	28.93	40.72	28.91

**Table B.5:**



**Synthetics SEGMENT 6**

id. #	epi lat ° N	epi lon ° E	depth [km]	$M_w$	start lat ° N	start lon ° E	end lat ° N	end lon ° E
1	41.14	29.53	5.8	4.7	41.14	29.53	41.14	29.54
2	41.04	29.62	5.8	4.5	41.04	29.61	41.04	29.62
3	40.99	28.05	5.8	4.8	41.00	28.04	40.99	28.05
4	40.68	28.68	5.8	4.7	40.68	28.68	40.68	28.69
5	40.66	29.14	5.5	4.8	40.66	29.13	40.66	29.15
6	40.84	28.76	5.8	4.7	40.85	28.75	40.84	28.76
7	40.76	28.65	5.2	5.0	40.75	28.66	40.76	28.65
8	40.73	27.98	5.2	4.7	40.73	27.99	40.73	27.98
9	40.89	28.19	5.2	4.9	40.89	28.19	40.90	28.18
10	41.02	29.52	5.8	4.7	41.02	29.53	41.02	29.52
11	41.00	28.26	5.5	4.8	41.00	28.27	41.00	28.25
12	40.99	29.86	5.6	4.5	40.99	29.87	40.99	29.86
13	41.04	29.65	5.2	4.9	41.04	29.65	41.03	29.65
14	40.69	29.46	5.2	4.7	40.69	29.46	40.70	29.47
15	41.21	29.16	5.5	5.0	41.21	29.15	41.20	29.16
16	40.84	28.30	5.8	4.7	40.83	28.30	40.84	28.29
17	40.78	28.04	5.5	4.7	40.77	28.04	40.78	28.03
18	40.69	29.10	5.5	4.6	40.69	29.10	40.70	29.09
19	40.68	29.39	5.5	4.6	40.68	29.39	40.69	29.38
20	40.69	28.81	5.2	4.9	40.69	28.81	40.68	28.80
21	40.82	28.67	5.2	4.7	40.82	28.67	40.82	28.68
22	40.91	28.14	5.8	4.8	40.91	28.14	40.91	28.13
23	41.06	28.46	5.5	4.6	41.06	28.47	41.06	28.46
24	40.84	28.56	5.2	4.9	40.84	28.56	40.84	28.56
25	41.09	28.26	5.2	4.7	41.09	28.26	41.09	28.25
26	40.93	29.33	5.2	4.7	40.93	29.33	40.94	29.32
27	41.03	29.17	5.5	4.9	41.03	29.17	41.02	29.18
28	40.76	28.64	5.5	4.9	40.76	28.65	40.76	28.64
29	41.08	28.75	5.2	4.9	41.07	28.75	41.08	28.75
30	41.02	28.10	5.5	4.5	41.02	28.09	41.01	28.10

**Table B.6:**



## Appendix C

# Coefficients for the Attenuation Laws

The following coefficients refer to attenuation laws in Chapter 4.4 (for the stochastically simulated database) and Chapter 4.4.1 (for observational data in other regions).

### C.0.1 Stochastically simulated database

Coefficients $C_1 \dots C_5$			
	PGA [g]	PGV [cm/s]	PGD [cm]
$C_1$	7.4554	6.1717	-0.2532
$C_2$	1.5051	1.7327	2.2179
$C_3$	-4.5484	-3.7001	-3.3494
$C_4$	8.0483	6.9512	6.4778
$C_5$	0.0083	0.0009	-0.0026
	PSA [g] 0.3 s	PSA [g] 1.0 s	PSA [g] 2.0 s
$C_1$	8.6970	0.3557	-7.9564
$C_2$	1.4696	1.6464	2.0683
$C_3$	-4.5887	-3.0947	-2.1255
$C_4$	8.2445	6.4643	4.9953
$C_5$	0.0088	-0.0034	-0.0121
	Intensity (FAS)	Arias [m/s]	CAV [cm/s]
$C_1$	0.8089	-8.9878	-2.6800
$C_2$	0.2317	2.6357	1.5308
$C_3$	-0.1073	-2.5273	-0.3360
$C_4$	0.6000	2.8835	0.5841
$C_5$	-0.0052	-0.0248	-0.0182

**Table C.1:** Coefficients  $C_1$  to  $C_5$  in (4.19) for amplitude, spectral and integrative ground motion parameters derived from the stochastically simulated database described in Chapter 3.

<b>Coefficient <math>C_6</math></b>			
soil	$M_w = 5.0$	$M_w = 6.0$	$M_w = 7.0$
NEHRP class B	-0.0301	0.0733	-0.1447
NEHRP class C	-0.0916	0.0695	-0.1201
NEHRP class D	-0.0628	0.1911	0.0581
	PGV		
NEHRP class B	-0.1894	-0.0442	-0.3447
NEHRP class C	-0.1528	0.0805	-0.2148
NEHRP class D	0.0824	0.4585	0.2533
	PGD		
NEHRP class B	-0.3126	-0.0153	-0.4234
NEHRP class C	-0.2389	0.1145	-0.2650
NEHRP class D	0.1821	0.6218	0.2595

**Table C.2:** Magnitude- and site-dependent coefficient  $C_6$  in (4.19) for PGA, PGV, and PGD.

<b>Coefficient <math>C_6</math></b>			
soil	$M_w = 5.0$	$M_w = 6.0$	$M_w = 7.0$
NEHRP class B	0.0094	0.1176	-0.0551
NEHRP class C	-0.0627	0.0651	-0.0728
NEHRP class D	-0.1037	0.0831	-0.0466
	PSA 1.0 s		
NEHRP class B	-0.2900	-0.0038	-0.3646
NEHRP class C	-0.2057	0.1241	-0.2229
NEHRP class D	0.1589	0.5484	0.2120
	PSA 2.0 s		
NEHRP class B	-0.4080	-0.0032	-0.4859
NEHRP class C	-0.2837	0.1756	-0.2974
NEHRP class D	0.2333	0.7403	0.2604

**Table C.3:** Magnitude- and site-dependent coefficient  $C_6$  in (4.19) for PSA at 0.3 s, 1.0 s and 2.0 s.

<b>Coefficient <math>C_6</math></b>			
soil	$M_w = 5.0$	$M_w = 6.0$	$M_w = 7.0$
NEHRP class B	-0.0481	-0.0013	-0.0404
NEHRP class C	-0.0422	0.0086	-0.0243
NEHRP class D	-0.0117	0.0555	0.0238
	Arias		
NEHRP class B	-0.1791	-0.2105	-0.3227
NEHRP class C	-0.1460	-0.1048	-0.1781
NEHRP class D	0.1699	0.3677	0.3309
	CAV		
NEHRP class B	-0.1092	-0.2118	-0.1418
NEHRP class C	-0.0354	-0.1238	-0.0553
NEHRP class D	0.1902	0.1754	0.2425

**Table C.4:** Magnitude- and site-dependent coefficient  $C_6$  in (4.19) for seismic intensity, Arias, and CAV.

Unit standard deviation $\sigma_{\ln(IM)}$			
soil	$M_w = 5.0$	$M_w = 6.0$	$M_w = 7.0$
PGA			
NEHRP class B	0.3064	0.3949	0.3409
NEHRP class C	0.3035	0.4051	0.3249
NEHRP class D	0.2925	0.3795	0.3234
PGV			
NEHRP class B	0.2958	0.3644	0.3040
NEHRP class C	0.2676	0.3549	0.3182
NEHRP class D	0.2761	0.3487	0.3155
PGD			
NEHRP class B	0.2828	0.3642	0.3307
NEHRP class C	0.2784	0.3643	0.3332
NEHRP class D	0.3109	0.3539	0.3200

**Table C.5:** Magnitude- and site-dependent  $\sigma_{\ln(IM)}$  in (4.19) for PGA, PGV, and PGD.

Unit standard deviation $\sigma_{\ln(IM)}$			
soil	$M_w = 5.0$	$M_w = 6.0$	$M_w = 7.0$
PSA 0.3 s			
NEHRP class B	0.3163	0.3951	0.3299
NEHRP class C	0.3045	0.3987	0.3127
NEHRP class D	0.3058	0.3849	0.3141
PSA 1.0 s			
NEHRP class B	0.2860	0.3918	0.3273
NEHRP class C	0.2790	0.3790	0.3137
NEHRP class D	0.2931	0.3629	0.3255
PSA 2.0 s			
NEHRP class B	0.3078	0.3639	0.3223
NEHRP class C	0.3242	0.3800	0.3226
NEHRP class D	0.3289	0.3685	0.3189

**Table C.6:** Magnitude- and site-dependent  $\sigma_{\ln(IM)}$  in (4.19) for PSA at 0.3 s, 1.0 s, and 2.0 s.

Unit standard deviation $\sigma_{\ln(IM)}$			
soil	$M_w = 5.0$	$M_w = 6.0$	$M_w = 7.0$
Intensity			
NEHRP class B	0.1063	0.0784	0.0751
NEHRP class C	0.1063	0.0773	0.0736
NEHRP class D	0.0981	0.0836	0.0869
Arias			
NEHRP class B	0.5735	0.7629	0.5988
NEHRP class C	0.5325	0.7432	0.5756
NEHRP class D	0.5397	0.7307	0.5825
CAV			
NEHRP class B	0.2852	0.3850	0.3075
NEHRP class C	0.2767	0.3698	0.2920
NEHRP class D	0.2800	0.3628	0.2904

**Table C.7:** Magnitude- and site-dependent  $\sigma_{\ln(IM)}$  in (4.19) for seismic intensity, Arias, and CAV.

## C.0.2 Common attenuation laws

**Coefficients for  $M \leq 6.5$**

	PGA	PSA 0.3 s	PSA 1.0 s	PSA 2.0 s
$C_1$	-0.62400	-0.05700	-1.70500	-2.94500
$C_2$	1.00000	1.00000	1.00000	1.00000
$C_3$	0.00000	-0.01700	-0.05500	-0.07000
$C_4$	-2.10000	-2.02800	-1.80000	-1.67000
$C_5$	1.29649	1.29649	1.29649	1.29649
$C_6$	0.25000	0.25000	0.25000	0.25000

**Table C.8:** Sadigh et al. (1997): Strong crustal earthquakes in California.

**Coefficients for strike-slip**

	PGA	PSA 0.3 s	PSA 1.0 s	PSA 2.0 s
$C_1$	-0.313	0.598	-1.133	-1.699
$C_2$	0.527	0.769	1.036	1.085
$C_3$	0.000	-0.161	-0.032	-0.085
$C_4$	-0.778	-0.893	-0.798	-0.812
$C_5$	-0.371	-0.401	-0.698	-0.655
$V_a$	1396.	2133.	1406.	1795.
$h$	5.570	5.940	2.900	5.850

**Table C.9:** Boore et al. (1997): PGA and PSA for earthquakes in Western North America.

**Coefficients**

	PSA 0.3 s	PSA 1.0 s	PSA 2.0 s
$C_1$	0.77000	-1.79000	-3.28000
$C_2$	0.00000	1.59000	2.23000
$C_3$	0.00000	0.66000	0.66000
$C_4$	0.00350	0.00850	0.01000
$C_5$	-0.00072	-0.00100	-0.00100
$C_6$	-0.40000	-0.38000	-0.36000
$C_7$	0.00000	0.57000	0.83000
$C_8$	0.00000	0.62000	0.62000

**Table C.10:** Campbell (1997): PSA for near-source observations.

# List of Figures

1.1	Pre-, co- and postseismic measures for seismic risk reduction . . . . .	3
1.2	Tectonics in the eastern Mediterranean . . . . .	8
1.3	Stations of the Istanbul earthquake early warning system as part of <i>IERREWS</i> . . . . .	9
1.4	Seismicity in the Marmara region . . . . .	10
2.1	Source time functions and their derivatives after Beresnev and Atkinson (1997) . . . . .	13
2.2	Frequency-dependent amplification functions after Boore and Joyner (1997) . . . . .	22
2.3	NEHRP soil classification map for the Marmara region . . . . .	22
3.1	Main processing steps in the stochastic simulation method . . . . .	25
3.2	Shaping window after Saragoni and Hart (1974) . . . . .	26
3.3	Example: Simulated mean horizontal components of acceleration . . . . .	33
3.4	Example: Simulated mean horizontal components of velocity . . . . .	34
3.5	Example: Simulated mean horizontal components of displacement . . . . .	35
3.6	Fault segments in the Sea of Marmara . . . . .	36
3.7	Distribution of epicenters of the synthetic database . . . . .	38
3.8	Amplification spectrum at station <i>TLC</i> in Romania . . . . .	40
3.9	Histograms of magnitudes and depths for the synthetic database . . . . .	41
3.10	Example: Ground motion simulations at the early warning sensors of <i>IERREWS</i> . . . . .	42
4.1	Building response after Hough (2004) . . . . .	48
4.2	Example: (Pseudo-) spectral acceleration determined from simulated acceleration time series . . . . .	49
4.3	Mean acceleration spectra for intensities III-XI after Sokolov (2002) . . . . .	51
4.4	Cumulative absolute velocity (CAV) . . . . .	52
4.5	Example: CAV determined from simulated acceleration time series . . . . .	53

List of Figures

---

4.6	Correlation between CAV and seismic intensity for observational earthquakes . . . . .	54
4.7	Correlation between CAV and seismic intensity for synthetic earthquakes . . . . .	54
4.8	Correlations between ground motion parameters and Fourier amplitudes . . . . .	56
4.9	Attenuation laws derived from the simulated data . . . . .	59
4.10	Magnitude- and site-dependent amplification factors relative to NEHRP class B . . . . .	60
4.11	Comparison of attenuation laws derived from the synthetic data and observational data . . . . .	62
4.12	Comparison of attenuation laws derived from the synthetic data and common relations . . . . .	64
4.13	Impact of slip distributions on the observed level of ground motion . . . . .	68
4.14	Impact of slip distributions on ground motion parameters PGA and CAV . . . . .	69
5.1	Stations of the Romanian Earthquake Early Warning System . . . . .	84
5.2	Records of the October 27, 2004, Vrancea earthquake ( $M_w = 5.9$ ) . . . . .	84
5.3	Warning time for the Romanian Earthquake Early Warning System . . . . .	85
5.4	Scaling relations for the Romanian Earthquake Early Warning System . . . . .	87
5.5	Linking the output of the Romanian earthquake early warning system to the Urban Shakemap Methodology for Bucharest . . . . .	89
6.1	Activation functions and Two-Layer Feed-Forward Neural Network . . . . .	96
6.2	Processing steps in a Two-Layer Feed-Forward Neural Network . . . . .	98
6.3	Pre-warning times in the Marmara region . . . . .	102
6.4	Time-dependent number of triggered early warning stations in <i>IERREWS</i> . . . . .	103
6.5	Simulated earthquakes in the Izmit Bay Area . . . . .	105
6.6	Confinement of the space of possible and likely source locations using two stations . . . . .	105
6.7	Accuracies of predicted hypocenter locations . . . . .	106
6.8	Example of linear and logarithmized CAV . . . . .	107
6.9	Accuracies of predicted magnitudes . . . . .	108
6.10	Number of triggered stations at different time steps . . . . .	109
6.11	General design of the Two-Layer Feed-Forward Neural Networks in PreSEIS . . . . .	110
6.12	Moving average architecture in PreSEIS . . . . .	111
6.13	Link between <i>Hypo</i> , $M_w$ , <i>Rupt</i> , and <i>Spec</i> . . . . .	114
6.14	Picking errors for P-wave onsets in the enlarged database . . . . .	116
6.15	Location and magnitude prediction errors for different numbers of hidden units . . . . .	116
6.16	Performance analyses for three optimization methods . . . . .	119



---

6.17	Comparison of performances for training and test subsets . . . . .	121
6.18	Scenario A: Acceleration times series and shake maps . . . . .	123
6.19	Scenario B: Acceleration times series and shake maps . . . . .	124
6.20	Scenario A: Shake maps for different ground motion parameters . . . . .	126
6.21	Scenario A and B: Performance analyses for correctly picked P-wave onsets . . . . .	127
6.22	Scenario A and B: Performance analyses for incorrectly picked P-wave onsets . . . . .	128
6.23	Scenario A: Predicted and observed level of ground motion . . . . .	130
6.24	Scenario B: Predicted and observed level of ground motion . . . . .	131
6.25	Scenario A: Alert maps . . . . .	132
6.26	Scenario B: Alert maps . . . . .	133
6.27	Scenario A: Predicted Fourier amplitude spectrum . . . . .	134
6.28	Scenario B: Predicted Fourier amplitude spectrum . . . . .	135
6.29	Scenario A and B: Shake maps modified by rupture directivity . . . . .	137



# Bibliography

- Aki, K. (1967). Scaling law of seismic spectrum. *J. Geophys. Int.*, 72:1217–1231.
- Aki, K. and Richards, P. (1980). *Quantitative Seismology, Theory and Methods*. W.H. Freeman, New York.
- Allen, R. (1978). Automatic earthquake recognition and timing from single traces. *Bull. Seism. Soc. Am.*, 68:1521–1532.
- Allen, R. (2005). Application of ElarmS across California. In *Earthquake Early Warning Workshop Abstracts, California Institute of Technology, Pasadena, July 13-15 2005*.
- Allen, R. and Kanamori, H. (2003). The potential for earthquake early warning in southern California. *Science*, 300:786–789.
- Ambraseys, N. (2002). The seismic activity of the Marmara Sea region over the last 2000 years. *Bull. Seism. Soc. Am.*, 92(1):1–18.
- Ambraseys, N. and Finkel, C. (1991). Long-term seismicity of Istanbul and the Marmara Sea region. *Terra Nova*, 3:527–539.
- Anderson, J. (2003). Strong-motion seismology. In Lee, W.H.K., K. H. J. P. and Kisslinger, C., editors, *International Handbook of Earthquake and Engineering Seismology, Part B*. Academic Press.
- Anderson, J. and Hough, S. (1984). A model for the shape of the Fourier amplitude spectrum of acceleration at high frequencies. *Bull. Seism. Soc. Am.*, 74:1969–1993.
- Arias, A. (1970). A measure of earthquake intensity. In *Seismic Design for Nuclear Power Plants*, pages 438–483. MIT Press, Cambridge, Massachusetts.
- Armijo, R., de Lepinay, B., Malavieille, J., et al. (2005). Submarine fault scarps in the Sea of Marmara pull-apart (North Anatolian Fault): implications for seismic hazard in Istanbul. *Geochem. Geophys. Geosys.*, (6). Q06009, doi:10.1029/2004GC000896.
- Armijo, R., Meyer, B., Navarro, S., King, G., and Barka, A. (2002). Asymmetric slip partitioning in the Sea of Marmara pull-apart: a clue to propagation processes of the North Anatolian Fault? *Terra Nova*, 14(2):80–86.
- Atkinson, G. and Boore, D. (1995). Ground motion relations for eastern north America. *Bull. Seism. Soc. Am.*, 85(1):17–30.
- Bakun, W., Fischer, F., Jensen, E., and VanSchaak, J. (1994). Early warning system for aftershocks. *Bull. Seism. Soc. Am.*, 84(2):359–365.

- Bard, P.-Y. (1999). Local effects on strong ground motion: Physical basis and estimation methods in view of microzoning studies. In *Proceedings of the advanced study course Seismotectonic and microzonation techniques in earthquake engineering: Integrated training in earthquake risk reduction practices*, Kefallinia.
- Barka, A. (1999). The 17 August 1999 Izmit earthquake. *Science*, 285:1858–1859.
- Bartlakowski, J., Wenzel, F., Radulian, M. and Ritter, J., and Wirth, W. (2006). Urban shakemap methodology for Bucharest. *Geophysical Research Letters*, 33.
- Benjamin, J. and Associates (1988). A criterion for determining exceedance of the operating basis earthquake. Technical report, Electric Power Research Institute, Palo Alto, California.
- Beresnev, I. (2001). What we can learn and cannot learn about earthquake sources from the spectra of seismic waves. *Bull. Seism. Soc. Am.*, 91(2):397–400.
- Beresnev, I. and Atkinson, G. (1997). Modeling finite-fault radiation from the  $\omega^n$  spectrum. *Bull. Seism. Soc. Am.*, 87(1):67–84.
- Beresnev, I. and Atkinson, G. (1998). FINSIM - a FORTRAN program for simulating stochastic acceleration time histories from finite faults. *Seism. Res. Lett.*, 69(1):27–32.
- Beresnev, I. and Atkinson, G. (2002). Source parameters of earthquakes in eastern and western north America based on finite-fault modeling. *Bull. Seism. Soc. Am.*, 92(2):695–710.
- Beroza, G. and Ellsworth, W. (1996). Properties of the seismic nucleation phase. *Tectonophysics*, 261:209–227.
- Bindi, D., Parolai, S., Grosser, H., Milkereit, C., and Karakisa, S. (2006). Crustal attenuation characteristics in northwestern Turkey in the range from 1 to 10 Hz. *Bull. Seism. Soc. Am.*, 96(1):200–214.
- Bishop, C. (1995). *Neural networks for pattern recognition*. Clarendon Press, Oxford.
- Boatwright, J. Thywissen, K. and Seekins, L. (2001). Correlation of ground motion and intensity for the January 17, 1994 Northridge, California earthquake. *Bull. Seism. Soc. Am.*, 91:739–752.
- Bolt, B. (1969). Duration of strong motion. In *Proceedings of the 4th World Conference on Earthquake Engineering*, pages 1304–1315, Santiago, Chile.
- Bonjer, K.-P., Oncescu, L., Driad, L., and Rizesscu, M. (1999). A note on empirical site responses in Bucharest, Romania. In Wenzel, F., Lungu, D., and Novak, O., editors, *Vrancea Earthquakes: Tectonics, Hazard and Risk Mitigation*, pages 149–162. Kluwer Academic Publishers.
- Boore, D. (1983). Stochastic simulation of high-frequency ground motions based on seismological models of the radiated spectra. *Bull. Seism. Soc. Am.*, 73:1865–1894.
- Boore, D. (1986). Short-period P- and S-wave radiation from large earthquakes: Implications for spectral scaling relations. *Bull. Seism. Soc. Am.*, 76(1):43–64.
- Boore, D. (1996). SMSIM - Fortran programs for simulating ground motions from earthquakes: version 1.0. US Geological Survey Open File Report 96-80-A.

- Boore, D. (2003). Simulation of ground motion using the stochastic method. *Pure and Applied Geophysics*, 160:635–676.
- Boore, D. and Boatwright, J. (1984). Average body-wave radiation coefficients. *Bull. Seism. Soc. Am.*, 74:1615–1621.
- Boore, D. and Joyner, W. (1997). Site amplifications for generic rock studies. *Bull. Seism. Soc. Am.*, 87(2):327–341.
- Boore, D., Joyner, W., and Fumal, T. (1997). Equations for estimating horizontal response spectra and peak acceleration from western north American earthquakes: A summary of recent work. *Seism. Res. Lett.*, 68(1):128–153.
- Borcherdt, R. (1994). Estimates of site-dependent response spectra for design (methodology and justification). *Earthquake Spectra*, 10(4):617–654.
- Brillinger, D. and Preisler, H. (1984). An exploratory analysis of the Joyner-Boore attenuation data. *Bull. Seism. Soc. Am.*, 74(4):1441–1450.
- Brillinger, D. and Preisler, H. (1985). Further analysis of the Joyner-Boore attenuation data. *Bull. Seism. Soc. Am.*, 75(2):1441–1450.
- Brinkman, R. (1976). *Geology of Turkey*. Ferdinand Enke Verlag, Stuttgart, Germany.
- Brune, J. (1970). Tectonic stress and the spectra of seismic shear waves from earthquakes. *J. Geophys. Res.*, 75:4997–5009.
- Brune, J. (1971). Correction. *J. Geophys. Res.*, 76:5002.
- Building Seismic Safety Council (1995). 1994 Edition NEHRP Recommended Provisions for Seismic Regulations for New Buildings, FEMA 222A/223A. Technical report, Federal Emergency Management Agency, Washington D.C.
- Burger, R., Somerville, P., Barker, J., Herrmann, R., and Helmberger, D. (1987). The effect of crustal structure on strong ground motion attenuation relations in eastern North America. *Bull. Seis. Soc. Am.*, 77:420–439.
- Campbell, K. (1981). Near-source attenuation of peak horizontal acceleration. *Bull. Seism. Soc. Am.*, 71(6):2039–2070.
- Campbell, K. (1997). Empirical near-source attenuation relations for horizontal and vertical components of peak ground acceleration, peak ground velocity, and pseudo-absolute acceleration response spectra. *Seis. Res. Lett.*, 68(1):154–179.
- Campbell, K. and Bozorgnia, Y. (2003). Updated near-source ground motion (attenuation) relations for the horizontal and vertical components of peak ground acceleration and acceleration response spectra. *Bull. Seism. Soc. Am.*, 93(1):314–331.
- Chernov, Y. and Sokolov, V. (1988). Earthquake felt intensity estimation using the strong ground motion spectra. *Engineering Seismology Problems*, 29:62–73.
- Chernov, Y. and Sokolov, V. (1999). Correlation of seismic intensity with Fourier acceleration spectra. *Physics and Chemistry of the Earth, Part A: Solid Earth and Geodesy*, 24(6):522–528.

## Bibliography

---

- Chiaruttini, C. and Salemi, G. (1993). Artificial intelligence techniques in the analysis of digital seismograms. *Computers and Geosciences*, 19(2):149–156.
- Cooper, M. (1868). Editorial in. *San Francisco Daily Evening Bulletin*, Nov. 3.
- Correig, A. (1996). On the measurement of the predominant and resonant frequencies. *Bull. Seism. Soc. Am.*, 86(2):416–427.
- Cua, G. (2004). *Creating the Virtual Seismologist: developments in ground motion characterization and seismic early warning*. PhD thesis, California Institute of Technology. <http://etd.caltech.edu/etd/available/etd-02092005-125601/>.
- Cua, G. and Heaton, T. (2003). An envelope-based paradigm for seismic early warning. *Eos. Trans. AGU, Fall Meet. Suppl.*, 84(46). Abstract S42B-0164.
- Dowla, F., Taylor, S., and Anderson, R. (1990). Seismic discrimination with artificial neural networks: preliminary results with regional spectral data. *Bull. Seism. Soc. Am.*, 80:1346–1373.
- Dreger, D. and Helmberger, D. (1993). Determination of source parameters at regional distances with three-component sparse data networks. *J. Geophys. Res.*, 98:8107–8125.
- Durukal, E. (2002). Critical evaluation of strong motion in Kocaeli and Duzce (Turkey) earthquakes. *Soil Dynamics and Earthquake engineering*, 22(7):589–609.
- Eguchi, R., Goltz, J., Seligson, H., Flores, P., Heaton, T., and Bortugno, E. (1997). Real-time loss estimation as an emergency response decision support system: The Early Post-Earthquake Damage Assessment Tool (EPEDAT). *Earthquake Spectra*, 13:815–832.
- Ellsworth, W. and Beroza, G. (1995). Seismic evidence for an earthquake nucleation phase. *Science*, 268:851–855.
- Erdik, M., Aydinoglu, N., Fahjan, Y., Sesetyan, K., Demircioglu, M., Siyahi, B., Durukal, E., Ozbey, C., Biro, Y., Akman, H., and Yuzugullu, O. (2003a). Earthquake risk assessment for Istanbul metropolitan area. *Earthquake Engineering and Engineering Vibration*, 2(1):1–23.
- Erdik, M., Doyoran, V., Akkas, N., and Gulkan, P. (1985). A probabilistic assessment of the seismic hazard in Turkey. *Tectonophysics*, 117:295–344.
- Erdik, M., Fahjan, Y., Ozel, O., Alcik, H., Mert, A., and Gul, M. (2003b). Istanbul Earthquake Rapid Response and the Early Warning System. *Bulletin of Earthquake Engineering*, 1:157–163.
- Ergin, M., Özalaybey, S., Aktar, M., and Yalcin, M. (2004). Site amplification at Avcilar, Istanbul. *Tectonophysics*, 391:335–346.
- Espinosa-Aranda, J., Carvajal, A., Martinez, A., and Hernandez, H. (2005). Seismic Alert Systems in Mexico. In *Earthquake Early Warning Workshop Abstracts, California Institute of Technology, Pasadena, July 13-15 2005*.
- Espinosa-Aranda, J., Jimenez, A., Contreras, O., Ibarrola, G., and Ortega, R. (1992). Mexico City Seismic Alert System. In *International Symposium on Earthquake Disaster Prevention, 1992, Mexico City*, volume 1, pages 315–324.

- Espinosa-Aranda, J., Jimenez, A., Ibarrola, G., Alcantar, F., Aguilar, A., Inostroza, M., and Maldonado, S. (1995). Mexico City Seismic Alert System. *Seism. Res. Lett.*, 66(6):42–53.
- EWCI (2003). Background paper by the ISDR Secretariat. In *Second International Conference on Early Warning, 16-18 October 2003*, Bonn, Germany. <http://www.ewc2.org>.
- Fiedrich, F., Gehbauer, F., Leebmann, J., Lungu, D., Markus, M., and Schweier, C. (2004). EQSIM: A new approach to damage estimation. In *Proceedings of the International Conference Earthquake Loss Estimation and Risk Reduction, 2, October 24-26 2002, Bucharest, Romania*, pages 273–286. Independent Film, Bucuresti, Romania.
- Field, E. and the SCEC Phase III Working Group (2000). Accounting for site effects in probabilistic seismic hazard analyses of southern California: Overview of the SCEC Phase III Report. *Bull. Seism. Soc. Am.*, 90(6B):S1–S31.
- Frohlich, C. and Pullim, J. (1999). Single-station location of seismic events: a review and plea for more research. *Phys. Earth Planet. Int.*, 113:277–291.
- Gee, L., Fulton, S., Dreger, D., Kaverina, A., Neuhauser, D., Murray, M., and Romanowicz, B. (2000). Recent enhancements to the Rapid Earthquake Data Integration (REDI) System. *Seism. Res. Lett.*, 71(2):232.
- Gee, L., Neuhauser, D., Dreger, D., Pasyanos, M., Uhrhammer, R., and Romanowicz, B. (1996). Real-time seismology at UC Berkeley; the Rapid Earthquake Data Integration Project. *Bull. Seism. Soc. Am.*, 86(4):936–945.
- Geller, R., Jackson, D., Kagan, Y., and Mulargia, F. (1997). Earthquakes cannot be predicted. *Science*, 275:1616–1617.
- Gerstenberger, M., Wiemer, S., Jones, L. M., and Reasenber, P. (2005). Real-time forecasts of tomorrow's earthquakes in California. *Nature Letters*, 435(19):328–330.
- Goltz, J. (2002). Introducing earthquake early warning in California: A summary of social science and public policy issues. A report to OES and the Operational Areas, Caltech Seismological Laboratory, Disaster Assistance Division. <http://www.cisn.org/docs/goltz.aguf03.html>.
- Goltz, J. (2003). Application for new real-time seismic information: The TriNet project in Southern California. *Seism. Res. Lett.*, 74(5):516–521.
- Grecksch, G. and Kümpel, H.-J. (1997). Statistical analysis of strong-motion accelerograms and its application to earthquake early-warning systems. *Geophys. J. Int.*, 129:113–123.
- Gülkan, P. and Kalkan, E. (2002). Attenuation modeling of recent earthquakes in Turkey. *Journal of Seismology*, 6:397–409.
- Gutenberg, B. and Richter, C. (1956). Earthquake magnitude, intensity, energy and acceleration. *Bull. Seism. Soc. Am.*, 46.
- Hanks, T. (1982).  $f_{max}$ . *Bull. Seism. Soc. Am.*, 72(6):1867–1879.
- Hanks, T. and Kanamori, H. (1979). A moment magnitude scale. *J. Geophys. Res.*, 84:2348–2350.

## Bibliography

---

- Hanks, T. and McGuire, R. (1981). The character of high-frequency strong ground motion. *Bull. Seism. Soc. Am.*, 71(6):2071–2095.
- Harben, P. (1991). Earthquake alert system feasibility study. Technical report, Lawrence Livermore National Laboratory, Livermore, CA. UCRL-LR-109625; <http://www.llnl.gov/hmc/eas/eas1.html>.
- Harmsen, S. (1997). Determination of site amplification in the Los Angeles urban area from inversion of strong motion records. *Bull. Seism. Soc. Am.*, 87:866–887.
- Hartzell, S. (1978). Earthquake aftershocks as Green's functions. *Geophys. Res. Lett.*, 5:1–4.
- Hasegawa, H. (1985). Attenuation of Lg waves in the Canadian shield. *Bull. Seism. Soc. Am.*, 75:1569–1582.
- Hatherly, P. (1986). Attenuation measurements on shallow seismic refraction data. *Geophysics*, 51(2):250–254.
- Hayama, T., Horiuchi, S., Tsukada, S., and Fujinawa, Y. (2005). A national research project on earthquake early warning system and its applications. In *Earthquake Early Warning Workshop Abstracts, July 13-15 2005, California Institute of Technology, Pasadena*.
- Heaton, T. (1985). A model for a seismic computerized alert network. *Science*, 228:987–990.
- Holden, R., Lee, R., and Reichle, M. (1989). Technical and economic feasibility of an earthquake warning system in California. Technical report, California Department of Conservation, Division of Mines and Geology.
- Horasan, G., Kaslilar-Özcan, A., Boztepe-Güney, A., and Türkelli, N. (1998). S-wave attenuation in the Marmara region, northwestern Turkey. *Geophys. Res. Lett.*, 25(14):2733–2736.
- Horiuchi, S., Negishi, H., Abe, K., Kamimura, A., and Fujinawa, Y. (2005). An automatic processing system for broadcasting earthquake alarms. *Bull. Seism. Soc. Am.*, 95(2):708–781.
- Hough, S. (2004). *Earthshaking Science, What we know (and don't know) about Earthquakes*. Princeton University Press, Princeton, Oxford.
- Hutchings, L. and Wu, F. (1990). Empirical Green's functions from small earthquakes: a waveform study of locally recorded aftershocks of the 1971 San Fernando earthquake. *J. Geophys. Res.*, 95:1187–1214.
- Imren, C., Le Pichon, X., Rangin, C., Demirbag, E., Ecevitoglu, B., and Gorur, N. (2001). The North Anatolian fault within the Sea of Marmara: A new interpretation based on multi-channel seismic and multi-beam bathymetry data. *Earth Planet. Sci. Lett.*, 186:143–158.
- Ionescu, C. and Marmureanu, A. (2005). Rapid early warning system (REWS) for Bucharest and industrial facilities. In *Earthquake Early Warning Workshop Abstracts, July 13-15 2005, California Institute of Technology, Pasadena*.
- Irikura, K. (1983). Semi-empirical estimation of strong ground motions during large earthquakes. *Bulletin of the Disaster Prevention Research Institute*, 33(2):63–104.



- Jennings, P. (2003). An introduction to the earthquake response of structures. In Lee, W.H.K., K. H. J. P. and Kisslinger, C. e., editors, *International Handbook of Earthquake and Engineering Seismology, Part B*. Academic Press.
- Jiang, J., Baird, G., and Blair, D. (1998). Polarization and amplitude attributes of reflected plane and spherical waves. *Geophys. J. Int.*, 132:577–583.
- Joswig, M. (1990). Pattern recognition for earthquake detection. *Bull. Seism. Soc. Am.*, 80(1):170–186.
- Joyner, W. and Boore, D. (1986). On simulating large earthquakes by Green's-function addition of smaller earthquakes. In Das, S., Boatwright, J., and Scholz, C., editors, *Proceedings of the Fifth Maurice Ewing Symposium on Earthquake Source Mechanics*, pages 269–274. American Geophysical Union.
- Joyner, W. and Boore, D. (1993). Method for regression analysis of strong motion data. *Bull. Seism. Soc. Am.*, 83(2):469–487.
- Joyner, W. and Boore, D. (1994). Errata: Method for regression analysis of strong motion data. *Bull. Seism. Soc. Am.*, 84:955–956.
- Kallweit, R. and Wood, L. (1982). The limits of resolution of zero-phase wavelets. *Geophysics*, 47(7):1035–1046.
- Kanamori, H. (1993). Locating earthquakes with amplitude; application to real-time seismology. *Bull. Seism. Soc. Am.*, 83(1):264–268.
- Kanamori, H. (1994). Mechanics of earthquakes. *Annu. Rev. Earth Planet. Sci.*, 22:207–237.
- Kanamori, H. (2005). Real-time seismology and earthquake damage mitigation. *Annual Reviews of Earth and Planetary Sciences*, 33:5.1–5.20.
- Kanamori, H. and Brodsky, E. (2001). The physics of earthquakes. *Physics Today*, 54(6):34–40.
- Kanamori, H., Hauksson, E., and Heaton, T. (1991). TERRAscope and CUBE project at Caltech. *Eos*, 72:564.
- Kanamori, H., Hauksson, E., and Heaton, T. (1997). Real-time seismology and earthquake hazard mitigation. *Nature*, 390:461–464.
- Kramer, S. (1996). *Geotechnical Earthquake Engineering*. International series in Civil Engineering and Engineering Mechanics. Prentice-Hall, New Jersey.
- Kramer, S., Mayfield, R., and Mitchell, R. (2003). Ground motions and liquefaction - The loading part of the equation. In *Proceedings of the U.S.-Taiwan Workshop on Soil Liquefaction, November 3-5, 2003*, Hsin-Chu, Taiwan.
- Krinitzky, E. and Chang, F. (1987). Parameters for specifying intensity-related earthquake ground motions. Technical report, U.S. Army Corps of Engineers Waterways Experiment Station, Vicksburg, Mississippi.
- Lahr, J. (1999). HYPOELLIPSE: A computer program for determining local earthquake hypocentral parameters, magnitude and first-motion pattern. Technical report, U.S. Geological Survey, Denver.

- Lang, K. and Hinton, G. (1988). The development of the time-delay neural network architecture for speech recognition. Technical report cmu-cs-88-152., Carnegie-Mellon University, Pittsburgh, PA.
- Lay, T. and Wallace, T. (1995). *Modern Global Seismology*. International Geophysics Series, Vol.58. Academic Press, San Diego, California.
- Le Pichon, X., Chamot-Rooke, N., Rangin, C., and Sengor, A. (2003). The North Anatolian fault in the Sea of Marmara. *J. Geophys. Res.*, 108(B4, 2179):ETG 1–1–20.
- Le Pichon, X., Sengor, A., Demirbag, E., Rangin, C., Imren, C., Armijo, R., Gorur, N., Cagatay, N., Mercier de Lepinay, B., Meyer, B., Saatçilar, R., and Tok, B. (2001). The active Main Marmara fault. *Earth Planet. Sci. Lett.*, 192:595–616.
- Leach, R. and Dowla, F. (1996). Earthquake early warning system using real-time signal processing. In *IEEE Workshop on Neural Networks for Signal Processing, September 4-6, Keihanna, Kyoto, Japan*. [http://www.llnl.gov/hmc/signal-process/web\\_p1.html](http://www.llnl.gov/hmc/signal-process/web_p1.html).
- Levenberg, K. (1944). A method for the solution of certain non-linear problems in least squares. *Quarterly Journal of Applied Mathematics*, II(2).
- Lockman, A. and Allen, R. (2003). Rapid magnitude determination using P-wave arrivals: Magnitude-period relations for Japan and the Pacific northwest. *Eos. Trans. AGU, Fall Meet. Suppl.*, 84(46). Abstract S42B-0161.
- Lockman, A. and Allen, R. (2005). Single-station earthquake characterization for early warning. *Bull. Seism. Soc. Am.*, 95(6):2029–2039. doi: 10.1785/0120040241.
- Magotra, N., Ahmed, N., and Chael, E. (1987). Seismic event detection and source location using single-station (three-component) data. *Bull. Seism. Soc. Am.*, 77(3):958–971.
- Marquardt, D. (1963). An algorithm for least-squares estimation of non-linear parameters. *Journal of the Society of Industrial and Applied Mathematics*, 11(2):431–441.
- McGuire, R. (1978). Seismic ground motion parameter relations. *Journal of the Geotechnical Engineering Division, ASCE*, 104(GT4):481–490.
- Miksat, J., Wenzel, F., and Sokolov, V. (2005). Low free-field accelerations of the 1999 Kocaeli earthquake? *Pure and Applied Geophysics*, 162:857–874.
- Minster, J., Day, S., and Shearer, P. (1990). Nonlinear Q and yield estimates. *EOS, Transactions*, 71(43):1477.
- Mohorovicic, A. (1915). Die Bestimmung des Epizentrum eines Erdbebens. *Gerl. Beitr. z. Geophys.*, 14:199–205. in German.
- Murphy, J. and O'Brien, L. (1977). The correlation of peak ground acceleration amplitude with seismic intensity and other physical parameters. *Bull. Seism. Soc. Am.*, 67:877–915.
- Nakamura, Y. (1985). A concept of one point detection system and its example using personal computer for earthquake warning. In *Proceedings of 18th Earthquake Engineering Symposium of Japan*.
- Nakamura, Y. (1989). Earthquake alarm system for Japan Railways. *Japanese Railway Engineering*, 28(4):3–7.

- Nakamura, Y. (1998). A new concept for the earthquake vulnerability estimation and its application to the early warning system. In *International Conference on Early Warning Systems for Natural Disaster Reduction, September 6-11 1998, Potsdam, Germany*.
- Nakamura, Y. (2004). On a rational strong motion index compared with other various indices. In *Proceedings of 13th World Conference on Earthquake Engineering, August 1-6 2004, Vancouver, Canada*.
- Nakamura, Y. (2005a). Observational results of UrEDAS at Pasadena and other locations. In *Earthquake Early Warning Workshop Abstracts, July 13-15 2005, California Institute of Technology, Pasadena*.
- Nakamura, Y. (2005b). Performance of an early warning system, Compact UrEDAS, during destructive earthquakes. In *Earthquake Early Warning Workshop Abstracts, July 13-15 2005, California Institute of Technology, Pasadena*.
- Nakamura, Y. and Saito, A. (1983). P/S phase recognition of seismic waves and epicentral azimuth using single station data. In *Proceedings of 17th Earthquake Engineering Symposium of Japan*, pages 95–98.
- Nakamura, Y. and Tucker, B. (1988). Japan's earthquake warning system - should it be imported to California? *California Geology*, 41:33–40.
- Nigam, N. and Jennings, P. (1969). Calculation of response spectra from strong-motion earthquake records. *Bull. Seism. Soc. Am.*, 59(2):909–922.
- Noda, S. and Meguro, K. (1995). A new horizon for sophisticated real-time earthquake engineering. *Journal of Natural Disaster Science*, 17(2):13–46.
- Normile, D. (2004). Some countries are betting that a few seconds can save lives. *Science*, 306:2178–2179.
- Odaka, T., Ashiya, K., Tsukada, S., Sato, S., Ohtake, K., and Nozaka, D. (2003). A new method of quickly estimating epicentral distance and magnitude from a single seismic record. *Bull. Seism. Soc. Am.*, 93(1):526–532.
- Ojo, S. and Mereu, R. (1986). The effect of random velocity functions on the travel times and amplitudes of seismic waves. *Geophys. J. R. Astr. Soc.*, 84:607–618.
- Olsen, K. (1994). *Simulation of Three-Dimensional Wave Propagation in the Salt Lake Basin*. PhD thesis, University of Utah, Salt Lake City.
- Olsen, K. and Archuleta, R. (1996). 3-D simulation of earthquakes on the Los Angeles fault system. *Bull. Seism. Soc. Am.*, 86:575–596.
- Olson, E. and Allen, R. (2005). The deterministic nature of earthquake rupture. *Nature Letters*, 438(10):212–215. doi:10.1038/nature04214.
- Oncescu, M. and Bonjer, K.-P. (1997). A note on the depth recurrence and strain release of large Vrancea earthquakes. *Tectonophysics*, 272:291–302.

- Osinov, V. (2003). Cyclic shearing and liquefaction of soil under irregular loading: an incremental model for the dynamic earthquake-induced deformation. *Soil Dynamics and Earthquake Engineering*, 23:535–548.
- Ozbey, C., Sari, A., Manuel, L., Erdik, M., and Fahjan, Y. (2004). An empirical attenuation relationship for northwestern Turkey ground motion using a random effects approach. *Soil Dyn. and Earthquake Eng.*, 24:115–125.
- Özel, O., Cranswick, E., Meremonte, M., Erdik, M., and Safak, E. (2002). Site effects in Avcilar, west of Istanbul, Turkey, from strong- and weak-motion data. *Bull. Seism. Soc. Am.*, 92(1):499–508.
- Parsons, T., Toda, S., Stein, R., Barka, A., and Dieterich, J. (2000). Heightened odds of large earthquakes near Istanbul: an interaction-based probability calculation. *Science*, 288:661–665.
- Plaut, D., Nowlan, S., and Hinton, G. (1986). Experiments on learning by back propagation, Technical Report CMU-CS-86-126.
- Plenefisch, T. (1996). *Untersuchungen des Spannungsfeldes im Bereich des Rheingrabens mittels der Inversion von Herdflächenlösungen und Abschätzung der bruchspezifischen Reibungsparameter*. PhD thesis, Karlsruhe University.
- Pujol, J. (2004). Earthquake location tutorial: Graphical approach and approximate epicentral location techniques. *Seism.Res.Lett.*, 75(1):63–74.
- Pulido, N., Ojeda, A., Atakan, K., and Kubo, T. (2004). Strong ground motion estimation in the Marmara sea region (Turkey) based on a scenario earthquake. *Tectonophysics*, 391:357–374.
- Re, M. (2005). Annual review: Natural catastrophes 2004. Technical report, Munich Re, Munich, Germany.
- Riedmiller, M. and Braun, H. (1993). A direct adaptive method for faster backpropagation learning: The RPROP algorithm. In *Proceedings of the IEEE International Conference on Neural Networks*, 28 March-1 April 1993, volume 1, pages 586–591.
- Rojas, R. (1993). *Theorie der neuronalen Netze*. Springer Verlag, Berlin.
- Rumelhart, D., Hinton, G., and Williams, R. (1986). *Parallel Distributed Processing: Explorations in the Microstructure of Cognition*, volume 1. M.I.T. Press, Cambridge.
- Rydelek, P. and Pujol, J. (2004). Real-time seismic warning with a 2-station subarray. *Bull. Seism. Soc. Am.*, 94:1546–1550.
- Sadigh, K., Chang, C.-Y., Egan, J., Makdisi, F., and Youngs, R. (1997). Attenuation relationships for shallow crustal earthquakes based on California strong motion data. *Seism. Res. Lett.*, 68(1):180–189.
- Saita, J. and Nakamura, Y. (2003). UrEDAS: The early warning system for mitigation of disasters caused by earthquakes and tsunamis. In Zschau, J. and Kueppers, A., editors, *Early warning systems for natural disaster reduction*, pages 453–460. Springer, Berlin.
- Sandham, W. and Leggett, M. (2003). In *Geophysical applications of artificial neural networks and fuzzy logic*. Kluwer Academic Publishers, Dordrecht, Boston, London.

- Saragoni, G. and Hart, G. (1974). Simulation of artificial earthquakes. *Earthquake Eng. Structural Dyn.*, 2:249–267.
- Sato, H. and Fehler, M. (1998). *Seismic wave propagation and scattering in the heterogeneous Earth*. Springer-Verlag, New York.
- Scherbaum, F., Schmedes, J., and Cotton, F. (2004). On the conversion of source-to-site distance measures for extended earthquake source models. *Bull. Seism. Soc. Am.*, 94(3):1053–1069.
- Schnabel, B., Lysmer, J., and Seed, H. (1972). SHAKE. A computer program for earthquake response analysis of horizontally layered sites. Report EERC 72-12, College of Engineering, University of California, Berkeley.
- Scrivner, C. and Helmberger, D. (1995). Preliminary work on an early warning and rapid response program for moderate earthquakes. *Bull. Seism. Soc. Am.*, 85(4):1257–1265.
- Seed, H. and Idriss, I. (1982). Ground motions and soil liquefaction during earthquakes. Earthquake Engineering Research Institute, Berkeley, California.
- Sheriff, R. and Geldart, L. (1995). *Exploration Seismology*. Cambridge University Press, Cambridge.
- Sokolov, V. (2002). Seismic intensity and Fourier acceleration spectra: Revised relationship. *Earthquake Spectra*, 18(1):161–187.
- Sokolov, V. and Chernov, Y. (1998). On the correlation of seismic intensity with Fourier acceleration spectra. *Earthquake Spectra*, 14(4):679–673.
- Sokolov, V. Y., Bonjer, K.-P., M., O., and Rizescu, M. (2005). Hard rock spectral models for intermediate-depth Vrancea (Romania) earthquakes. *Bull. Seism. Soc. Am.*, 95:1749–1765.
- Somerville, P., Irikura, K., Graves, R., Sawada, S., Wald, D., Abrahamson, N., Iwasaki, Y., Kagawa, T., Smith, N., and Kowada, A. (1999). Characterizing crustal earthquake slip models for the prediction of strong ground motion. *Seism. Res. Lett.*, 70:59–80.
- Sperner, B., Müller, B., Heidbach, O., Delvaux, D., Reinecker, J., and Fuchs, K. (2003). Tectonic stress in the Earth's crust: advances in the World Stress Map project. In Nieuwland, D., editor, *New insights in structural interpretation and modelling*, pages 101–116. Special Publication 212, Geological Society, London.
- Sperner, B. and the CRC 461 team (2005). Monitoring of slab detachment in the SE-Carpathians. In *Perspectives in Modern Seismology*, number 105 in Lecture Notes in Earth Sciences, pages 189–204. Springer Verlag Heidelberg.
- Stein, R., Barka, A., and Dieterich, J. (1997). Progressive failure on the North Anatolian fault since 1939 by earthquake stress triggering. *Geophys. J. Int.*, 128:594–604.
- Stewart, J., Chiou, S., Bray, J., Graves, R., Somerville, P., and Abrahamson, N. (2001). Ground motion evaluation procedures for performance-based design. PEER Report 2001/09, Pacific Earthquake Engineering Research Center, College of Engineering, University of California, Berkeley.
- Su, F., Zeng, Y., and Anderson, J. (1999). Earthquake source and nonlinear site effects on the spectral attenuation parameter kappa. *EOS, Transactions*, 80(46):699–700.

- Swingler, K. (1996). *Applying neural networks - A practical guide*. Academic Press Inc., San Diego.
- Teng, T.-l., Wu, L., Shin, T.-C., Tsai, Y.-B., and Lee, W. (1997). One minute after: Strong-motion map, effective epicenter, and effective magnitude. *Bull. Seism. Soc. Am.*, 87(5):1209–1219.
- Toksöz, M., Shakal, A., and Michael, A. (1979). Space-time migration of earthquakes along the North Anatolian fault zone and seismic gaps. *Pageoph*, 117:1258–1270.
- Trifunac, M. and Brady, A. (1975). On the correlation of seismic intensity with peaks of recorded strong ground motion. *Bull. Seism. Soc. Am.*, 65:139–162.
- Trifunac, M. and Todorovska, M. (1997). Northridge, California, earthquake of 1994: density of red-tagged buildings versus peak horizontal velocity and intensity of shaking. *Soil Dyn. Earthquake Engrg.*, 16(3):209–222.
- Tsuboi, S., Saito, M., and Kikuchi, M. (2002). Real-time earthquake warning by using broadband P waveform. *Geophys. Res. Lett.*, 29(24):2187. doi:10.1029/2002GL016101.
- Udias, A. (1999). *Principles of Seismology*. Cambridge University Press, Cambridge.
- Vanderkulk, W., Rosen, F., and Lorenz, S. (1965). Large aperture seismic array signal processing study. Technical report, Rockville, Maryland.
- Waibel, A., Hanazawa, T., Hinton, G., Shikano, K., and Lang, K. (1989). Phoneme recognition using time-delay neural networks. *IEEE Transactions on Acoustics, Speech, and Signal Processing*, ASSP-37:328–339.
- Wald, D., Quitoriano, V., Heaton, T., and Kanamori, H. (1999a). Relationships between peak ground acceleration, peak ground velocity and modified Mercalli Intensity in California. *Earthquake Spectra*, 15:557–564.
- Wald, D., Quitoriano, V., Heaton, T., Kanamori, H., Scrivner, C., and Worden, C. (1999b). TriNet ShakeMaps: Rapid generation of instrumental ground motion and intensity maps for earthquakes in southern California. *Earthquake Spectra*, 15:537–556.
- Wald, D., Wald, L., Worden, B., and Goltz, J. (2003). ShakeMap - a tool for earthquake response. Technical report, U. S. Geological Survey.
- Wald, L. and Mori, J. (2000). Evaluation of methods for estimating linear site-response amplification in the Los Angeles region. *Bull. Seism. Soc. Am.*, 90(6B):S32–S42.
- Walter, W. and Hartse, H. (2002). Monitoring the Comprehensive Nuclear-Test-Ban Treaty; seismic event discrimination and identification. *Pure Appl. Geophys.*, 159(4):619–903.
- Wells, D. and Coppersmith, K. (1994). New empirical relationships among magnitude, rupture length, rupture width, rupture area and surface displacement. *Bull. Seism. Soc. Am.*, 84(4):974–1002.
- Wenzel, F., Baur, M., Fiedrich, F., Ionescu, C., and Oncescu, M. (2001). Potential of earthquake early warning systems. *Natural Hazards*, 23:407–416.
- Wenzel, F., Oncescu, M., Baur, M., and Fiedrich, F. (1999). An early warning system for Bucharest. *Seism. Res. Lett.*, 70(2):161–169.

- Wieland, M. (2001). Earthquake alarm, rapid response and early warning systems: Low cost systems for seismic risk reduction. In *International Workshop on Disaster Reduction, August 19-22, 2001*, Reston, VA.
- Wirth, W. (2004). *Seismische Bodenbewegung in Bukarest (Rumänien) - Untersuchung lateraler Variationen und Modellierung mit empirischen Greenschen Funktionen, Dissertation vom 12.11.2004*. PhD thesis, Universität Karlsruhe, Fakultät für Physik, Karlsruhe, Germany. <http://www.ubka.uni-karlsruhe.de>.
- Withers, M., Bittenbinder, A., Bogaert, B., Herrmann, R., and Talwani, P. (2000a). Near real-time data exchange and rapid earthquake information for the central and Eastern U.S. *Seis. Res. Lett.*, 71(2):235.
- Withers, M., Bodin, P., and Gomberg, J. (2000b). New Madrid rapid earthquake information system. *Seism. Res. Lett.*, 71(1):115.
- Wu, Y.-M. and Kanamori, H. (2005a). Experiment on an onsite early warning method for the Taiwan early warning system. *Bull. Seism. Soc. Am.*, 95:347–353.
- Wu, Y.-M. and Kanamori, H. (2005b). Rapid assessment of damaging potential of earthquakes in Taiwan from the beginning of P waves. *Bull. Seism. Soc. Am.*, 95:1181–1185.
- Wu, Y.-M., Kanamori, H., Allen, R., and Hauksson, E. (2005). An onsite earthquake early warning method for the Southern California Seismic Network. *Bull. Seism. Soc. Am.* submitted.
- Wu, Y.-M., Shin, T.-C., and Chang, C.-H. (2001). Near real-time mapping of peak ground acceleration and peak ground velocity following a strong earthquake. *Bull. Seism. Soc. Am.*, 91(5):1218–1228.
- Wu, Y.-M., Shin, T.-C., Chen, C.-C., Tsai, Y.-B., Lee, W., and Teng, T. (1997). Taiwan rapid earthquake information release system. *Seism. Res. Lett.*, 68(6):931–943.
- Wu, Y.-M., Shin, T.-C., and Tsai, Y.-B. (1998). Quick and reliable determination of magnitude for seismic early warning. *Bull. Seism. Soc. Am.*, 88(5):1254–1259.
- Wu, Y.-M. and Teng, T.-I. (2002). A virtual subnetwork approach to earthquake early warning. *Bull. Seism. Soc. Am.*, 92(5):2008–2018.
- Wyss, M. (1997). Second round of evaluations of proposed earthquake precursors. *Pure Appl. Geophys.*, 149:3–16.
- Yamada, M. and Heaton, T. (2005). Extending the Virtual Seismologist to finite ruptures; An example from the Chi-Chi earthquake. In *Earthquake Early Warning Workshop Abstracts, July 13-15 2005, California Institute of Technology, Pasadena*.
- Yankee Atomic Electric Company (1991). Standardization of the cumulative absolute velocity. Technical report, Electric Power Research Institute, Bolton, Massachusetts.
- Zell, A. (1994). *Simulation Neuronaler Netze*. Addison-Wesley.
- Zhao, L.-S. and Helmberger, D. (1994). Source estimation from broadband regional seismograms. *Bull. Seism. Soc. Am.*, 84(1):91–104.

## Bibliography

---

Zschau, J., Isikara, M., Ergünay, O., Yalcin, M., and Erdik, M. (2003). Towards an earthquake early warning system for the megacity of Istanbul. In Zschau, J. and Küppers, A., editors, *Early warning systems for natural disaster reduction*. Springer, Berlin.



## Used Software

Stochastic simulations of seismic ground motions in this work were generated by usage of a modified program version of FINSIM (Beresnev and Atkinson, 1997, 1998). For neural computations, statistics as well as for visualization I have applied the mathematical program MATLAB (*MathWorks Inc.*) with Neural Network, Statistics and Mapping Toolboxes.

This thesis was written with word processing package  $\text{T}_{\text{E}}\text{X}$ , the macro package  $\text{L}^{\text{A}}\text{T}_{\text{E}}\text{X } 2_{\epsilon}$ , and several extensions. The bibliography was generated with  $\text{B}_{\text{I}}\text{B}_{\text{T}}\text{E}_{\text{X}}$ .



# Danksagung / Acknowledgments

Ich danke Prof. Dr. Friedemann Wenzel für Stellung des Promotionsthemas und Übernahme des Hauptreferats meiner Dissertation. Er hat mir durch zahlreiche Konferenz- und Workshopeteilnahmen einen wertvollen wissenschaftlichen Austausch auf nationaler und internationaler Ebene ermöglicht. Von seinem breiten Wissen, seinen weitsichtigen Planungen und Kontakten habe ich sowohl wissenschaftlich als auch menschlich sehr profitieren können. Ich danke ihm auch für sein mir entgegengebrachtes Vertrauen bei der Übergabe der Position der Geschäftsführerin des SFB 461, durch welche ich viele interessante und abwechslungsreiche Aspekte auch jenseits des wissenschaftlichen Alltags kennen lernen durfte.

I thank Prof. Dr. Mustafa Erdik for co-supervision of my PhD thesis, which meant a big honour to me. It was always a pleasure meeting and discussing with him at several conferences or during my visit in Istanbul. Thanks to all the nice people at the Kandilli Observatory, in particular to Eser, Yasin and Karin for their support.

Großer Dank gilt natürlich meinen Korrekturlesern Björn, Adrien, Vladimir, Joachim, Oliver und Ellen, die der Arbeit durch ihre hilfreichen Anregungen und Korrekturen den "letzten Schliff" verliehen haben. Und natürlich danke ich auch Thomas für eine äusserst geniale L<sup>A</sup>T<sub>E</sub>X-Vorlage und Julia für ihre Zusammenarbeit bei der Verknüpfung von Erdbeben-Frühwarnung und Urbaner Shakemap für Bukarest.

Ich danke der Deutschen Forschungsgemeinschaft und dem Land Baden-Württemberg für ihre finanzielle Unterstützung meiner Promotion im Rahmen des Sonderforschungsbereiches (SFB) 461: Von wissenschaftlichen Grundlagen zu Ingenieurmaßnahmen.

Ich danke den Mitarbeitern des Geophysikalischen Institutes für eine sehr angenehme Arbeitsatmosphäre mit regem wissenschaftlichem als auch zwischenmenschlichem Austausch. Ich werde mich gern an die gemeinsamen Spaziergänge zum Supermarkt und unsere Diskussionen beim Mittagessen erinnern. Ich habe viele Leute in meiner Zeit am Geophysikalischen Institut kennen lernen dürfen, die Karlsruhe inzwischen meist verlassen haben: meinen Amtsvorgänger Michael, meinen ehemaligen Zimmergenossen Wolfgang, Thomas, mit dem auch hier und da mal ein Eis/Bier etc. konsumiert wurde, dem ebenfalls Ex-Kieler Eric, Christoph und Christian. Wertvollen Input habe ich in den letzten Monaten auch von Adrien, Joachim und Ellen erhalten. Vielen Dank auch an Euch!

Nicht zu vergessen sind natürlich die festen Mitarbeiter am Geophysikalischen Institut, die durch ihre tägliche Unterstützung im Bereich der EDV, Sekretariat und E-Labor wissenschaftliche Arbeit erst ermöglichen. Vielen Dank an Petra Knopf, Thomas Nadolny, Rainer Plokarz, Gaby Bartman, Monika Hebben, Claudia Payne, Werner Scherer und Hartmut Thomas. Das Beste spart man sich bekanntlich bis zum Schluss: Liebe Silvia, ich danke dir für Deine wertvolle Unterstützung in der

## Danksagung / Acknowledgement

---

SFB-Geschäftsstelle, Deine große Hilfsbereitschaft und natürlich für äusserst nette Plaudereien bei Kaffee und Tee!

Ich hatte eine sehr schöne Zeit in Karlsruhe und dafür möchte ich mich bei Euch allen von Herzen bedanken! Ich würde mich sehr freuen, wenn sich mit dem einen oder anderen die Wege zu einem späteren Zeitpunkt mal wieder kreuzen würden...

Mein größter Dank gilt natürlich Björn und meiner Familie für ihre wertvolle moralische und finanzielle Unterstützung. Ihre aufmunternden Worte haben entscheidend zu der Fertigstellung dieser Dissertation beigetragen.

# Lebenslauf

## Persönliche Daten

Name: Maren Böse  
Geburtsdatum: 13. Dezember 1976  
Nationalität: deutsch  
Geburtsort: Hamburg

## Schulbildung

1983 - 1987 Grundschule Gorch-Fock, Hamburg  
1987 - 1996 Gymnasium Willhöden, Hamburg  
12.06.1996 Allgemeine Hochschulreife

## Hochschulbildung

1996 - 2002 Studium der Geophysik an der  
Christian-Albrechts-Universität zu Kiel  
10.06.2002 Diplom  
seit Juli 2002 Doktorandin an der Fakultät für Physik  
der Universität Karlsruhe (TH)  
seit Januar 2005 Geschäftsführerin des SFB 461: 'Starkbeben:  
Von geowissenschaftlichen Grundlagen  
zu Ingenieurmaßnahmen'